Stochastic transport models in confined networked environments

Daniel Wilson

Wadham College

University of Oxford

A thesis submitted for the degree of

Doctor of Philosophy in Mathematics

Trinity 2019

Abstract

Diffusion of macromolecules within the intracellular environment, tissue generation in scaffolds, and the transport of blood cells through aortic media, are examples of processes which hinge upon the optimal transport of biological agents within complex crowded environments. For example, the organelles within a typical mammalian cell create an environment with a range of heterogeneous microscopic spatial structure known to impede macromolecular motion. A significant challenge for biomathematicians is to develop mathematical transport models on macroscopic length scales that incorporate the key effects of the microscopic spatial structure and the spatial exclusion between biological agents. A useful abstractification is to approximate complex environments as networked topologies that are capable of describing a huge range of heterogeneous spatial structures. This thesis focusses broadly on the extension of stochastic transport models confined to networked environments and their analysis. We introduce a framework for macromolecular transport in a domain that is deconstructed into two region types; one where molecules move freely, and another where there are strong macromolecular crowding effects. Through analysis of the equilibration time, algorithms for optimal network construction are designed and tested. Additionally, we explore search processes for multiple interacting searchers within a networked environment. Quantifying the efficiency of the search process via the parallel cover time, we provide optimal strategies that minimise the cover time of a fixed population of particles. Finally, we propose a new measure of particle displacement that accounts for the total winding of the path of a particle as it moves through a network, finding that statistics of the particle displacement are a function of network topology. Together, this work represents a key step in developing generic algorithms for topological optimisation of stochastic networked systems. Such concepts are of growing importance within modern information theory, biophysics, biotechnology, network science, statistical physics, traffic flow and robotics.

Statement of Originality

This thesis is submitted to the University of Oxford in partial fulfilment of the requirements of the degree of Doctor of Philosophy. This thesis contains no material which has been previously submitted for a degree or diploma at this University or any other institution. This research represents my own original work towards this research degree. The research in Chapter 4 has been published in the *Physical Review E* as Wilson et al. [1]. The research in Chapter 5 has been published in the *SIAM Journal on Applied Mathematics* as Wilson et al. [2].

Contents

List of Figures

Chapter 1

Introduction

Transport processes have the ability to alter the atmosphere of our planet. Recent changes in cloud migration patterns at both the north and south poles are thought to be contributing to climate change [3, 4]. As the planet warms, the mass migration of various species of insects to cooler climates is predicted to spread new diseases and damage our agriculture [5]. More positively, advances in medicine have resulted in the development of targeted drug delivery therapies [6]. These treatments utilise the transport processes existing within our bodies to deliver drugs directly to cancerous tissues, and have the potential to be significantly more effective and less invasive than current radiation therapies. There are countless other examples of transport phenomena that have a direct impact on our lives, and, as such, the study of transport processes has been, and still is, an area of great interest across all research disciplines.

When selecting mathematical models to study transport processes there are two modelling paradigms to which one can subscribe, deterministic models or stochastic models. Each paradigm has its advantages and disadvantages as well as applications to which they are most suited. For example, most studies that investigate traffic flow for vehicular transport [7, 8] use a deterministic framework. Equations of motion that describe the dynamics of both vehicle concentration and average speed are anal-

ysed to answer questions about the optimal design of road geometry [9]. The first mathematical models of avascular tumour growth also used a deterministic framework [10, 11]. These models were then used to design efficient drug therapies to control the size of the tumour [12, 13]. However, recent biological experiments suggest that stochastic phenotypic plasticity plays a significant role in the evolution of drug resistant tumours [14]. As such, new models that account for stochasticity in avascular tumour growth have risen in popularity [15, 16]. Stochasticity is inherent in many biological processes, particularly in intracellular transport processes. For an excellent review of stochastic transport models in intracellular environments see Bressloff and Newby [17] and references therein.

In addition to stochasticity, an important part of many transport processes is the interactions between the individuals (cells, cars, particles, etc.) being transported. It is known that the individual interactions between agents can contribute to emergent global behaviour at the population level. Examples include the collective motion of animals, fish, insects and birds [18, 19], and the collective migration of cell populations during development [20, 21] and regeneration [22]. An advantage of individual-based models (IBMs) is that it is easy to incorporate complex interactions and mechanisms. However, in comparison to deterministic models, IBMs are computationally expensive to simulate and it is usually difficult to determine the behaviour of a model over the entire range of the model parameters. One of the most important, yet often overlooked, ways in which biomolecules interact is through crowding. Reports suggest that up to 40% of the intracellular environment is occupied by biomolecules such as proteins, lipids and nucleic acids [23]. Incorporating the effects of crowding at the particle level has been shown to dominate population-level behaviour [24, 25]. Coarse-grained descriptions of IBMs, in the form of macroscopic partial differential equations (PDEs) that account for the microscopic effects of crowding, are available [26–28]. However, only the simplest models are amenable to these coarse-graining

techniques and analytic solutions are only available for transport processes within simple geometries.

Geometry can influence the dynamics of a transport process significantly. As an example, the geometry of dendritic spines, which are protrusions on the exterior of neuronal cells, have been shown to regulate the diffusion of calcium ions [29]. The spine geometry consists of a narrow neck connected to a large bulky head, and the narrowness of the neck limits the diffusion of calcium ions out of the head. As a result, the disproportionately high concentration of calcium in the head of the spine is used for synaptic transmission between neurons. Another famous example of when electro-physiology is affected by geometry is the beating of a heart [30]. Realistic models of a beating heart discretise computerised images of the whole organ into a fine mesh and numerically solve transport equations for the propagation of the electric potential using finite element methods [31]. Such techniques are highly computationally intensive and require a deterministic framework.

An alternative method to study transport processes and incorporate complex geometries is to consider pore networks [32]. The void space in carbonate and sandstone samples have been described as a network of pores connected by throats. Studies of the fluid dynamics within these pore networks have accurately predicted the permeabilities in the different rock samples [33]. Therefore pore networks are a useful tool to study transport whilst maintaining the spatial structure of the geometry. One advantage of pore networks is that they have significantly fewer nodes than a finite element mesh, thus simulation of transport processes is computationally less expensive. The influence of geometry is often overlooked when modelling biological transport processes. This is in part due to the technical challenges it presents. However, representation of a complex geometry as a network, such as a pore network, would allow for investigations into the functional role of geometry in transport processes.

The intracellular environment is a highly porous medium [34], and reports suggest

that up to 40 % of the environment is occupied by macromolecules [23]. Due to this high occupancy, the effects of macromolecules interacting with one another, known as agent-agent crowding, are non-negligible [23, 24, 35]. Thus, a significant challenge for bio-mathematicians is to develop mathematical transport models on the scale of the whole cell that incorporate the key effects of the microscopic spatial structure as well as agent-agent macromolecular crowding. This thesis aims to develop mathematical models of stochastic transport in confined networked environments that explicitly incorporate crowding effects. The aim is that these new mathematical models will help reveal the effects that geometry and crowding have on important transport statistics of interest.

1.1 Questions, aims and thesis outline

In this section we introduce some more focussed questions surrounding the development of stochastic transport models in confined networked environments. Simultaneously, we briefly outline the chapters of the thesis and discuss how they provide answers to these focussed questions.

Chapter 2: To investigate the role of both geometry and crowding on stochastic transport processes, we first need to understand their roles separately. Intuitively, we can reason that the inclusion of agent-agent crowding effects could result in a "slowing down" of the transport process as particles get in each others way, but is our intuition correct and can this "slowing down" effect be quantified? The work by Dagdug et al. [36] concerns the equilibration time of a population of non-interacting particles which diffuse between two chambers connected via a narrow capillary. This simple domain is a caricature of a heterogeneous confined environment [37] and is the building block for nano-tube vesicle networks [38, 39]. The equilibration time is a measure of the time taken for the distribution of the particles to approach its equilibrium

distribution, and therefore is an ideal transport statistic to measure the effect that crowding has on "slowing down" the transport process. In the paper by Dagdug et al. [36] an expression for the equilibration time is calculated. In their model particles have two different diffusion coefficients, one for particles in the chambers and another for particles in the capillary. As the diffusion coefficient in the chambers increases, the rate at which particles enter the capillary also increases and, as a result, the equilibration time decreases. However, we hypothesise that this monotonic decrease in the equilibration time disappears if crowding is incorporated in the capillary. This is because, as the rate to enter the capillary increases, the occupancy of the capillary will increase and eventually cause a bottleneck that will significantly increase the equilibration time. To test our hypothesis, in Chapter 2 we investigate the equilibration time of a population of particles diffusing between two chambers (which we refer to as reservoirs) connected by a capillary (which we refer to as a narrow channel) with crowding in the capillary. We discover that our hypothesis is correct and quantify the equilibration time in terms of the following model parameters: population size, length of the capillary, and the distinct parameters which control the transport of particles within the chambers and within the capillary.

Chapter 3: We know that macromolecular crowding slows down the equilibration of particles, but what effect does geometry, particularly network topology, have on the equilibration time of a population of particles with crowding effects? It is intuitive that some environments will encourage equilibration more than others, but can the effects be quantified and the spatial structure of optimal networks be characterised? Such questions have applications in the design of nano-porous materials [40]. In Chapter 3 we extend the framework introduced in Chapter 2 to networked environments consisting of reservoirs connected by narrow channels. These networks are reminiscent of both pore networks, extracted from images of the void space of rocks [32], and nano-tube vesicle networks [39]. Using this framework we explore the

effect of topology on equilibration times and identify the networks that encourage faster equilibration.

Chapter 4: A search process is a type of transport process in which the particles, more commonly referred to as searchers, search for targets. Often searchers are not aware of their targets location and stochastic transport can be beneficial in reducing search times compared to deterministic search algorithms [41]. Consider a search process where proteins move along a strand of DNA in search of a target site with which to bind [42]. A strand of DNA is usually considered to be a one-dimensional domain, and its tortuosity in three-dimensional space is often overlooked. However, recent studies of facilitated diffusion have suggested that proteins detach from the DNA strand and diffuse in space to reattach to the DNA strand at a different location [17, 42, 43]. The spatial structure of the protein-DNA complex has been described as a networked environment [44]. Multiple proteins search in parallel along a given DNA strand at any one time and macromolecular crowding has been shown to affect the time taken for proteins to find targets [43]. An interesting question is whether we can quantify the density of proteins along a strand of DNA that optimises the search times. How does this optimal density depend upon the topology of the spatial DNA network? In Chapter 4 we consider optimising searcher density on general networked topologies to minimise the cover time of searchers. The cover time is an upper bound on the time taken for searchers to find targets, and is considered a fundamental measure of efficiency for stochastic search processes [45–48]. The research in this chapter has been published in the *Physical Review E* as Wilson et al. [1].

Chapter 5: Stochastic transport processes are often characterised via transport statistics, such as equilibration times and cover times. Naturally the statistics we choose to study depend upon what questions we wish to ask. In this thesis we often ask what is the effect of network topology on transport statistics of interest? An equally important question is whether the transport statistics we are choosing are

capable of describing networked transport in a meaningful way. Perhaps the most common statistic to describe a transport process is the displacement of a particle. The displacement of a particle that undergoes a stochastic transport process on a network is often measured as the shortest distance between the initial and current positions of the particle [49, 50]. However, this measure of displacement completely ignores the distance accumulated as a particle winds around cycles in a network. In fact, the emergent transport behaviour of cargo in the intracellular environment is correlated to the number of cycles traversed by a random walk on a network describing the conformational states of molecular motors [51, 52]. Kundu et al. [53] introduce the winding number of a Brownian particle on a ring lattice as the number of complete rotations made anticlockwise or clockwise around the ring. In Chapter 5 we generalise the winding number in Kundu et al. [53] and introduce the winding distance as a measure of displacement of a Brownian particle for general networked topologies. We show that for some networks, the winding distance as a measure of displacement can be characterised as ballistic for large times. We further generalise our framework to investigate the winding distance to anomalously diffusive transport processes, which are coarse-grained models to describe tagged particle dynamics in a crowded environment. The research in this chapter has been published in the *SIAM Journal on Applied Mathematics* as Wilson et al. [2].

Chapter 6: In this final chapter we summarise the main results from this thesis, discuss their contribution towards understanding the role of geometry and crowding on stochastic transport processes, and consider avenues for future research.

Chapter 2

Equilibration times in heterogeneous crowded environments: a two reservoir model

Understanding the flocking of starlings [54], the assembly of autonomous robotic systems [55], and the migration of cranial neural crest cells during early embryonic development [56], all require the study of collective motion for an interacting system of particles (birds, robots, or cells). Theoreticians, to make analytical progress, are often required to assume that the particle system is in equilibrium. This assumption is only valid when the timescale(s) of interest are much larger than the time taken for the particle system to equilibrate. In intracellular environments, however, many cell processes [17, 57–59] hinge upon time sensitive transport of macromolecules, such as proteins, nucleic acids and lipids, through crowded environments. Agent-agent crowding effects can increase the time needed for a population of particles to reach equilibrium. Surprisingly, there has been little research that quantifies the

equilibration time for transport processes in crowded environments.

In addition to crowding, geometry plays a crucial role in the regulation of diffusive transport processes. For example, dendritic spines are protrusions on the exterior of neuron cells that participate in synaptic transmission between neurons [29, 60]. Synaptic transmission requires a high concentration of calcium ions within the dendritic spine. The transport of calcium within the spine is modelled as a diffusive process in a heterogeneous domain consisting of a narrow cylindrical neck attached to a vacuous bulky head [61, 62]. The narrow width of the neck has been shown to reduce the number of macromolecules that leave the spine due to macromolecular crowding [63]. Thus, the combination of geometry and crowding ensures a high concentration of calcium ions for synaptic transmission. The non-uniform distribution of mitochondria within typical mammalian cells [64] provides an additional example of a heterogeneous environment comprised of both narrow and vacuous regions.

To begin to understand the roles of both geometry and agent-agent crowding upon diffusive transport processes in complex environments, we develop a caricature transport model that combines both heterogeneous environments and crowding effects. We consider a continuous-time Markov chain (CTMC) for a population of interacting particles residing within a heterogeneous domain consisting of two region types. The domain has two reservoirs, which represent vacuous regions where particles do not compete for space. The two reservoirs are connected via a one-dimensional lattice and each lattice site can hold at most one particle at any time. The lattice connecting the reservoirs is referred to as the narrow channel. From classical probability theory, the equilibration time is calculated as the spectral gap of the transition matrix of the CTMC. However, the high dimensionality of the configuration space renders computation of the eigenvalues infeasible. Therefore, a complementary coarse-grained model with significantly lower dimensionality is introduced and studied when the total occupancy of the narrow channel is both low and high. Analytical formulae for the equi-

libration time are derived that show excellent agreement with the high-dimensional CTMC. Finally, the coarse-grained model is generalised to allow for partial exclusion of particles within the narrow channel: each lattice site has a maximum number of particles it can support at any time which is greater than one. The results from this chapter provide a functional relationship between the equilibration time of a population of interacting parameters and the model parameters, such as the length of the narrow channel and the size of the population. The framework introduced in this chapter presents the first step towards developing a unified framework for transport processes with macromolecular crowding in complex environments.

2.1 The full Markov model

Consider a domain consisting of two identical reservoirs connected by a one-dimensional lattice with K lattice sites, which we refer to as the narrow channel (see Figure 2.1). A total of N particles populate this domain and their configuration at time t is described by the state vector $\vec{S}(t) = (L(t), N_1(t), \ldots, N_K(t), R(t))$. The variables $L(t)$ and $R(t)$ denote the number of particles in the left and right reservoirs at time t, respectively, and $N_i(t)$ denotes the number of particles in lattice site i at time t. Let $\Omega_{N,K}$ be the set of legal configurations, these are vectors $\vec{s} = (n_L, n_1, \ldots, n_K, n_R)$ such that $n_L + n_R + \sum_{i=1}^{K} n_i = N$, where $n_i \in \{0, 1\}$ for $1 \leq i \leq K$ and $n_L, n_R \in \mathbb{N}$. The rates at which states transition to new states depend upon what type of transition event occurs. Particles within the narrow channel jump to adjacent lattice sites or reservoirs at rate α (see Figure 2.1 (i)), whereas particles within the left and right reservoirs jump into the lattice sites one and K, respectively, at rate γ (see Figure 2.1 (ii)). The restriction in the state vectors that $n_i \in \{0, 1\}$, enforces volume exclusion along the narrow channel, and any attempted jump into an occupied lattice site is aborted (see Figure 2.1 (iii), red arrow). Formally, the state vector $\vec{S}(t)$ evolves

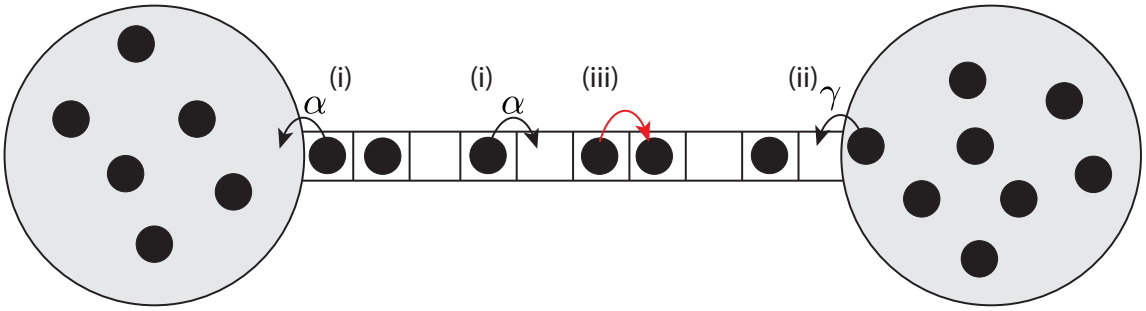

Figure 2.1: A diagrammatic representation of the two reservoir model. The two reservoirs represent regions in space that can support many particles whose motion is unhindered by the effects of volume exclusion. The one-dimensional lattice connecting the two reservoirs is the narrow channel. Each lattice site can support at most a single particle, as such, particles can only jump into vacant neighbouring lattice sites.

according to the following CTMC. A particle in the narrow channel in lattice site i jumps to the adjacent lattice site $i+1$ at rate $\alpha N_i(t)\,(1-N_{i+1}(t))$ for $1 \leq i \leq K-1$. If there is no particle in lattice site i at time t, $N_i(t)=0$, or the adjacent lattice site is occupied, $N_{i+1}(t)=1$, the transition rate, $\alpha N_i(t)\,(1-N_{i+1}(t))$, is zero. Due to the absence of volume exclusion in the reservoirs, a particle jumps from lattice site K into the right reservoir at rate $\alpha N_K(t)$. Similarly, a particle jumps from lattice site i to adjacent lattice site $i-1$ at rate $\alpha N_i(t)\,(1-N_{i-1}(t))$ for $2 \leq i \leq K$, and a particle jumps from lattice site one into the left reservoir at rate $\alpha N_1(t)$. One of the particles in the left reservoir jumps into lattice site one at rate $\gamma L(t)\,(1-N_1(t))$, which is non-zero only if lattice site one is vacant. Finally, $\gamma R(t)\,(1-N_K(t))$ is the rate at which a particle in the right reservoir jumps into lattice site K.

A transition matrix, Q, for the CTMC is constructed as follows. Let $\mathcal{I}\,(\Omega_{N,K})$ be an index set, such that if $u \in \mathcal{I}\,(\Omega_{N,K})$ then $\vec{s}_u \in \Omega_{N,K}$. For $u, v \in \mathcal{I}\,(\Omega_{N,K})$ and $u \neq v$ the matrix entry $Q_{u,v}$ is equal to the rate at which state $\vec{s}_u$ transitions to state $\vec{s}_v$, as detailed above. If a transition cannot occur via a single jump event the matrix entry $Q_{u,v}$ is zero. The diagonal entries are equal to the negative of the row sums, $Q_{u,u} = -\sum_{v \neq u} Q_{u,v}$ for $1 \leq u \leq |\Omega_{N,K}|$. Let $p_u(t) = \mathbb{P}\left(\vec{S}(t) = \vec{s}_u\right)$ for $u \in \mathcal{I}\,(\Omega_{N,K})$, then the

evolution of the probability vector $\vec{p}(t)$, where $[\vec{p}(t)]_u = p_u(t)$, is described by a system of ordinary differential equations (ODEs) $\mathrm{d}\vec{p}(t)/\mathrm{d}t = \vec{p}\, Q$. With initial distribution $\vec{p}(0)$, the solution to this system of ODEs is $\vec{p}(t) = \vec{p}(0)\exp(Qt)$. The spectrum of the matrix Q reveals important properties of the CTMC. In particular, it is well known that the stationary distribution, $\vec{p}(\infty)$, is the principal left-eigenvector of the transition matrix Q. Additionally, through spectral decomposition, the eigenvalues of Q provide timescales upon which the eigenmodes of the vector $\vec{p}(t)$ decays to equilibrium [65]. Thus, the smallest non-trivial[1] eigenvalue in absolute value, $|\lambda_2|$, is known as the spectral gap and is the slowest decaying mode. For a CTMC, the reciprocal of the spectral gap, $\tau = |\lambda_2|^{-1}$, is the canonical measurement for the time required to decay to equilibrium. We refer to τ as the equilibration time for the full Markov model (FMM).

In the absence of volume exclusion along the narrow channel, the equilibration time[2] as a function of γ, the jump rate out of the reservoirs, is monotonically decreasing (see Figure 2.2, dashed curve). However, with volume exclusion incorporated along the narrow channel, the monotonicity of the equilibration time is lost (see Figure 2.2, solid curve). As the jump rate out of the reservoirs increases, more particles enter the narrow channel and undergo a volume excluding random walk. Eventually this single-file diffusion of particles manifests in an increase in the time taken for a particle to switch reservoirs, thus an overall increase in the equilibration time. Here, we seek to understand how the following model parameters affect the equilibration time in the two reservoir model: population size, N; channel length, K; and the distinct jump rates, α and γ.

Conceptually, it is quite straightforward to investigate the effects of volume exclusion on the equilibration time through spectral analysis of the transition matrix.

[1]The transition matrix necessarily has a principal eigenvalue of zero.

[2]Note that the equilibration time for a population of non-interacting particles is equivalent to that of a single particle, due to their independence.

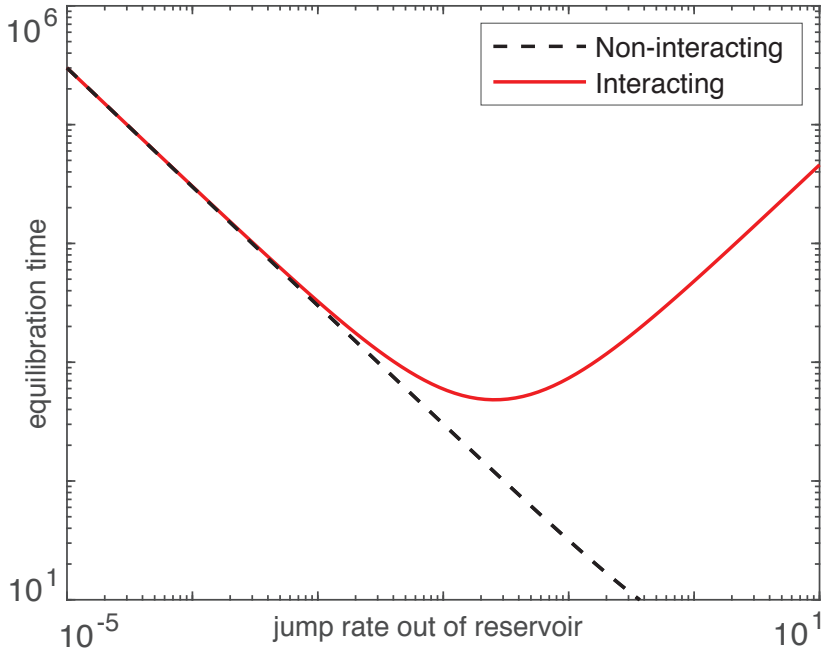

Figure 2.2: The equilibration time of the two reservoir model without particle interactions in the narrow channel (solid black curve), and with particle interactions (dashed red curve). The parameter values are $\alpha = 1$, $N = 100$ and $K = 5$.

However, for even moderate channel lengths, K, the dimensionality of the FMM is extremely high. Suppose there are a total of m particles in the narrow channel. The remaining $N-m$ particles must be split between the two reservoirs, which can occur in $N-m+1$ distinct configurations. For each configuration there are an additional $\binom{K}{m}$ distinct ways to arrange the particles within the channel. Thus, the dimensionality of the FMM is

$$|\Omega_{N,K}| = \sum_{m=0}^{\min(N,K)} (N-m+1)\binom{K}{m}. \tag{2.1}$$

For $N \gg K$, such that $(N-m+1)$ is approximately constant, $|\Omega_{N,K}| \sim \mathcal{O}\left(2^K N\right)$. Due to the factor of 2^K, transition matrices, even for models with moderately small channel lengths, have extremely high dimensionality, and the spectral gap is computationally intractable. Thus, we need to consider coarse-grained models with significantly reduced dimensionality in order to make progress. We first consider equilibrium properties of the FMM that will prove useful.

2.1.1 Equilibrium properties

Define $\rho_i^{(1)}(O,t) = \mathbb{P}(N_i(t)=1)$ to be the occupancy probability of lattice site i at time t. Then $\rho_i^{(1)}(\emptyset,t) = \mathbb{P}(N_i(t)=0)$ is the probability that at time t the site i is vacant, and necessarily $\rho_i^{(1)}(O,t) + \rho_i^{(1)}(\emptyset,t) = 1$. Similarly, let $\rho_L^{(1)}(n,t) = \mathbb{P}(L(t)=n)$ be the probability that n particles occupy the left reservoir at time t. The superscripts, (1), are the order of the probability functions and denote the number of lattice site or reservoir occupancies that the probabilities depend on. We additionally define the two-site probability functions $\rho_{i,i+1}^{(2)}(O,\emptyset,t)$ as the probability that both lattice site i is occupied and lattice site $i+1$ is vacant at time t. Similarly, $\rho_{L,1}^{(2)}(n,O,t)$ is the probability that the left reservoir is occupied by n particles and the first lattice site in the narrow channel is occupied at time t.

To derive ODEs for the single-site probability functions, we consider the evolution of the probabilities over the interval $[t,t+\Delta t]$, where $\Delta t \ll 1$, such that in this interval the probability of more than one jump event occurring is $\mathcal{O}((\Delta t)^2)$. The waiting time for a jump event along the narrow channel is exponentially distributed with rate α, and lies within the interval $[t,t+\Delta t]$ with probability $\alpha\Delta t$ to leading order. Consider $\rho_i^{(1)}(O,t+\Delta t)$ for $2 \le i \le K-1$, so the lattice site is not adjacent to a reservoir. There are three possibilities that result in lattice site i being occupied at time $t+\Delta t$. Firstly, lattice site i is already occupied at time t and no jump event is attempted, this occurs with probability $(1-2\alpha\Delta t)\,\rho_i^{(1)}(O,t)$. Secondly, lattice site i is occupied at time t by a particle that attempts but fails to jump into an occupied neighbouring lattice site, with probability $\alpha\Delta t\left(\rho_{i,i+1}^{(2)}(O,O,t) + \rho_{i-1,i}^{(2)}(O,O,t)\right)$. Finally, lattice site i is vacant at time t and a particle in a neighbouring lattice site jumps into lattice site i, this occurs with probability $\alpha\Delta t\left(\rho_{i,i+1}^{(2)}(\emptyset,O,t) + \rho_{i-1,1}^{(2)}(O,\emptyset,t)\right)$. Combining

these three cases yields an expression for $\rho_i^{(1)}(O, t+\Delta t)$ as follows,

$$\begin{aligned}\rho_i^{(1)}(O,t+\Delta t) &= (1-2\alpha\Delta t)\,\rho_i^{(1)}(O,t) \\ &\quad +\alpha\Delta t\left(\rho_{i,i+1}^{(2)}(O,O,t)+\rho_{i-1,1}^{(2)}(O,O,t)\right) \\ &\quad +\alpha\Delta t\left(\rho_{i,i+1}^{(2)}(\emptyset,O,t)+\rho_{i-1,1}^{(2)}(O,\emptyset,t)\right) \\ &\quad +\mathcal{O}\left((\Delta t)^2\right). \end{aligned} \tag{2.2}$$

It is possible to combine the two-site probability functions into single-site functions using conservation statements [66, 67], for example $\rho_{i,i+1}^{(2)}(O,O,t)+\rho_{i,i+1}^{(2)}(\emptyset,O,t)=\rho_{i+1}^{(1)}(O,t)$. Therefore, rearranging Equation (2.2) yields

$$\begin{aligned}\frac{\rho_i^{(1)}(O,t+\Delta t)-\rho_i^{(1)}(O,t)}{\Delta t} &= \alpha\left(\rho_{i+1}^{(1)}(O,t)+\rho_{i-1}^{(1)}(O,t)\right) \\ &\quad -2\alpha\rho_i^{(1)}(O,t)+\mathcal{O}(\Delta t). \end{aligned} \tag{2.3}$$

Letting $\Delta t \to 0$, we obtain the following ODE

$$\frac{\mathrm{d}\rho_i^{(1)}(O,t)}{\mathrm{d}t}=\alpha\left(\rho_{i+1}^{(1)}(O,t)+\rho_{i-1}^{(1)}(O,t)-2\rho_i^{(1)}(O,t)\right), \tag{2.4}$$

for $2 \leq i \leq K-1$. The evolution equation for $\rho_1^{(1)}(O,t)$ is derived similarly. For $\Delta t \ll 1$ we approximate $\rho_1^{(1)}(O,t+\Delta t)$ in terms of the one- and two-site probability functions that affect the occupancy of lattice site one in at most one jump,

$$\begin{aligned}\rho_1^{(1)}(O,t+\Delta t) &= (1-2\alpha\Delta t)\,\rho_1^{(1)}(O,t)+\alpha\Delta t\rho_{1,2}^{(2)}(O,O,t) \\ &\quad +\alpha\Delta t\rho_{1,2}^{(2)}(\emptyset,O,t)+\gamma\Delta t\sum_{n=1}^{N} n\rho_{L,1}^{(2)}(n,\emptyset,t) \\ &\quad +\mathcal{O}\left((\Delta t)^2\right). \end{aligned} \tag{2.5}$$

Manipulating Equation (2.5) and reducing the order of the probability functions re-

sults in the ODE

$$\frac{\mathrm{d}\rho_1^{(1)}(O,t)}{\mathrm{d}t} = \gamma \sum_{n=0}^{N} n\rho_{L,1}^{(2)}(n,\emptyset,t) + \alpha\rho_2^{(1)}(O,t) - 2\alpha\rho_1^{(1)}(O,t). \tag{2.6}$$

Via symmetry, a similar ODE can be written for $\rho_K^{(1)}(O,t)$, and the last probability function to consider is $\rho_L^{(1)}(n,t)$ (noting that $\rho_R^{(1)}(n,t)$ can also be written via symmetry). Following the above procedure, we derive

$$\begin{aligned}\frac{\mathrm{d}\rho_L^{(1)}(n,t)}{\mathrm{d}t} &= \alpha\left(\rho_{L,1}^{(2)}(n-1,O,t) - \rho_{L,1}^{(2)}(n,O,t)\right) \\ &\quad +\gamma\left((n+1)\,\rho_{L,1}^{(2)}(n+1,\emptyset,t) - n\rho_{L,1}^{(2)}(n,\emptyset,t)\right).\end{aligned} \tag{2.7}$$

Let $\langle L(t)\rangle = \sum_{n=0}^{N} n\rho_L^{(1)}(n,t)$, be the average number of particles in the left reservoir at time t. Multiplying Equation (2.7) by n, and summing over n from zero to N, results in the ODE

$$\begin{aligned}\frac{\mathrm{d}\langle L(t)\rangle}{\mathrm{d}t} &= \alpha\sum_{n=0}^{N} n\rho_{L,1}^{(2)}(n-1,O,t) - \alpha\sum_{n=0}^{N} n\rho_{L,1}^{(2)}(n,O,t) \\ &\quad +\gamma\sum_{n=0}^{N} n\,(n+1)\,\rho_{L,1}^{(2)}(n+1,\emptyset,t) \\ &\quad -\gamma\sum_{n=0}^{N} n^2\rho_{L,1}^{(2)}(n,\emptyset,t).\end{aligned} \tag{2.8}$$

Simplifying the right-hand side of Equation (2.8) and collating with Equations (2.6) and (2.4) yields the following system of ODEs

$$\frac{\mathrm{d}\langle L(t)\rangle}{\mathrm{d}t} = \alpha\rho_1^{(1)}(O,t) - \gamma\sum_{n=0}^{N} n\rho_{L,1}^{(2)}(n,\emptyset,t), \tag{2.9a}$$

$$\frac{\mathrm{d}\rho_1^{(1)}(O,t)}{\mathrm{d}t} = \gamma\sum_{n=0}^{N} n\rho_{L,1}^{(2)}(n,\emptyset,t) + \alpha\rho_2^{(1)}(O,t) - 2\alpha\rho_1^{(1)}(O,t), \tag{2.9b}$$

$$\vdots$$

$$\vdots$$

$$\frac{\mathrm{d}\rho_i^{(1)}(O,t)}{\mathrm{d}t} = \alpha\left(\rho_{i+1}^{(1)}(O,t) + \rho_{i-1}^{(1)}(O,t) - 2\rho_i^{(1)}(O,t)\right), \tag{2.9c}$$

$$\vdots$$

$$\frac{\mathrm{d}\rho_K^{(1)}(O,t)}{\mathrm{d}t} = \gamma\sum_{n=0}^{N} n\rho_{K,R}^{(2)}(\emptyset,n,t) + \alpha\rho_{K-1}^{(1)}(O,t) - 2\alpha\rho_K^{(1)}(O,t), \tag{2.9d}$$

$$\frac{\mathrm{d}\langle R(t)\rangle}{\mathrm{d}t} = \alpha\rho_K^{(1)}(O,t) - \gamma\sum_{n=0}^{N} n\rho_{K,R}^{(2)}(\emptyset_K,n,t), \tag{2.9e}$$

where, by symmetry, the evolution equations for $\rho_K^{(1)}(O,t)$ and $\langle R(t)\rangle$ are derived from Equations (2.6) and (2.8), respectively.

The probability functions in equilibrium are calculated by setting the left-hand side of Equations (2.9) to zero. The occupancy probabilities $\rho_i^{(1)}(O,\infty)$ are identical for all lattice sites i, and equal to some constant ρ^*, termed the *equilibrium density*. Additionally, $\alpha\rho^* = \gamma\sum_{n=0}^{N} n\rho_{L,1}^{(2)}(n,\emptyset,\infty) = \gamma\sum_{n=0}^{N} n\rho_{K,R}^{(2)}(\emptyset,n,\infty)$, where the term $\gamma\sum_{n=0}^{N} n\rho_{L,1}^{(2)}(n,\emptyset,\infty)$ is the average rate at which particles successfully jump out of the left reservoir in equilibrium, and depends upon a two-site probability function that we have no closed expression for. Writing down the system of ODEs for every two-site probability function provides an expression for $\rho_{L,1}^{(2)}(n,\emptyset,\infty)$. However, the expression will depend upon three-site probability functions. Repeating this procedure results in a hierarchy of problems to solve with increasing complexity. A known solution is to use a moment-closure approximation to close the system [66, 68]. For example, the mean-field approximation (MFA) assumes independence of the occupancy of distinct lattice sites and reservoirs, such that $\rho_{L,1}^{(2)}(n,\emptyset,\infty) \approx \rho_L^{(1)}(n,\infty)\,\rho_1^{(1)}(\emptyset,\infty)$. Therefore, the average rate out of the left reservoir in equilibrium is approximated by $(1-\rho^*)\langle L(\infty)\rangle$.

The equilibrium distribution for the FMM, $\vec{p}(\infty)$, is accessible via the normalised principal left-eigenvector of the transition matrix in Section 2.1. For a two reser-

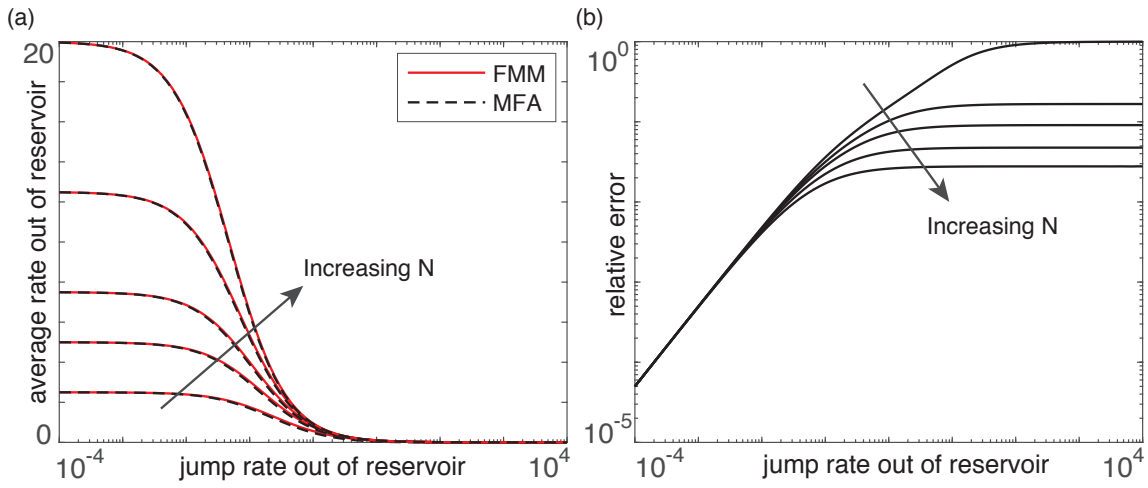

Figure 2.3: The validity of the MFA over a variety of population sizes. (a): The average rate out of the left reservoir calculated from the equilibrium distribution, $\vec{p}(\infty)$, for the FMM (solid curves). The average rate out of the left reservoir, $(1-\rho^*)\langle L(\infty)\rangle$ (dashed curves). (b): The relative error, $\mathcal{E}_{\text{rate}}$, given by Equation (2.10). The model parameters are $\alpha = 1$, $K = 5$ and $N \in \{5, 10, 15, 25, 40\}$.

voir model with sufficiently low dimensionality (channel length $K = 5$), $\vec{p}(\infty)$ is used to calculate the average rate out of the left reservoir and the approximation $(1-\rho^*)\langle L(\infty)\rangle$ (see Figure 2.3(a)). The MFA provides an excellent approximation over the entire range of γ, the jump rate out of the reservoirs. However, in order to quantify the validity of the MFA we define, $\mathcal{E}_{\text{rate}}$, the relative error as

$$\mathcal{E}_{\text{rate}} = \frac{\left| \sum_{n=0}^{N} n\rho_{L,1}^{(2)}(n,\emptyset,\infty) - (1-\rho^*)\langle L(\infty)\rangle \right|}{\left| \sum_{n=0}^{N} n\rho_{L,1}^{(2)}(n,\emptyset,\infty) \right|}. \tag{2.10}$$

The relative error increases as γ increases (see Figure 2.3(b)), this is because as more particles occupy the narrow channel the MFA worsens due to an increase in spatial correlations between particles. However, $\mathcal{E}_{\text{rate}}$ decreases over all values of γ for larger population sizes (see Figure 2.3(b), arrow).

The occupancy of a lattice site along the narrow channel is either one or zero, so the probability a lattice site is occupied is equivalent to the average occupancy of

that lattice site. Therefore $\langle L(t)\rangle + \sum_{i=1}^{K} \rho_i^{(1)}(O,t) + \langle R(t)\rangle$ is the average number of particles in the entire domain. The population is conserved, for all times t, and in equilibrium $2\langle L(\infty)\rangle + K\rho^* = N$, where by symmetry $\langle R(\infty)\rangle = \langle L(\infty)\rangle$. Substituting $\langle L(\infty)\rangle = (N - \rho^* K)/2$ into $\alpha\rho^* \approx \gamma(1-\rho^*)\langle L(\infty)\rangle$ (set the right-hand side of Equation (2.9a) to zero and apply the MFA), results in the quadratic expression

$$K\gamma(\rho^*)^2 - [2\alpha + \gamma(N+K)]\rho^* + N\gamma \approx 0. \tag{2.11}$$

Let $\tilde{\rho}^*$ be the approximate equilibrium density, defined as the smallest root of the quadratic equation found by solving Equation (2.11) as an equality (the only root that lies between zero and one). Therefore, the approximate equilibrium density is

$$\tilde{\rho}^* = \frac{2\alpha + \gamma(N+K) - \sqrt{[2\alpha + \gamma(N+K)]^2 - 4NK\gamma^2}}{2K\gamma}. \tag{2.12}$$

The expression for $\tilde{\rho}^*$ in Equation (2.12) shows excellent agreement with the true equilibrium density, calculated via $\vec{p}(\infty)$, provided that the population size is sufficiently high (see Figure 2.4(a)). Plots of the relative error, $\mathcal{E}_{\rho^*} = |\rho^* - \tilde{\rho}^*|/\rho^*$, demonstrate that the approximate equilibrium density improves over all values of γ as the population size increases (see Figure 2.4(b), arrow). The analytical expression for the equilibrium density in Equation (2.12) allows us to understand how the model parameters, α, γ, N and K, affect the occupancy of the narrow channel lattice sites. In the next sections we derive coarse-grained models in both the low- and high-density regimes, and use Equation (2.12) to be explicit for which regions in the model parameter space of the FMM our coarse-grained models are valid.

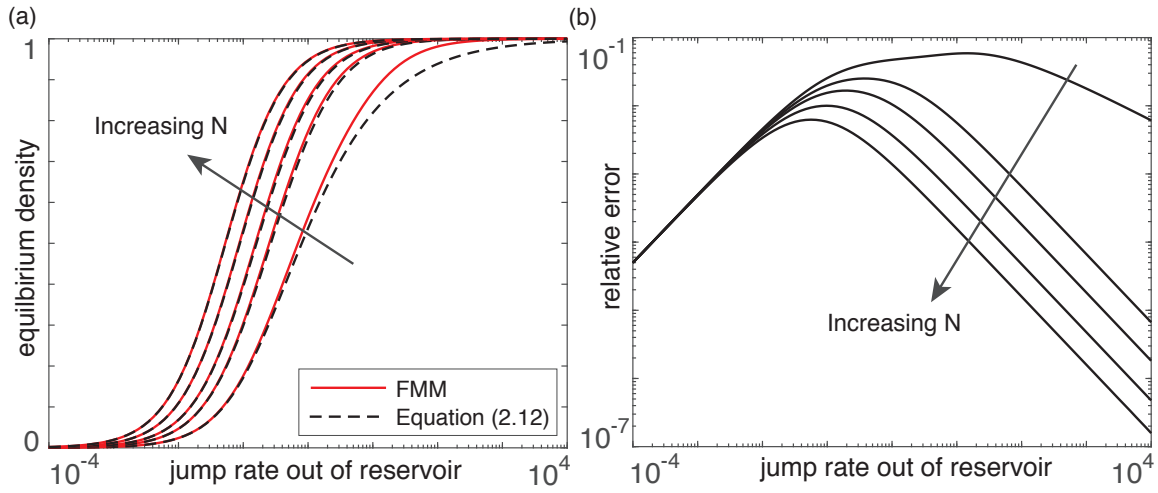

Figure 2.4: The validity of the approximate equilibration density. (a): The equilibrium density ρ^* is calculated from the equilibrium distribution, $\vec{p}(\infty)$, for the FMM (solid curves). The approximate equilibrium density $\tilde{\rho^*}$ is given by Equation (2.12) (dashed curves). (b): The relative error, $\mathcal{E}_{\rho^*} = |\tilde{\rho^*} - \rho^*|/\rho^*$ for a variety of population sizes. The model parameters are $\alpha = 1$, $K = 5$ and $N \in \{5, 10, 15, 25, 40\}$.

2.2 A reduced Markov model: the low-density regime

Explicit modelling of the narrow channel is responsible for the extremely high dimensionality of the FMM. To mitigate this issue, in this section a reduced Markov model (RMM) is introduced, where a particle jumps directly between the reservoirs with transition rates that incorporate the impact of the narrow channel. The model parameters of the FMM are selected to satisfy $\gamma(N-K) \ll 2\alpha$, such that the model is in the low-density regime[3], i.e. $\rho^* \ll 1$. In this regime the occupancy of the narrow channel is low, and it is predicted that the effects of volume exclusion are negligible. The transition rates for the RMM are derived from the *particle switching time*, which is the time taken for a particle in one reservoir to cross the narrow channel and enter the other reservoir. Suppose, initially, that every lattice site is vacant and the left

[3]Recall, that $\alpha\rho^* = \gamma \sum_{n_L=0}^{N} n_L \rho^{(2)}(n_L, \emptyset_1, \infty)$ from Section 2.1.1. In the low-density regime, $\rho^* \ll 1$, and so $\rho^{(2)}(n_L, \emptyset_1, \infty) \approx \rho^{(1)}(n_L, \infty)$ as the first lattice site is almost always empty. Therefore, $\alpha\rho^* \approx \gamma\langle L(\infty)\rangle$, and as $\langle L(\infty)\rangle = (N - \rho^* K)/2$ we find that $\rho^* \sim \gamma N/(2\alpha + \gamma K)$, thus we require that $\gamma(N-K) \ll 2\alpha$.

reservoir is occupied by n_L particles. The particle switching time, $T_{\text{switch}}(n_L)$, is described by two additional random variables T_{enter} and T_{absorb}. Firstly, any one of the n_L particles in the left reservoir will enter the narrow channel after an exponentially distributed amount of time, T_{enter}, with rate parameter γn_L. Lattice site one is now occupied by a particle which undergoes a symmetric random walk on the lattice of the narrow channel. Eventually, at time T_{absorb}, the particle is absorbed into either the left reservoir, with probability $K/(K+1)$, or the right reservoir, with probability $1/(K+1)$. If a particle is absorbed into the left reservoir, no switch has occurred and a new particle must enter the narrow channel. The whole process repeats until eventually a particle is absorbed into the right reservoir, at which point the particle switching is complete. The number of attempts before absorption of a particle into the right reservoir, G_{K+1}, is geometrically distributed with success probability $1/(K+1)$. The particle switching time is therefore written as the following random sum

$$T_{\text{switch}}(n_L) = \sum_{j=1}^{G_{K+1}} T^j_{\text{enter}} + T^j_{\text{absorb}}, \tag{2.13}$$

where the T^j_{enter} are independent and identically distributed (i.i.d.) exponential random variables with rate parameter γn_L and the T^j_{absorb} are i.i.d. first passage times for particles in lattice site one to hit either reservoir.

The RMM in the low-density regime therefore has transition rates, $k_{\text{LD}}(n_L)$, which are equated to the reciprocal of the mean particle switching time, $k_{\text{LD}}(n_L) = \langle T_{\text{switch}}(n_L)\rangle^{-1}$, where $\langle T_{\text{switch}}(n_L)\rangle = \langle G_{K+1}\rangle\left(\langle T_{\text{enter}}\rangle + \langle T_{\text{absorb}}\rangle\right)$. First passage times on a finite lattice are well studied [69] and $\langle T_{\text{absorb}}\rangle = K/2\alpha$. The transition rate for a particle to switch from the left to the right reservoir in the RMM is therefore

$$k_{\text{LD}}(n_L) = \frac{1}{K+1}\left(\frac{1}{\gamma n_L} + \frac{K}{2\alpha}\right)^{-1}. \tag{2.14}$$

By symmetry, the transition rate for a particle to switch from the right to the left

reservoir is found by replacing n_L with n_R in Equation (2.14).

The validity of the RMM relies on how well the particle switching time, $T_{\text{switch}}(n_L)$, is approximated by an exponential distribution with rate parameter $k_{\text{LD}}(n_L)$. Consider the limit $\alpha \to \infty$, where α is the jump rate of a particle at any of the lattice sites within the narrow channel. The time for a particle in lattice site one to be absorbed by either reservoir tends to zero, i.e. $T_{\text{absorb}} \to 0$. The particle switching time simplifies and can be written as $T_{\text{switch}}(n_L) = \sum_{j=1}^{G_{K+1}} T^j_{\text{enter}}$, which is exponentially distributed with rate parameter $\gamma n_L/(K+1)$. For finite but large α, recall that $\gamma N \ll 2\alpha$ in the low-density regime. We wish to investigate how well the particle switching time can be approximated by an exponential distribution. Therefore in the next section we derive the full distribution of the particle switching time.

2.2.1 Full distribution of the particle switching time

In this section, the full distribution of the particle switching time is characterised via the moment generating function (MGF). Consider a continuous random variable X, with a probability density function $f_X(x)$, supported on $[0, \infty)$. The MGF of X is defined as $M_X(s) = \int_0^\infty e^{sx} f_X(x)\, \mathrm{d}x$. For a discrete random variable N, with probability mass function $p_N(n)$ supported on the non-negative integers, the probability generating function (PGF) is defined as $P_N(s) = \sum_{n=0}^{\infty} p_N(n) s^n$. Two useful properties of the MGF are briefly discussed. Firstly, let $Z = \sum_{i=1}^{N} X^i$ for i.i.d continuous random variables X^i, then $M_Z(s) = P_N\left(M_X(s)\right)$. Secondly, for independent continuous random variables X and Y, their sum has MGF $M_{X+Y}(s) = M_X(s) M_Y(s)$. Applying these results to $T_{\text{switch}}(n_L)$ in Equation (2.13) yields

$$M_{T_{\text{switch}}(n_L)}(s) = P_{G_{K+1}}\left[M_{T_{\text{enter}}}(s) M_{T_{\text{absorb}}}(s)\right]. \tag{2.15}$$

Recall G_{K+1} and T_{enter} are geometrically and exponentially distributed, respectively. Their generating functions are therefore $P_{G_{K+1}}(s) = s/((K+1)-Ks)$ and $M_{T_{\text{enter}}}(s) = \gamma n_L/(\gamma n_L - s)$. Substituting the generating functions into Equation (2.15) yields

$$M_{T_{\text{switch}}(n_L)}(s) = \frac{\gamma n_L M_{T_{\text{absorb}}}(s)}{(K+1)(\gamma n_L - s) - \gamma n_L K M_{T_{\text{absorb}}}(s)}. \tag{2.16}$$

To obtain a closed expression for the MGF of the particle switching time, we require $M_{T_{\text{absorb}}}(s)$, the MGF of the first passage time on a finite lattice. It is convenient to note that the Laplace transform, $L_X(s)$, of the probability distribution for a random variable X is equivalent to the MGF up to a change in sign of the explanatory variable, i.e. $L_X(s) = M_X(-s)$.

2.2.1.1 Laplace transform of the first passage time on a finite lattice

The following derivation is adapted from "A guide to first passage processes" by Redner [69]. Consider a finite lattice with lattice sites $\{0, 1, \ldots, K+1\}$, where one to K are the narrow channel lattice sites, and lattice sites zero and $K+1$ correspond to the left and right reservoirs, respectively. A particle is initially located in lattice site one, and jumps to adjacent lattice sites at a rate α, until absorption at either site zero or $K+1$. The probability, $p_i(t)$, that the particle is located at lattice site i at time t, evolves according to the chemical master equations

$$\begin{aligned}
\frac{\mathrm{d}p_0(t)}{\mathrm{d}t} &= \alpha p_1(t), && && \text{(2.17a)}\\
\frac{\mathrm{d}p_1(t)}{\mathrm{d}t} &= \alpha p_2(t) - 2\alpha p_1(t), && && \text{(2.17b)}\\
\frac{\mathrm{d}p_i(t)}{\mathrm{d}t} &= \alpha\left(p_{i+1}(t) + p_{i-1}(t)\right) - 2\alpha p_i(t), && 2 \leq i \leq K-1, && \text{(2.17c)}\\
\frac{\mathrm{d}p_K(t)}{\mathrm{d}t} &= \alpha p_{K-1}(t) - 2\alpha p_K(t), && && \text{(2.17d)}\\
\frac{\mathrm{d}p_{K+1}(t)}{\mathrm{d}t} &= \alpha p_K(t), && && \text{(2.17e)}
\end{aligned}$$

with initial conditions $p_i(0) = \delta_{1,i}$ for $0 \leq i \leq K+1$. The first passage time to hit either end of the lattice, T_{absorb}, has probability distribution function $f_{\text{absorb}}(t)$. The probability a particle has been absorbed by time t is given by $p_0(t) + p_{K+1}(t)$. Introducing the Laplace transformations $L_{T_{\text{absorb}}}(s) = \int_0^\infty e^{-st} f_{\text{absorb}}(t)\mathrm{d}t$, $\tilde{P}_i(s) = \int_0^\infty e^{-st} p_i(t)\mathrm{d}t$, and noting that $p_0(t) + p_{K+1}(t) = \int_0^t f_{\text{absorb}}(u)\mathrm{d}u$, yields the expression $L_{T_{\text{absorb}}}(s) = s\left(\tilde{P}_0(s) + \tilde{P}_{K+1}(s)\right)$. To calculate the Laplace transformations of the occupancy probabilities $\tilde{P}_0(s)$ and $\tilde{P}_{K+1}(s)$ it is convenient to rescale time. Letting $\hat{t} = \alpha t$ and $\hat{p}_i(\hat{t}) = p_i(t)$, and applying the Laplace transformation, $\hat{P}_i(s) = \int_0^\infty \hat{p}_i(\hat{t}) \exp(-s\hat{t})\mathrm{d}\hat{t}$, to the system of ODEs in Equations (2.17), results in the system of algebraic equations

$$\begin{aligned}
\hat{P}_0(s) &= \frac{a}{1-2a}\hat{P}_1(s), && \text{(2.18a)}\\
\hat{P}_1(s) &= a\hat{P}_2(s) + a, && \text{(2.18b)}\\
\hat{P}_i(s) &= a\hat{P}_{i+1}(s) + a\hat{P}_{i-1}(s), \qquad 2 \leq i \leq K-1, && \text{(2.18c)}\\
\hat{P}_K(s) &= a\hat{P}_{K-1}(s), && \text{(2.18d)}\\
\hat{P}_{K+1}(s) &= \frac{a}{1-2a}\hat{P}_K(s), && \text{(2.18e)}
\end{aligned}$$

where $a = 1/(s+2)$. Rearranging Equations (2.18), and introducing variables f_i such that $f_0 = 1$, $f_1 = a^2$ and $f_i = a^2/(1 - f_{i-1})$, yields the first order recurrence relation

$$\hat{P}_i(s) = \frac{f_i}{a}\hat{P}_{i+1}(s) + \frac{\prod_{j=2}^{i} f_j}{a^{i-2}}, \tag{2.19}$$

for $2 \leq i \leq K-1$. Combining Equations (2.18d), (2.18e) and (2.19) gives

$$\hat{P}_{K+1}(s) = \frac{\prod_{j=2}^{K} f_j}{(1-2a)a^{K-3}}. \tag{2.20}$$

Following Redner [69] we substitute $f_i = g_i/h_i$ into $f_i = a^2/(1 - f_{i-1})$, and find that $g_i = a^2 h_{i-1}$ and $h_i = h_{i-1} - a^2 h_{i-2}$. The second order linear recurrence relation for

h_i has the general solution

$$h_i = A_+ (\lambda_+)^i + A_- (\lambda_-)^i , \tag{2.21}$$

where $\lambda_\pm = \left(1 \pm \sqrt{1-4a^2}\right)/2$. Noting that $f_i = a^2 h_{i-1}/h_i$ and $f_1 = a^2$, the constants A_+ and A_- are chosen such that $h_0 = h_1 = 1$ (the only requirement is $h_0/h_1 = 1$). The particular solution for h_i is

$$h_i = \left(\frac{1-\lambda_-}{\lambda_+ - \lambda_-}\right)(\lambda_+)^i + \left(\frac{\lambda_+ - 1}{\lambda_+ - \lambda_-}\right)(\lambda_-)^i . \tag{2.22}$$

Again noting that $f_i = a^2 h_{i-1}/h_i$, the product, $\prod_{j=2}^{K} f_j$, in Equation (2.20) is simply $a^{2K-2} h_1/h_K$, and therefore

$$\hat{P}_{K+1}(s) = \frac{a^{K+1}}{1-2a} \frac{\lambda_+ - \lambda_-}{(\lambda_+)^{K+1} - (\lambda_-)^{K+1}}. \tag{2.23}$$

Similar analysis of Equations (2.18) yields

$$\hat{P}_0(s) = \frac{a^2}{1-2a} \cdot \frac{(\lambda_+)^K - (\lambda_-)^K}{(\lambda_+)^{K+1} - (\lambda_-)^{K+1}}. \tag{2.24}$$

Recalling that $L_{T_{\text{absorb}}}(s) = s\left(\tilde{P}_0(s) + \tilde{P}_{K+1}(s)\right)$, and noting that $\tilde{P}_i(s) = \alpha^{-1}\hat{P}_i\left(\alpha^{-1}s\right)$ gives

$$L_{T_{\text{absorb}}}(s) = \frac{s}{\alpha}\left(\hat{P}_0\left(\frac{s}{\alpha}\right) + \hat{P}_{K+1}\left(\frac{s}{\alpha}\right)\right). \tag{2.25}$$

Introducing $\phi(s) = \tanh^{-1}\left(\sqrt{1 - 4\alpha^2/(s+2\alpha)^2}\right)$, and combining Equations (2.23), (2.24) and (2.25), results in

$$L_{T_{\text{absorb}}}(s) = \frac{\sinh(\phi(s)) + \sinh(K\phi(s))}{\sinh((K+1)\phi(s))}. \tag{2.26}$$

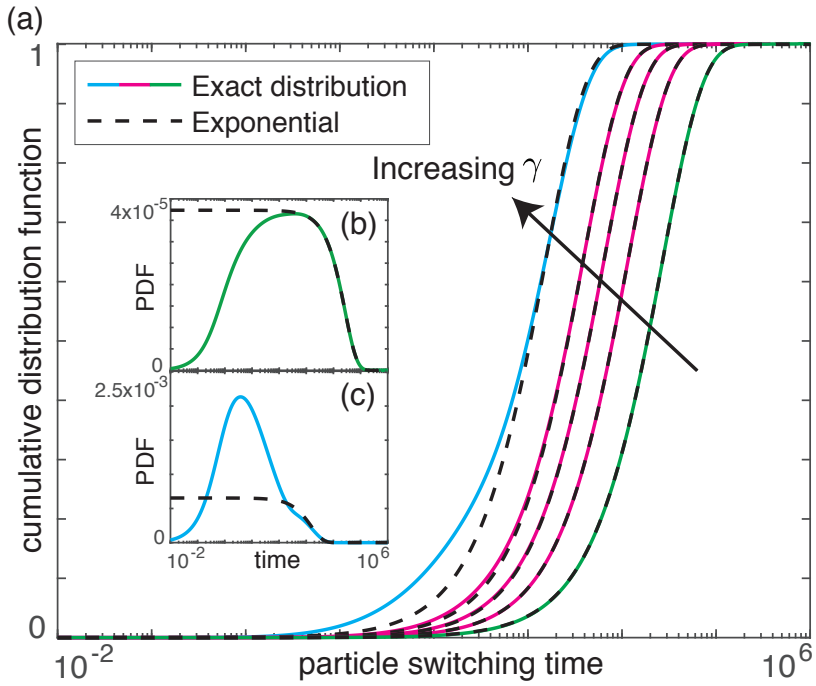

Figure 2.5: The particle switching time distribution (solid curves) compared with an exponential distribution (dashed curves). (a): The CDFs for the particle switching time and the exponential distribution with rate parameter $k_{\mathrm{LD}}(n_L)$ given by Equation (2.14) over a range of reservoir jump rates γ. (b): The PDF of the particle switching time when $\gamma = 10^{-5}$ and the low-density assumption is valid. (c): The PDF of the particle switching time when $\gamma = 10^{-3}$ and the low-density assumption does not hold. The parameters used are $\alpha = 1$, $n_L = 200$, $K = 50$ and the reservoir jump rates are $\gamma \in \{10^{-5}, 2.5 \times 10^{-5}, 5 \times 10^{-5}, 10^{-4}, 10^{-3}\}$.

Recalling that $M_{T_{\mathrm{absorb}}}(s) = L_{T_{\mathrm{absorb}}}(-s)$, the MGF for the particle switching time in Equation (2.16) has the closed form

$$M_{T_{\mathrm{switch}}(n_L)}(s) = \frac{\gamma n_L \left(\dfrac{\sinh(\phi'(s)) + \sinh(K\phi'(s))}{\sinh((K+1)\phi'(s))} \right)}{(K+1)(\gamma n_L - s) - \gamma n_L K \left(\dfrac{\sinh(\phi'(s)) + \sinh(K\phi'(s))}{\sinh((K+1)\phi'(s))} \right)}, \quad (2.27)$$

where $\phi'(s) = \phi(-s)$.

The cumulative distribution function (CDF) of $T_{\mathrm{switch}}(n_L)$ is calculated numerically from Equation (2.27) using a Talbot inversion scheme [70] over a range of values for γ, the reservoir jump rate (see Figure 2.5(a)). There is excellent agreement be-

tween the CDF of $T_{\text{switch}}(n_L)$ and the CDF of an exponential random variable with parameter $k_{\text{LD}}(n_L)$ given in Equation (2.14), for low values of γ. In particular, for parameters such that $\rho^* = 0.01$, other than for very short times the probability distribution function (PDF) shows excellent agreement (see Figure 2.5(b)).

However, as the reservoir jump rate increases (see Figure 2.5(a), arrow) the agreement between CDFs for the exponential distribution and the particle switching time worsens. For parameters such that $\rho^* \approx 0.1$, the distribution of the particle switching time only has an exponential tail (see Figure 2.5(c)).

2.2.2 Equilibration time of the reduced Markov model

In the low-density regime we have verified that the particle switching time can be considered to be approximately exponential, but how does the equilibration time of the RMM compare to the FMM? The state vectors of the RMM are (n_L, n_R) for non-negative integers n_L and n_R such that $n_L + n_R = N$. Therefore, the RMM has a state space with dimensionality $N+1$ and the state vectors can be written as $(i, N-i)$ for $0 \leq i \leq N$. The state $(i, N-i)$ transitions to the state $(i-1, N-i+1)$ if one of the i particles in the left reservoir switches to the right reservoir. This transition occurs at rate $k_{\text{LD}}(i) = \langle T_{\text{switch}}(i) \rangle^{-1}$ given in Equation (2.14). Similarly, a transition from state $(i, N-i)$ to state $(i+1, N-i-1)$ occurs at rate $k_{\text{LD}}(N-i) = \langle T_{\text{switch}}(N-i) \rangle^{-1}$. The RMM in the low-density regime has a tridiagonal transition matrix, Q^{LD}, where the entries on the sub-diagonal are $Q^{\text{LD}}_{i,i-1} = k_{\text{LD}}(i)$, the super-diagonal has entries $Q^{\text{LD}}_{i,i+1} = k_{\text{LD}}(N-i)$, and the diagonal is given by $Q^{\text{LD}}_{i,i} = -\left(k_{\text{LD}}(i) + k_{\text{LD}}(N-i)\right)$. The equilibration time for the RMM is calculated as the reciprocal of the spectral gap of Q^{LD} and it agrees excellently with the equilibration time for the FMM (see Figure 2.6) for small values of γ. Differences between the equilibration times of the FMM and RMM only become noticeable when $\gamma \sim 0.002$, thus, there is good agreement for model parameters where the equilibrium density satisfies $\rho^* \lesssim 0.1$.

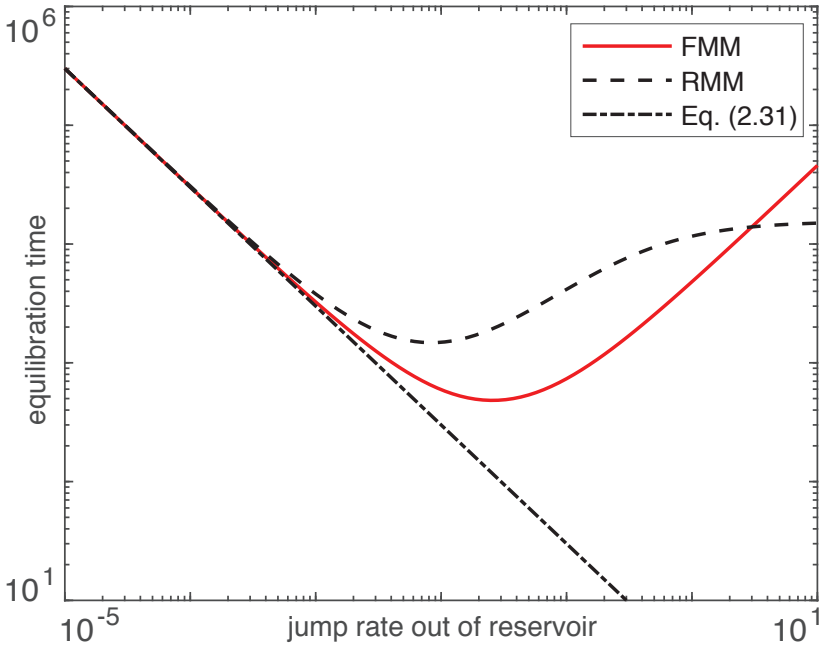

Figure 2.6: The equilibration time of the FMM (red solid curve), the RMM in the low-density regime (black dashed curve) and the analytical low-density equilibration time given in Equation (2.31) (black dot-dashed curve). The model parameters are $\alpha = 1$, $N = 100$ and $K = 5$.

2.2.2.1 Analytical formula for the equilibration time

Let $p(i,t)$ be the probability that the left reservoir is occupied by i particles at time t. The chemical master equations that govern the evolution of $p(i,t)$ are as follows

$$\begin{aligned}\frac{\mathrm{d}p(i,t)}{\mathrm{d}t} &= k_{\mathrm{LD}}(N-i+1)p(i-1,t) - k_{\mathrm{LD}}(N-i)p(i,t) \\ &\quad + k_{\mathrm{LD}}(i+1)p(i+1,t) - k_{\mathrm{LD}}(i)p(i,t), \end{aligned} \tag{2.28}$$

where $k_{\mathrm{LD}}(i) = \langle T_{\mathrm{switch}}(i)\rangle^{-1}$ from Equation (2.14) and $0 \leq i \leq N$. The occupancy of each reservoir cannot exceed N or be less than zero, as such we impose that $k_{\mathrm{LD}}(N+1) = k_{\mathrm{LD}}(0) = 0$.

For large populations, $N \gg 1$, let $x = i/N$ be the fraction of the population occupying the left reservoir. Making the continuous approximation that $x \in [0,1]$, introducing $Q(x,t) = p(i,t)$, and Taylor expanding Equation (2.28) in terms of $\epsilon =$

$1/N$ yields the Fokker-Planck equation

$$\begin{aligned}\frac{\partial Q(x,t)}{\partial t} &= \epsilon\frac{\partial}{\partial x}\left\{\left[g_{\mathrm{LD}}(x)-g_{\mathrm{LD}}(1-x)\right]Q(x,t)\right\} \\ &\quad +\frac{\epsilon^2}{2}\frac{\partial^2}{\partial x^2}\left\{\left[g_{\mathrm{LD}}(x)+g_{\mathrm{LD}}(1-x)\right]Q(x,t)\right\}, \end{aligned} \tag{2.29}$$

where $g_{\mathrm{LD}}(x) = k_{\mathrm{LD}}(xN)$, and with zero-flux boundary conditions at $x = 0$ and $x = 1$. Equation (2.29) is a linear advection diffusion PDE, and the term $[g_{\mathrm{LD}}(x) - g_{\mathrm{LD}}(1 - x)]Q(x,t)$ is the advective flux. For $0 < x < 1/2$ and $1/2 < x < 1$ the advective flux is negative and positive, respectively. Therefore the advective flux acts as a force to push the system towards the equilibrium mean value $x = 1/2$, where each reservoir is occupied by half the population. For initial conditions far from equilibrium, the advective flux is large and the distribution of particles between the reservoirs relaxes quickly to be close to equilibrium. Thus the timescale to reach equilibrium can be calculated by localising the PDE in Equation (2.29) about $x = 1/2$. Suppose $x = 1/2 + z$ for $|z| \ll 1$. We introduce $\tilde{Q}(z,t) = Q(x,t)$ and localise Equation (2.29) to obtain

$$\frac{\partial \tilde{Q}(z,t)}{\partial t} = 2\epsilon g'_{\mathrm{LD}}\left(\frac{1}{2}\right)\frac{\partial}{\partial z}\left[z\tilde{Q}\right] + \epsilon^2 g_{\mathrm{LD}}\left(\frac{1}{2}\right)\frac{\partial^2 \tilde{Q}}{\partial z^2}. \tag{2.30}$$

Equation (2.30) is the Fokker-Planck equation for an Ornstein-Uhlenbeck process, also known as a mean-reverting process [71]. For initial conditions $\tilde{Q}(z,0) = \delta(z-y)$, the mean, $\mu(t)$, of the Ornstein-Uhlenbeck process is known, $\mu(t) = y\exp\left[-2\epsilon g'_{\mathrm{LD}}(1/2)t\right]$. The mean decays on the timescale $\left(2\epsilon g'_{\mathrm{LD}}(1/2)\right)^{-1}$. From Equation (2.14), recalling that $g_{\mathrm{LD}}(x) = k_{\mathrm{LD}}(xN)$, the equilibration time, τ_{LD}, in the low-density regime is therefore

$$\begin{aligned}\tau_{\mathrm{LD}} &= \frac{K+1}{2\gamma}\left(1+\frac{\gamma NK}{4\alpha}\right)^2 \\ &\sim \frac{K+1}{2\gamma}. \end{aligned} \tag{2.31}$$

The asymptote in Equation (2.31) is valid when $\gamma NK \ll 4\alpha$, which is a stricter condition than the condition for the FMM to be in the low-density regime, which is $\gamma(N-K) \ll 2\alpha$. The analytical formula for the equilibration time in Equation (2.31) agrees with the equilibration time of the FMM (see Figure 2.6, dot-dashed curve) for small values of γ. As for the equilibration time for the RMM from the transition matrix Q^{LD}, Equation (2.31) is valid for equilibrium densities $\rho^* \lesssim 0.1$.

2.3 A reduced Markov model: the high-density regime

Consider the FMM with model parameters that satisfy $\gamma\,(N-K) \gg 2\alpha$, this is sufficient[4] to guarantee $\rho^* \sim 1$, and the FMM is in the high-density regime. As for the low-density regime, we seek a RMM where particles jump directly between the left and right reservoirs and the narrow channel length is incorporated in the transition rates of these jumps. Due to the high equilibrium density, many of the lattice sites in the narrow channel are occupied at a given time, and volume exclusion effects are no longer negligible. To characterise the time taken for a particle to be exchanged between the reservoirs, particle-hole duality [72] is invoked and the dynamics of a non-interacting vacancy along the narrow channel is considered.

Consider an initial configuration of particles where every lattice site is occupied. The remaining $N-K$ particles are distributed with n_L and n_R in the left and right reservoirs, respectively. The only movements not blocked by exclusion are either, the particle in lattice site one jumps into the left reservoir, or the particle in lattice site K jumps into the right reservoir, both jumps occur at rate α. In the latter case, the right reservoir is occupied by n_R+1 particles and lattice site K becomes vacant. The

[4]Substitute $\rho^* = 1-\delta$ into the quadratic in Equation (2.11). Assuming that $\delta \ll 1$ and linearising in δ yields $\delta = 2\alpha/(2\alpha+\gamma(N-K))$. Thus, as $\delta \ll 1$ the model parameters must satisfy $\gamma\,(N-K) \gg 2\alpha$.

rate at which the vacant lattice site K is re-occupied by a particle from the right reservoir is $\gamma(n_R+1)$, this competes with the rate α, the rate at which the particle in lattice site $K-1$ jumps into lattice site K. As $\gamma(N-K) \gg \alpha$, if $n_R \sim \mathcal{O}(N-K)$ the vacant lattice site K is almost immediately re-occupied by a particle from the right reservoir and no exchange of particles occurs. However, eventually the particle in lattice site $K-1$ will jump before any particle in the right reservoir, resulting in a vacancy at lattice site $K-1$. Let the lattice sites with indices between two and $K-1$ be referred to as the internal lattice sites of the narrow channel. Then $T_{v,\text{enter}}$ is the time taken for a vacancy to first enter the internal lattice sites of the narrow channel. A vacancy in the internal lattice sites follows a symmetric random walk with jump rates α in both directions, until eventually, at time $T_{v,\text{absorb}}$, the vacancy is absorbed at external lattice sites K or one. If the vacancy is absorbed at lattice site K then almost immediately a particle in the right reservoir jumps into lattice site K and there has been no particle exchange between the two reservoirs. However, if a particle is absorbed at lattice site one, then again almost immediately a particle in the left reservoir jumps into lattice site one. However, there are now n_L-1 and n_R+1 particles, in the left and right reservoirs, respectively, and a particle has been exchanged between the left and right reservoirs. A vacancy at lattice site $K-1$ hits lattice site one before lattice site K with probability $1/(K-1)$. The number of attempts before the vacancy is absorbed at lattice site one, G_{K-1}, is geometrically distributed with success probability $1/(K-1)$. The time taken for a vacancy to enter the internal lattice sites at lattice site $K-1$ and be absorbed in lattice site one, is referred to as the *vacancy switching time* and is denoted by $T_{v,\text{switch}}(n_R)$. The vacancy switching time is expressed as the following random sum

$$T_{v,\text{switch}}(n_R) = \sum_{j=1}^{G_{K-1}} \left(T^j_{v,\text{enter}} + T^j_{v,\text{absorb}} \right), \tag{2.32}$$

where $T^j_{v,\text{enter}}$ and $T^j_{v,\text{absorb}}$ are independent instances of the random variables $T_{v,\text{enter}}$ and $T_{v,\text{absorb}}$, respectively. The RMM in the high-density regime has transition rates, $k_{\text{HD}}(n_R) = \langle T_{v,\text{switch}}(n_R)\rangle^{-1}$, for a particle to be exchanged from the left to the right reservoir. In contrast to the low-density regime, the transition rates of the RMM depend upon the occupancy of the reservoir which gains a particle in the transition event. The first moment of the vacancy switching time in Equation (2.32) is $\langle T_{v,\text{switch}}(n_R)\rangle = \langle G_{K-1}\rangle\left(\langle T_{v,\text{enter}}\rangle + \langle T_{v,\text{absorb}}\rangle\right)$, where $\langle G_{K-1}\rangle = K-1$ and from first passage times on a finite lattice [69], $\langle T_{v,\text{absorb}}\rangle = (K-2)/2\alpha$. Recall that $T_{v,\text{enter}}$ is the time for a vacancy to enter lattice site $K-1$. Initially every lattice site is full and the particle at lattice site K jumps into the right reservoir after an exponentially distributed amount of time, X, with rate parameter α. Then either the particle in lattice site $K-1$ jumps into lattice site K at rate α, or a particle in the right reservoir jumps into lattice site K at rate $\gamma(n_R+1)$. The time taken for either jump to occur is exponentially distributed, Y, with rate parameter $\alpha+\gamma(n_R+1)$. The vacancy at lattice site K enters lattice site $K-1$ with probability $q = \alpha/\left(\alpha+\gamma(n_R+1)\right)$, thus $T_{v,\text{enter}} = \sum_{j=1}^{G(q)} X^j + Y^j$, where $G(q)$ is a geometric random variable with success probability q, and X^j and Y^j are independent instances of the exponential random variables with rate parameters α and $\alpha+\gamma(n_R+1)$, respectively. The first moment of $T_{v,\text{enter}}$ is

$$\langle T_{v,\text{enter}}\rangle = \frac{\alpha+\gamma(n_R+1)}{\alpha}\left(\frac{1}{\alpha}+\frac{1}{\alpha+\gamma(n_R+1)}\right). \tag{2.33}$$

From Equation (2.33), and recalling that $\langle T_{v,\text{switch}}(n_R)\rangle = \langle G_{K-1}\rangle\left(\langle T_{v,\text{enter}}\rangle + \langle T_{v,\text{absorb}}\rangle\right)$ and $k_{\text{HD}}(n_R) = \langle T_{v,\text{switch}}(n_R)\rangle^{-1}$, the transition rates for the RMM in the high-density regime are

$$k_{\text{HD}}(n_R) = \frac{1}{K-1}\left(\frac{\gamma(n_R+1)+2\alpha}{\alpha^2}+\frac{K-2}{2\alpha}\right)^{-1}. \tag{2.34}$$

The validity of the RMM depends on how accurately $T_{v,\text{switch}}(n_R)$ is approximated by the exponential distribution with rate parameter $k_{\text{HD}}(n_R)$. To investigate the

accuracy of approximating the vacancy switching time as an exponential distribution we consider the full distribution of the vacancy switching time.

2.3.1 Full distribution of the vacancy switching time

The MGF for the vacancy switching time, $M_{T_{v,\text{switch}}(n_R)}(s)$, is derived analogously to the MGF for the particle switching time in Section 2.2.1. In Equation (2.32) the vacancy switching time is expressed as a geometric random sum, therefore, similar to Equation (2.16), we have

$$M_{T_{v,\text{switch}}(n_R)}(s) = \frac{M_{T_{v,\text{enter}}}(s) M_{T_{v,\text{absorb}}}(s)}{(K-1) - (K-2) M_{T_{v,\text{enter}}}(s) M_{T_{v,\text{absorb}}}(s)}. \tag{2.35}$$

Recall that $T_{v,\text{enter}}$ is also expressed as a geometric random sum. Then a simple calculation yields

$$M_{T_{v,\text{enter}}}(s) = \frac{\alpha^2}{s^2 - (2\alpha + \gamma(n_R+1))\, s + \alpha^2}. \tag{2.36}$$

The MGF for the first passage time of a particle on a finite lattice has been derived in Section 2.2.1.1. The first passage time for the vacancy is defined on a lattice with sites $\{1, \ldots, K\}$, so by shortening the lattice length by two lattice sites in Equation (2.26), we have

$$M_{T_{v,\text{absorb}}}(s) = \frac{\sinh\left(\phi'(s)\right) + \sinh\left((K-2)\phi'(s)\right)}{\sinh\left((K-1)\phi'(s)\right)}, \tag{2.37}$$

where $\phi'(s) = \tanh^{-1}\left(\sqrt{1 - 4\alpha^2/(s-2\alpha)^2}\right)$. Combining Equations (2.35), (2.36) and (2.37) results in

$$M_{T_{v,\text{switch}}(n_R)}(s) = \frac{\alpha^2 \left(\dfrac{\sinh(\phi'(s)) + \sinh((K-2)\phi'(s))}{\sinh((K-1)\phi'(s))}\right)}{(K-1)h(s) - \alpha^2(K-2)\left(\dfrac{\sinh(\phi'(s)) + \sinh((K-2)\phi'(s))}{\sinh((K-1)\phi'(s))}\right)}, \tag{2.38}$$

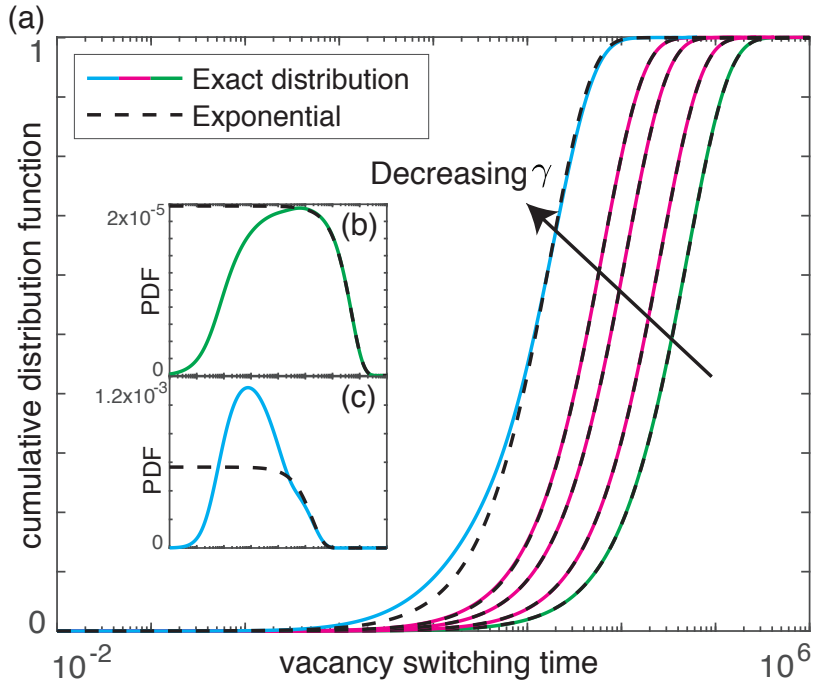

Figure 2.7: The vacancy switching time distribution (solid curves) compared with an exponential distribution (dashed curves). (a): The CDFs for the vacancy switching time and the exponential distribution with rate parameter $k_{\mathrm{HD}}(n_R)$ given by Equation (2.14) over a range of jump rates γ. (b): The PDF of the vacancy switching time when $\gamma = 5$ where the high-density assumption is valid. (c): The PDF of the vacancy switching time when $\gamma = 0.05$ and the high-density assumption does not hold. The parameters used are, $\alpha = 1$, $n_R = 200$, $K = 50$ and the reservoir jump rates are $\gamma \in \{0.05, 0.5, 1, 2.5, 5\}$.

where $h(s) = s^2 - (2\alpha + \gamma(n_R + 1))s + \alpha^2$.

The CDF of the vacancy switching time is calculated, as in Section 2.2.1, via a Talbot inversion scheme [70] over a range of values for γ (see Figure 2.7(a)). Excellent agreement is observed between the CDF of $T_{v,\mathrm{switch}}(n_R)$ and the CDF of an exponential random variable with parameter $k_{\mathrm{HD}}(n_R)$ given in Equation (2.34) for large values of γ. In particular, for parameters such that $\rho^* = 0.997$, other than for very short times the PDF shows excellent agreement (see Figure 2.7(b)). As the reservoir jump rate is reduced (see Figure 2.7(a), arrow) the CDFs between the exponential distribution and the vacancy switching time show good agreement until the parameters are such that $\rho^* \lesssim 0.8$ (see Figure 2.7(c)). In summary, we have verified that the vacancy switching

time can be considered to be approximately exponential in the high-density regime. As in Section 2.2.2 we now consider the equilibration time for the RMM in the high-density regime.

2.3.2 Equilibration time of the reduced Markov model

The state vectors of the RMM are (n_L, n_R) for non-negative integers n_L and n_R such that $n_L + n_R = N_{\mathrm{HD}}$, where $N_{\mathrm{HD}} = N - K$, as the K lattice sites are almost always occupied in the high-density regime. It is convenient to write the state vectors as $(i, N_{\mathrm{HD}} - i)$ for $0 \leq i \leq N_{\mathrm{HD}}$. The state vector $(i, N_{\mathrm{HD}} - i)$ transitions to state $(i-1, N_{\mathrm{HD}} - i + 1)$ if there is a particle exchange from the left to the right reservoir, which occurs at rate $k_{\mathrm{HD}}(N_{\mathrm{HD}} - i) = \langle T_{v,\mathrm{switch}}(N_{\mathrm{HD}} - i)\rangle^{-1}$ given by Equation (2.34). Similarly, a transition from state $(i, N_{\mathrm{HD}} - i)$ to state $(i+1, N_{\mathrm{HD}} - i - 1)$ occurs at rate $k_{\mathrm{HD}}(i) = \langle T_{v,\mathrm{switch}}(i)\rangle^{-1}$. The RMM in the high-density regime has a tridiagonal transition matrix, Q^{HD}, where the entries on the sub-diagonal are $Q^{\mathrm{HD}}_{i,i-1} = k_{\mathrm{HD}}(N_{\mathrm{HD}} - i)$, the super-diagonal has entries $Q^{\mathrm{HD}}_{i,i+1} = k_{\mathrm{HD}}(i)$, and the diagonal entries are given by $Q^{\mathrm{HD}}_{i,i} = -\left(k_{\mathrm{HD}}(N_{\mathrm{HD}} - i) + k_{\mathrm{HD}}(i)\right)$. The equilibration time for the RMM is calculated as the reciprocal of the spectral gap of Q^{HD} and agrees excellently with the equilibration time for the FMM (see Figure 2.8) for large values of γ. As γ decreases, differences between the equilibration times of the FMM and RMM only become noticeable when $\gamma \sim 0.2$, thus there is good agreement for model parameters where the equilibrium density satisfies $\rho^* \gtrsim 0.9$.

2.3.2.1 Analytical formula for the equilibration time

Let $p(i,t)$ be the probability that the left reservoir is occupied by i particles at time t. The chemical master equations that govern the evolution of $p(i,t)$ are as follows

$$\begin{aligned}\frac{\mathrm{d}p(i,t)}{\mathrm{d}t} &= k_{\mathrm{HD}}(i-1)p(i-1,t) - k_{\mathrm{HD}}(i)p(i,t) \\ &+ k_{\mathrm{HD}}(N_{\mathrm{HD}}-i-1)p(i+1,t) - k_{\mathrm{HD}}(N_{\mathrm{HD}}-i)p(i,t), \end{aligned} \tag{2.39}$$

where $k_{\mathrm{HD}}(i) = \langle T_{v,\mathrm{switch}}(i)\rangle^{-1}$ from Equation (2.34) and $0 \leq i \leq N_{\mathrm{HD}}$. The occupancy of each reservoir cannot exceed N_{HD} or be less than zero, as such we impose that $k_{\mathrm{HD}}(N_{\mathrm{HD}}+1) = k_{\mathrm{HD}}(0) = 0$. The analysis proceeds identically to Section 2.2.2.1 where the equilibration time is calculated from an Ornstein-Uhlenbeck process that is derived from localising the Fokker-Planck equation arising from Equation (2.39). The timescale, τ_{HD}, on which the RMM in the high-density regime decays to equilibrium is given by $\tau_{\mathrm{HD}} = -\left(N_{\mathrm{HD}}/2g'_{\mathrm{HD}}\left(1/2\right)\right)$, where $g_{\mathrm{HD}}\left(x\right) = k_{\mathrm{HD}}\left(N_{\mathrm{HD}}x\right)$. Therefore, in terms of the model parameters of the FMM we have

$$\begin{aligned}\tau_{\mathrm{HD}} &= \frac{(K-1)\left[\dfrac{\gamma N_{\mathrm{HD}}}{2\alpha} + \left(\dfrac{\gamma+2\alpha}{\alpha} + \dfrac{K-2}{2}\right)\right]^2}{2\gamma} \\ &\sim \frac{\gamma(N-K)^2(K-1)}{8\alpha^2}. \end{aligned} \tag{2.40}$$

The asymptote in Equation (2.40) is valid for model parameters that satisfy $\gamma(N-K) \gg \alpha(K+2)+2\gamma$, a stricter condition than the condition for the FMM to be in the high-density regime, which is $\gamma(N-K) \gg 2\alpha$. The analytical formula in Equation (2.40) agrees with the FMM (see Figure 2.8, dot-dashed curve) for large values of γ. As for the equilibration time for the RMM, from the transition matrix Q^{HD}, Equation (2.40) is valid for equilibrium densites $\rho^* \gtrsim 0.9$.

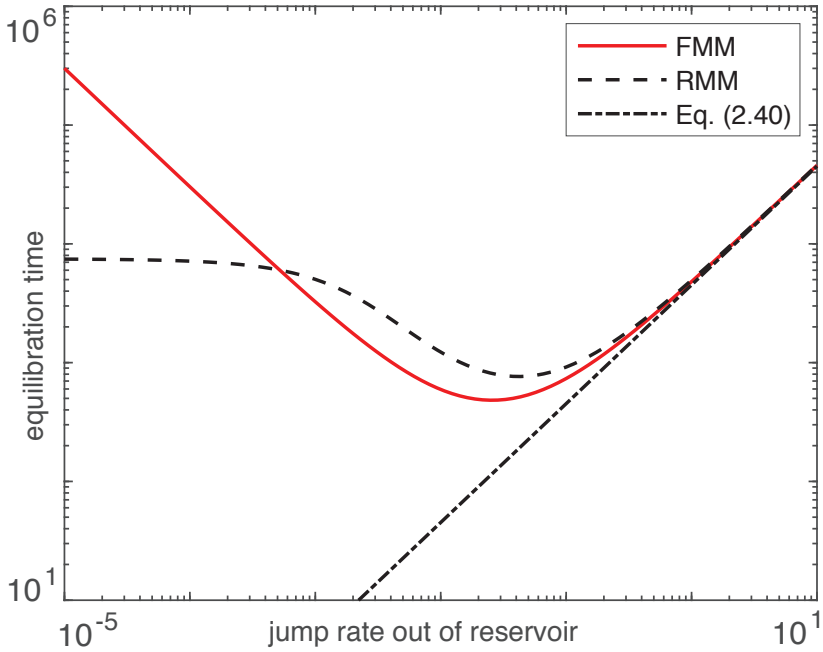

Figure 2.8: The equilibration time of the FMM (red solid curve), the RMM in the high-density regime (black dashed curve) and the high-density equilibration time given by Equation (2.40) (black dot-dashed curve). The model parameters are $\alpha = 1$, $N = 100$ and $K = 5$.

2.4 Partial exclusion in the narrow channel

Macromolecular transport within confined geometries, such as micro-vessels in the vasculature of the heart [73] or ion channels within the cellular membrane [74], do not always exhibit strict volume exclusion. Confined geometries often have width a few times larger than the size of the macromolecule, and thus partially excluding transport models are used to investigate transport through a crowded environment [37, 75].

To extend our model to allow for partial exclusion, we redefine the FMM such that the lattice sites can be occupied simultaneously by at most C particles, where C is the carrying capacity of the narrow channel lattice sites. The configuration of particles at time t is described by the state vector $\vec{S}(t) = (L(t), N_1(t), \ldots, N_K(t), R(t))$. The variables $L(t)$ and $R(t)$ denote the number of particles in the left and right reservoirs

at time t, respectively, and $N_i(t)$ denotes the number of particles in lattice site i at time t. Let the configuration space $\Omega_{N,K,C}$ be the set of legal configurations, these are the vectors $\vec{s} = (n_L, n_1, \ldots, n_K, n_R)$ such that $n_L + n_R + \sum_{i=1}^{K} n_i = N$, where $n_i \in \{0, \ldots, C\}$ for $1 \leq i \leq K$ and $n_L, n_R \in \mathbb{N}$.

The FMM is a CTMC defined on the configuration space $\Omega_{N,K,C}$, and the rates at which states transition to new states depend upon what type of transition event occurs. Following Taylor et al. [75] the jump rate of a particle in lattice site i depends linearly upon the occupancy of the lattice site that the particle attempts to jump to. Suppose the configuration of particles is in state vector $\vec{S}(t)$ at time t. A particle jumps from lattice site i to lattice site $i \pm 1$ with rate $\alpha N_i(t)\,(1 - N_{i\pm1}(t)/C)$ for $2 \leq i \leq K-1$. A particle jumps from lattice site one into the left reservoir, or from lattice site K into the right reservoir, with rates $\alpha N_1(t)$ and $\alpha N_K(t)$, respectively. Finally a particle jumps from the left reservoir into lattice site one, or from the right reservoir into lattice site K, with rates $\gamma L(t)\,(1 - N_1(t)/C)$ and $\gamma R(t)\,(1 - N_K(t)/C)$, respectively. A transition matrix can be constructed just as for the FMM in Section 2.1, from which the equilibration time is computed as the reciprocal of the spectral gap. For small values of γ the equilibration time is independent of the carrying capacity (see Figure 2.9, solid curves), as the number of particles in the narrow channel is few and they do not feel the effects of partial exclusion. For larger values of γ, sites in the narrow channel have a greater occupancy and the equilibration times differ as the carrying capacity varies. For a fixed value of γ, as C increases the effects of exclusion are reduced and so the equilibration times fall (see Figure 2.9, arrow).

The configuration space, $\Omega_{N,K,C}$, has dimensionality

$$|\Omega_{N,K,C}| = \sum_{m=0}^{\min(N,CK)} (N - m + 1) \binom{K}{m}^{(C)}, \tag{2.41}$$

where $\binom{K}{m}^{(C)}$ is the extended binomial coefficient[5], and is the number of distinct ways in which m unlabelled particles can be placed in K labelled lattice sites allowing at most C particles in each lattice site. For a large population, such that $N \gg CK$, we have $|\Omega_{N,K,C}| \sim \mathcal{O}\left(N\left(C+1\right)^K\right)$. Thus, even for moderately sized models the dimensionality of the state space for the FMM is extremely high. The RMM can be easily extended in the high-density regime (there is no difference in the low-density regime for $C > 1$) to provide an analytical equation for the equilibration time.

2.4.1 A reduced Markov Model in the high-density regime

As for the strict volume exclusion process considered in Section 2.3, where $C = 1$, consider an initial configuration where every lattice site in the narrow channel is fully occupied. The remaining $N_{\mathrm{HD}} = N - CK$ particles are then distributed between the left and right reservoirs, with n_L and n_R in each reservoir, respectively. We select the transition rates in the RMM to match the first moment of the vacancy switching time, $T_{v,\mathrm{switch}}(n_R)$, the time for a vacancy to enter the narrow channel at site K and be absorbed into the left reservoir. Recall, $T_{v,\mathrm{switch}}(n_R)$ can be expressed as the random sum

$$T_{v,\mathrm{switch}}(n_R) = \sum_{j=1}^{G_{K-1}} \left(T^j_{v,\mathrm{enter}} + T^j_{v,\mathrm{absorb}}\right), \tag{2.42}$$

where G_{K-1} is a Geometric random variable with success probability $1/(K-1)$, $T^j_{v,\mathrm{enter}}$ are independent instances of the time taken for a vacancy to enter the internal lattice sites, and $T^j_{v,\mathrm{absorb}}$ are independent instances of the time taken for a vacancy to hit either of the external lattice sites one or K. A single vacancy in lattice site $i \in \{2,\ldots,K-1\}$ jumps to an adjacent lattice site $i \pm 1$, if a particle in that lattice site moves into the vacancy in lattice site i. This jump occurs at rate $\alpha N_{i\pm1}(t)\left(1 - N_i(t)/C\right)$. If there is only one vacancy in the channel then $N_{i\pm1}(t) = C$

[5]The extended binomial coefficient, $\binom{K}{m}^{(C)}$, is the coefficient of x^m in the polynomial $\left(\sum_{i=0}^{C} x^i\right)^K$.

and $N_i(t) = C - 1$, and the jump rate $\alpha N_{i\pm1}(t)\,(1 - N_i(t)/C)$ simplifies to equal α. Therefore the dynamics of a single vacancy within the internal lattice sites remain unchanged for higher carrying capacities. A vacancy enters lattice site K after an exponentially distributed time X with rate αC. Then either a particle in the reservoir enters lattice site K, which occurs at rate $\gamma\,(n_R + 1)\,/C$, or a particle in lattice site $K - 1$ jumps into lattice site K, which occurs at rate α. Either of these events occur after an exponentially distributed time Y with rate $\alpha + \gamma\,(n_R + 1)\,/C$. Defining $G(q)$ as a Geometric random variable with success probability $q = \alpha C/\,(\alpha C + \gamma\,(n_R + 1))$, we can write down $T_{v,\text{enter}} = \sum_{j=1}^{G(q)} X^j + Y^j$, where X^j and Y^j are i.i.d instances of the random variables X and Y, respectively. The transition rates for the RMM in the high-density regime are defined as $k_{\text{HD}}\,(n_R; C) = \langle T_{v,\text{switch}}(n_R)\rangle^{-1}$, and a simple calculation yields

$$k_{\text{HD}}\,(n_R; C) = \frac{1}{K-1}\left(\frac{\gamma(n_R+1) + C(C+1)\alpha}{C^2\alpha^2} + \frac{K-2}{2\alpha}\right)^{-1}. \tag{2.43}$$

Following the derivation presented in Section 2.3.2.1, the chemical master equations that describe the probability functions of the RMM being in each state at time t can be written down using the transition rates in Equation (2.43). Through analysis of the corresponding Fokker-Planck equation, a timescale for equilibration in the high-density regime is calculated as $\tau_{\text{HD}}(C) = -\left(N_{\text{HD}}/2g'_{\text{HD}}(1/2; C)\right)$, where $g_{\text{HD}}(x; C) = k_{\text{HD}}\,(N_{\text{HD}}x; C)$. The analytical formula for the equilibration time is given by

$$\begin{aligned}\tau_{\text{HD}}(C) &= \frac{\alpha^2C^2(K-1)\left(\dfrac{\gamma N_{\text{HD}}}{2\alpha^2C^2} + \dfrac{\gamma + \alpha C(C+1)}{\alpha C^2} + \dfrac{K-2}{2\alpha}\right)^2}{2\gamma} \\ &\sim \frac{\gamma\,(N - CK)^2\,(K-1)}{8\alpha^2C^2},\end{aligned} \tag{2.44}$$

where the asymptote in Equation (2.44) is valid for model parameters such that

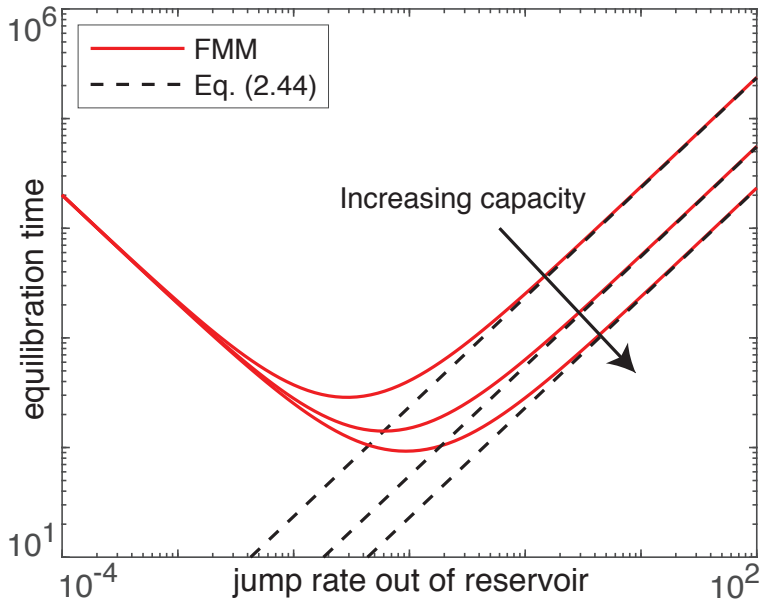

Figure 2.9: The equilibration time for the FMM (solid curves), the equilibration time for the RMM in the high-density regime (dashed curves) from Equation (2.44). The model parameters are $\alpha = 1$, $N = 100$, $K = 3$ and $C \in \{1, 2, 3\}$. The length of the narrow channel has been shortened compared to Figures 2.6 and 2.8, due to an increase in dimensionality as seen in Equation (2.41).

$\gamma(N - CK) \gg 2\alpha\gamma + 2\alpha^2 C(C + 1) + \alpha C^2(K - 2)$, and agrees excellently with the equilibration time of the FMM for large values of γ (see Figure 2.9).

2.5 Summary

In this chapter, the FMM for a population of interacting particles in a two reservoir model was introduced. The narrow channel is modelled as a one-dimensional lattice, and the equilibrium occupancy probability of each lattice site is approximated analytically. The equilibration time of the FMM is calculated as the reciprocal of the spectral gap of a CTRW transition matrix. However, due to the high dimensionality of the FMM, for all but the most simple systems the equilibration time is computationally infeasible to calculate. Therefore two coarse-grained models (RMMs) were introduced in parameter regimes where the occupancy of the narrow channel is both

low and high. The RMMs allow us to model particles as directly jumping between the two reservoirs, and the jumps occur at rates that incorporate the length of the narrow channel. The equilibration time of the RMM accurately predicts the equilibration time of the FMM in both the low- and high-density regimes. Classical probabilistic techniques are applied to the chemical master equations that describe the probability distribution of the RMM to derive analytic expressions for the equilibration time. These analytic expressions explicitly state the functional relationship between the equilibration time of the population and the model parameters: population size; narrow channel length; and the jump rates of particles between the narrow channel lattice sites and to and from the reservoirs. Finally the model was generalised to allow partial exclusion of particles in the narrow channel.

The work in this chapter has paved the way for developing mathematical transport models with macromolecular crowding that explore equilibration times in complex heterogeneous geometries. Such models will be fundamental to furthering our understanding of the roles that geometry and crowding have within diffusive transport processes in complex environments. In Chapter 3 we extend the two reservoir model to a generalised network of reservoirs, where the edges of the network represent narrow channels between the reservoirs.

Chapter 3

Equilibration times in heterogeneous environments: a generalised reservoir model and optimal networks

The diffusion of fluids in porous media [76, 77], phosphates within mammalian cardiomyocytes [64, 78], and oxygen within synthetically engineered scaffolds [79] are all examples of diffusive transport processes within complex heterogeneous environments. Modelling each of these transport processes requires mathematical models on macroscopic length scales that incorporate the microscopic spatial structure. In particular, the cytoplasm within mammalian cells has been shown to have heterogeneous porosity [80] and approximately one quarter of the free space is occupied by macromolecules such as proteins and nucleic acids [35]. As such, there is demand for mathematical models that account for both microscopic spatial heterogeneity and macromolecular crowding. To investigate how macromolecular crowding and heterogeneous spatial structure affects the transport of diffusive particles, we extend the

two reservoir model seen in Chapter 2 to a generalised network of reservoirs connected by narrow channels. The narrow channels are modelled as one-dimensional lattices where each lattice site can be occupied by at most one particle at a time. The reservoirs can support many particles and particle motility is unhindered by the effects of volume exclusion. Firstly, the FMM is formally introduced for a population of particles on a general network. Equilibrium properties of the FMM are considered and used to derive RMMs for parameter regimes where the occupancies of the narrow channel lattice sites are both low and high. The equilibration time for a population of particles in a network is identified with the reciprocal of the spectral gap of a remarkably low-dimensional matrix. This low dimensionality facilitates the numerical investigation of "optimal networks"; those that minimise the equilibration time subject to a restriction in the total edge length of a network. These networks define an optimal frontier (see Section 3.3.2) over the space of all connected networks. For homogeneous reservoir jump rates, numerical results suggest that the optimal frontier follows a universal curve independent of the spatial configuration of reservoirs. A weighted degree distribution is used to demonstrate striking differences between optimal and non-optimal networks. For networks with large numbers of reservoirs, two efficient algorithms for approximate optimal network construction are presented and tested. The work in this chapter presents a fundamental step in understanding how both geometry and crowding affects diffusive transport at the population level.

3.1 The full Markov model

Consider a network $\mathcal{G} = \{\mathcal{V}, \mathcal{E}\}$, where $\mathcal{V}$ is the set of reservoirs (nodes) and $\mathcal{E}$ the set of narrow channels (edges) that connect the reservoirs. Assigning indices e to each narrow channel arbitrarily, the narrow channels have non-dimensional length $K_e \in \mathbb{Z}_{\geq 1}$ for $1 \leq e \leq |\mathcal{E}|$, which denotes the number of lattice sites in the narrow

channel. Each narrow channel is assigned an arbitrary polarity and the lattice sites have indices $\{1, \ldots, K_e\}$. A total of N particles populate the network and their configuration at time t is described by the state vector $\vec{S}(t)$. The state vector is written as a concatenation of additional vectors, $\vec{S}(t) = (\vec{R}(t), \vec{N}_1(t), \ldots, \vec{N}_{|\mathcal{E}|}(t))$, where, for $1 \leq i \leq |\mathcal{V}|$, $[\vec{R}(t)]_i = R_i(t)$ is the number of particles in reservoir i at time t. For $1 \leq e \leq |\mathcal{E}|$ and $1 \leq k \leq K_e$, $[\vec{N}_e(t)]_k = N_{e,k}(t)$ is the occupancy of the k-th lattice site along the e-th narrow channel. Let $\Omega_{N,\mathcal{G}}$ be the set of legal configurations for a population of N particles on the network $\mathcal{G}$. The set $\Omega_{N,\mathcal{G}}$ consists of vectors $\vec{s} = (\vec{r}, \vec{n}_1, \ldots, \vec{n}_{|\mathcal{E}|})$, where $[\vec{r}]_i = r_i \geq 0$ for $1 \leq i \leq |\mathcal{V}|$, and $[\vec{n}_e]_k = n_{e,k} \in \{0, 1\}$ for $1 \leq e \leq |\mathcal{E}|$ and $1 \leq k \leq K_e$, such that $\sum_{i=1}^{|\mathcal{V}|} r_i + \sum_{e=1}^{|\mathcal{E}|} \sum_{k=1}^{K_e} n_{e,k} = N$. The restriction $n_{e,k} \in \{0, 1\}$ is to enforce volume exclusion for particles in the lattice sites along the narrow channels.

As in Chapter 2, a particle occupying any lattice site within any narrow channel, attempts to jump to an adjacent lattice site or reservoir at rate α. Particles in the i-th reservoir will attempt to jump into the first lattice site of a connecting narrow channel at rate γ_i. These reservoir jump rates are distinct to reflect heterogeneity amongst the reservoirs. Formally, the state vector $\vec{S}(t)$ evolves according to the following continuous-time Markov chain (CTMC). A particle in narrow channel e occupying the k-th lattice site, jumps to the adjacent lattice site $k+1$ at rate $\alpha N_{e,k}(t)\,(1 - N_{e,k+1}(t))$ for $1 \leq k \leq K_e - 1$. Note that this transition rate is zero if either the k-th lattice site is empty, $N_{e,k}(t) = 0$, or the adjacent lattice site is occupied, $N_{e,k+1}(t) = 1$. A particle in lattice site K_e along the narrow channel e jumps into the reservoir connected to lattice site K_e at rate $\alpha N_{e,K_e}(t)$. Similarly, a particle occupying the k-th lattice site along narrow channel e jumps to the adjacent site $k-1$ at rate $\alpha N_{e,k}(t)\,(1 - N_{e,k-1}(t))$ for $2 \leq k \leq K_e$, and a particle in the first lattice site jumps into the connected reservoir at rate $\alpha N_{e,1}(t)$. Finally, a particle in the i-th reservoir jumps into the first lattice site of a connected narrow channel e at rate $\gamma_i\,(1 - N_{e,1}(t))$ or $\gamma_i\,(1 - N_{e,K_e}(t))$ depending

on the orientation of the narrow channel e. A transition matrix Q for the CTMC is constructed as follows. Let $\mathcal{I}(\Omega_{N,\mathcal{G}})$ be an index set, such that if $u \in \mathcal{I}(\Omega_{N,\mathcal{G}})$ then $\vec{s}_u \in \Omega_{N,\mathcal{G}}$. For $u, v \in \mathcal{I}(\Omega_{N,\mathcal{G}})$ and $u \neq v$ the matrix entry $Q_{u,v}$ is equal to the rate at which state $\vec{s}_u$ transitions to state $\vec{s}_v$, as detailed above. If a transition cannot occur via a single jump event the matrix entry $Q_{u,v}$ is zero. The diagonal entries are equal to the negative of the row sums, $Q_{u,u} = -\sum_{v \neq u} Q_{u,v}$ for $1 \leq u \leq |\Omega_{N,\mathcal{G}}|$. As in Chapter 2, the reciprocal of the spectral gap of Q is the canonical measurement for the equilibration time of a population of particles in a networked environment [50].

The dimensionality of the CTMC is even higher than that of the two reservoir model in Chapter 2. Suppose there are a total of m particles in all the lattice sites across all the narrow channels. The remaining $N - m$ particles must be distributed between the $|\mathcal{V}|$ reservoirs, which can occur in $\binom{N+|\mathcal{V}|-(m+1)}{N-m}$ distinct configurations. For each configuration there are an additional $\binom{K_{\text{tot}}}{m}$ distinct ways to arrange the m particles within the narrow channels, where $K_{\text{tot}} = \sum_{j=1}^{|\mathcal{E}|} K_{e_j}$ is the total edge length of the network. Thus, the dimensionality of the FMM is

$$|\Omega_{N,\mathcal{G}}| = \sum_{m=0}^{\min(N,K_{\text{tot}})} \binom{N + |\mathcal{V}| - (m+1)}{N-m} \binom{K_{\text{tot}}}{m}. \tag{3.1}$$

For $N \gg K_{\text{tot}}$, such that $N - m$ is approximately constant, $|\Omega_{N,\mathcal{G}}| \sim \mathcal{O}\left(2^{K_{\text{tot}}} N^{|\mathcal{V}|-1}\right)$. Even for networks with a small number of reservoirs and short channel lengths, the FMM has extremely high dimensionality, rendering the spectral gap of the transition matrix Q computationally intractable. As in Chapter 2, we consider coarse-grained models with significantly reduced dimensionality in order to make progress. We first consider equilibrium properties of the FMM that will prove useful.

3.1.1 Equilibrium properties

Define $\rho_i^{(1)}(n,t) = \mathbb{P}(R_i(t) = n)$, to be the probability that the i-th reservoir is occupied by n particles at time t. Define $\rho_e^{(1)}(O(k),t) = \mathbb{P}(N_{e,k}(t) = 1)$ to be the probability that the k-th lattice site along narrow channel e is occupied, where $1 \leq k \leq K_e$. Similarly, let $\rho_e^{(1)}(\emptyset(k),t) = \mathbb{P}(N_{e,k}(t) = 0)$ be the probability that the k-th lattice site is vacant. For a network $\mathcal{G} = \{\mathcal{V}, \mathcal{E}\}$, we seek a system of ODEs that describe the evolution of the single-site probability functions. For the i-th reservoir let $\mathcal{N}(i)$ be the indices for the narrow channels that are connected at one end to the i-th reservoir. For notational convenience suppose that every narrow channel connected to reservoir i has polarity such that the lattice site adjacent to reservoir i has index one[1]. Define $\langle R_i(t)\rangle = \sum_{n=0}^{N} n\rho_i^{(1)}(n,t)$, to be the average number of particles in the i-th reservoir at time t. Following an analogous derivation of Equation (2.9a) in Section 2.1.1 yields

$$\frac{\mathrm{d}\langle R_i(t)\rangle}{\mathrm{d}t} = \alpha \sum_{e\in\mathcal{N}(i)} \rho_e^{(1)}(O(1),t) - \gamma_i \sum_{e\in\mathcal{N}(i)} \sum_{n=0}^{N} n\rho_{i,e}^{(2)}(n,\emptyset(1),t), \tag{3.2a}$$

for $1 \leq i \leq |\mathcal{V}|$, where $\rho_{i,e}^{(2)}(n,\emptyset(1),t)$ is the two-site probability that the i-th reservoir is occupied by n particles and the first lattice site along narrow channel e is vacant at time t. From Section 2.1.1, ODEs for the occupancy probabilities of the lattice sites of a narrow channel e connecting reservoirs i and j are

$$\begin{aligned}
\frac{\mathrm{d}\rho_e^{(1)}(O(1),t)}{\mathrm{d}t} &= \gamma_i \sum_{n=0}^{N} n\rho_{i,e}^{(2)}(n,\emptyset(1),t) + \alpha\rho_e^{(1)}(O(2),t) \\
&\quad -2\alpha\rho_e^{(1)}(O(1),t), \qquad (3.2b)\\
\frac{\mathrm{d}\rho_e^{(1)}(O(k),t)}{\mathrm{d}t} &= \alpha\rho_e^{(1)}(O(k+1),t) + \alpha\rho_e^{(1)}(O(k-1),t) \\
&\quad -2\alpha\rho_e^{(1)}(O(k),t), \qquad (3.2c)
\end{aligned}$$

[1]Such an assumption cannot be true for all reservoirs simultaneously. However, the lattice site indices in Equation (3.2) can be adapted trivially for other polarity configurations.

$$\frac{\mathrm{d}\rho_e^{(1)}\left(O(K_e),t\right)}{\mathrm{d}t} = \gamma_j \sum_{n=0}^{N} n\rho_{j,e}^{(2)}\left(n,\emptyset(K_e),t\right) + \alpha\rho_e^{(1)}\left(O(K_e-1),t\right) - 2\alpha\rho_e^{(1)}\left(O(K_e),t\right), \tag{3.2d}$$

for $2 \leq k \leq K_e - 1$. Equating the right-hand side of Equations (3.2) to zero provides a set of algebraic equations for the single-site probability functions in terms of two-site probability functions. Assuming the FMM obeys the detailed balance equations (see Appendix 3.5.1 for details) the equilibrium occupancy probability for any lattice site on the narrow channel e is equal to some constant ρ_e^*, i.e. $\rho_e^{(1)}\left(O(k),\infty\right) = \rho_e^*$ for $1 \leq k \leq K_e$. Additionally, for two distinct reservoirs i and j connected by a narrow channel e, we have $\alpha\rho_e^* = \gamma_i \sum_{n=0}^{N} n\rho_{i,e}^{(2)}\left(n,\emptyset(1),\infty\right) = \gamma_j \sum_{n=0}^{N} n\rho_{j,e}^{(2)}\left(n,\emptyset(K_e),\infty\right)$. Applying the MFA

$$\rho_{i,e}^{(2)}\left(n,\emptyset(1),\infty\right) \approx \rho_i^{(1)}\left(n,\infty\right)\rho_e^{(1)}\left(\emptyset(1),\infty\right), \tag{3.3}$$

as in Section 2.1.1, yields

$$\alpha\tilde{\rho}_e^* = \gamma_i\langle R_i(\infty)\rangle\left(1-\tilde{\rho}_e^*\right), \tag{3.4}$$

and similarly,

$$\alpha\tilde{\rho}_e^* = \gamma_j\langle R_j(\infty)\rangle\left(1-\tilde{\rho}_e^*\right), \tag{3.5}$$

where $\tilde{\rho}_e^*$ denotes the approximation to the exact equilibrium densities ρ_e^* due to the MFA. Therefore, $\gamma_i\langle R_i(\infty)\rangle = \gamma_j\langle R_j(\infty)\rangle$ for directly connected reservoirs i and j. For a connected network there exists a path between all pairs of reservoirs, therefore $\gamma_i\langle R_i(\infty)\rangle$ is equal to some constant γ^* for all reservoirs. Noting that $\alpha\tilde{\rho}_e^* = \gamma^*\left(1-\tilde{\rho}_e^*\right)$ for all narrow channels e, reveals that the equilibrium density $\tilde{\rho}_e^*$ is equal to a constant $\tilde{\rho}^* = \gamma^*/(\alpha+\gamma^*)$ for all narrow channels. Combining $\sum_{i=1}^{|\mathcal{V}|}\langle R_i\rangle + K_{\mathrm{tot}}\tilde{\rho}^* = N$, and $\langle R_i\rangle = \gamma^*/\gamma_i$, yields $\gamma^* = \left(N - K_{\mathrm{tot}}\tilde{\rho}^*\right)h(\vec{\gamma})/|\mathcal{V}|$, where $[\vec{\gamma}]_i = \gamma_i$ and $h(\vec{\gamma})$ is the harmonic mean of the reservoir jump rates. Substituting the

expression for γ^* into $\tilde{\rho}^* = \gamma^*/(\alpha + \gamma^*)$ results in the quadratic equation

$$K_{\text{tot}} h(\vec{\gamma}) \left(\tilde{\rho}^*\right)^2 - \left(h(\vec{\gamma}) \left(N + K_{\text{tot}}\right) + |\mathcal{V}|\alpha\right) \tilde{\rho}^* + N h(\vec{\gamma}) = 0. \tag{3.6}$$

Taking the smaller root of Equation (3.6) (the only root between zero and one) yields

$$\rho^* = \frac{h(\vec{\gamma}) \left(N + K_{\text{tot}}\right) + \alpha|\mathcal{V}| - \sqrt{\left(h(\vec{\gamma}) \left(N + K_{\text{tot}}\right) + \alpha|\mathcal{V}|\right)^2 - 4N K_{\text{tot}} h(\vec{\gamma})^2}}{2K_{\text{tot}} h(\vec{\gamma})}. \tag{3.7}$$

When $|\mathcal{V}| = 2$ and $\gamma_1 = \gamma_2 = \gamma$, Equation (3.7) simplifies to Equation (2.12), the approximate equilibrium density for the two reservoir model.

For a three reservoir model (see Figure 3.1(a), inset) we select the reservoir jump rates to be $\vec{\gamma} = \delta\,(0.5, 0.75, 1)$, such that the harmonic mean, $h(\vec{\gamma}) = 9\delta/13$, can be controlled by a single parameter. The exact equilibrium density ρ^* for a three reservoir model, is calculated from the principal left-eigenvector of the transition matrix Q from the FMM. The density $\tilde{\rho}^*$ in Equation (3.7) approximates ρ^* excellently when the population size is sufficiently large (see Figure 3.1(a), arrow). The relative error, $\mathcal{E}_{\rho^*} = |\rho^* - \tilde{\rho}^*|/\rho^*$, quantifies the inaccuracy of the approximate equilibrium density, and the error decreases over all values of the harmonic mean of the reservoir jump rates as the population size increases (see Figure 3.1(b)).

3.2 The reduced Markov model

As in Chapter 2, the high dimensionality of the FMM comes from explicitly modelling the occupancy of every lattice site along every narrow channel. Understanding the functional relationship between the model parameters of the FMM and the equilibrium density in Equation (3.7), allows for the derivation of two RMMs, one in each of the low- and high-density regimes. These coarse-grained models suppose that the

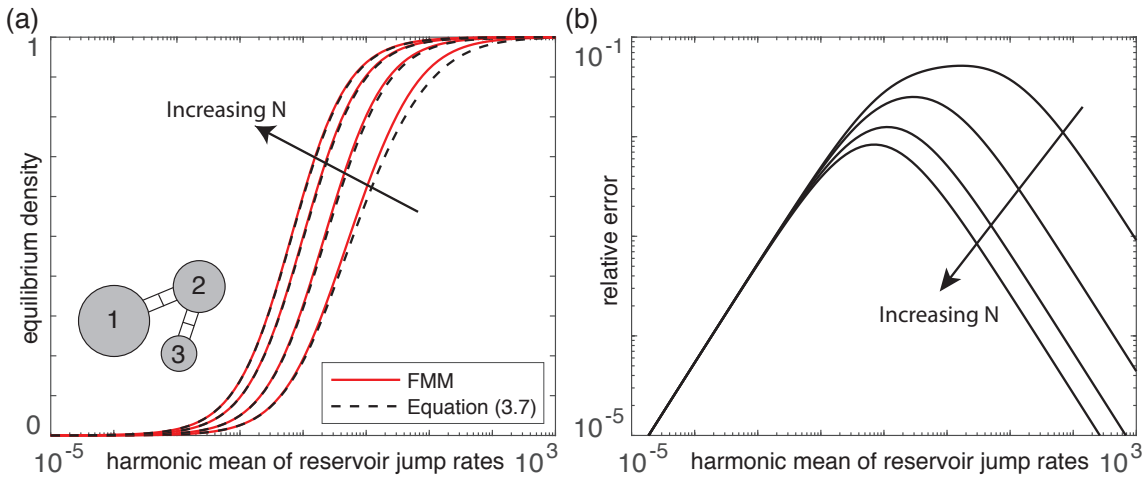

Figure 3.1: The approximate equilibrium density for a three reservoir network. (a): The approximate equilibrium density in Equation (3.7) (dashed black curve) against the true equilibrium density (solid red curve). (b): The relative error of the approximate equilibrium density for a range of population sizes. The parameters are $K_{(1,2)} = K_{(2,3)} = 2$, $\vec{\gamma} = \delta\,(0.5, 0.75, 1)$, such that $h(\vec{\gamma}) = 9\delta/13$, $\alpha = 1$ and $N \in \{5, 10, 20, 30\}$.

population of particles is distributed only amongst the reservoirs, and the particles transition directly between reservoirs that are connected via a narrow channel (see Figure 3.2 for a diagrammatic representation). The transition rates are calculated using the first moments of the particle switching times and the vacancy switching times from Chapter 2, for the low- and high-density regimes, respectively.

3.2.1 The low-density regime

The model parameters are selected to satisfy $h(\vec{\gamma})\,(N - K_{\text{tot}}) \ll |\mathcal{V}|\alpha$, to guarantee that the FMM is in the low-density regime[2], i.e. $\rho^* \ll 1$. The state vectors of the RMM are $\vec{n} = (n_1, \ldots, n_{|\mathcal{V}|})$, where n_i is the number of particles in reservoir i, such that $\sum_{i=1}^{|\mathcal{V}|} n_i = N$. A particle can jump directly between two distinct reservoirs i

[2]Recall, that $\alpha\rho^* = \gamma_i \sum_{n_i=0}^{N} n_i \rho^{(2)}\,(n_i, \emptyset_e(1), \infty)$ for the i-th reservoir and connecting narrow channel e. In the low-density regime $\rho^* \ll 1$, and so $\rho^{(2)}\,(n_i, \emptyset_e(1), \infty) \approx \rho^{(1)}\,(n_i, \infty)$ as each narrow channel lattice site is almost always empty. Therefore, $\alpha\rho^* \approx \gamma_i \langle R_i(\infty)\rangle$. Recall that $\gamma_i \langle R_i(\infty)\rangle$ is a constant for all reservoirs and is equal to $(N - K_{\text{tot}}\rho^*)\,h(\vec{\gamma})/|\mathcal{V}|$, therefore we have $\rho^* \sim h(\vec{\gamma})N/\left(|\mathcal{V}|\alpha + h(\vec{\gamma})K_{\text{tot}}\right)$. As we require that $\rho^* \ll 1$, we have $h(\vec{\gamma})\,(N - K_{\text{tot}}) \ll |\mathcal{V}|\alpha$.

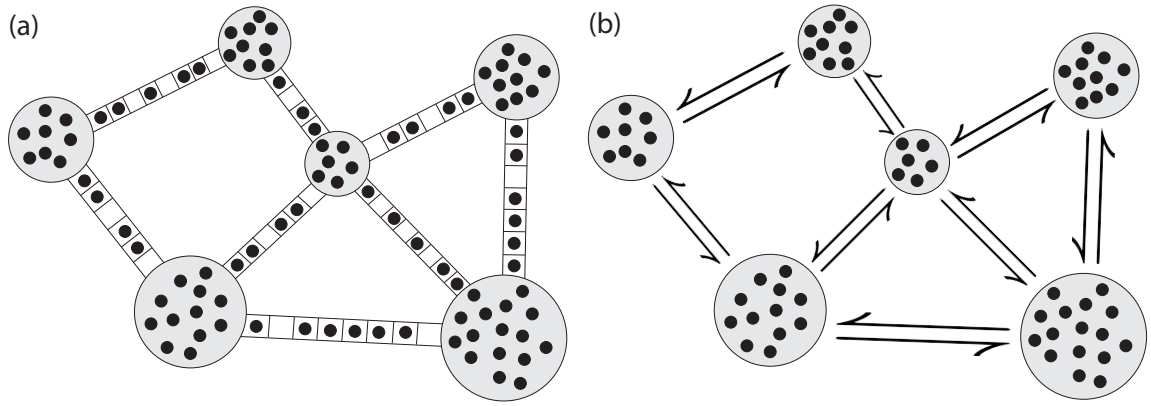

Figure 3.2: A representation of the FMM and the RMM for general networked environments. (a): The FMM where all narrow channels are modelled explicitly. (b): The RMM where the particles transition directly between reservoirs, and the narrow channel lengths are incorporated in these transition rates.

and j only if there is a narrow channel that connects them. The waiting time for this jump event to occur is calculated via the particle switching time for the two reservoir model in Chapter 2. Let the vector $\vec{\nu}_{i,j}$ for $i \neq j \in \{1, \ldots, |\mathcal{V}|\}$, be defined as $[\vec{\nu}_{i,j}]_k = \delta_{j,k} - \delta_{i,k}$ for $1 \leq k \leq |\mathcal{V}|$, where $\delta_{j,k}$ and $\delta_{i,k}$ are Kronecker deltas. A transition from state vector $\vec{n}$ to $\vec{n} + \vec{\nu}_{i,j}$, corresponds to a particle jumping from reservoir i to reservoir j. Such a transition can only occur if reservoirs i and j are directly connected via a narrow channel. For connected reservoirs, the transition occurs at rate $k_{i,j}^{\mathrm{LD}}\left(n_i; \gamma_i, K_{(i,j)}\right)$ which, adapted from Equation (2.14), is given by

$$k_{i,j}^{\mathrm{LD}}\left(n_i; \gamma_i, K_{(i,j)}\right) = \frac{1}{K_{(i,j)} + 1}\left(\frac{1}{\gamma_i n_i} + \frac{K_{(i,j)}}{2\alpha}\right)^{-1}, \tag{3.8}$$

where $(i, j) \in \mathcal{E}$, is the narrow channel that connects reservoirs i and j and $K_{(i,j)}$ is the length of the narrow channel. Note that this change in notation to denote edges will be used for the remainder of this chapter.

From Equation (3.8) a transition matrix for the RMM can be constructed, and the equilibration time is calculated as the reciprocal of the spectral gap of the transition matrix. However, the dimensionality of the RMM is $\mathcal{O}\left(N^{|\mathcal{V}|-1}\right)$, and therefore

calculating the spectral gap for the RMM is computationally infeasible other than for small networks. Further dimensionality reduction is achieved by studying the chemical master equations as seen in Section 2.2.2.1 of Chapter 2. Let the adjacency matrix $\mathcal{A}$ be a $|\mathcal{V}| \times |\mathcal{V}|$ matrix with entry $\mathcal{A}_{i,j}$ equal to one if a narrow channel connecting reservoirs i and j is present in the network, and zero otherwise. Additionally, define $p(\vec{n}, t)$ to be the probability that the particles are distributed amongst the reservoirs with state vector $\vec{n}$ at time t. The chemical master equations governing the evolution of $p(\vec{n}, t)$ are

$$\frac{\mathrm{d}p(\vec{n},t)}{\mathrm{d}t} = \sum_{i=1}^{|\mathcal{V}|}\sum_{j=1}^{|\mathcal{V}|} \mathcal{A}_{i,j}\left\{k_{i,j}^{\mathrm{LD}}\left(n_i+1;\gamma_i,K_{(i,j)}\right)p(\vec{n}-\vec{\nu}_{i,j},t) - k_{i,j}^{\mathrm{LD}}\left(n_i;\gamma_i,K_{(i,j)}\right)p(\vec{n},t)\right\}, \tag{3.9}$$

where $k_{i,j}^{\mathrm{LD}}\left(0;\gamma_i,K_{(i,j)}\right) = k_{i,j}^{\mathrm{LD}}\left(N;\gamma_i,K_{(i,j)}\right) = 0$ to avoid transitions to states with non-negative entries, or entries that exceed the total population.

To derive the Fokker-Planck equation corresponding to Equation (3.9), we introduce $\vec{x} = (x_1, \ldots, x_{|\mathcal{V}|})$, where $x_i = n_i/N$ is the fraction of the population that occupies the i-th reservoir. For $N \gg 1$, the fractions x_i are approximately continuous and lie in the interval $[0, 1]$. Introducing $Q(\vec{x}, t) = p(\vec{n}, t)$ and performing a Taylor expansion in $\epsilon = 1/N$ of Equation (3.9), yields the linear Fokker-Planck equation

$$\frac{\partial Q(\vec{x},t)}{\partial t} = \sum_{i=1}^{|\mathcal{V}|}\sum_{j=1}^{|\mathcal{V}|} \mathcal{A}_{i,j}\left\{\epsilon\nabla_{i,j}\left[g_{i,j}^{\mathrm{LD}}\left(\vec{x}\right)Q(\vec{x},t)\right] + \frac{\epsilon^2}{2}\nabla_{i,j}^2\left[g_{i,j}^{\mathrm{LD}}\left(\vec{x}\right)Q(\vec{x},t)\right]\right\}, \tag{3.10}$$

where $g_{i,j}^{\mathrm{LD}}\left(\vec{x}\right) = k_{i,j}^{\mathrm{LD}}\left(Nx_i;\gamma_i,K_{(i,j)}\right)$ and the parameter references to γ_i and $K_{(i,j)}$ are dropped for convenience. The operator $\nabla_{i,j}$ is defined as $\partial/\partial x_i - \partial/\partial x_j$, and the PDE in Equation (3.10) is defined on the domain $\vec{x} \in [0, 1]^{|\mathcal{V}|}$, with zero-flux boundary conditions. Equation (3.10) is a linear advection diffusion PDE and is the multivariate generalisation of Equation (2.29) in Section 2.2.2.1.

The equilibrium vector $\vec{x}^*$, is the distribution of particles that satisfies the follow-

ing equations

$$\sum_{j=1}^{|\mathcal{V}|} \mathcal{A}_{i,j} \left[g_{i,j}^{\mathrm{LD}}(x_i^*) - g_{j,i}^{\mathrm{LD}}(x_j^*) \right] = 0, \tag{3.11}$$

for $1 \leq i \leq |\mathcal{V}|$. Equations (3.11) are known as the global balance equations. The distribution of particles $\vec{x}^*$ that solves the global balance equations is such that the total transition rate out of each reservoir is equal to the total transition rate in. Under the condition that $\gamma_i N x_i^* \ll 2\alpha / K_{(i,j)}$ for all narrow channels $(i,j) \in \mathcal{E}$, the rate function $g_{i,j}^{\mathrm{LD}}(x_i) = k_{i,j}^{\mathrm{LD}}\left(N x_i; \gamma_i, K_{(i,j)}\right)$ from Equation (3.8) is approximately $g_{i,j}^{\mathrm{LD}}(x_i) \approx \gamma_i N x_i / \left(K_{(i,j)} + 1\right)$. Substituting this approximation into Equation (3.11), yields the following system of equations

$$\sum_{j=1}^{|\mathcal{V}|} \frac{N \mathcal{A}_{i,j}}{K_{(i,j)} + 1} \left(\gamma_i x_i^* - \gamma_j x_j^* \right) = 0, \tag{3.12}$$

for $1 \leq i \leq |\mathcal{V}|$. The unique solution[3] to Equations (3.12) is given by

$$x_i^* = \frac{\gamma_i^{-1}}{\sum_{k=1}^{|\mathcal{V}|} \gamma_k^{-1}}, \tag{3.13}$$

for $1 \leq i \leq |\mathcal{V}|$. Noting that $\gamma_i x_i^* = h(\vec{\gamma})/|\mathcal{V}|$, the condition $\gamma_i N x_i^* \ll 2\alpha / K_{(i,j)}$ for all narrow channels $(i,j) \in \mathcal{E}$, is equivalent to

$$h(\vec{\gamma}) N \ll |\mathcal{V}| \alpha \min_{(i,j) \in \mathcal{E}} \left\{ \frac{2}{K_{(i,j)}} \right\}. \tag{3.14}$$

The condition in Equation (3.14) is stricter than the condition to be in the low-density regime, $h(\vec{\gamma})\left(N - K_{\mathrm{tot}}\right) \ll |\mathcal{V}|\alpha$. However, if the condition in Equation (3.14) is not satisfied, the equilibrium vector $\vec{x}^*$ can instead be calculated by solving Equations (3.11) numerically, for example with the Newton-Raphson method.

[3]For $\vec{b}$ such that $[\vec{b}]_i = \gamma_i x_i^*$ and matrix $\mathcal{M}$ such that for $i \neq j$, $\mathcal{M}_{i,j} = N\mathcal{A}_{i,j} / \left(K_{(i,j)} + 1\right)$ and $\mathcal{M}_{i,i} = -\sum_{j \neq i}^{|\mathcal{V}|} \mathcal{M}_{i,j}$, Equations (3.12) are equivalent to $\mathcal{M}\vec{b} = \vec{0}$. For a connected network the null space of $\mathcal{M}$ is spanned by the constant vector, and along with the condition that $\sum_{i=1}^{|\mathcal{V}|} x_i^* = 1$, the solution is given by $x_i^* = \gamma_i^{-1} / \sum_{k=1}^{|\mathcal{V}|} \gamma_k^{-1}$.

To extract an equilibration time from the Fokker-Planck equation in Equation (3.10), we localise the PDE about the equilibrium vector as seen in Section 2.2.2.1. Let $\vec{z}$ be a perturbation about the equilibrium vector, such that $\vec{x} = \vec{x}^* + \vec{z}$ and $|z_i| \ll 1$ for $1 \leq i \leq |\mathcal{V}|$. Introducing $\tilde{Q}(\vec{z}, t) = Q(\vec{x}, t)$ and localising Equation (3.10) about $\vec{x}^*$ yields

$$\begin{aligned}\frac{\partial \tilde{Q}(\vec{z},t)}{\partial t} &= \epsilon \sum_{i=1}^{|\mathcal{V}|} \frac{\partial \tilde{Q}}{\partial z_i} \left\{ \sum_{j=1}^{|\mathcal{V}|} \mathcal{A}_{i,j} \left[g_{i,j}^{\mathrm{LD}}(x_i^*) - g_{j,i}^{\mathrm{LD}}(x_j^*) \right] \right\} \\ &\quad + \epsilon \sum_{i=1}^{|\mathcal{V}|} \frac{\partial}{\partial z_i} \left\{ \left[\left(\sum_{j=1}^{|\mathcal{V}|} \mathcal{A}_{i,j} \left(g_{i,j}^{\mathrm{LD}} \right)' (x_i^*) \right) z_i - \left(\sum_{j=1}^{|\mathcal{V}|} \mathcal{A}_{i,j} \left(g_{j,i}^{\mathrm{LD}} \right)' (x_j^*) z_j \right) \right] \tilde{Q} \right\} \\ &\quad + \frac{\epsilon^2}{2} \sum_{i=1}^{|\mathcal{V}|} \frac{\partial}{\partial z_i} \left\{ \sum_{j=1}^{|\mathcal{V}|} \mathcal{A}_{i,j} \left[g_{i,j}^{\mathrm{LD}}(x_i^*) + g_{j,i}^{\mathrm{LD}}(x_j^*) \right] \left(\frac{\partial}{\partial z_i} - \frac{\partial}{\partial z_j} \right) \tilde{Q} \right\}. \end{aligned} \tag{3.15}$$

Note that the first bracketed term on the right-hand side of Equation (3.15) is equal to zero from Equation (3.11). Adopting Einstein summation notation, Equation (3.15) is rewritten as

$$\frac{\partial \tilde{Q}(\vec{z},t)}{\partial t} = F_{i,j}^{\mathrm{LD}} \frac{\partial}{\partial z_i} \left[z_j \tilde{Q} \right] + D_{i,j}^{\mathrm{LD}} \frac{\partial^2 \tilde{Q}}{\partial z_i \partial z_j}, \tag{3.16}$$

with zero-flux boundary conditions at $z_i \to \pm\infty$, where $F_{i,j}^{\mathrm{LD}}$ and $D_{i,j}^{\mathrm{LD}}$ are entries of the drift and diffusion matrices, F^{LD} and D^{LD}, respectively. The entries of the drift matrix F^{LD} are

$$F_{i,j}^{\mathrm{LD}} = -\epsilon \mathcal{A}_{i,j} \left(g_{j,i}^{\mathrm{LD}} \right)' (x_j^*), \tag{3.17a}$$

for $i \neq j$, and

$$F_{i,i}^{\mathrm{LD}} = \epsilon \sum_{j=1}^{|\mathcal{V}|} \mathcal{A}_{i,j} \left(g_{i,j}^{\mathrm{LD}} \right)' (x_i^*), \tag{3.17b}$$

for $1 \leq i \leq |\mathcal{V}|$. The entries of the diffusion matrix D^{LD} are

$$D_{i,j}^{\mathrm{LD}} = -\frac{\epsilon^2}{2} \mathcal{A}_{i,j} \left(g_{i,j}^{\mathrm{LD}}(x_i^*) + g_{j,i}^{\mathrm{LD}}(x_j^*) \right), \tag{3.18a}$$

for $i \neq j$, and

$$D^{\mathrm{LD}}_{i,i} = \frac{\epsilon^2}{2} \sum_{j=1}^{|\mathcal{V}|} \mathcal{A}_{i,j} \left(g^{\mathrm{LD}}_{i,j}(x^*_i) + g^{\mathrm{LD}}_{j,i}(x^*_j) \right), \tag{3.18b}$$

for $1 \leq i \leq |\mathcal{V}|$.

The PDE in Equation (3.16) is in the form of a linear Fokker-Planck equation for a multivariate Ornstein-Uhlenbeck process. Defining the vector of moments $\vec{\mu}(t)$, such that $[\vec{\mu}(t)]_i = \int_{\mathbb{R}^{|\mathcal{V}|}} z_i \tilde{Q}(\vec{z}, t) \mathrm{d}\vec{z}$, multiplying Equation (3.16) by z_i for $1 \leq i \leq |\mathcal{V}|$, and integrating over $\mathbb{R}^{|\mathcal{V}|}$ yields

$$\frac{\mathrm{d}\vec{\mu}(t)}{\mathrm{d}t} = -F^{\mathrm{LD}} \vec{\mu}(t). \tag{3.19}$$

The system of ODEs in Equation (3.19) has solution $\vec{\mu}(t) = \exp\left(-tF^{\mathrm{LD}}\right) \vec{\mu}(0)$ and the eigenvalues of F^{LD} dictate the timescales on which the moments approach equilibrium [71]. Therefore in the low-density regime, the slowest timescale on which the Ornstein-Uhlenbeck process decays to equilibrium is the reciprocal of the spectral gap of the drift matrix F^{LD}. Recall that the dimension of the transition matrix Q of the FMM is $\mathcal{O}\left(N^{|\mathcal{V}|-1} 2^{K_{\mathrm{tot}}}\right)$. The drift matrix F^{LD} has dimension $|\mathcal{V}|$, significantly lower than the dimension of the FMM. Therefore the spectral gap of F^{LD} is extremely cheap to compute even for large networks.

To test how well the spectral gap of the drift matrix approximates the equilibration time of the FMM, we consider a small network example. Consider a network with three reservoirs, where reservoirs one and two are connected with a narrow channel of length two, and reservoirs two and three are connected with a narrow channel, also of length two (see Figure 3.3, inset). Let the reservoir rate parameters be $\vec{\gamma} = \delta(0.5, 0.75, 1)$, such that the harmonic mean of the reservoir jump parameters, $h(\vec{\gamma}) = 9\delta/13$, is controlled by a single parameter. For small values of δ, such that $h(\vec{\gamma})\,(N - K_{\mathrm{tot}}) \ll |\mathcal{V}|\alpha$, the FMM is in the low-density regime, and the reciprocal of the spectral gap for the drift matrix F^{LD} accurately predicts the equilibration time

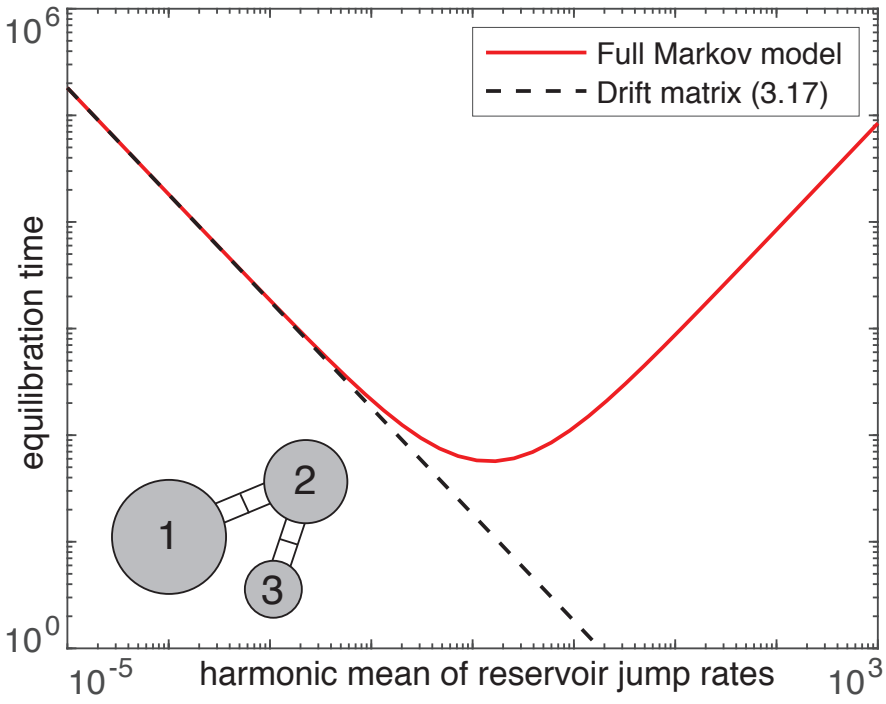

Figure 3.3: Equilibration time of the FMM (solid red curve) and the reciprocal of the spectral gap of the drift matrix in Equation (3.17) (dashed black curve) for a three-reservoir network (inset). The parameters are $K_{(1,2)} = K_{(2,3)} = 2$, $\vec{\gamma} = \delta(0.5, 0.75, 1)$ such that $h(\vec{\gamma}) = 9\delta/13$, $\alpha = 1$, and $N = 25$.

of the FMM (see Figure 3.3, dashed curve). The impressive dimensionality reduction is demonstrated by noting that the transition matrix of the FMM has a dimension of 6968, whereas the drift matrix F^{LD} has a dimension of three.

3.2.2 The high-density regime

We now turn to consider the high-density regime where particle interactions are no longer negligible. The model parameters of the FMM are selected to satisfy $h(\vec{\gamma})\,(N - K_{\mathrm{tot}}) \gg |\mathcal{V}|\alpha$, this is sufficient to guarantee that the FMM is in the high-density regime[4]. The state vectors of the RMM are $\vec{n} = (n_1, \ldots, n_{|\mathcal{V}|})$, where n_i is the number of particles in the i-th reservoir. In the high-density regime the K_{tot} narrow

[4]Recall that the equilibrium density ρ^*, approximately satisfies the quadratic in Equation (3.6). Let $\rho^* = 1 - \varepsilon$ where $\varepsilon \ll 1$. Linearising Equation (3.6) and solving in terms of ε, yields $\varepsilon = |\mathcal{V}|\alpha / \left(h(\vec{\gamma})\,(N - K_{\mathrm{tot}}) + |\mathcal{V}|\alpha\right)$. As $\varepsilon \ll 1$ we must have $h(\vec{\gamma})\,(N - K_{\mathrm{tot}}) \gg |\mathcal{V}|\alpha$.

channel lattice sites are almost always occupied. Therefore, for the RMM we select state vectors $\vec{n}$ such that $\sum_{i=1}^{|\mathcal{V}|} n_i = N_{\mathrm{HD}}$, where $N_{\mathrm{HD}} = N - K_{\mathrm{tot}}$. The waiting time for a particle to jump between two distinct reservoirs i and j is calculated via the vacancy switching time for the two reservoir model in Chapter 2. As in Section 3.2.1, let the vector $\vec{\nu}_{i,j}$ for $i \neq j \in \{1, \ldots, |\mathcal{V}|\}$, be defined as $[\vec{\nu}_{i,j}]_k = \delta_{j,k} - \delta_{i,k}$ for $1 \leq k \leq |\mathcal{V}|$. A transition from state vector $\vec{n}$ to $\vec{n} + \vec{\nu}_{i,j}$ corresponds to a particle jumping from reservoir i to reservoir j. This transition event occurs at rate $k_{i,j}^{\mathrm{HD}}\left(n_j; \gamma_j, K_{(i,j)}\right)$ which, adapted from Equation (2.34), is given by

$$k_{i,j}^{\mathrm{HD}}\left(n_j; \gamma_j, K_{(i,j)}\right) = \frac{1}{K_{(i,j)} - 1}\left(\frac{\gamma_j(n_j+1) + 2\alpha}{\alpha^2} + \frac{K_{(i,j)} - 2}{2\alpha}\right)^{-1}. \tag{3.20}$$

Note that, in the high-density regime, the transition rates depend on the occupancy of the reservoir that gains a particle in the transition event. This is in contrast to the transition rates in the low-density regime which depend on the occupancy of the reservoir that loses a particle.

Let $p(\vec{n}, t)$ be the probability that the particles are distributed amongst the reservoirs with state vector $\vec{n}$ at time t. Then $p(\vec{n}, t)$ evolves according to the chemical master equations

$$\frac{\mathrm{d}p(\vec{n}, t)}{\mathrm{d}t} = \sum_{i=1}^{|\mathcal{V}|}\sum_{j=1}^{|\mathcal{V}|} \mathcal{A}_{i,j}\left\{k_{i,j}^{\mathrm{HD}}\left(n_j - 1; \gamma_j, K_{(i,j)}\right) p(\vec{n} - \vec{\nu}_{i,j}, t) - k_{i,j}^{\mathrm{HD}}\left(n_j; \gamma_j, K_{(i,j)}\right) p(\vec{n}, t)\right\}, \tag{3.21}$$

where $k_{i,j}^{\mathrm{HD}}\left(0; \gamma_j, K_{(i,j)}\right) = k_{i,j}^{\mathrm{HD}}\left(N_{\mathrm{HD}}; \gamma_j, K_{(i,j)}\right) = 0$. The derivation and subsequent linearisation of the Fokker-Planck equation arising from Equation (3.21) proceeds analogously to Section 3.2.1. The resulting PDE is the Fokker-Planck equation for a multivariate Ornstein-Uhlenbeck process. The timescale on which this process decays to equilibrium is calculated as the reciprocal of the spectral gap of a drift matrix F^{HD}. Introducing $g_{i,j}^{\mathrm{HD}}(x_j) = k_{i,j}^{\mathrm{HD}}\left(N_{\mathrm{HD}} x_j; \gamma_j, K_{(i,j)}\right)$ and $\epsilon = 1/N_{\mathrm{HD}}$, the entries of the drift

matrix F^{HD} are

$$F^{\mathrm{HD}}_{i,j} = \epsilon \mathcal{A}_{i,j} \left(g^{\mathrm{HD}}_{i,j} \right)' (x^*_j), \tag{3.22a}$$

for $i \neq j$, and

$$F^{\mathrm{HD}}_{i,i} = -\epsilon \sum_{j=1}^{|\mathcal{V}|} \mathcal{A}_{i,j} \left(g^{\mathrm{HD}}_{j,i} \right)' (x^*_i), \tag{3.22b}$$

for $1 \leq i \leq |\mathcal{V}|$, where $\vec{x}^*$ is the equilibrium vector that satisifes the global balance equations

$$\sum_{j=1}^{|\mathcal{V}|} \mathcal{A}_{i,j} \left[g^{\mathrm{HD}}_{i,j} \left(x^*_j \right) - g^{\mathrm{HD}}_{j,i} \left(x^*_i \right) \right] = 0, \tag{3.23}$$

for $1 \leq i \leq |\mathcal{V}|$. Similar to the low-density regime in Section 3.2.1, the equilibrium vector can be approximated by

$$x^*_j \approx \frac{\gamma_j^{-1}}{\sum_{k=1}^{|\mathcal{V}|} \gamma_k^{-1}}, \tag{3.24}$$

for $1 \leq j \leq |\mathcal{V}|$, under the condition that

$$h(\vec{\gamma}) N \gg |\mathcal{V}| \max_{1 \leq j \leq |\mathcal{V}|} \{\gamma_j\} + |\mathcal{V}| \alpha \left[1 + \max_{(i,j) \in \mathcal{E}} \left\{ \frac{K_{(i,j)}}{2} \right\} \right]. \tag{3.25}$$

If this condition is not met, the equilibration vector $\vec{x}^*$ can be found by solving Equations (3.23) numerically, for example by the Newton-Raphson method. The reciprocal of the spectral gap of F^{HD} accurately predicts the equilibration time of the FMM in the high-density regime (see Figure 3.4, dashed curve), for the same three-reservoir network seen in Section 3.2.1. The low dimensionality of the drift matrix F^{HD} provides a useful tool to explore the effect of network topology on the equilibration time of a population of diffusing particles in heterogeneous crowded environments.

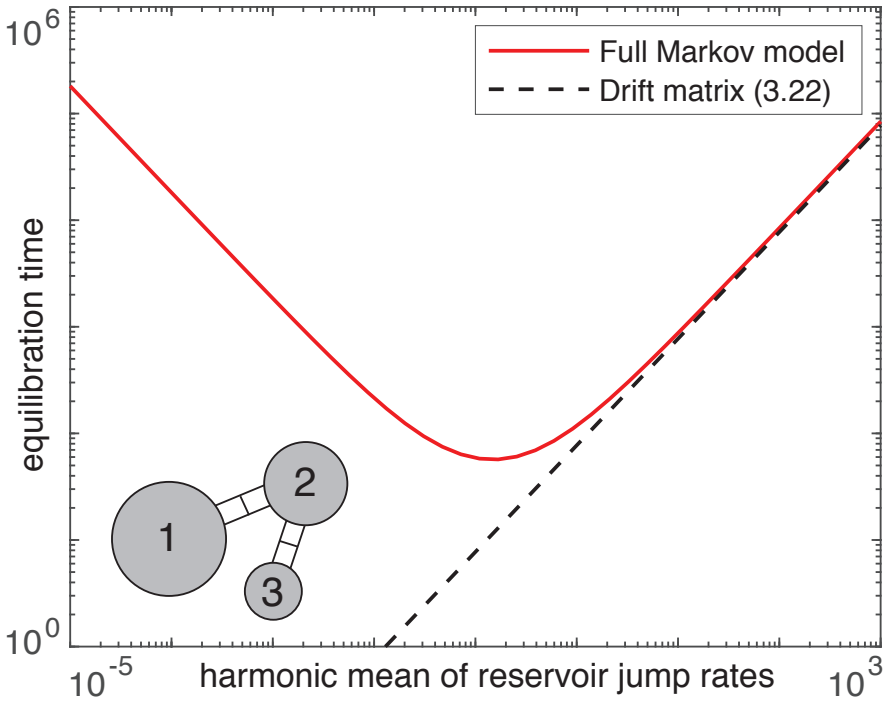

Figure 3.4: Equilibration time of the FMM (solid red curve) and the reciprocal of the spectral gap of the drift matrix in Equation (3.22) (dashed black curve) for a three-reservoir network (inset). The parameters are $K_{(1,2)} = K_{(2,3)} = 2$, $\vec{\gamma} = \delta(0.5, 0.75, 1)$ such that $h(\vec{\gamma}) = 9\delta/13$, $\alpha = 1$, and $N = 25$.

3.3 Optimising spatially embedded networked topologies

The significant reduction in dimensionality between the FMM and the drift matrix in Equation (3.22) allows for a thorough investigation into the relationship between network topology and the equilibration time of a population of diffusing particles. To focus attention, in the rest of this chapter we consider spatial networks that arise from connecting reservoirs embedded in three-dimensional Euclidean space. Let $\vec{x}_i \in \mathbb{R}^3$ be the position vector of the i-th reservoir, where $1 \leq i \leq |\mathcal{V}|$. Then $k_{i,j} = ||\vec{x}_i - \vec{x}_j||$, is the Euclidean distance between two distinct reservoirs i and j. The lengths of the narrow channels in the FMM previously considered were non-dimensional. For our spatial networks, we suppose that the lattice sites have

width Δ and the number of lattice sites connecting reservoirs i and j is taken to be $K_{(i,j)} = \lceil k_{i,j}/\Delta \rceil$. Each reservoir is given the same jump rate γ, such that the effect of network topology on the equilibration time of a population of diffusing particles can be investigated without the influence of heterogeneity in the reservoir jump rates. Therefore $h(\vec{\gamma}) = \gamma$ and the condition for the FMM to be in the high-density regime becomes $\gamma N_{\mathrm{HD}} \gg |\mathcal{V}|\alpha$. From Equation (3.25), we assume the stricter condition $\gamma N_{\mathrm{HD}} \gg |\mathcal{V}|\gamma + |\mathcal{V}|\alpha \left[1 + \max_{(i,j)\in\mathcal{E}} \left\{K_{(i,j)}/2\right\}\right]$, such that the rate function, $g^{\mathrm{HD}}_{i,j}(x_j)$, is approximately[5]

$$g^{\mathrm{HD}}_{i,j}(x_j) \approx \frac{\alpha^2}{K_{(i,j)}\gamma N_{\mathrm{HD}} x_j}. \tag{3.26}$$

For equal reservoir jump rates, the equilibrium vector is $\vec{x}^* = (|\mathcal{V}|^{-1}, \ldots, |\mathcal{V}|^{-1})$ and the entries of the drift matrix, F^{HD}, from Equation (3.22), are given by

$$F^{\mathrm{HD}}_{i,j} \approx -\mathcal{A}_{i,j} \frac{\alpha^2 |\mathcal{V}|^2}{K_{(i,j)}\gamma N^2_{\mathrm{HD}}}, \tag{3.27}$$

for $i \neq j$ and $F^{\mathrm{HD}}_{i,i} = -\sum_{j\neq i} F^{\mathrm{HD}}_{j,i}$ for $1 \leq i \leq |\mathcal{V}|$. Recall that in the high-density regime, $\rho^* \approx \gamma N_{\mathrm{HD}}/(\gamma N_{\mathrm{HD}} + |\mathcal{V}|\alpha)$. Noting that $(1-\rho^*)/\rho^* \approx |\mathcal{V}|\alpha/\gamma N_{\mathrm{HD}}$ the entries of the drift matrix F^{HD} are rewritten as

$$F^{\mathrm{HD}}_{i,j} \approx -\mathcal{A}_{i,j} \frac{\gamma (1-\rho^*)^2}{K_{(i,j)} (\rho^*)^2}, \tag{3.28}$$

for $i \neq j$ and $F^{\mathrm{HD}}_{i,i} = -\sum_{j\neq i} F^{\mathrm{HD}}_{j,i}$ for $1 \leq i \leq |\mathcal{V}|$.

3.3.1 All connected networked topologies for five reservoirs

Using the spectral gap of the drift matrix in Equation (3.28), we calculate the equilibration time for all connected networked topologies for a particular configuration of five randomly positioned reservoirs. For an ensemble of five reservoirs, there are a

[5] We make the additional assumption that $\Delta \ll \min_{(i,j)\in\mathcal{E}} \{k_{i,j}\}$, such that $K_{(i,j)} \gg 1$ and $K_{(i,j)} - 1 \approx K_{(i,j)}$.

total of 728 connected networked topologies. The position vectors $\vec{x}_i$ for $1 \leq i \leq 5$ are sampled independently and uniformly within the unit sphere. The reciprocal of the spectral gap of the drift matrix in Equation (3.28) is used to calculate the equilibration time for all 728 networks. In Figure 3.5 the equilibration times are plotted against the total edge length, $K_{\text{tot}} = \sum_{(i,j)\in\mathcal{E}} K_{(i,j)}$, for each network. The equilibration times vary over two orders of magnitude, demonstrating how sensitive the time taken to equilibrate is to network topology. The network with the smallest equilibration time is the complete network (see Figure 3.5(xiv)). This is unsurprising as including additional narrow channels allows particles to transition between reservoirs more frequently, and therefore decreases the equilibration time. However, real-world spatial networks often have a total number of edges significantly lower than the complete network [81, 82]. We introduce a restriction to the total edge length (see Figure 3.5, vertical line), and consider the subset of topologies with total edge length less than or equal to the restricted value (see Figure 3.5, black dots). We refer to the network which minimises the equilibration time subject to the restriction in the total edge length as an optimal network (see Figure 3.5(viii)). Varying the restricted value over the entire range of total edge lengths reveals a frontier of optimal networks (see Figure 3.5(i)–(xiv)). The first network on the frontier is necessarily the minimum spanning tree (MST), the network with the smallest total edge length (see Figure 3.5(i)). The last network on the frontier is the complete network (see Figure 3.5(xiv)). The remainder of this chapter investigates properties of this frontier. Can we quantify the frontier for larger numbers of reservoirs? What are the important topological features of optimal networks that lie on this frontier? Can we develop systematic algorithms that construct optimal or close-to-optimal networks for a fixed realisation of reservoirs? To answer these questions, we begin by formalising the optimal frontier for an arbitrary number of reservoirs.

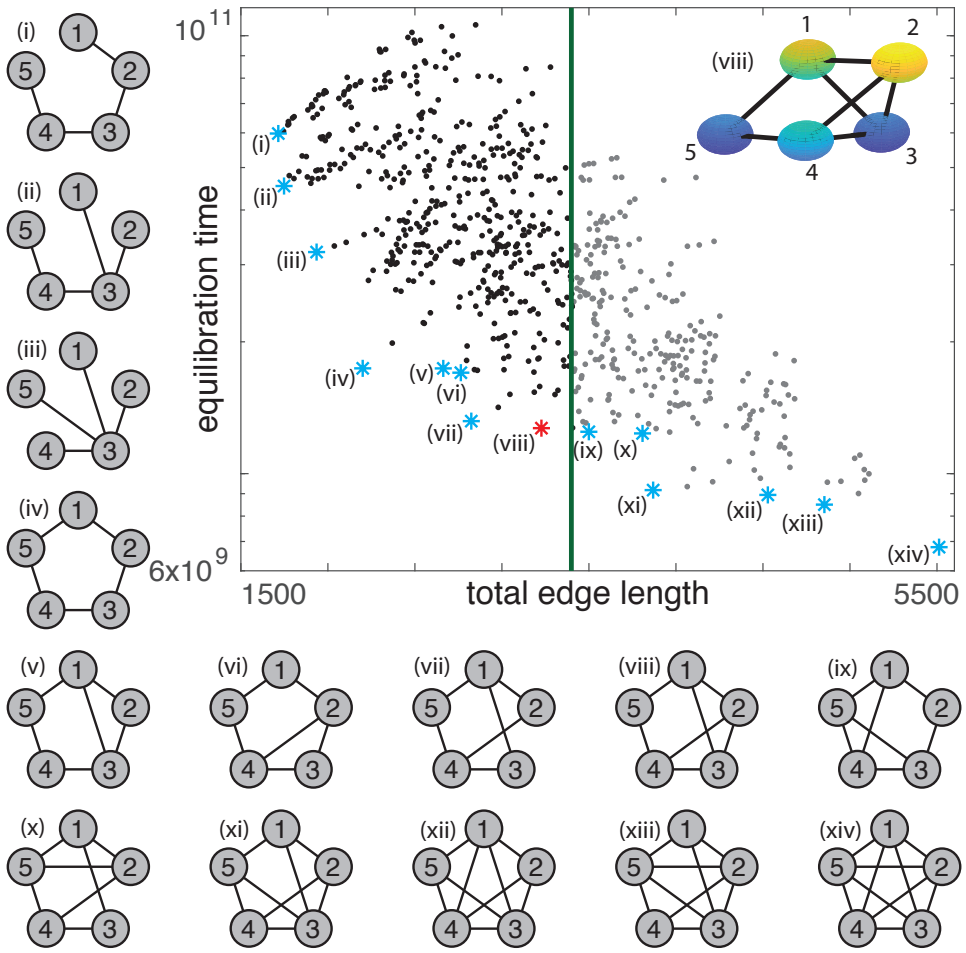

Figure 3.5: Equilibration time against the total edge length for all 728 connected networked topologies on five randomly distributed reservoirs (inset spheres). The optimal frontier is highlighted with asterisks. (i)–(xiv): The topologies of the networks that lie on the optimal frontier. The parameters are $\Delta = 10^{-3}$, $\rho^* = 0.99$ and $\gamma = 0.16$.

3.3.2 The optimal frontier

Define $\mathcal{C}_{|\mathcal{V}|}$ to be the set of all connected networks on $|\mathcal{V}|$ labelled nodes. The distinct networks are given an arbitrary ordering, such that $\mathcal{G}_\ell = \{\mathcal{V}, \mathcal{E}_\ell\}$ for $1 \leq \ell \leq |\mathcal{C}_{|\mathcal{V}|}|$, where $\mathcal{E}_\ell$ is the set of edges present in the ℓ-th network. Let $\mathcal{X} = \{\vec{x}_i\}_{1 \leq i \leq |\mathcal{V}|}$, be the spatial configuration of the reservoirs, where $\vec{x}_i$ is the position vector of the i-th reservoir. The narrow channel connecting distinct reservoirs i and j, has $K_{(i,j)} = \lceil ||\vec{x}_i - \vec{x}_j||/\Delta \rceil$ lattice sites, where Δ is the width of each site. For each network

$\mathcal{G}_\ell \in \mathcal{C}_{|\mathcal{V}|}$ there is a corresponding total edge length $K_{\text{tot},\ell}(\mathcal{X}) = \sum_{(i,j)\in\mathcal{E}_\ell} K_{(i,j)}$, and equilibration time $\mathcal{T}_\ell(\mathcal{X})$, calculated as the reciprocal of the spectral gap of the drift matrix in Equation (3.28). Let $K_{\min}(\mathcal{X}) = \min_{1\leq\ell\leq|\mathcal{C}_{|\mathcal{V}|}|}\{K_{\text{tot},\ell}(\mathcal{X})\}$; the network that achieves this minimum is the MST. Similarly, $K_{\max}(\mathcal{X}) = \max_{1\leq\ell\leq|\mathcal{C}_{|\mathcal{V}|}|}\{K_{\text{tot},\ell}(\mathcal{X})\}$, where the complete network is always the network that maximises the total edge length. To define the optimal frontier for a configuration $\mathcal{X}$, a restriction to the total edge length r, is introduced such that $r \in [K_{\min}(\mathcal{X}), K_{\max}(\mathcal{X})]$. The optimal network that minimises the equilibration time with a total edge length less than or equal to r is denoted $\mathcal{G}_{\text{opt}(r)}$, where

$$\text{opt}(r) = \underset{1\leq\ell\leq|\mathcal{C}_{|\mathcal{V}|}}{\text{argmin}}\left\{\mathcal{T}_\ell(\mathcal{X}) : K_{\text{tot},\ell}(\mathcal{X}) \leq r\right\}. \tag{3.29}$$

The optimal frontier $F_{\text{opt}}(\mathcal{X})$ is defined as the set of coordinates

$$F_{\text{opt}}(\mathcal{X}) = \bigcup_{r\in[K_{\min}(\mathcal{X}),K_{\max}(\mathcal{X})]}\left\{\left(K_{\text{tot,opt}(r)}(\mathcal{X}), \mathcal{T}_{\text{opt}(r)}(\mathcal{X})\right)\right\}. \tag{3.30}$$

To compare optimal frontiers for different configurations, $\mathcal{X}$, two rescalings are introduced. Firstly, for each network $\mathcal{G}_\ell \in \mathcal{C}_{|\mathcal{V}|}$, the rescaled total edge length (RTEL), $\tilde{K}_{\text{tot},\ell}(\mathcal{X})$, is defined as

$$\tilde{K}_{\text{tot},\ell}(\mathcal{X}) = \frac{(K_{\text{tot},\ell}(\mathcal{X}) - K_{\min}(\mathcal{X}))}{(K_{\max}(\mathcal{X}) - K_{\min}(\mathcal{X}))}. \tag{3.31}$$

The RTEL lies between zero and one, and is equal to zero and one for the MST and the complete network, respectively. Secondly, for each network $\mathcal{G}_\ell \in \mathcal{C}_{|\mathcal{V}|}$, the equilibration factor, $\tilde{\mathcal{T}}_\ell(\mathcal{X})$, is defined as

$$\tilde{\mathcal{T}}_\ell(\mathcal{X}) = \frac{\mathcal{T}_\ell(\mathcal{X})}{\mathcal{T}_{\min}(\mathcal{X})}, \tag{3.32}$$

where $\mathcal{T}_{\min}(\mathcal{X})$ is the equilibration time for the complete network. For every network $\mathcal{G}_\ell \in \mathcal{C}_{|\mathcal{V}|}$, the equilibration factor $\tilde{\mathcal{T}}_\ell(\mathcal{X})$, is greater than or equal to one, and quantifies how many times slower equilibration occurs in the network $\mathcal{G}_\ell$ compared to the complete network. The indices for networks that lie on the optimal frontier are redefined as

$$\tilde{\text{opt}}(\delta) = \underset{1\leq\ell\leq|\mathcal{C}_{|\mathcal{V}|}|}{\text{argmin}} \left\{\tilde{\mathcal{T}}_\ell(\mathcal{X}) : \tilde{K}_{\text{tot},\ell}(\mathcal{X}) \leq \delta\right\}, \tag{3.33}$$

for $\delta \in [0,1]$. The rescaled optimal frontier, $\tilde{F}_{\text{opt}}(\mathcal{X})$, for a configuration $\mathcal{X}$ is defined as

$$\tilde{F}_{\text{opt}}(\mathcal{X}) = \bigcup_{\delta\in[0,1]} \left\{\left(\tilde{K}_{\text{tot},\tilde{\text{opt}}(\delta)}(\mathcal{X}), \tilde{\mathcal{T}}_{\tilde{\text{opt}}(\delta)}(\mathcal{X})\right)\right\}. \tag{3.34}$$

The variable $\tilde{\mathcal{T}}_{\tilde{\text{opt}}(\delta)}(\mathcal{X})$ is the lowest equilibration factor from the subset of networks with RTEL less than or equal to δ. We refer to $\tilde{\mathcal{T}}_{\tilde{\text{opt}}(\delta)}(\mathcal{X})$ as the *optimal equilibration factor*.

In Figure 3.5 the optimal frontier was presented for a random configuration of five reservoirs. The set of all connected networks, $\mathcal{C}_5$, has 728 elements, therefore sweeping the entire network space to calculate the optimal frontier is computationally feasible. However, as the number of reservoirs increases the set of connected networks grows drastically in size[6]. Therefore, the optimal frontier for configurations with a greater number of reservoirs must be estimated numerically. The numerical procedure used to estimate the optimal frontiers is detailed in Appendix 3.5.2. The position vectors of each reservoir are sampled independently and uniformly from the unit sphere. For configurations of ten reservoirs, 250 configurations were sampled and the optimal frontiers estimated numerically. The coordinates of the optimal frontier are binned and the ensemble averages are presented in Figure 3.6. This procedure is repeated for configurations of both 30 and 50 reservoirs. As the number of reservoirs increases, the optimal frontier follows almost exactly the same curve, particularly for RTELs greater

[6]For as few as ten reservoirs there are greater than 3.4×10^{13} distinct connected networks.

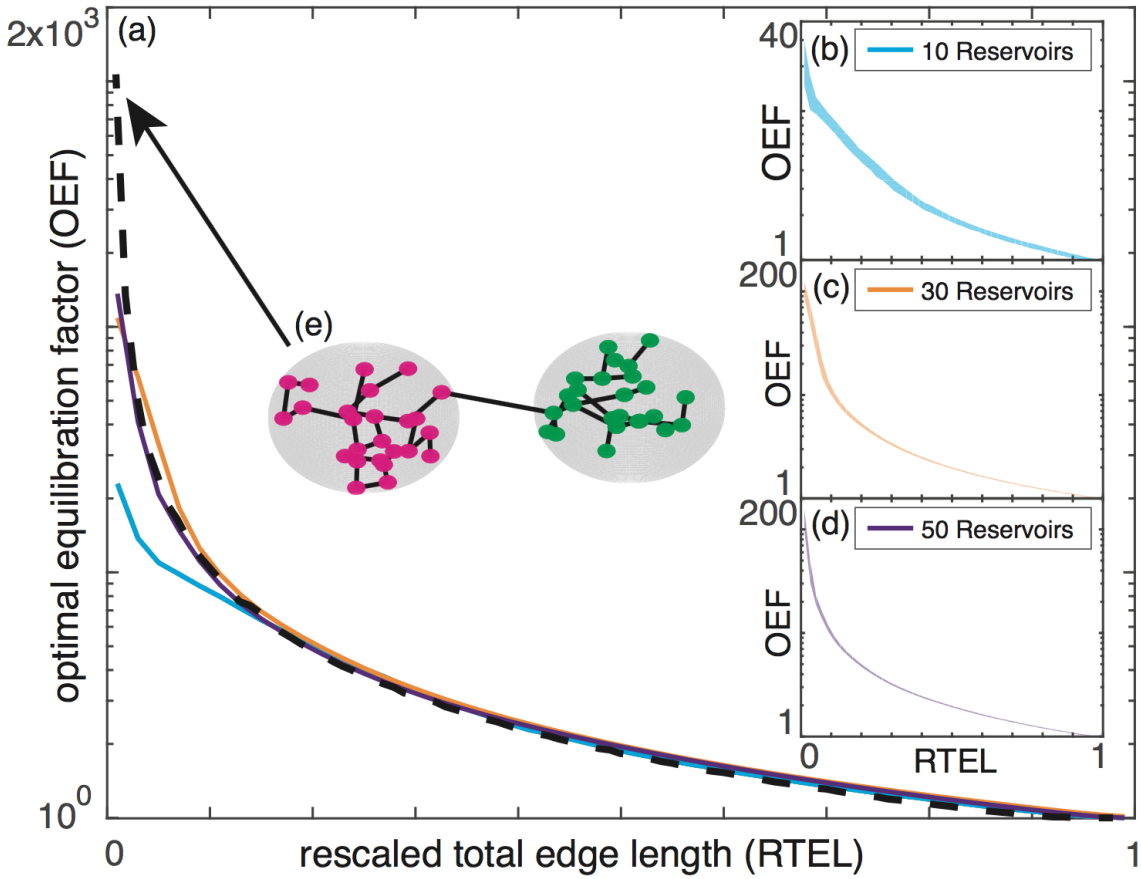

Figure 3.6: (a): Averaged coordinates of the optimal frontiers from 250 configurations of 10 (cyan curve), 30 (orange curve), 50 (purple curve) reservoirs, and a single configuration of 50 reservoirs sampled from two separated spheres (dashed curve). (b)-(d): Shaded regions represent the averaged coordinates of the optimal frontiers plus and minus a standard deviation. (e): A single realisation of reservoirs sampled from two separated spheres, where the network shown is the MST.

than 0.2 (see Figure 3.6(a)). Furthermore, the variation in the optimal frontiers is vanishingly small as the number of reservoirs increases (see Figure 3.6(b)–(d)). These results suggest that the optimal frontier may follow a universal curve.

Thus far, the positions of the reservoirs have been sampled uniformly from the unit sphere. For a heterogeneous distribution we consider a two-sphere configuration of 50 reservoirs, where the positions of 25 reservoirs are sampled uniformly from the unit sphere centred about $(0, 0, 0)$, and another 25 reservoirs are uniformly sampled from a unit sphere centred about $(3, 0, 0)$ (see Figure 3.6(e)). Despite a high optimal

equilibration factor for the MST (see Figure 3.6, arrow), the majority of the optimal frontier for the two sphere configuration follows the same curve as the one sphere configurations (see Figure 3.6, dashed curve). Therefore, spatial heterogeneity in the distribution of the reservoirs does not seem to affect the optimal frontier. All configurations considered in Figure 3.6 consist of reservoirs with equal jump rates. For a discussion of the optimal frontier with heterogeneous jump rates see Section 6.2.2.

3.3.3 The weighted degree distribution of optimal networks

In this section we investigate topological properties of networks that lie on the optimal frontier. Consider a configuration of reservoirs $\mathcal{X} = \{\vec{x}_i\}_{1\leq i\leq|\mathcal{V}|}$, where $\vec{x}_i$ is the position vector of the i-th reservoir and the Euclidean distance between two reservoirs i and j is $k_{i,j} = ||\vec{x}_i - \vec{x}_j||$. For lattice sites of width Δ the number of lattice sites in a narrow channel is $K_{(i,j)} = \lceil k_{i,j}/\Delta \rceil$. However, for $\Delta \ll \min_{1\leq i\neq j\leq|\mathcal{V}|}\{k_{i,j}\}$, we have $K_{(i,j)} \approx k_{i,j}/\Delta$. The entries of the drift matrix in Equation (3.28) are rewritten using the dimensional parameters $k_{i,j}$ and Δ as

$$F^{\mathrm{HD}}_{i,j} \approx -\mathcal{A}_{i,j}\frac{\gamma\Delta\left(1-\rho^*\right)^2}{k_{i,j}\left(\rho^*\right)^2}, \tag{3.35}$$

for $i \neq j$ and $F^{\mathrm{HD}}_{i,i} = -\sum_{j\neq i} F^{\mathrm{HD}}_{j,i}$ for $1 \leq i \leq |\mathcal{V}|$. For each network, the equilibration factor in Equation (3.32) is calculated as the ratio of two spectral gaps, and, as such, is independent of the constants ρ^*, γ and Δ in Equation (3.35). Therefore, the equilibration factors can be calculated from the rescaled drift matrix, $\tilde{F}^{\mathrm{HD}}$, with entries

$$\tilde{F}^{\mathrm{HD}}_{i,j} = \mathcal{A}_{i,j}\frac{1}{k_{i,j}}, \tag{3.36}$$

for $i \neq j$, where $\mathcal{A}_{i,j}$ are the entries of the adjacency matrix, and $\tilde{F}^{\mathrm{HD}}_{i,i} = -\sum_{j\neq i}\tilde{F}^{\mathrm{HD}}_{i,j}$ for $1 \leq i \leq |\mathcal{V}|$. Note that the equilibration factors are only a function of network topology and the Euclidean distances between reservoirs.

To study the topology of optimal networks, we introduce an order to the reservoirs in a given configuration. Viewing the non-zero entries $k_{i,j}^{-1}$ of the rescaled drift matrix as rates of transitions between reservoirs, we define the potential transition rate (PTR), R_i, of the i-th reservoir as

$$R_i = \sum_{j \neq i} \frac{1}{k_{i,j}}. \tag{3.37}$$

Ordering the reservoirs by their PTRs such that $R_1 < R_2 < \cdots < R_{|\mathcal{V}|}$, reveals interesting topological features of networks that lie on the optimal frontier. In Figure 3.7 we highlight three networks at different positions along the optimal frontier. The network in Figure 3.7 with the lowest RTEL has degree distribution $(1, 1, 2, 1, 1, 2, 1, 3, 3, 5)$, where the reservoirs are ranked lowest to highest by their PTRs. Therefore reservoirs with higher PTRs appear to have large degrees for optimal networks with low RTELs. However, from Equation (3.37), we find that the edges connected to reservoirs with high PTRs will have some of the shortest edge lengths. Therefore, even for non-optimal networks with low RTELs, we expect reservoirs with higher PTRs to have greater degree than reservoirs with low PTRs. To compare the topological structure of both optimal and non-optimal networks we introduce the following weighted degree distribution.

For a network $\mathcal{G} \in \mathcal{C}_{|\mathcal{V}|}$ with adjacency matrix $\mathcal{A}$, the i-th reservoir has weighted degree

$$W_i\left(\mathcal{G}; \mathcal{X}\right) = \frac{\sum_{j \neq i} \mathcal{A}_{i,j} k_{i,j}^{-1}}{\sum_{j \neq i} k_{i,j}^{-1}}. \tag{3.38}$$

The numerator in Equation (3.38) is equal to the total rate out of the i-th reservoir in the network $\mathcal{G}$, and the denominator is the PTR of the i-th reservoir. Therefore, the weights $W_i\left(\mathcal{G}; \mathcal{X}\right)$ lie between zero and one and represent the fraction of the PTR of the i-th reservoir which is present in the network $\mathcal{G}$. Translating the weights in

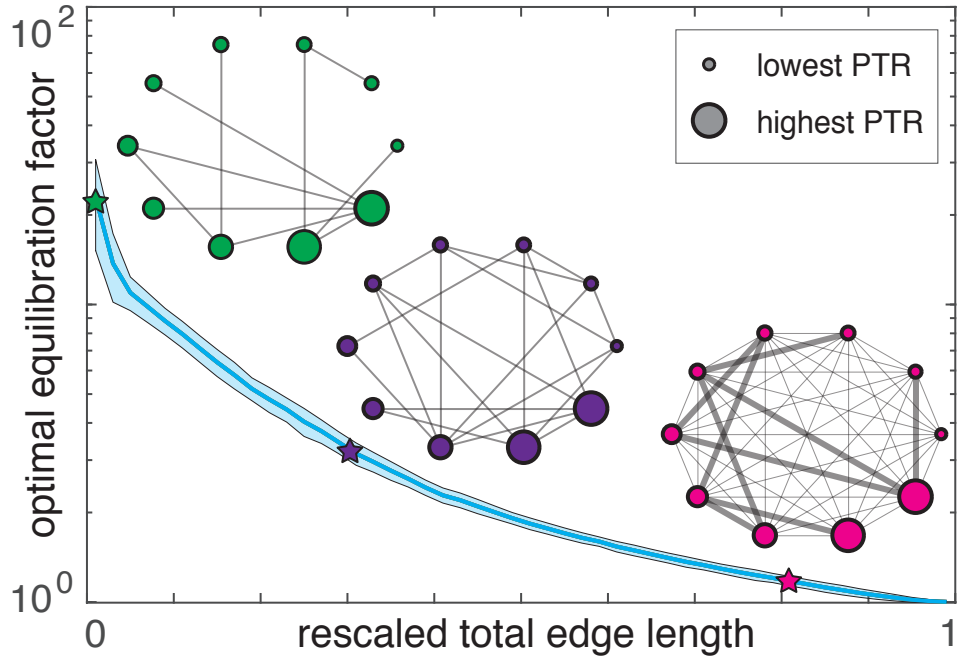

Figure 3.7: The averaged coordinates of the optimal frontiers from 250 configurations of ten reservoirs (solid curve) plus and minus a standard deviation (shaded region). Three contrasting networks are shown along the frontier. The size of the nodes represents the PTRs of the reservoirs, which are ordered anti-clockwise from lowest to highest. Thick lines in the right-most network represent the edges which are missing from the network.

Equation (3.38) by the average weighted degree of the network, yields

$$\tilde{W}_i\left(\mathcal{G};\mathcal{X}\right) = W_i\left(\mathcal{G};\mathcal{X}\right) - \frac{\sum_{j=1}^{|\mathcal{V}|} W_j\left(\mathcal{G};\mathcal{X}\right)}{|\mathcal{V}|}. \tag{3.39}$$

If $\tilde{W}_i\left(\mathcal{G};\mathcal{X}\right) < 0$, then the weight of the i-th reservoir is less than the average weight of the network, and we refer to the i-th reservoir as being under represented in the network. Similarly, if $\tilde{W}_i\left(\mathcal{G};\mathcal{X}\right) > 0$ we refer to the i-th reservoir as being over represented in the network.

To compare the weighted degree distributions for optimal and non-optimal networks, the RTEL is split into ten equally sized intervals (see Figure 3.8(a)). For each interval, the weighted degree distributions are evaluated for an ensemble of optimal networks and an ensemble of non-optimal networks that are randomly sampled from

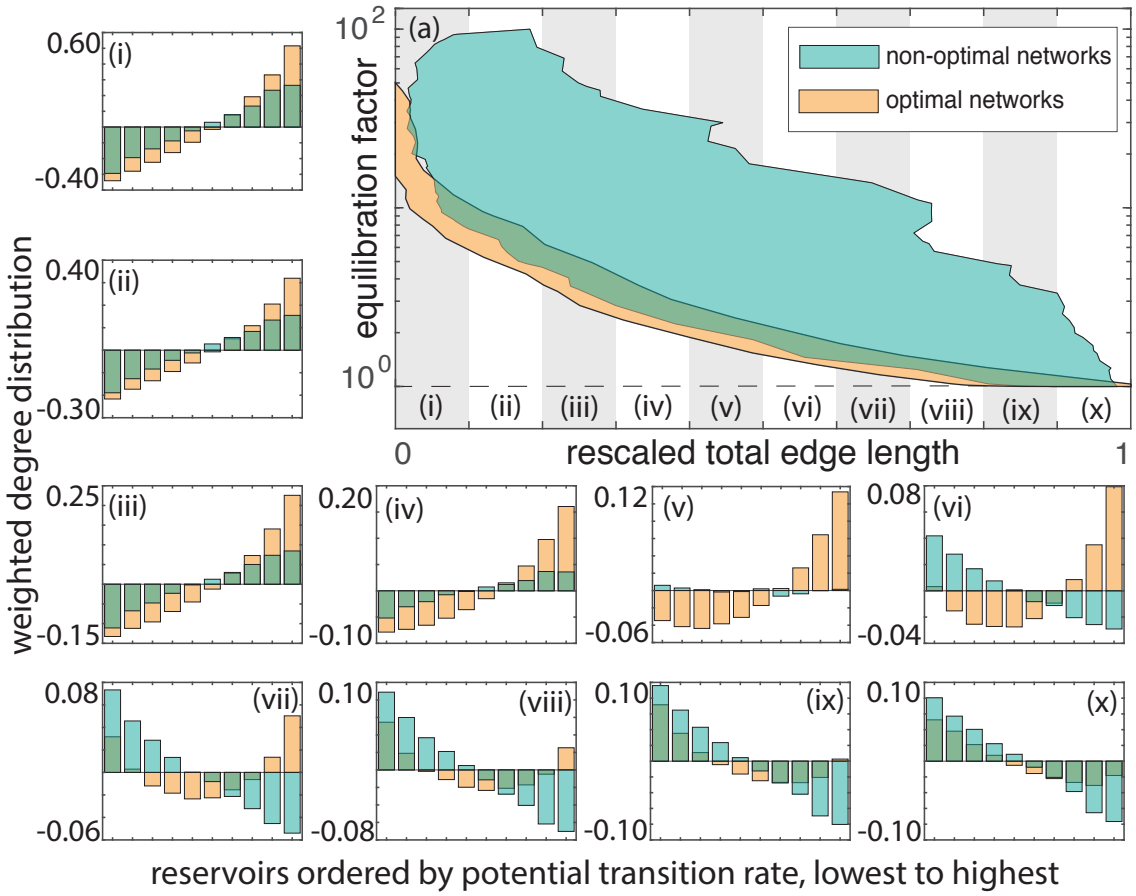

Figure 3.8: (a): The range of equilibration factors for non-optimal networks (green domain) and optimal networks (orange domain) from 5000 configurations of ten reservoirs. (i)-(x): The weighted degree distributions for both optimal and non-optimal networks, translated by each networks average weighted degree, for different values of the RTEL. The reservoirs are ordered from left to right in increasing order of their PTR.

the set of all connected networked topologies (see Figure 3.8(i)–(x)). For details of the numerical procedures used, see Appendix 3.5.2. For both optimal and non-optimal networks with low RTELs, reservoirs with high and low PTRs are over and under represented, respectively (see Figure 3.8(i)–(iii)). However, for optimal networks the range of the weighted degree distribution is greater than for non-optimal networks. As the RTEL increases, the weighted degree distributions for non-optimal networks become approximately uniform (see Figure 3.8(iv) and (v)). In comparison, optimal networks have remarkably different weighted degree distributions. Reservoirs with

both low and high PTRs are over represented in the networks, and reservoirs with PTRs that rank in the middle are under represented (see Figure 3.8(v)–(viii) and Figure 3.7, middle inset). These results suggest that optimal networks favour long edges connecting reservoirs that are far apart, and edges of moderate length are unfavourable. For RTELs close to one, both optimal and non-optimal networks favour reservoirs that have low PTRs (see Figure 3.8 (ix) and (x)). However, for optimal networks, reservoirs with high PTRs are less under represented than for non-optimal networks.

The weighted degree distribution has highlighted striking differences in the topological structure of optimal networks compared to non-optimal networks. However, the numerical simulations required to study the weighted degree distributions are highly computationally expensive. As such, we consider more efficient algorithms to construct optimal or close-to-optimal networks.

3.3.4 Efficient algorithms for optimal networks

The optimal frontiers presented thus far have been numerically estimated via a simulated annealing algorithm (see Appendix 3.5.2 for details). Such algorithms search stochastically within the set of all connected networks to find networks that minimise the equilibration time. Therefore, the algorithmic complexity of the simulated annealing algorithm scales with the dimensionality of the set $\mathcal{C}_{|\mathcal{V}|}$. Even the set of all trees, a small subset of $\mathcal{C}_{|\mathcal{V}|}$, has dimensionality $|\mathcal{V}|^{|\mathcal{V}|-2}$. Therefore, as the number of reservoirs increases we require more efficient algorithms to construct optimal or close-to-optimal networks.

In this section we propose two algorithms which start at the MST, the left-most network on the optimal frontier, and add narrow channels in a particular order with no rewiring until the complete network is reached. The ensemble of networks produced by the algorithms approximate the optimal frontier. The first algorithm is the *shortest*

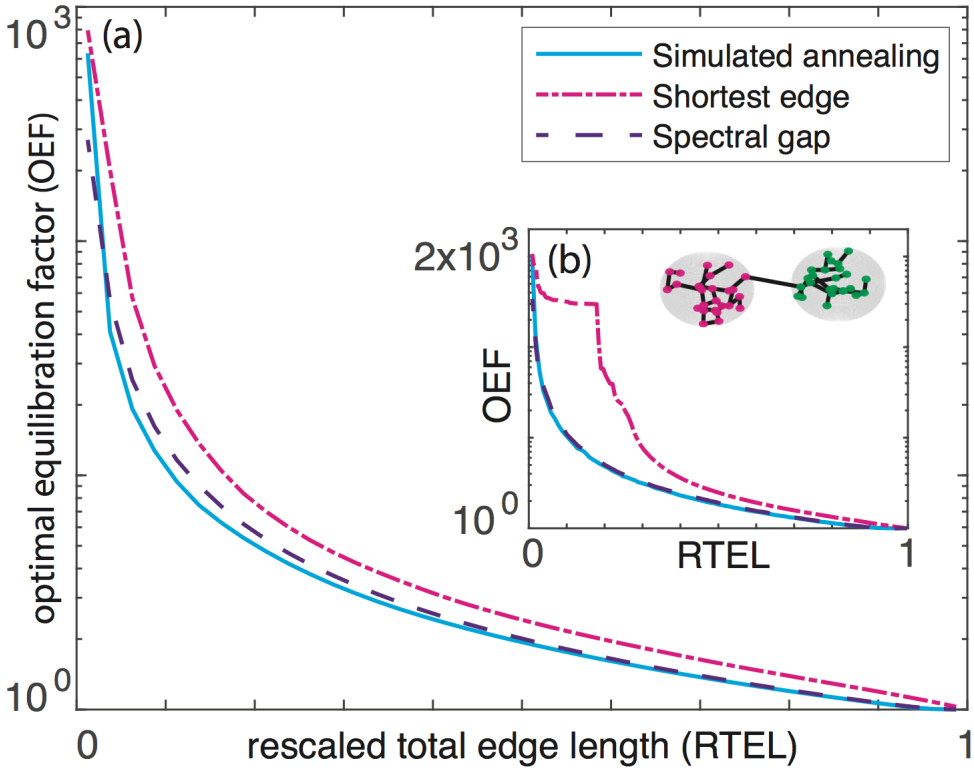

Figure 3.9: (a): Averaged coordinates of optimal frontiers for 250 configurations of 50 reservoirs. (b): Coordinates of the optimal frontier for a single realisation of a two sphere configuration. The optimal frontiers are approximated using the simulated annealing algorithm (solid curve), the shortest edge algorithm (dot-dashed curve) and the spectral gap algorithm (dashed curve).

edge algorithm. The narrow channels are ordered from shortest to longest in length, and added to the MST sequentially (see Appendix 3.5.3 for details). Selecting the shortest narrow channels first favours connecting reservoirs that have high PTRs, as was shown for optimal networks in Section 3.3.3. The complexity of the shortest edge algorithm comes from the sorting algorithm chosen to order the narrow channels, thus is computationally inexpensive. However, the optimal frontiers estimated via the shortest edge algorithm do not compare well with optimal frontiers estimated via simulated annealing (see Figure 3.9(a), dot-dashed curve). In particular, for the two sphere configuration of reservoirs the shortest edge algorithm performs very poorly (see Figure 3.9(b), dot-dashed curve). The algorithm initially selects narrow channels

that connect reservoirs within the same spheres, as these narrow channels have the shortest lengths. Therefore, the networks produced by the shortest edge algorithm have bottlenecks which are known to have very large equilibration times [83]. The networks produced by the shortest edge algorithm for configurations of reservoirs with heterogeneous spatial structure are not even close to optimal.

The second algorithm is the *spectral gap algorithm*. Starting from the MST, every possible narrow channel is temporarily added to the MST and the equilibration times are calculated via the spectral gap of the rescaled drift matrix in Equation (3.36). The narrow channel which is permanently added to the MST is then the channel that corresponds to the network with the maximal spectral gap, or equivalently minimal equilibration time. This process is repeated until the complete network is reached. The spectral gap algorithm has a higher computational cost than the shortest edge algorithm, but the frontiers produced are much closer to the optimal frontiers estimated via simulated annealing (see Figure 3.9(a), dashed curve). For the two sphere configuration of reservoirs, the spectral gap algorithm performs particularly well (see Figure 3.9(b), dashed curve). Therefore, the spectral gap algorithm is capable of constructing optimal networks for configurations of reservoirs with heterogeneous spatial structure.

3.4 Summary

In this chapter we introduced a stochastic transport model for an interacting population of particles that diffuse within a heterogeneous networked environment. The nodes of the network represent reservoirs, where particles do not compete for space, and are connected via narrow channels, where the diffusing particles exhibit volume exclusion. Firstly, we extended the analysis of the two reservoir model seen in Chapter 2, to a generalised network of reservoirs. The equilibration time for a population of

particles diffusing in a network is calculated as the reciprocal of the spectral gap of a drift matrix. The remarkable dimensionality reduction of the drift matrix compared to the transition matrix of the FMM allowed for an investigation into topological optimisation. We introduced the optimal frontier, the curve describing the minimal equilibration time subject to a constraint in the total edge length of the network. Numerical evidence was provided for a possible universal curve that describes the optimal frontier for configurations of reservoirs from both homogeneous and heterogeneous distributions. A weighted degree distribution demonstrated how networks that lie on the optimal frontier are strikingly topologically distinct to non-optimal networks, that are sampled randomly for the set of all connected networks. Finally, to approximate the optimal frontier efficiently for larger numbers of reservoirs, two algorithms were introduced and compared.

The work presented in this chapter provides a fundamental step towards a mathematical theory for the transport of macromolecules in highly complex and heterogeneous environments. The networks considered in this chapter are representations of complex environments, and are reminiscent of pore-space topography networks [32, 84]. These networks have been extracted from micro-CT images of the pore-space in a variety of sandstone and carbonate samples, and used to study fluid transport within porous media [32, 33]. As biological imaging techniques continue to advance, such as light-sheet microscopy [64, 85], high resolution images of the intracellular environment will become readily available. At such small scales the effects of crowding are non-negligible [24, 35, 86] and mathematical transport models in confined networked environments will become essential.

3.5 Appendices

In this section we discuss the detailed balance assumption and outline the numerical methods and algorithms used throughout this chapter.

3.5.1 The detailed balance assumption

In this section we provide numerical justification that the detailed balance equations hold for the FMM. Consider a network $\mathcal{G} = \{\mathcal{V}, \mathcal{E}\}$, the FMM for a population of N particles has the set of legal configurations $\Omega_{N,\mathcal{G}}$. Let Q be the transition matrix for the FMM, and $\vec{p}(\infty)$ be the equilibrium distribution calculated from the principal left-eigenvector of the transition matrix Q. The detailed balance equations are

$$Q_{u,v}[\vec{p}(\infty)]_u = Q_{v,u}[\vec{p}(\infty)]_v, \tag{3.40}$$

for $1 \leq u, v \leq |\Omega_{N,K}|$. The high-dimensional and complex structure of the transition matrix renders Equations (3.40) difficult to solve analytically. In lieu of a proof that the detailed balance equations hold, we introduce the detailed balance error

$$\mathcal{E}^{\mathrm{DB}}_{u,v} = |Q_{u,v}[\vec{p}(\infty)]_u - Q_{v,u}[\vec{p}(\infty)]_v|, \tag{3.41}$$

for $1 \leq u, v \leq |\Omega_{N,K}|$. Consider a three-reservoir network (see Figure 3.10, inset) with distinct narrow channel lengths and reservoir jump rates that are distributed independently and uniformly in the unit interval. For each pair of states in the set of legal configurations that have a non-zero transition rate[7], an average detailed balance error is calculated over 100 samples of the reservoir jump rates. For all pairs of states that have non-zero transition rates the average detailed balance error is less than 2×10^{-16} (see Figure 3.10) and the detailed balance error averaged over all pairs of

[7]The detailed balance equations hold trivially for pairs of states with a zero transition rate.

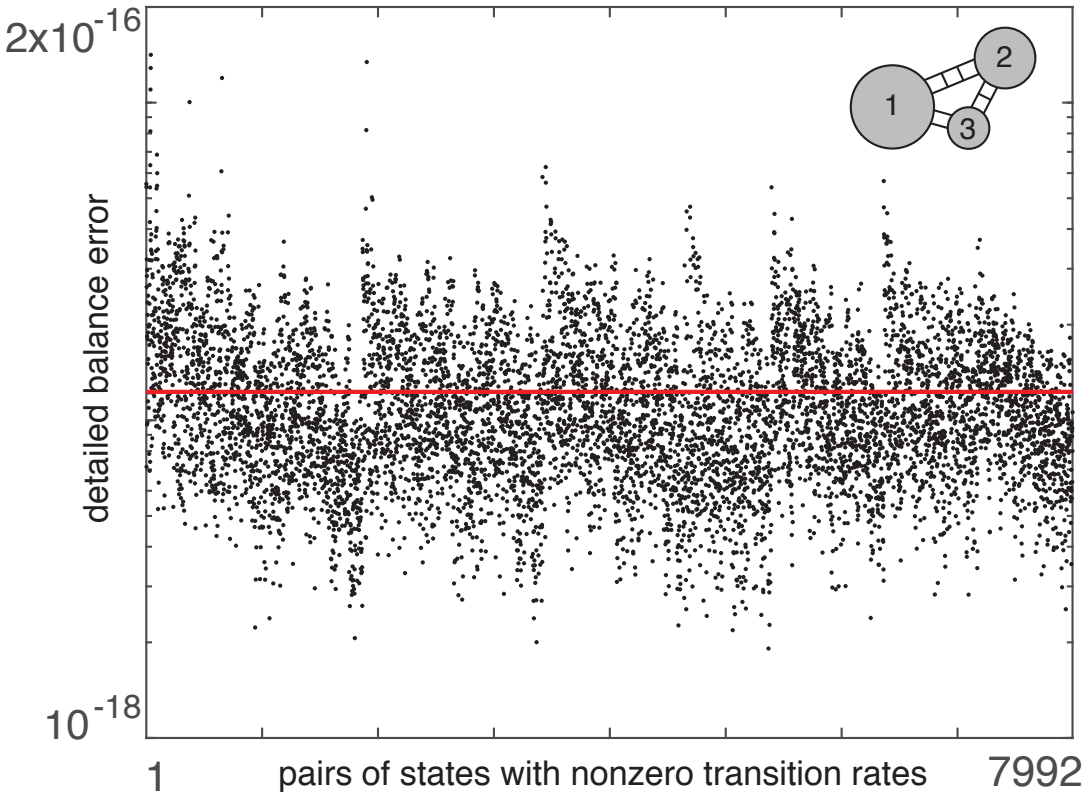

Figure 3.10: The averaged detailed balance error over 100 randomly distributed reservoir jump rates $\vec{\gamma}$. The parameters are $K_{1,2} = 3$, $K_{2,3} = 2$, $K_{1,3} = 1$, $\alpha = 1$ and $N = 10$.

states is 1.23×10^{-17} (see Figure 3.10, horizontal line). Thus the detailed balance error is zero to computer precision, providing numerical evidence that the detailed balance equations are satisfied. Of course this is unsurprising as the FMM is a passive transport process. If the detailed balance equations did not hold, active transport would emerge around closed loops within a network.

Under the detailed balance assumption, we prove that for any narrow channel e, the single site occupancy probabilities $\rho_e^{(1)}(O(k), \infty)$ are all equal to some constant ρ_e^* for $1 \leq k \leq K_e$, where K_e is the number of lattice sites in the narrow channel. We define $S(e, k)$ to be the set of indices for the configuration states where the k-th lattice site on narrow channel e is occupied and the $(k+1)$-st lattice site is vacant. For $u \in S(e, k)$, we define $v(u)$ as the index of the configuration state identical to u but the

particle in lattice site k now occupies lattice site $k+1$. Note that $Q_{u,v(u)} = Q_{v(u),u} = \alpha$. By decomposing the two-site probability functions into entries of $\vec{p}(\infty)$, we show

$$\rho_e^{(2)}\left(O(k), \emptyset(k+1), \infty\right) = \rho_e^{(2)}\left(\emptyset(k), O(k+1), \infty\right), \tag{3.42}$$

as follows,

$$\begin{aligned}
\alpha\rho_e^{(2)}\left(O(k), \emptyset_e(k+1), \infty\right) &= \alpha \sum_{u \in S(e,k)} [\vec{p}(\infty)]_u && \text{(3.43a)} \\
&= \sum_{u \in S(e,k)} Q_{u,v(u)} [\vec{p}(\infty)]_u && \text{(3.43b)} \\
&= \sum_{u \in S(e,k)} Q_{v(u),u} [\vec{p}(\infty)]_{v(u)} && \text{(3.43c)} \\
&= \alpha \sum_{u \in S(e,k)} [\vec{p}(\infty)]_{v(u)} && \text{(3.43d)} \\
&= \alpha\rho_e^{(2)}\left(\emptyset(k), O(k+1), \infty\right), && \text{(3.43e)}
\end{aligned}$$

where the equality between Equations (3.43b) and (3.43c) holds due to the detailed balance equations. We note that

$$\rho_e^{(2)}\left(O(k), \emptyset(k+1), \infty\right) = \rho_e^{(1)}\left(O(k), \infty\right) - \rho_e^{(2)}\left(O(k), O(k+1), \infty\right), \tag{3.44}$$

and similarly,

$$\rho_e^{(2)}\left(\emptyset(k), O(k+1), \infty\right) = \rho_e^{(1)}\left(O(k+1), \infty\right) - \rho_e^{(2)}\left(O(k), O(k+1), \infty\right). \tag{3.45}$$

Combining Equations (3.42), (3.44) and (3.45), we have

$$\rho_e^{(1)}\left(O(k), \infty\right) = \rho_e^{(1)}\left(O(k+1), \infty\right), \tag{3.46}$$

for $1 \leq k \leq K_e - 1$. Therefore, we have shown that

$$\rho_e^{(1)}\left(O(k), \infty\right) = \rho_e^*, \tag{3.47}$$

for some constant ρ_e^*, for $1 \leq k \leq K_e$.

3.5.2 Estimating the optimal frontier: simulated annealing

In this section we provide details of the simulated annealing algorithm used to estimate optimal frontiers. For a fixed configuration of reservoirs $\mathcal{X}$, the range of total edge lengths is $[K_{\min}(\mathcal{X}), K_{\max}(\mathcal{X})]$, where $K_{\min}(\mathcal{X})$ and $K_{\max}(\mathcal{X})$ are the total edge lengths for the MST, calculated via Prim's algorithm [87], and the complete network, respectively. The optimal frontier is estimated by searching stochastically for networks that minimise the equilibration time subject to constraints in the total edge length. These constraints are denoted $\mathcal{K}_i$ and are given by

$$\mathcal{K}_i = K_{\min}(\mathcal{X}) + i\left(\frac{K_{\max}(\mathcal{X}) - K_{\min}(\mathcal{X})}{100}\right), \tag{3.48}$$

for $1 \leq i \leq 100$. The MST with the lowest equilibration time is the first network on the optimal frontier. The MST is taken as the current network $\mathcal{G}_{\text{curr}}$ and has total edge length and equilibration time given by the coordinates $(K_{\text{curr}}, \mathcal{T}_{\text{curr}})$. From the current network, a candidate network $\mathcal{G}_{\text{cand}}$ is sampled as follows. Two distinct reservoirs are sampled uniformly and if the edge connecting them is present in $\mathcal{G}_{\text{curr}}$, it is removed in $\mathcal{G}_{\text{cand}}$ and vice versa. If $\mathcal{G}_{\text{cand}}$ is disconnected the network is abandoned and a new candidate network is sampled from $\mathcal{G}_{\text{curr}}$. For a connected candidate network the total edge length and equilibration are given by $(K_{\text{cand}}, \mathcal{T}_{\text{cand}})$. The acceptance probability,

ρ_{acc}, for the candidate network is

$$\rho_{\text{acc}} = \begin{cases} 0, & \text{if } K_{\text{cand}} > \mathcal{K}_i, \\ \exp\left(-\left[\dfrac{\mathcal{T}_{\text{cand}} - \mathcal{T}_{\text{curr}}}{\xi \mathcal{T}_{\text{min}}}\right]\right), & \text{if } K_{\text{cand}} < \mathcal{K}_i \text{ and } \mathcal{T}_{\text{cand}} > \mathcal{T}_{\text{curr}}, \\ 1, & \text{otherwise,} \end{cases} \tag{3.49}$$

where $\mathcal{T}_{\text{min}}$ is the equilibration time of the complete network and ξ is the temperature parameter which controls the probability of accepting a candidate network that has a higher equilibration time than the current network. For each $\mathcal{K}_i$, the random search process terminates once any one of two criteria are met. The two criteria are: 10^5 candidate networks have been considered; or 1.5×10^4 candidate networks have been accepted. As the search process progresses the temperature parameter ξ is lowered in stages. The initial temperature is $\xi = 10^2$, and once the number of accepted candidate networks reaches $\{1.5 \times 10^3, 3.5 \times 10^3, 7 \times 10^3, 10^4, 1.25 \times 10^4, 1.4 \times 10^4\}$ the value of ξ is reduced to $\{1, 10^{-1}, 10^{-2}, 10^{-3}, 10^{-4}, 10^{-5}\}$, respectively. For each $\mathcal{K}_i$, once the random search has terminated the network with the minimum equilibration time is added to the optimal frontier if it has both a greater total edge length and a smaller equilibration time than the existing frontier. The random search for $\mathcal{K}_{i+1}$ is initialised with the current network being the last accepted candidate network from the previous random search for $\mathcal{K}_i$.

3.5.2.1 Non-optimal networks

In Figure 3.8 we present equilibration factors for non-optimal networks that are randomly selected from the set of all connected networked topologies. The numerical procedure used to generate these networks is similar to the simulated annealing algorithm presented above. The main difference is that the acceptance probability in

Equation (3.49) becomes

$$\rho_{\text{acc}} = \begin{cases} 0, & \text{if } K_{\text{cand}} > \mathcal{K}_i, \\ 1, & \text{otherwise,} \end{cases} \tag{3.50}$$

The random search for the restricted value $\mathcal{K}_i$ is terminated after 100 candidate networks have been accepted. To avoid the networks being too similar the candidate networks are sampled by changing 100 randomly selected edges in the previous network.

3.5.3 Shortest edge algorithm

The shortest edge algorithm provides an ensemble of networks that interpolate between the MST and the complete network to approximate the optimal frontier. Edges are selected sequentially in increasing order of their length. A pseudo algorithm is presented below.

1: For a configuration of reservoirs $\mathcal{X}$, calculate the MST with the smallest equilibration time using Prim's algorithm [87].

2: Calculate the equilibration time, $\mathcal{T}_{\text{MST}}$, and the total edge length, K_{MST}, for the MST. The coordinate $(K_{\text{MST}}, \mathcal{T}_{\text{MST}})$ is the first entry in the optimal frontier.

3: Set the current network to be the MST.

4: **while** there are absent edges remaining **do**

5: Add the shortest absent edge to the current network. Calculate and store the equilibration time and the total edge length.

6: **end while**

3.5.4 Spectral gap algorithm

The spectral gap algorithm provides an ensemble of networks that interpolate between the MST and the complete network to approximate the optimal frontier. Edges are selected sequentially to minimise the equilibration time at each step. A pseudo algorithm is presented below.

1: For a configuration of reservoirs $\mathcal{X}$, calculate the MST with the smallest equilibration time using Prim's algorithm [87].

2: Calculate the equilibration time, $\mathcal{T}_{\mathrm{MST}}$, and the total edge length, K_{MST}, for the MST. The coordinate $(K_{\mathrm{MST}}, \mathcal{T}_{\mathrm{MST}})$ is the first entry in the optimal frontier.

3: Set the current network to be the MST.

4: **while** there are absent edges remaining **do**

5: **for** each absent edge **do**

6: From the current network, add each absent edge one at a time and calculate the equilibration time.

7: **end for**

8: Add the absent edge that minimises the equilibration time to the current network. Calculate and store the equilibration time and the total edge length.

9: **end while**

Chapter 4

Topology-dependent density optima for efficient simultaneous network exploration

From animals foraging to T-cells hunting pathogens to proteins examining DNA, nature relies on carefully optimised random searches at many scales [86, 88–96]. This concept is not limited to biology: robotic self-assembly [55], traffic flow management [97–99] and computer resource allocation [100] hinge on optimising decentralised exploration. In these distributed processes, the searcher, be it a protein, an animal or a network token, must often visit not just one site but many locations connected in a network [45]. The critical measure of efficiency is then the time to visit every node of the network, called the cover time [48]. Single-searcher cover times are known on simple networks such as linear chains, rings and other regular lattices [47, 101–104], and significant progress has been made on establishing transport statistics for more general networks [45, 46, 105–109], providing a means to design topologies that can be searched efficiently. However, when multiple parallel searchers compete for space or resources, as often occurs in the examples above, the design of optimal search

strategies remains a significant open question.

The exclusion process represents the most fundamental model of competition for space [110–112]. It has been key to understanding such diverse phenomena as cell migration [113], molecular traffic [114, 115], surface roughening [116] and queueing [117]. Capitalising on this breadth, we use the exclusion process to model parallel searching of a network and introduce the *searcher-averaged parallel cover time* (APCT), the average per-searcher time for all searchers to visit all nodes within a network. Strategy optimisation then demands an understanding of how both network topology and searcher density impact the APCT. Consider, for example, a scenario with as many searchers as nodes. Placing all searchers on the network simultaneously results in an infinite APCT, while a simple 'serial' strategy where a single searcher is placed on the network, removed once it has visited every node and replaced with a new searcher, one at a time, is almost always inefficient. It is therefore critical to determine the optimal, or most efficient, density of parallel searchers minimising the APCT.

This chapter proceeds as follows. The concept of the APCT and optimal density is formalised for a symmetric exclusion process on a general network. The APCT and optimal density are estimated numerically for a class of Newman-Watts type networks, demonstrating the topological sensitivity of the density optima. Analytical results of the APCT and optimal density are provided for the complete network, the ring lattice and for general networked topologies using a MFA. However, numerical estimations of the optimal density for general networks demonstrates that the MFA performs poorly. The spectral gap, which quantifies the convergence rate of a single-searcher random walk, is a strong predictor of the density optima for general networks, and we show that it out performs any degree-based statistic. Next we consider the optimal strategies that minimise the total time taken for a fixed number of particles to cover a fixed topology. For a large number of searchers the optimal strategy is simple, perform search batches in series with searcher density equal to the optimal

density for the particular network. Finally we broaden our results by generalising to flux-conserving asymmetric exclusion processes, where remarkably the relationship between density optima and the spectral gap is no longer monotonic. We conclude the chapter with a brief summary and a discussion of avenues for future research.

4.1 Average parallel cover time and optimal searcher density

We employ a symmetric exclusion process of M parallel searchers on a network with N vertices (where $M < N$). First, an initial configuration of searchers is generated uniformly at random with each searcher occupying its own node. The searchers then perform mutually-excluding continuous-time random walks (CTRWs) with i.i.d. exponential waiting times of mean $\tau = 1$. When a searcher attempts to move, an adjacent node is picked uniformly at random; if the node is vacant the searcher moves there, and if not the move is aborted. Let T_r^i be the time for searcher i to first visit r distinct nodes [1]. We define the parallel cover time $\mathcal{C}_M = \max_{1\leq i\leq M}\{T_N^i\}$ as the time for all M searchers to each visit all N nodes, and the expectation $\langle \mathcal{C}_M \rangle$ to be taken simultaneously over the space of all initial configurations and random walk instances[2]. The APCT is defined as $\mathcal{S}_M = \langle \mathcal{C}_M \rangle / M$, and quantifies the economy of scale in parallel searching: if $\langle \mathcal{C}_M \rangle < M\mathcal{S}_1$ for some $M > 1$ there is an efficiency gain in parallel searching beyond the simple serial search strategy where particles cover the network one at a time. For a given network, let M^* be the optimal number of searchers, that is, the M for which $\mathcal{S}_M$ is minimised, and let $\rho^* = M^*/N$ be

[1] In practice we evaluate T_r^i by counting the number of attempted jumps made by all parallel searchers until walker i visits the r-th distinct site and rescaling by the average waiting time $1/M$. This is equivalent to describing the CTRW by a discrete-time random walk with time step $1/M$ which is sufficient when seeking only first moments as we do here.

[2] This is contrary to the usual cover time, where a maximum over initial position is taken [118]. Here, this is combinatorially intractable on most networks when $M \gg 1$, and our definition allows us to consider topological effects removed from any influence of initial conditions.

the equivalent optimal density. To investigate the relationship between networked topology and ρ^* in the next section we focus on a simple class of ring-like topologies.

4.2 Efficient search for ring-like topologies

Parallel search of a ring lattice is optimal at a strikingly low density, $\rho^* = 0.05$ when $N = 100$ (see Figure 4.1(a), and Appendix 4.7.1 for details of the numerical procedure used to estimate optimal density), and it becomes increasingly inefficient as M increases. This is due to the strong confinement effects of single-file diffusion [72, 119–123]. That said, parallel searching is still more efficient than simple serial searching for a range of ρ (see Figure 4.1(a), dashed line). Remarkably, however, a parallel search on a ring lattice can be made significantly more efficient by introducing only a small number of additional edges. To demonstrate, we consider a form of the Newman–Watts ensemble [124] that interpolates between the two extremal topologies of the ring lattice and the complete network. Starting from a ring lattice, we add a fixed number of random additional edges, or shortcuts (see Figure 4.1(b), inset). The optimal density rapidly approaches that of the complete network, $\rho^* = 0.47$, even with only 3–4% of the possible shortcuts added on $N = 100$ nodes (see Figure 4.1(b)).

4.2.1 APCT on the complete network

Parallel search efficiency on the complete network with N nodes can be evaluated exactly. First we calculate the APCT without interactions. Let X_r^i be the time taken for the i^{th} searcher to first visit $r+1$ distinct sites, given it has just visited r distinct sites. Note that X_r^i is geometrically distributed with success probability $(N-r)/(N-1)$. Then the mean cover time for the single searcher is

$$\langle \mathcal{C}_1 \rangle = \sum_{r=0}^{N-1} \langle X_r^i \rangle = (N-1)h(N-1), \tag{4.1}$$

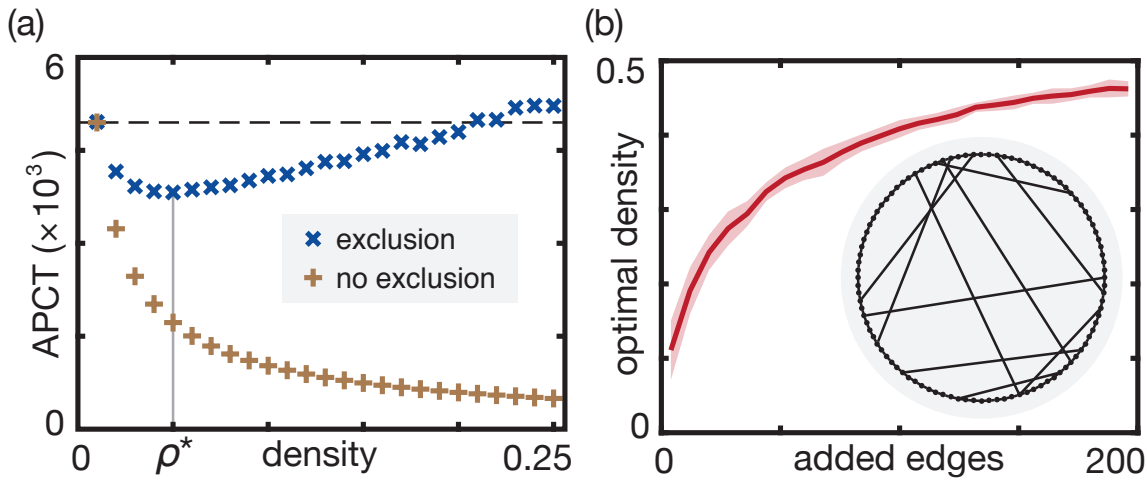

Figure 4.1: (a): APCT on the ring lattice for interacting (×) and non-interacting (+) searchers as a function of searcher density $\rho = M/N$, where $N = 100$. The optimal density ρ^* (marked) can be seen as the minimum of the APCT; the dashed horizontal line denotes the density below which parallel search is faster than serial search. Each APCT was calculated from 10^5 random walk instances. (b): Mean optimal density of Newman–Watts networks with $N = 100$ as a function of the number of shortcuts (example inset). Coloured band indicates ± 1 standard deviation. Optimal densities were calculated (see Appendix 4.7.1) for 1000 Newman–Watts realisations for a range of added edges.

where $h(i)$ is the i-th harmonic number. For M non-interacting searchers we start with M distinct sites covered (if every searcher initially occupies its own node) and the parallel cover time is the time taken to visit MN distinct sites (N distinct sites for each of the M searchers). We define Y_r to be total number of jumps by all searchers until the overall number of sites visited by the entire population to hit $r+1$ given r distinct sites have just been visited. Y_r is now geometrically distributed with success probability $(MN - r)/(M(N-1))$. Therefore

$$\langle C_M \rangle = 1/M \sum_{r=M}^{NM-1} \langle Y_r \rangle = (N-1)h(M(N-1)), \tag{4.2}$$

where the pre-factor of $1/M$ appears as the expected time for the next jump for M random searchers. Thus the APCT for the complete network for non-interacting

searchers is

$$\tilde{\mathcal{S}}_M = \frac{N-1}{M} h(M(N-1)). \tag{4.3}$$

In order to include the effect of interactions, we need to calculate the probability that an attempted jump is not blocked by another searcher. Due to the unique topology of the complete network this probability is simply $(N-M)/(N-1)$. We can redefine the geometrically distributed variables Y_r to have success probability $(MN-r)/(M(N-1)) \times (N-M)/(N-1)$. The APCT for the complete network with M interacting searchers is therefore

$$\mathcal{S}_M = \frac{(N-1)^2}{M(N-M)} h(M(N-1)). \tag{4.4}$$

To find the optimal density, the density which minimises $\mathcal{S}_M$, we make a continuous approximation and introduce $\rho = M/N$. Taking the limit $N \to \infty$ gives

$$\mathcal{S}_M = \frac{(N-1)^2}{N\rho(N-N\rho)} h(N\rho(N-1)) \sim \frac{1}{\rho(1-\rho)} \log\left(\rho N^2\right). \tag{4.5}$$

Differentiating the asymptote in Equation (4.5) and equating the derivative to zero yields

$$\frac{1-\rho^*}{1-2\rho^*} = \log(\rho^*) + \log(N^2). \tag{4.6}$$

For Equation (4.6) to hold as $N \to \infty$ we need that $\rho^* \to 1/2$ (as $\rho^* \to 0$ yields a trivial solution). Thus the optimal density for parallel search on the complete network tends to $\rho^* = 1/2$. Substituting $\rho^* = 1/2 + \xi$ into Equation (4.6) and linearising in ξ we arrive at

$$\xi \approx \frac{1}{2}\left[1 - 2\log\left(\frac{N^2}{2}\right)\right]^{-1}. \tag{4.7}$$

For large N, $\xi \sim -(8\log N)^{-1}$ and so $\xi < 0$ and $\xi \to 0$, thus $\rho^* \to 1/2$ from below. Moreover, for $N = 100$ we have $\xi \approx -0.03$ and so $\rho^* \approx 0.47$ as we saw numeri-

cally. From Equations (4.3) and (4.4) we note that $\mathcal{S}_M = (N-1)\,/\,(N-M)\,\tilde{\mathcal{S}}_M$, thus the interacting cover time is the cover time without exclusion rescaled by the average number of additional jumps required due to aborted moves. This rescaling is equivalent to the MFA which we discuss below.

4.2.2 The mean-field approximation

In probability theory, statistics of an interacting population of particles, such as the cover time of competing parallel searchers, are often estimated by reducing the complexity and studying a non-interacting particle system. The effects of particle interactions are then approximated as a spatially homogenous rescaling of the non-interacting statistic, this rescaling is referred to as the MFA. For the case of the parallel cover time, the MFA is to approximate the mean interacting cover time, $\langle \mathcal{C} \rangle$, as the mean non-interacting cover time, $\langle \tilde{\mathcal{C}} \rangle$, multiplied by ϕ, the proportion of additional jumps needed due to aborted moves. To calculate ϕ, we require the probability of an attempted move being successful, therefore we consider the occupancy probabilities of nodes adjacent to a searcher. Let $\mathcal{O}_\nu$ denote the occupancy of node ν, where a value 1 corresponds to the node being occupied and a value 0 to the node being vacant. For a searcher at node ω, let ν be the neighbouring site which the searcher attempts a move to. The probability the neighbouring node is vacant (i.e. the move is successful) is $\mathbb{P}(\mathcal{O}_\nu = 0 | \mathcal{O}_\omega = 1)$. Bayes' rule allows this probability to be written in terms of a two-site occupancy probability, $\mathbb{P}(\mathcal{O}_\nu = 0, \mathcal{O}_\omega = 1)/\mathbb{P}(\mathcal{O}_\omega = 1)$. The MFA comes from approximating the two-site occupancy probability to be the product of single-site occupancy probabilities: $\mathbb{P}(\mathcal{O}_\nu = 0, \mathcal{O}_\omega = 1) \approx \mathbb{P}(\mathcal{O}_\nu = 0)\mathbb{P}(\mathcal{O}_\omega = 1)$. Therefore the probability of the attempted move being successful is approximately $\mathbb{P}(\mathcal{O}_\nu = 0)$ and thus is independent of the searcher location ω. This probability is the fraction of the number of vacant sites over the number of total sites that are not ω, namely, $(N-M)/(N-1)$. We approximate $\langle \mathcal{C} \rangle \approx \langle \tilde{\mathcal{C}} \rangle \times (N-1)/(N-M)$ or

equivalently $\langle \mathcal{C} \rangle \approx \phi \langle \tilde{\mathcal{C}} \rangle$, where $\phi = (1 - N^{-1})/(1 - \rho)$ and $\rho = M/N$.

We consider the cover time of a single searcher on a general network. Chupeau et al. [45] revealed that single searcher cover times over a broad range of search processes, including random walks on complex networks, all follow a universal Gumbel distribution. As such, we suppose that the cover time is Gumbel distributed with parameters $\mu \in \mathbb{R}$ and $\beta > 0$. The probability density function, $p(t)$, of the cover time is

$$p(t) = \frac{1}{\beta} \exp\left[-\frac{t-\mu}{\beta} - \exp\left(-\frac{t-\mu}{\beta} \right) \right], \tag{4.8}$$

where the mean cover time is $\gamma\beta + \mu > 0$ and γ is the Euler–Mascheroni constant. Introducing the general scaling $x = (t-\mu)/\beta$ gives the standard Gumbel distribution.

Now let the maximum cover time of M independent random walkers be $\sigma = \max\{t_1, \ldots, t_M\}$, or in the rescaled variables $y = \max\{x_1, \ldots, x_M\}$. Due to independence of the individual cover times, y is also Gumbel distributed with $\langle y \rangle = \gamma + \log(M)$. We transform the coordinates back to give $\langle \sigma \rangle = \beta\{\gamma + \log(M) + \mu/\beta\}$. The APCT for M non-interacting searchers is then

$$\tilde{\mathcal{S}}_M = \frac{\beta}{M} \left\{ \gamma + \log(M) + \frac{\mu}{\beta} \right\}. \tag{4.9}$$

Note that for the APCT with interactions we cannot make analytic progress with $\sigma = \max\{t_1, \ldots, t_M\}$, as before, because the individual cover times, t_i, are no longer independent and so we cannot easily apply extremal value theory [**?**]. However the MFA, $\mathcal{S}_M = \phi \tilde{\mathcal{S}}_M$ where $\phi = (1-N^{-1})/(1-\rho)$, then gives an approximate expression for the APCT with interactions

$$\mathcal{S}_M \approx \frac{\beta\,(1 - N^{-1})}{N\rho(1-\rho)} \left\{ \gamma + \log(N\rho) + \frac{\mu}{\beta} \right\}. \tag{4.10}$$

We seek the density that minimises the APCT for a network that has a single particle

cover time that is Gumbel distributed with parameters (μ, β). Setting $d\mathcal{S}_M/d\rho = 0$ to find the optimal density yields

$$\frac{1-\rho^*}{1-2\rho^*} = \gamma + \frac{\mu}{\beta} + \log(N) + \log(\rho^*), \tag{4.11}$$

similar to Equation (4.6). Note that $\gamma + \mu/\beta > 0$ as the mean cover time must be positive and β is always positive. Then for Equation (4.11) to hold as $N \to \infty$ we require that $\rho^* \to 1/2$ (as $\rho^* \to 0$ yields a trivial solution). Substituting $\rho^* = 1/2 + \xi$ into Equation (4.11) and linearising in ξ we find that

$$\xi \approx \frac{1}{2}\left[1 - 2\left(\gamma + \frac{\mu}{\beta} + \log\frac{N}{2}\right)\right]^{-1}. \tag{4.12}$$

Thus, as $N \to \infty$, we have $\xi < 0$ and $\xi \to 0$, so we conclude that $\rho^* \to 1/2$ from below. However, we have seen that for the ring lattice (see Figure 4.1(a)) this is far from the true ρ^* evaluated numerically. In general, naïve MFAs [110–112] can lead to drastically inaccurate estimation of the APCT and optimal density. Insight into this inaccuracy can be drawn from asymptotic estimates of the APCT on the ring lattice in the high-density regime.

4.2.3 Symmetric search on the ring lattice in the high-density regime

In this section we consider symmetric search on the ring lattice. Deriving expressions for the APCT in the high-density regime, we compare to the APCT estimated using the MFA and find that the two expressions are of different orders of magnitude, thus highlighting the failure of the MFA to accurately predict the optimal density. Inspired by particle-hole duality [72], we calculate APCTs on the ring lattice in the high-density regime by instead considering the movement of the vacancies rather

than the particles. Starting with a single vacancy we calculate the APCT on the ring lattice, before generalising our results to several vacancies.

4.2.3.1 One vacancy

Consider a ring lattice of N nodes with $M = N-1$ searchers each occupying their own node. Rather than modelling the searchers moving we can instead model the vacancy as a random walker. If the vacancy jumps $N-1$ times clockwise (anti-clockwise) then every single searcher has jumped one site anti-clockwise (clockwise). Thus we can see that the mean cover time for all searchers to visit all nodes is the mean first passage time of the vacancy to visit $(N-1)^2+1$ distinct lattice sites on an infinite lattice in one dimension. On an infinite lattice, it is a well known result [103] that the mean first passage time for the span of the random walk to visit r distinct nodes is $r(r-1)/2$. Therefore the mean cover time for $N-1$ interacting searchers on a ring is

$$\langle \mathcal{C}_{N-1} \rangle = \binom{(N-1)^2+1}{2}. \tag{4.13}$$

The APCT for the ring lattice with $N-1$ parallel searchers is therefore

$$\mathcal{S}_{N-1} = \frac{1}{N-1}\binom{(N-1)^2+1}{2}. \tag{4.14}$$

For large N, this is $\mathcal{O}(N^3)$. We extend the derivation of the APCT seen above to the case where there are several vacancies in the ring lattice.

4.2.3.2 Several vacancies

We again have a ring lattice with N nodes. Let $M = N-k$ be the number of searchers and suppose that $k \ll N$ so we are still in the high-density regime. We now consider, as before, the random walk of the k vacancies instead of the searchers directly. In the limit of large N the vacancies are non-interacting and therefore we can treat

the vacancies as being approximately independent. The net displacement of the k vacancies can then be approximated as the sum of k independent normally distributed random variables with mean zero. Equivalently we consider a single vacancy that moves on average k times faster, that is, with mean waiting time $\tau_{\text{vac}} = 1/k$. This random walker needs to visit $(N-1)(N-k)+1$ distinct sites in order for the all the searchers to have visited every site, thus the mean cover time is

$$\langle \mathcal{C}_{N-k} \rangle \sim \frac{1}{k} \binom{(N-1)(N-k)+1}{2}. \tag{4.15}$$

Note that the factor of $1/k$ appears because the collective vacancy moves k times faster than a single vacancy. The APCT for the ring lattice in the high-density regime is therefore

$$\mathcal{S}_{N-k} \sim \frac{1}{k(N-k)} \binom{(N-1)(N-k)+1}{2}. \tag{4.16}$$

This estimate does extremely well in predicting the APCT (see Figure 4.2). It is exact for $k = 1$, and only noticeably deviates when $\rho \lesssim 0.85$ for $N = 100$. Equation (4.16) reveals that the APCT at high-density is $\mathcal{O}(N^3)$, while the MFA suggests an APCT, $\phi\tilde{\mathcal{S}}_N$, with magnitude at most[3] $\mathcal{O}(N^2 \log(N))$, highlighting the failure of the MFA to capture spatial correlations.

4.3 General topologies and the spectral gap

Due to the failure of the MFA to predict density optima, in this section we explore global topological heuristics to accurately predict optimal densities for general networked topologies. We find that the spectral gap of the transition matrix for a

[3]Suppose the single particle cover time is Gumbel distributed. From Equation (4.10) we find $\mathcal{S}_M \sim \mathcal{O}(\gamma\beta + \mu + \beta\log(N))$. Note $\gamma\beta + \mu$ is equal to the first moment which is $\mathcal{O}(N^2)$. In Appendix 4.7.3 the maximum likelihood estimator for β is less than the sample mean of the cover times, therefore β is at most $\mathcal{O}(N^2)$.

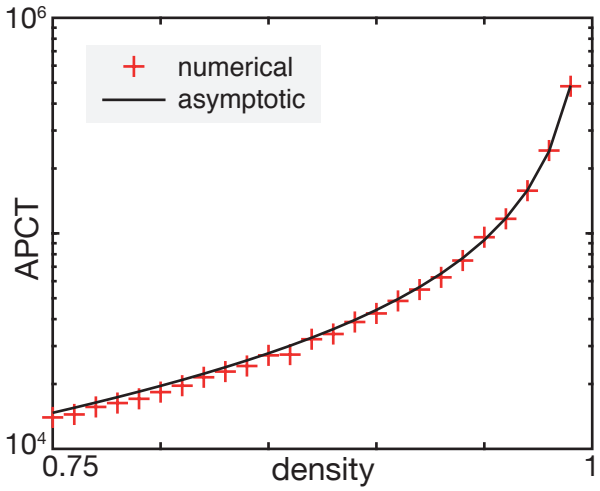

Figure 4.2: APCT for the ring lattice in the high-density regime where $N = 100$. The +'s represent data generated from simulations of the search process, the solid curve is an interpolation of the APCT calculated using the asymptotic estimates in Equation (4.16). All APCTs were calculated from 10^5 random walk instances.

single-searcher random walk accurately predicts the spectral gap. Furthermore the spectral gap out performs other simpler degree-based statistics.

Given the adjacency matrix $\mathbf{A}$ and the diagonal matrix $\mathbf{D}$ whose entries are the node degrees, define the random walk transition matrix $\mathbf{P} = \mathbf{D}^{-1}\mathbf{A}$. The eigenvalues $\{\lambda_i\}$ of $\mathbf{P}$ determine how fast the probability distribution of a single-searcher random walk converges to its equilibrium [118]. The largest eigenvalue is necessarily $\lambda_1 = 1$, and we define the spectral gap, $\lambda_{\mathcal{SG}}$, as the difference in magnitude between the first and second largest eigenvalues $\lambda_{\mathcal{SG}} = 1 - \max_{2 \leqslant i \leqslant N}\{|\lambda_i|\}$. The closer $\lambda_{\mathcal{SG}}$ is to zero, the slower a random walk converges [118]. The spectral gap is then a natural candidate for predicting density optima because the features of networks that slow down convergence, such as bottlenecks (identified through nodes of high betweenness centrality [83]), also significantly increase the parallel cover time. Furthermore, single-searcher cover times can be related to the eigenvalues of the combinatorial Laplacian $\mathbf{L} = \mathbf{D} - \mathbf{A}$ [46] which, in turn, relate to those of $\mathbf{P} = \mathbf{I} - \mathbf{D}^{-1}\mathbf{L}$ via the normalised Laplacian [125].

There is a tight relationship between the spectral gap and the optimal density of

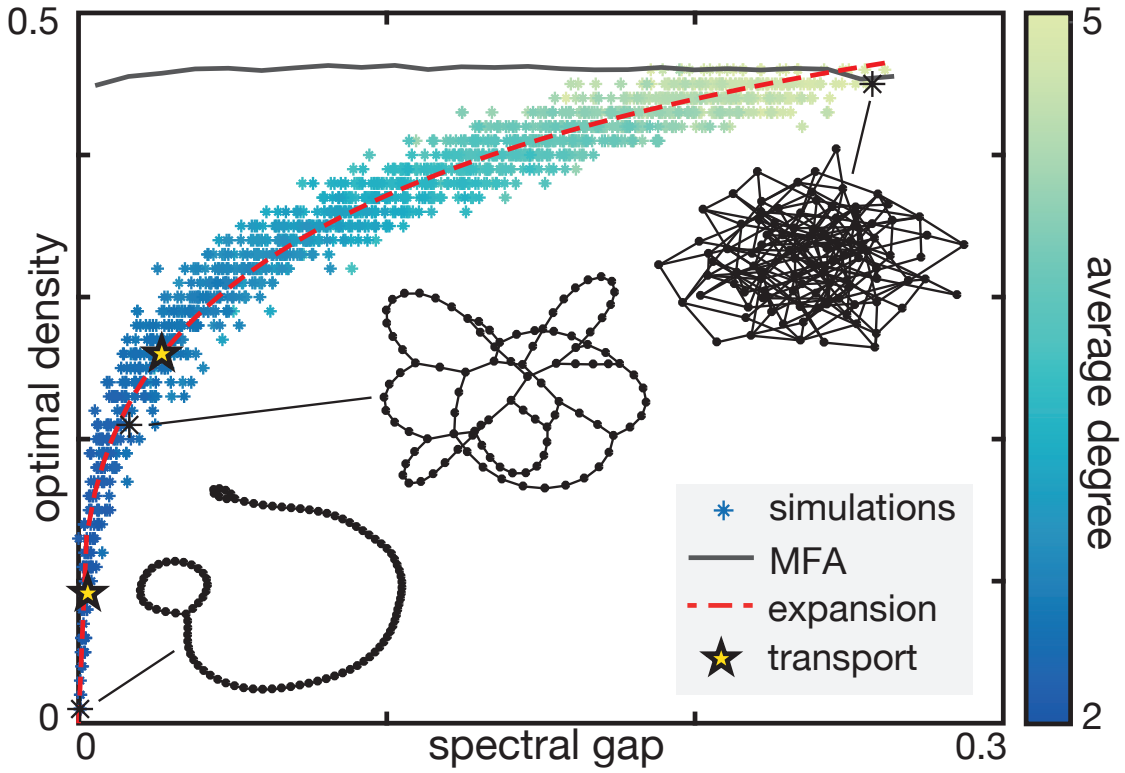

Figure 4.3: Spectral gap predicts optimal parallel search density. Optimal densities were calculated for 1500 random networks on $N = 100$ nodes with average degree between two and five (see Appendix 4.7.2). Each point represents one network with average degree indicated by colour, with three topologically contrasting networks highlighted. The solid grey curve denotes the mean MFA-predicted optimal density as a function of $\lambda_{\mathcal{SG}}$ from numerically-determined single-searcher cover times. The dashed red curve shows best-fit expansion $\rho^*(\lambda_{\mathcal{SG}}; 0.7556, 0.2933)$. Two real-world transport networks are indicated by stars: the London Underground (lower) and American airports (upper).

searchers for general networks (see Figure 4.3). Sampling over random networks of minimum degree two and average degree between two and five (see Appendix 4.7.2) reveals that topology has a huge impact on optimal parallel search strategies: for a small spectral gap (see Figure 4.3, left-most inset) networks have low average degree and a high concentration of nodes of degree two, resulting in many linear chains along which the single-file diffusion of searchers significantly increases the cover time [72, 119–123]. Indeed, for a linear chain the parallel cover time is finite only for a sin-

gle searcher; for two or more searchers the left- (right-) most searcher will never reach the right- (left-) most site due to the effect of single-file diffusion. The naïve MFA fails to capture this relationship (see Figure 4.3, grey curve, and Appendix 4.7.3), demonstrating the importance of long-lived occupancy correlations. The MFA only becomes valid for networks of average degree nearing five, where the density optima approach that of the complete network ($\rho^* = 0.47$ for $N = 100$). Typically, these networks have a small fraction of degree two nodes and are more highly connected (see Figure 4.3, right-most inset). A power series $\rho^*(\lambda_{\mathcal{SG}}; a, b) = \lambda_{\mathcal{SG}}^b[1/2 - (1/2 - a)(1 - \lambda_{\mathcal{SG}})]$, constructed such that $\rho^*(1) = 1/2$ to match the $N \to \infty$ limit of the complete graph, matches the data well (see Figure 4.3, red curve) and provides an easily-computed predictive approximation.

Beyond random networks, we find that two real-world transport networks further validate this relationship in practice (see Figure 4.3). Firstly we consider the London Underground network (from [81], which includes the Docklands Light Railway, with one spurious disconnected node deleted from the dataset). The average degree of this network is 2.31 where the number of nodes is 306, the spectral gap of the symmetric random walk of a single searcher is 0.003 and the estimated optimal density is 0.0915 (see Figure 4.3). Our second real world network is the top 500 busiest US airports, where the nodes represent each airport and an edge connects two nodes if there is at least one direct flight between the two airports [82]. The average degree of the network is 11.9 where the number of nodes is 500. The spectral gap of the symmetric random walk of a single searcher is 0.0237 and the numerically estimated optimal density is 0.26. Despite the network's high average degree the optimal density is still prohibitively low, which is well predicted via its spectral gap (see Figure 4.3). The spectral gap is cheap to compute, however it is difficult to predict how the gap changes as we alter the underlying network, for example, by adding or deleting edges. It is then natural to ask whether it is possible to use simpler degree based statistics

as a predictor of optimal density.

4.3.1 Quantifying the predictive capacity of the spectral gap versus the average degree

Here, we evidence the lesser predictive capacity of the average degree compared to the spectral gap. We present estimates for the uncertainty coefficient between the optimal density, ρ^*, and two network properties: the spectral gap, $\lambda_{\mathcal{SG}}$, and the average degree, $\bar{d}$. For two random variables X and Y, the uncertainty coefficient is defined as $U(X|Y) = I(X,Y)/H(X)$, where $I(X,Y)$ is the mutual information between X and Y and $H(X)$ is the Shannon entropy of X. This measures what proportion of the total possible information about X we can learn by observing Y, with $0 \leq U(X|Y) \leq 1$. A coefficient of zero means that X and Y are independent, while a coefficient of one means that Y completely predicts X.

As we do not have access to the distributions for the optimal density or the spectral gap, we must rely on estimations of the mutual information. We use the algorithm proposed by Ross [126]. For the data presented in Figure 4.3 the uncertainty coefficient between the optimal density and the spectral gap is estimated to be $U(\rho^*|\lambda_{\mathcal{SG}}) = 0.4835$ while for the same networks the average degree gives an uncertainty coefficient of $U(\rho^*|\bar{d}) = 0.3769$, demonstrating greater mutual information between the optimal density and the spectral gap compared to the average degree.

To see this, in Figure 4.4(a) we replot Figure 4.3 with average degree on the horizontal axis. While there is still a good correlation, visual inspection suggests that the networks with low average degree are not as well correlated as with the spectral gap, with a greater number of outliers. Our two real-world networks are notable examples: the London Underground network, marked in Figure 4.4(a), clearly deviates from the bulk, while the US airports network is an even worse match to the trend at the off-axis point $\bar{d} = 11.9, \rho^* = 0.26$. Indeed, consider two of the sampled

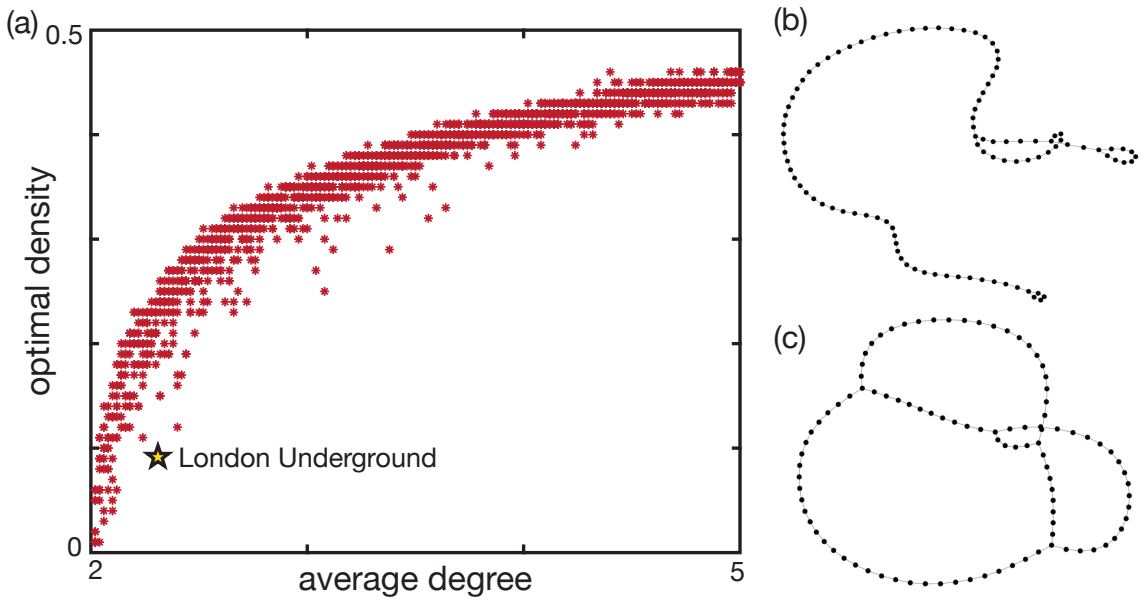

Figure 4.4: (a): The same networks as in Figure 4.3, with optimal density now plotted against average network degree. (b) – (c): Two sampled networks from Figure 4.3 that have identical degree distribution but markedly different optimal densities: (b) $\rho^* = 0.01$, (c) $\rho^* = 0.11$.

networks from Figure 4.3, shown in Figures 4.4(b) and 4.4(c), which have identical degree distributions $\{3, 3, 3, 3, 2, \ldots, 2\}$: we find that the network in Figure 4.4(b) has an optimal density $\rho^* = 0.01$ while that in Figure 4.4(c) has $\rho^* = 0.11$, differing by a factor of 11. Thus average degree (or any degree distribution statistic) can be a poor predictor of optimal density. However, the spectral gaps for these networks are, respectively, $\lambda_{\mathcal{SG}} = 0.0005$ and $\lambda_{\mathcal{SG}} = 0.0012$, with the more-than-doubled spectral gap of (c) compared to (b) accounting for its higher optimal density, particularly since small changes in $\lambda_{\mathcal{SG}}$ near zero have large effects on ρ^*.

4.4 Optimising parallel search strategies

Our results enable the design of optimal search strategies for arbitrary numbers of searchers. Suppose M_{tot} searchers, potentially more than N, need to each cover a given network. A hybrid series–parallel strategy comprises sequentially introducing

batches of searchers, with each batch covering the network in parallel to completion before being removed and replaced by the next batch. Let k_i be the number of times i parallel searchers are introduced sequentially; for example, $k_1 = 3$ and $k_2 = 4$ denotes performing three successive searches with one searcher and four successive searches with two searchers. A hybrid strategy is then defined by the vector $\mathbf{k} = (k_1, \ldots, k_{N-1})$. The optimal strategy, $\mathbf{k}_{\text{opt}}$, minimises the overall cover time $\mathcal{T} = \sum_{i=1}^{N-1} k_i \langle \mathcal{C}_i \rangle$ subject to the constraint $\sum_{i=1}^{N-1} i k_i = M_{\text{tot}}$. As M_{tot} increases, the solution of this integer programming problem typically yields a strategy comprising a mixture of searcher numbers near the optimal density (see Figure 4.5).

To investigate the optimal strategy in the regime where $M_{\text{tot}} \gg N \gg 1$ we consider the corresponding continuous optimisation problem. Let $\bar{\mathcal{C}}(\rho)$ be the mean parallel cover time of the search process with searcher density $\rho \sim i/N$ for $N \gg 1$. We define $k(\rho)$ as the real-valued strategy function (as $M_{\text{tot}} \gg N$) that gives the frequency of serial searches that have searcher density ρ. Thus our optimisation process is to select $k(\rho)$ such that we minimise the total cover time functional

$$\Gamma[k] = \int_0^1 k(\rho)\bar{\mathcal{C}}(\rho)\mathrm{d}\rho, \tag{4.17}$$

subject to the constraint

$$N \int_0^1 \rho k(\rho)\mathrm{d}\rho = M_{\text{tot}}. \tag{4.18}$$

We introduce a rescaled strategy function $f(\rho) = N\rho k(\rho)/M_{\text{tot}}$ and total cover time $\tilde{\Gamma}[f] = \Gamma[k]/M_{\text{tot}}$. We note that the rescaled cover time is

$$\tilde{\Gamma}[f] = \int_0^1 \frac{f(\rho)\bar{\mathcal{C}}(\rho)}{N\rho}\mathrm{d}\rho = \int_0^1 f(\rho)\mathcal{A}(\rho)\mathrm{d}\rho, \tag{4.19}$$

where $\mathcal{A}(\rho) = \bar{\mathcal{C}}(\rho)/(N\rho)$ is the APCT. Our final version of the optimisation problem

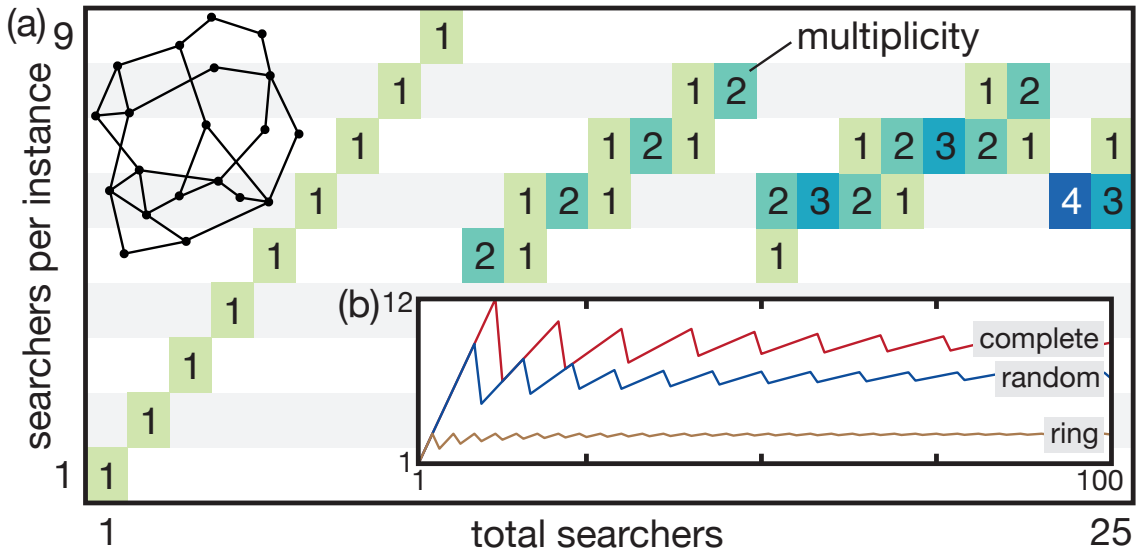

Figure 4.5: (a): Optimal search strategy as M_{tot} is increased for a random network of $N = 20$ nodes (inset) with $\rho^* = 0.35$. Values at fixed M_{tot} give the non-zero components of the strategy vector $\mathbf{k}_{\text{opt}}$. (b): Mean number of searchers per instance $\langle \mathbf{k}_{\text{opt}} \rangle$ for the optimal search strategies of the complete network, the random network in (a) and the ring lattice on $N = 20$ nodes, showing the approach of $\langle \mathbf{k}_{\text{opt}} \rangle$ towards the optimal APCT densities $\rho^* = 0.45$, 0.35 and 0.15, respectively, for large M_{tot}. APCTs are averages over 10^5 random walk instances.

is to minimise

$$\tilde{\Gamma}[f] = \int_0^1 f(\rho)\mathcal{A}(\rho)\mathrm{d}\rho, \tag{4.20}$$

subject to the constraint

$$\int_0^1 f(\rho)\mathrm{d}\rho = 1. \tag{4.21}$$

The APCT, $\mathcal{A}(\rho)$, has a minimum value at the optimal density $\rho^* \in (0, 1)$, thus the function that will solve our optimisation problem is $f(\rho) = \delta(\rho - \rho^*)$ or equivalently the optimal strategy is $k(\rho) = M_{\text{tot}}\delta(\rho - \rho^*)/(N\rho)$, i.e. to have all serial searches operating at the optimal density ρ^*. Thus for large networks whose optimal density becomes difficult to evaluate, our results present a simple strategy to optimise mutually excluding search: approximate ρ^* via the easily-computed spectral gap (see Figure 4.3), and then perform searches in batches at this density.

4.5 Asymmetric search processes

Until now, we have only considered the symmetric exclusion process, where searchers uniformly sample a target node from their neighbours. However, many biological and physical systems are not in equilibrium, possessing non-zero probability currents in stationary state that markedly change the possible physical behaviours [115]. To model this, we now explore directed networks with bias in the choice of target node. To avoid searchers accumulating at nodes we restrict to flux-conserving (balanced) networks, where each vertex has an equal number of inwards- and outwards-biased edges (and is therefore necessarily of even degree; see Figure 4.7(a)). For each edge biased $u \to v$, we define the transition probabilities as $p_{u\to v} = (1+2\varepsilon)/d_u$ and $p_{v\to u} = (1-2\varepsilon)/d_v$, where d_u, d_v are the vertex degrees and $\varepsilon \in [0, 1/2]$ controls the bias. Thus the probability a searcher exits a node through an outwardly biased edge is $1/2 + \varepsilon$.

Asymmetric processes facilitate a significantly greater optimal density than the equivalent unbiased process on the ring lattice. We find numerically that the optimal density for $N = 100$ and $\varepsilon = 0.25$ is $\rho^* = 0.51$ compared to $\rho^* = 0.05$ in the symmetric case $\varepsilon = 0$. This is a marked increase in ρ^* that even exceeds the unbiased complete network for which $\rho^* < 0.5$. Here, conservation of flux forces there to be only two viable orientations for the edges, all either clockwise or anticlockwise, effectively adding a constant drift to the symmetric process. As for symmetric exclusion, intuition can be drawn from asymptotic estimates of the APCT in the high-density regime for the ring lattice.

4.5.1 Asymmetric search on the ring lattice in the high-density regime

We define a random walk on the integers, $\mathbb{Z}$, where a single searcher starts at the origin and at each timestep moves to the right with probability p or left with probability $q = 1 - p$. Chong et. al [127] showed that the expected number of steps to reach m distinct sites (not including the origin) is

$$\langle T_m \rangle = \frac{g_{m-1} h_{m-1}}{s_{m-1} s_m}, \tag{4.22}$$

where $g_k = \sum_{i=0}^{k} (i+1) p^{k-i} q^i$, $h_k = \sum_{i=0}^{k} (i+1) p^i q^{k-i}$, and $s_k = \sum_{i=0}^{k} p^i q^{k-i}$. For a ring lattice of length N we can therefore write down directly the expected cover time as

$$\langle C_1 \rangle = \frac{g_{N-2} h_{N-2}}{s_{N-2} s_{N-1}}. \tag{4.23}$$

For $p > q$ and large N it is known [127] that the cover time is asymptotically

$$\langle C_1 \rangle \sim \frac{1}{p-q} \left(N - 1 - \frac{q}{p-q} + \mathcal{O}\left(N^2 (q/p)^N \right) \right). \tag{4.24}$$

As in Section 4.2.3 we employ particle-hole duality to calculate the APCT in the high-density regime.

4.5.1.1 Single vacancy

We now consider $N - 1$ interacting searchers on a ring lattice of length N with asymmetric transition probabilities p and q. In order to calculate the parallel cover time we consider the vacancy as a random walker on the integers $\mathbb{Z}$. The vacancy has to visit $(N-1)^2$ distinct sites (not including the origin) in order for every searcher to have visited every site. Therefore, if we let $m = (N-1)^2$, the average number of

jumps the vacancy has to make is given in Equation (4.22). In the limit of large N we have that the APCT for $N-1$ searchers is

$$\mathcal{S}_{N-1} \sim \frac{1}{(p-q)(N-1)}\left((N-1)^2 - \frac{q}{p-q}\right). \tag{4.25}$$

Thus, for moderate bias where $p-q$ is not small, the APCT for $N-1$ searchers is two orders of magnitude smaller than the APCT in the case of the symmetric exclusion process.

4.5.1.2 Several vacancies

We consider the case where we have k vacancies, where $k \ll N$. As for the symmetric exclusion process we consider instead a single asymmetric random walker that moves on average k times faster than a single vacancy, and we are interested in the time taken for the vacancy to visit $m = (N-1)(N-k)$ new sites (not including the origin). Therefore we can write down the APCT for the high-density regime as

$$\begin{aligned} \mathcal{S}_{N-k} &\sim \frac{1}{(p-q)k(N-k)}\left((N-1)(N-k) - \frac{q}{p-q}\right) \\ &\sim \frac{N-1}{(p-q)k}. \end{aligned} \tag{4.26}$$

In Figure 4.6 we provide a plot of the APCT for an asymmetric random walk on a ring lattice with transition probabilities $p = 0.75$ and $q = 0.25$ for all numbers of searchers, as well as the estimates in the high-density regime, where we see excellent agreement for $k \leq 5$. In Equation (4.26) we have shown that, for large N and small vacancy count k, the APCT for $M = N-k$ searchers with $p > q$ is approximately $\mathcal{S}_{N-k} \sim (N-1)/(p-q)k$. This is $\mathcal{O}(N)$ for a non-negligible bias, two powers of N fewer than Equation (4.16). In addition, the APCTs in the low- and high-density regimes are both $\mathcal{O}(N)$ in contrast to the unbiased process, whose low- and high-

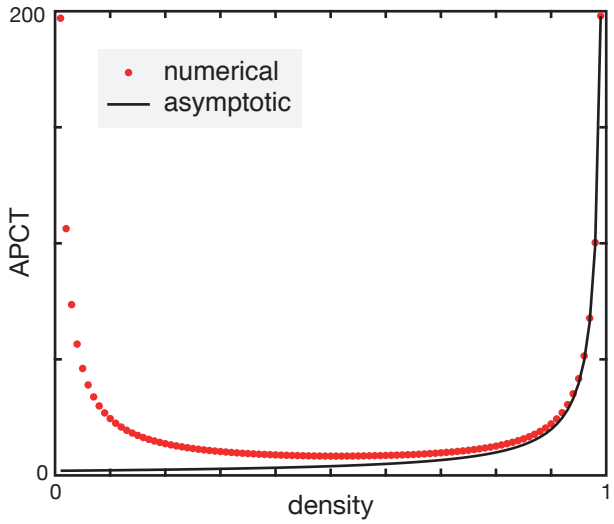

Figure 4.6: The APCTs of an asymmetric exclusion process on the ring lattice, where $p = 0.75$ and $q = 0.25$, from simulation (circles) and from the analytical approximation in the high-density regime (solid line; Equation (4.26)). All APCTs were calculated using 10^5 random walk instances.

density APCTs we recall as $\mathcal{O}(N^2)$ and $\mathcal{O}(N^3)$, respectively, indicating bias induces a qualitative change in the APCT.

4.5.2 Asymmetric search on general topologies

Beyond the ring lattice, general flux-conserving networks of low degree also see a significantly enhanced optimal density for sufficient bias, with a far narrower distribution of optimal densities (see Figure 4.7(b)). Dramatic increases in optimal density particularly occur for networks with $\lambda_{\mathcal{SG}} \approx 0$ (see Figure 4.7(c)): these have a high concentration of degree two nodes implying many linear chains, the edges of which must have the same directional bias (see Figure 4.7(a)). More surprisingly, for networks with extremely small spectral gaps ($\lambda_{\mathcal{SG}} \approx 0$) we see a non-monotonic relationship between $\lambda_{\mathcal{SG}}$ and ρ^* on average. This phenomenon is also captured by the APCT at optimal density (see Figure 4.7(d)) where networks with $\lambda_{\mathcal{SG}} \approx 0$ typically have APCTs below those of networks with greater $\lambda_{\mathcal{SG}}$. This shows that the addition of flux-conserving bias can have a counterintuitive impact on search efficiency and

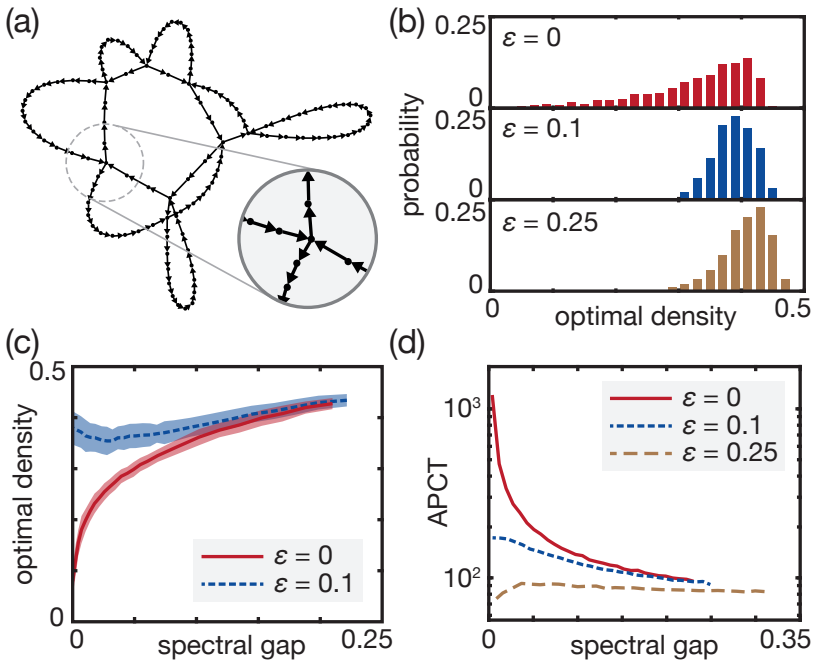

Figure 4.7: (a): A random network for the asymmetric exclusion process, where $N = 100$. The arrows depict the directional bias of the random searchers between nodes. (b): Frequency of optimal densities for a variety of biases. (c): Mean optimal density as a function of spectral gap for symmetric ($\varepsilon = 0$) and asymmetric ($\varepsilon = 0.1$) exclusion processes. Coloured bands are ± 1 standard deviations. (d): APCT at optimal searcher density for a variety of biases. Results in (b) and (d) are from the same ensemble of 2250 random networks of average degree between 2 and 5 (see Appendix 4.7.4). In (c) an additional 2000 networks are included with average degree between 2 and 3. APCTs in (d) are averages over 10^5 random walk instances.

optimality. For example, consider $M_{\text{tot}} = 100$ searchers on the random network in Figure 4.7(a) using the optimal serial–parallel strategy versus the same search on the ring lattice. Without bias ($\varepsilon = 0$), the random network has an average search time of 6.6×10^4 and the ring lattice has time 4.8×10^5. In contrast, with $\varepsilon = 0.25$ these times become 8.5×10^3 and 8.3×10^2, respectively. Thus, random flux-conserving bias inverts the relative efficiency of the networks, implying care must be taken when attempting to improve the efficiency of network search processes by naïve biasing. Furthermore, there are multiple topologically distinct ways to bias the edges of the same undirected network, even when fluxes are balanced. These different biases can induce different cover time properties. For example, consider the five distinct ori-

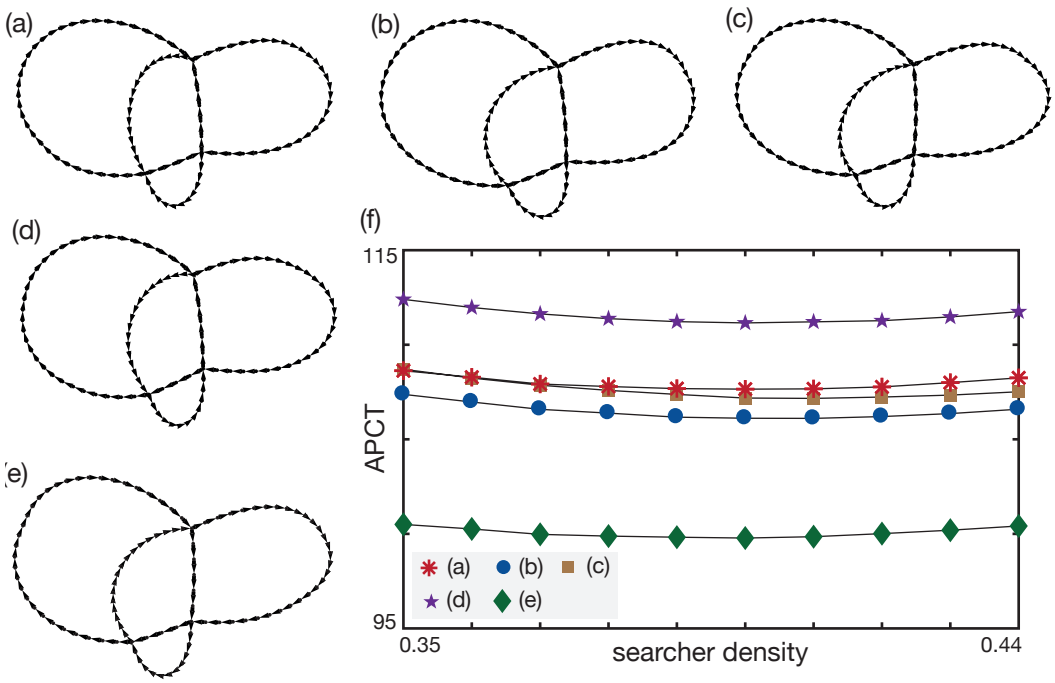

Figure 4.8: (a)–(e): Five distinct flux-conserving (balanced) bias orientations for a given fixed undirected network. (f): The APCTs for each of the graphs (a)–(e) as a function of searcher density near the optima. Each APCT is calculated from 10^6 random walk instances.

entations of the same network in Figure 4.8(a)–(e). For bias strength $\varepsilon = 0.1$, the different orientations have optimal densities $\rho^* = 0.40, 0.41, 0.41,$ 0.40 and 0.40 for (a) to (e), respectively. While these differences are slight, the corresponding APCTs differ more markedly (see Figure 4.8(f)), and such differences will be particularly important if a large number of searchers are being employed in a hybrid series–parallel search strategy. In larger networks, we would expect this variation between different directional biases to be amplified.

4.6 Summary

In this chapter we have introduced the APCT as a fundamental measure of how efficiently a network can support mutually excluding random search processes. Our central result is that the density of searchers that minimises the APCT depends

heavily, yet predictably, on network topology, implying that search strategies can be made efficient by careful optimisation of topology and searcher quantity. In particular, we found that the optimal density of concurrent searchers can vary from 1–2% to nearly 50% depending on topology, and showed that this topological dependence can be effectively captured by the spectral gap for both artificial random graphs and real-world transport networks. Finally, we generalised to a biased, non-equilibrium process and uncovered a qualitative change in the topological dependence of optimal densities. This evidences how the transport process itself must be taken into account when optimising random searches, and leads us to ask whether there is an efficient statistical characterisation of the topology–transport interplay for general active networked processes [52, 114, 128, 129]. More broadly, our work provides an accessible route into the design of optimal search strategies in complex environments involving equilibrium and non-equilibrium processes. In addition we have paved the way towards new strategies for topology optimisation in process allocation and flow transport problems across physical and biological networked systems.

4.7 Appendices

The following appendices detail the numerical methods used to calculate various statistics, and to generate random networks.

4.7.1 Numerical evaluation of cover time statistics and optimal densities

All cover time statistics presented in this chapter were calculated as follows. We do not explicitly sample from the exponential waiting time distribution; rather, we sample the next attempted jump and update the time statistic of interest, t, by the average waiting time, $t = t + \tau/M$. As we are only interested in the first moments of

the cover times, linearity of expectation implies that this suffices.

We now detail our numerical procedure for evaluating optimal densities. Suppose we have a network with N nodes and we wish to calculate the optimal number of parallel searchers, M^*, that minimises the APCT. For efficiency we begin using a small number of random walk instances (initially 10^3) that we increase as we get closer to M^*. Starting at $M = 1$ we calculate the average cover time $\mathcal{S}_1$, then increase M by one and run another sample of random walk instances, calculating $\mathcal{S}_2$ and so on. After generating a new APCT for $j+1$ parallel searchers we ask whether $\mathcal{S}_{j+1} > \mathcal{S}_j$ to see whether j is a candidate for M^*. If not we increase M by one, however if so then we increase the number of random walk instances to 10^4 and return to the previous number of parallel searchers j, where we recalculate $\mathcal{S}_j$ and $\mathcal{S}_{j+1}$, and check again to see if $\mathcal{S}_{j+1} > \mathcal{S}_j$. Once we have moved to 10^4 random walk instances we still check to see if the new APCT is greater than the old one, as before. Once we find a density of parallel searchers that appears to be the minimum we increase the number of random walk instances used for the final time to 10^5. Then the number of searchers that are found to minimise the APCT using 10^5 random walk instances is taken to be M^*, the optimal number of searchers. This was typically enough realisations such that the standard error when calculating the APCTs resulted in mutually excluding 95% confidence intervals either side of the optimal density.

4.7.2 Generating random symmetric networks

In this section we explain the procedure used to sample the random networks seen in Figure 4.3.

1: Select m and N, the required number of edges and the number of nodes of the network respectively, such that $m \geq N$.

2: Sample uniformly the target degree distribution, $\vec{d}$, such that every node has degree at least two, i.e. $\vec{d} = 2(1, \ldots, 1) + \text{Multinomial}(2(m - N), N)$.

3: Allocate d_i stubs to the i-th node for $i \in \{1, \ldots, N\}$.

4: **while** there are stubs remaining **do**

5: **if** the only remaining connections to choose from result in self-loops or multiple-edges **then** start over and return to step 2.

6: **else** select two distinct nodes (avoiding self-loops) with stubs remaining uniformly at random and connect them with an edge only if they have not already been connected (avoiding multiple-edges).

7: **end if**

8: **end while**

9: **if** the resulting network is not connected **then** return to step 2.

10: **else** take the resulting network to be a single realisation.

11: **end if**

4.7.3 Applying the mean-field approximation

In order to justify the assumption that the cover times are approximately Gumbel distributed, for all 1500 networks used to generate Figure 4.3 we simulated $n = 10^6$ cover times, t_i, for single searchers and used the data to calculate maximum likelihood estimators for the Gumbel distribution which are

$$\hat{\beta} = \frac{1}{n}\sum_{i=1}^{n} t_i - \frac{\sum_{i=1}^{n} t_i \exp(-t_i/\hat{\beta})}{\sum_{i=1}^{n} \exp(-t_i/\hat{\beta})}, \tag{4.27}$$

and

$$\hat{\mu} = -\hat{\beta}\log\left\{\frac{1}{n}\sum_{i=1}^{n}\exp(-t_i/\hat{\beta})\right\}. \tag{4.28}$$

Using the maximum likelihood estimators we rescaled the cover times using the transformation $x = (t - \hat{\mu})/\hat{\beta}$ and present the distribution of cover times for each of the networks against the standard Gumbel distribution. We see in Figure 4.9 that across the entire range of the networks seen in Figure 4.3 the Gumbel approximation is valid.

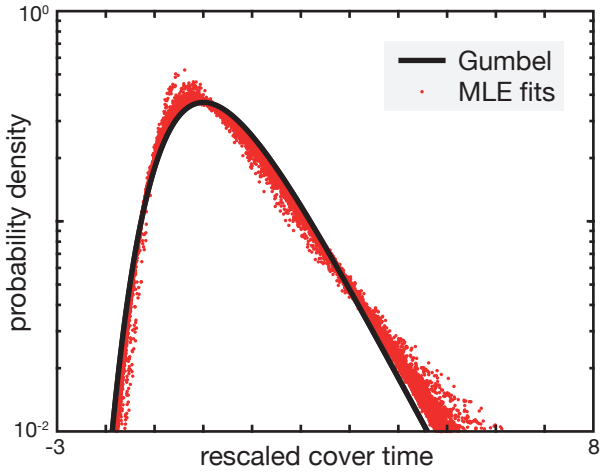

Figure 4.9: The rescaled distributions for the cover times of all 1500 networks used to generate Figure 4.3 (red) against the standard Gumbel distribution (black). The cover time distributions for each network are estimated using 10^6 random walk instances.

Therefore, the optimal densities under the MFA, presented in Figure 4.3, were calculated as $\rho^* = 1/2 + \xi$, where ξ is found in Equation (4.12) and we use the maximum likelihood estimators for the single-searcher cover time.

4.7.4 Generating random balanced directed networks

In this section we describe the sampling procedure for the asymmetric random networks in Figure 4.7.

1: Select m and N, the required number of edges and the number of nodes of the network respectively, such that $m \geq N$.

2: Sample uniformly the target degree distribution for outwardly biased edges, $\vec{d}_{\text{out}}$, such that every node has outward degree at least one, i.e. $\vec{d}_{\text{out}} = (1, \ldots, 1) + \text{Multinomial}(m - N, N)$.

3: Set the degree distribution for the inwardly biased edges to be $\vec{d}_{\text{in}} = \vec{d}_{\text{out}}$.

4: Allocate $\vec{d}_{\text{out}}(i) = \vec{d}_{\text{in}}(i)$ outward stubs and inward stubs to the i-th node for $i \in \{1, \ldots, N\}$.

5: **while** there are stubs remaining **do**

6: **if** the only remaining connections to choose from result in self-loops or multiple-edges **then** start over and return to step 2.

7: **else** select uniformly at random a node with an outward stub and a distinct node with an inward stub. Connect these two nodes with an edge with preferential direction from the outward node to the inward node as long as these nodes have not been connected before.

8: **end if**

9: **end while**

10: **if** the resulting network is not connected **then** return to step 2.

11: **else** take the resulting network to be a single realisation.

12: **end if**

Chapter 5

Displacement of transport processes on networked topologies

The migration of stem cells during embryogenesis [130]; the transport of proteins along microtubules within eukaryotic cells [131]; and the rotational dynamics of polymers [132] are all examples of biological transport processes that take place in complex environments. Transport processes in such environments are not just of interest within the biological sciences, but are ubiquitous in the study of traffic flow [133, 134] and human crowd management [135]. Many of these transport processes are inherently random, and they can be investigated through studying statistics of stochastic transport models. A critical transport statistic used to classify the character of a transport process is the mean squared displacement (MSD), which at time t is denoted by $\langle x^2(t)\rangle$. A particle whose position undergoes Brownian motion and lies on the real line has MSD that evolves linearly in time, $\langle x^2(t)\rangle \propto t$. This is a defining feature of what is referred to as classical diffusion. For more general transport processes the MSD follows a power law, $\langle x^2(t)\rangle \propto t^\alpha$, and the transport process is referred to as: sub-diffusive if $0 < \alpha < 1$; diffusive if $\alpha = 1$; super-diffusive or sub-ballistic if $1 < \alpha < 2$; and ballistic if $\alpha = 2$.

For simple geometries such as the real line it is unambiguous how to define displacement: setting the origin of the real line to be at the initial position of the particle, the displacement is defined as the current position of the particle, $x(t)$. However, for more complex geometries there are several ways to measure displacement. Consider a Brownian particle on a comb lattice [69, 136–139], a topological structure consisting of an infinite backbone (the real line) with teeth (dendrites) of infinite length that protrude periodically out of the backbone. The MSD, when displacement is measured as the distance traversed along the backbone only, is sub-diffusive with $\langle x^2(t)\rangle \propto t^{1/2}$ for long times [138]. The particle spends large amounts of time diffusing along the protruding teeth, during which no transport along the backbone occurs. These long periods of time, where the displacement along the backbone does not change, are responsible for the sub-diffusive nature of the MSD. However, if we define displacement to also include the distance travelled down the teeth then we do not retain the sub-diffusive MSD. The choice of definition for displacement can therefore have a large impact on what we can learn about the transport process.

For topological structures that are embedded within a two- or three-dimensional domain a common definition of displacement is the Euclidean distance between the current and initial positions. With this definition, the potential for geometry to induce a qualitative change in the displacement of a particle has been widely investigated for a class of complex structures known as fractals [140–145]. In fact, for Brownian particles on these structures, a random walk dimension, d_w, can be defined such that $\langle x^2(t)\rangle \propto t^{2/d_w}$ [146, 147]. However, if the topological structure cannot be embedded within a Euclidean domain then this measure of displacement is no longer appropriate. For random walks on general networked topologies (not necessarily embedded in a Euclidean domain), a measure of displacement sometimes used in the literature is the shortest path between the current and initial positions [49]. However, the shortest path does not include information about the actual path the particle took. Statistics

of the path of a particle are of interest across research fields such as polymer physics [148], flux lines within superconductors [149], and more broadly in the winding statistics of stochastic processes. Previous studies of winding statistics have focussed on the winding angle of a Brownian particle in a planar domain [150, 151]. However, there has been little research on winding statistics for particles constrained to more complex environments. Kundu et. al [53] have studied winding statistics of a Brownian particle constrained to the unit circle. They calculate the exact distribution of the net number of clockwise or anticlockwise rotations as a function of time. We investigate the winding statistics of particles constrained to more complex networks. We introduce a new definition of displacement, which we term the *winding distance*, and investigate how it evolves over time as a function of network topology.

The remainder of this chapter is organised as follows. In Section 5.1 we motivate and define our notion of displacement of a particle on a finite network by introducing a topological structure we term the *displacement tree*. In order to analyse the displacement of a Brownian particle on a finite network at long times, we identify a relationship between displacement along the displacement tree and displacement on the half line with periodic bias. We calculate the strength of this bias as a function of the average degree of the network, a very simple topological property. In Section 5.2 we study the displacement of a diffusive particle on the half line subject to periodic bias via a multiple scales approach introduced by Chapman and Shabala [152]. We derive a macroscopic advection-diffusion PDE to describe the evolution of the distribution of the winding distance of a particle. The diffusive and advective transport coefficients are calculated in terms of topological properties of the network. We uncover a topological condition that enables us to distinguish whether the long-time behaviour of the displacement of a Brownian particle is characteristically diffusive or ballistic, and a prediction of the timescale on which the transition between the two behaviours occurs. In Section 5.3 we generalise the transport process of the particle

from Brownian motion to a CTRW model of anomalous diffusion. Repeating the multiple scales approach in Section 5.2 we derive a macroscopic fractional advection-diffusion PDE for the evolution of the winding distance of an anomalously diffusive particle on a network. As in Section 5.2, we obtain a prediction of the timescale on which a particle transitions from the short-time to the long-time behaviour and discuss its asymptotic properties for small values of α. Finally, in Section 5.4 we summarise our results and discuss the scope for future work.

5.1 Displacement on networks

Consider a network $\mathcal{G} = \{\mathcal{V}, \mathcal{E}\}$, where $\mathcal{V}$ is the set of vertices and $\mathcal{E}$ the set of edges. Each edge has an associated edge length $L_e > 0$ for all $e \in \mathcal{E}$. A point particle traverses the edges of the network, and on any given edge its position at time t is denoted by $X(t)$. In order for the position $X(t)$ on the edge e to uniquely identify the location of the particle on the network, each edge is oriented such that the vertex located at one end of the edge has position 0 and the other vertex has position L_e (the choice of which vertex has which position is arbitrary). The position of a particle on each edge evolves according to a standard Brownian motion. When a particle reaches a vertex, located at positions 0 or L_e, an adjacent edge e_* is selected uniformly at random[1][2]. The new position of the particle is then either $X(t) = 0$ or $X(t) = L_{e_*}$ depending on how the edge e_* is oriented. The initial condition for the particle can be either a position $x_0 \in (0, L_e)$ on a known edge e of the network, or the particle can reside initially on a vertex of the network. In the latter case an initial edge is sampled uniformly from all adjacent edges to the initial vertex.

[1]The standard numerical scheme for simulating a Brownian motion is the Euler-Maruyama method. For this scheme a particle performs jumps at discrete time steps of length Δt and, as such, a particle will never reach a vertex but jump past it. For a discussion of how to implement the selection of adjacent edges see Appendix 5.5.1.

[2]The sampling procedure for the adjacent edge is formally incorporated in the definition of a Walsh Brownian motion, for more details see [153].

Rather than the position of a particle at time t, it is often of interest to consider some measure of how far the particle has travelled up to and including time t. Such measures can be considered to be different definitions for the displacement of the particle. To aid discussion of different definitions of displacement, we introduce a simple class of networks. Let $\mathcal{G}_n$ be the network comprising two vertices connected by n edges of the same length, L. The shortest path definition for displacement on networks sometimes used in the literature [49] is the length of the shortest path between the position at time t and the initial position (at time $t = 0$). In certain situations, for example when considering the rotation of polymers around cylindrical fibres [148], we are interested in the winding statistics of stochastic processes in constrained topologies [53]. Therefore, the shortest path definition for displacement can be an undesirable transport statistic as it does not include any information about the winding of a particle between the initial and current times. Instead, consider a particle attached to an "extendable leash". In Figure 5.1(a) we present two trajectories on the network $\mathcal{G}_3$. The initial position of the particle is the left-most vertex (Figure 5.1(a); unfilled circle), and one end of the leash remains stationary at this vertex at all times. The position of the particle evolves according to a Brownian motion. After selecting an initial edge uniformly at random, the particle moves around the network and the leash extends and contracts accordingly. To emphasise the distinction between the two definitions of displacement, in Figure 5.1(a) we consider again the two possible trajectories. The first has the final position of the particle on the upmost edge with the leash hooked around the right-most vertex (Figure 5.1(a), solid line with label one). The second trajectory has the same final position as the first. However, in this case, the particle travelled directly along the upmost edge (Figure 5.1(a), dashed line with label two) and consequently the leash corresponding to the second trajectory is shorter. The length of the leash is what we refer to as the *winding distance* of the particle and is the definition of displacement we consider in this chapter.

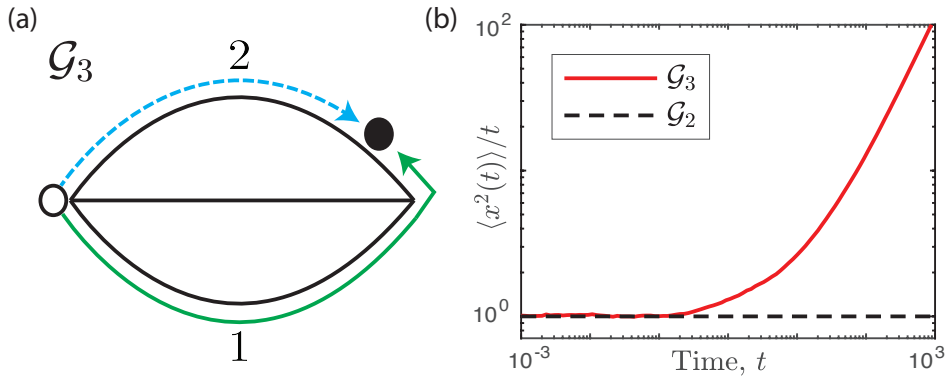

Figure 5.1: (a): Demonstrating the definition of displacement of a particle as the winding distance. The network $\mathcal{G}_3$ with two different trajectories that have the particle positioned at the same location on the network. (b): MSD for a particle on $\mathcal{G}_3$ calculated from 10^4 realisations of a Brownian motion (red solid curve), compared with the MSD for a particle on $\mathcal{G}_2$ (black dashed curve). The diffusion coefficient is $D = 1/2$, the time-step is $\Delta t = 10^{-5}$ and the edge lengths are all equal to one.

For the circle network, $\mathcal{G}_2$, the winding distance of a particle is equivalent to the displacement of a particle whose position evolves according to a Brownian motion on the infinite one-dimensional line [53, 154]. Therefore, the winding distance, $x(t)$, of a Brownian particle at time t on the unit circle is well studied, and the MSD is $\langle x^2(t)\rangle = 2Dt$ for all times t, where D is the diffusion coefficient. To investigate the evolution of the winding distance of a particle on the network $\mathcal{G}_3$ (Figure 5.1(a)), we perform numerical realisations of a Brownian motion. From 10^4 sample paths an estimate for the MSD is calculated and Figure 5.1(b) shows the evolution of $\langle x^2(t)\rangle/t$ on a logarithmic scale. Initially $\langle x^2(t)\rangle = 2Dt$, as on short timescales the particle has not left the initial edge and so is classically diffusive. However as time increases, the solid (red) curve in Figure 5.1(b) deviates away from the line $\langle x^2(t)\rangle = 2Dt$ (Figure 5.1(b), dashed line) and in the long-time limit settles to $\langle x^2(t)\rangle \propto t^2$. This characteristic change in the MSD from diffusive to ballistic behaviour can be explained by considering the behaviour of a particle at the vertices. The first trajectory in Figure 5.1(a) (solid line) reaches the right-most vertex via the bottom edge. At this vertex the particle then selects a new edge uniformly at random. If the new

edge is either the top or middle edge (which occurs with total probability 2/3), then moving along the new edge towards the left-most vertex will increase the displacement. However, if the new edge is the bottom edge (which occurs with probability 1/3), then the displacement will decrease if the particle travels (back) along the bottom edge. Consider temporarily, a particle which hops directly between the vertices in $\mathcal{G}_3$ over an edge, selected uniformly at random. The winding distance is now a stochastic process, which increases by L if the new edge that the particle hops over is distinct from the previous edge, or decreases by L if the new edge is the same as the previous edge. Thus the winding distance evolves as a biased random walk on $\{0, L, 2L, \ldots\}$ with probability 2/3 to jump in the positive direction. This is a well-studied random walk that is known to have a ballistic MSD for all times t. Thus, the introduction of continuous stochastic motion along the edges of the network is responsible for the transition from diffusive to ballistic behaviour.

For diffusive transport processes, can we identify which topologies will cause the displacement of a particle to become characteristically ballistic? Given a topology that will induce ballistic behaviour, can we predict the timescale on which this transition will occur and how it depends on properties of the network? How does topology affect transport statistics for other transport processes? In order to investigate these questions we first introduce a useful topological structure.

5.1.1 The displacement tree

Recall that, for the circle $\mathcal{G}_2$, the winding distance of a particle is equivalent to the displacement of a particle on the real line. A similar relationship can be identified between the winding distance of a particle on a network and the displacement of a particle on a new topological structure we term the *displacement tree*. To construct a displacement tree, $\mathcal{T}_3$, for the network $\mathcal{G}_3$ we need to select an initial position for the particle, which we take as the left-most vertex (see Figure 5.2, unfilled circles).

The three choices for the initial edge result in three potential initial trajectories for the particle. Consequently the tree $\mathcal{T}_3$ starts with its root, corresponding to the initial vertex, from which three parallel trajectories protrude (see Figure 5.2). Now consider a particle that has just reached the right-most vertex of $\mathcal{G}_3$; the particle must choose a new edge. If it chooses the edge it just traversed and travels back along that edge the displacement of the particle will decrease. Travelling along the other two edges will result in an increase in displacement. To represent these possibilities, each of the three initial trajectories of the displacement tree branch into two new trajectories for the two edge choices that, if travelled along, will increase displacement. Repeating this procedure produces an infinite tree that spans the entire ensemble of possible trajectories for a particle on $\mathcal{G}_3$, oriented such that trajectories that increase displacement lead to the right. The winding distance of a Brownian particle on $\mathcal{G}_3$ is therefore equivalent to how far a Brownian particle has travelled along $\mathcal{T}_3$ (see Figure 5.2).

The displacement tree $\mathcal{T}_3$ has a very simple structure: as the edges of $\mathcal{G}_3$ are all of equal length, L, the branching points appear on the tree periodically along all trajectories at positions kL for integers $k \geq 1$. We define a protruding edge on the displacement tree to be an edge that emerges from a branching point and leads to the right. Both the vertices in $\mathcal{G}_3$ have degree three and so the number of protruding edges from any of the branching points in the displacement tree is the same, and equal to two. We refer to these displacement trees as regular: every possible trajectory of a particle on $\mathcal{T}_3$ of some fixed displacement will have passed the same number of branching points, all of which had the same number of protruding edges. As a result, we can equate the displacement of a particle on such a regular displacement tree with the displacement of a particle undergoing a new transport process on the non-negative half line.

Consider a particle whose position on the regular displacement tree, $X(t)$, lies

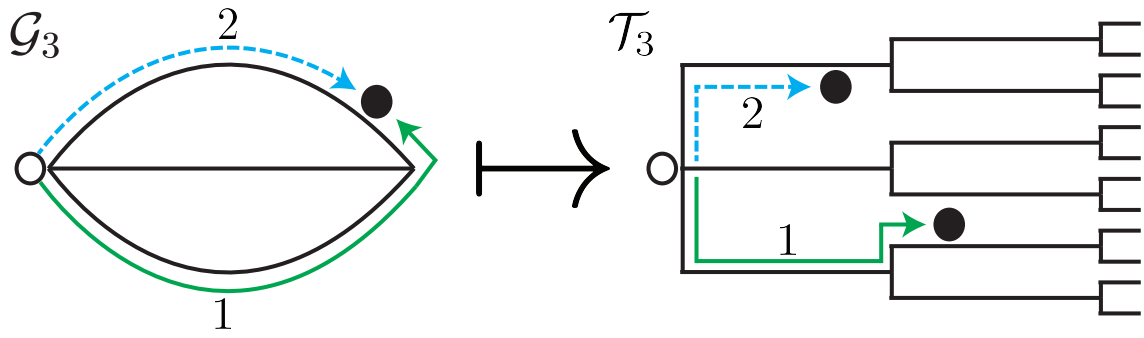

Figure 5.2: Demonstrating the equivalence of the winding distance of a particle on the network $\mathcal{G}_3$ and the displacement of a particle on the displacement tree $\mathcal{T}_3$. Two possible trajectories that end at the same location on the network $\mathcal{G}_3$ are highlighted in dashed and dot-dashed lines. On the corresponding displacement tree, $\mathcal{T}_3$, the two trajectories have different displacements.

within the interval $[(k-1)L, kL]$ for some positive integer k. The position of the particle evolves according to a Brownian motion unless the particle is positioned on one of the boundaries of the interval, $X(t) = kL$ or $X(t) = (k-1)L$. These boundary positions correspond to the branching points on the displacement tree and, as such, a particle moves to the right of these points with probability $2/3$ and to the left with probability $1/3$. It is equivalent to just consider a particle on the non-negative half line, where the particle moves between the intervals $[(k-1)L, kL]$ for integers $k \geq 1$. For a particle with position $X(t) = kL$, the probability $2/3$ to move to the right is incorporated as a Robin boundary condition. The particle is absorbed into the new interval $[kL, (k+1)L]$ (a move to the right along the displacement tree) with probability $2/3$ and reflected back into the interval $[(k-1)L, kL]$ (a move to the left along the displacement tree) with probability $1/3$. For a particle positioned at $X(t) = (k-1)L$, the particle is absorbed into the new interval $[(k-2)L, (k-1)L]$ (a move to the left along the displacement tree) with probability $1/3$ and reflected back into the interval $[(k-1)L, kL]$ (a move to the right along the displacement tree) with probability $2/3$. This transport process is a Brownian motion on the non-negative half line with singular periodic bias of strength $2/3$.

5.1.2 Extending to general networked topologies

Networks that represent complex environments will not necessarily have regular displacement trees. For a general network, $\mathcal{G} = \{\mathcal{V}, \mathcal{E}\}$, the edge lengths, L_e for $e \in \mathcal{E}$, are not always of equal length and the vertices will not always have equal degree. An example of such a network is shown in Figure 5.3(a) where two vertices are connected by three multiple edges, similarly to $\mathcal{G}_3$, but now the top, middle and bottom edges have edge lengths $3L$, L and $2L$, respectively. Consider two possible trajectories for a particle starting at the left-most node; trajectory one is highlighted with a solid line in Figure 5.3(b), has a length of $4L$, and finishes at a vertex on the network $\mathcal{G}$, i.e. a branching point on the displacement tree (see Figure 5.3(c), solid line with label one). Trajectory two is highlighted with a dashed line in Figure 5.3, also has a length of $4L$ but finishes along an edge, not at a branching point. Therefore knowledge of the displacement of a particle is not sufficient to determine whether the particle is at a branching point on the displacement tree. In order to circumvent this problem we introduce a topologically equivalent network $\mathcal{G}_L = \{\mathcal{V}_L, \mathcal{E}_L\}$ which is formed by introducing additional vertices into $\mathcal{G}$ that occur with equal-spacing of length L (see Figure 5.3(a), black squares). The corresponding displacement tree for $\mathcal{G}_L$ has branching points that occur periodically at positions kL for integers $k \geq 1$ along every trajectory (see Figure 5.3(c), black squares). Note that all the additional branching points introduced will have only one protruding edge as the additional vertices in $\mathcal{G}_L$ have degree two. As a result, they will not introduce a bias. For general networks $\mathcal{G} = \{\mathcal{V}, \mathcal{E}\}$, as long as the edge lengths, L_e, are rational, or can be approximated as such, there will always exist $L > 0$ such that $L_e = m_e L$ for some positive integer m_e for all $e \in \mathcal{E}$, and so the transformation from $\mathcal{G}$ to $\mathcal{G}_L$ can be applied.

As for $\mathcal{G}_3$, for these more general networks $\mathcal{G}_L$, it would be convenient to equate the displacement of a particle diffusing on the displacement tree to the displacement

of a particle on the half line. The displacement tree for $\mathcal{G}_L$ has branching points along all trajectories at positions kL for integers $k \geq 1$. However, the number of protruding edges is not constant across trajectories with the same length. Consider again the highlighted trajectories of length $4L$ in Figure 5.3(c). The branching point at the end of trajectory one (blue) has two protruding edges. A particle at this branching point travels along an edge that will increase displacement with probability $2/3$. However, trajectory two (green) ends at a branching point with only one protruding edge. The probability of a particle travelling along an edge that will increase displacement is $1/2$. To make progress, we consider a particle on the displacement tree whose position lies in the interval $[(k-1)L, kL]$. For a particle at the boundary position $X(t) = kL$ we seek an averaged probability, ρ_k^+, to select an edge on the displacement tree which lies to the right of the branching points at kL. The probability of moving further along the displacement tree if the particle is at vertex $\nu \in \mathcal{V}_L$ is $(d_\nu - 1)/d_\nu$ where d_ν is the degree of the vertex ν. Weighting this by $p_k(\nu)$, the probability that the particle occupies vertex ν given it has displacement kL, and summing over $\nu \in \mathcal{V}_L$, yields

$$\rho_k^+ = \sum_{\nu \in \mathcal{V}_L} \frac{d_\nu - 1}{d_\nu} \times p_k(\nu). \tag{5.1}$$

The probabilities ρ_k^+ are used to define the Robin boundary conditions for the transport process on the half line, just as for symmetric displacement trees. Consider a particle in the interval $[(k-1)L, kL]$ with position at the boundary $X(t) = kL$. The particle is absorbed into the adjacent interval $[kL, (k+1)L]$ (a move to the right along the asymmetric displacement tree) with probability ρ_k^+. The particle is reflected back into the interval $[(k-1)L, kL]$ (a move to the left along the asymmetric displacement tree) with probability $1 - \rho_k^+$. Therefore, Equation (5.1) provides the sequence of probabilities, $\{\rho_1^+, \rho_2^+, \ldots\}$, to be absorbed at position kL into the interval $[kL, (k+1)L]$ (see Figure 5.3(d)). The probabilities $p_k(\nu)$ are difficult to calculate as they depend heavily on the topology of the network and the initial position of the

particle. However, the displacement of a particle transitions to ballistic behaviour when the periodic bias felt at positions kL dominates over the unbiased Brownian motion. As such, we consider the displacement of a particle in the long-time limit, which is when the particle has traversed sufficiently many edges for the bias to dominate. The branching points in the displacement tree (corresponding to vertices in the network with degree greater than two) introduce an asymmetry, biasing particles further along the tree (to the right). As a particle moves further along the tree we are interested in the limit to which the sequence of effective biases $\{\rho_1^+, \rho_2^+, \ldots\}$ converges. Assume temporarily that the networks we consider are both finite and have an aperiodic displacement tree[3]. Then, as $k \to \infty$, the probability $p_k(\nu)$ converges to the equilibrium distribution for a discrete random walk on the vertices of $\mathcal{G}_L$ which is $p_\infty(\nu) = d_\nu / \sum_{\omega \in \mathcal{V}_L} d_\omega$ [4]. The sequence $\{\rho_1^+, \rho_2^+, \ldots\}$ therefore converges to the limit

$$\rho_\infty^+ = \sum_{\nu \in \mathcal{V}_L} \frac{d_\nu - 1}{d_\nu} \times \frac{d_\nu}{\sum_{\omega \in \mathcal{V}_L} d_\omega} = 1 - \frac{1}{\bar{d}}, \tag{5.2}$$

where $\bar{d} = 2|\mathcal{E}_L|/|\mathcal{V}_L|$ is the average degree of $\mathcal{G}_L$. Equation (5.2) provides an approximation for the probability of a particle to be absorbed at kL into the interval $[kL, (k+1)L]$ once the particle is sufficiently far along the half line, that is, for large integers k. Note that the assumption that the network is finite is not a necessary one. Some infinite networks, such as a honeycomb lattice, have displacement trees where the equilibrium distribution $p_\infty(\nu)$ does exist. We can also relax the assumption that the displacement tree is aperiodic; see Appendix 5.5.2.

In summary, in the long-time limit we have identified a link between the displacement of a diffusing particle on a general network and displacement on the half line

[3]A network has an aperiodic displacement tree if the average degree of the branching points at position kL tends to a unique constant value as $k \to \infty$, rather than a periodic sequence of values.

[4]For general finite Markov Chains an equilibrium distribution for the occupancy probability of each state in the chain exists if and only if the chain (here the network) is irreducible and aperiodic. All connected undirected networks however are necessarily irreducible.

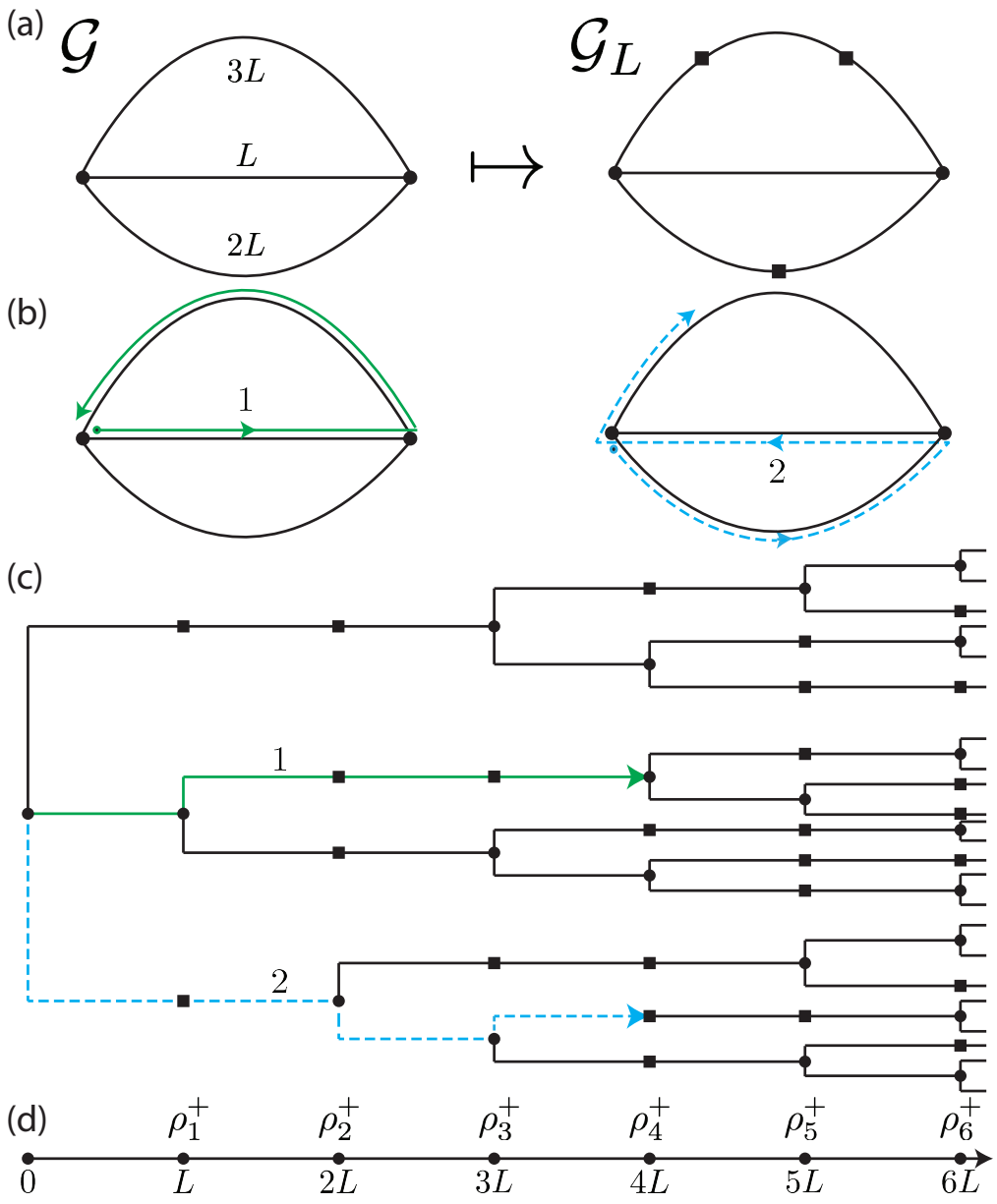

Figure 5.3: (a): Demonstrating the mapping of a network $\mathcal{G}$ to the topologically equivalent network $\mathcal{G}_L$ by introducing additional vertices here represented as squares. (b): Two possible trajectories each of length $4L$ are highlighted with solid and dashed lines on the network $\mathcal{G}$. The first trajectory ends at a vertex, whereas the second trajectory ends midway through an edge. (c): The asymmetric displacement tree for the network $\mathcal{G}$ and $\mathcal{G}_L$. The additional vertices introduced on the network $\mathcal{G}_L$ are represented as black squares on the tree. The two trajectories considered in (b) are highlighted on the tree using solid and dashed lines. (d): The half line $[0, \infty)$ with vertices at positions kL for integers $k \geq 1$. The sequence of effective biases are shown $\{\rho_1^+, \rho_2^+, \ldots\}$.

with a constant periodic bias. The focus of the next section is to use multiple scales analysis to explore the transport properties of the process on the half line.

5.2 Periodic bias on the half line: multiple scales analysis

In this section we consider the transport properties of a Brownian motion on the half line with periodic bias using an approach from a recent paper by Chapman and Shabala [152]. The paper introduces a method of multiple scales to derive the macroscopic transport equations of a random walk on a periodic lattice with spatially dependent transition rates. The slow scale is continuous and evolves as the particle walks over many periods of the lattice. The fast scale is discrete and is defined on a unit periodic interval made up of N lattice sites. In contrast to [152], in this work we are interested in the transport of a Brownian particle and so we take the limit $N \to \infty$ to obtain a continuous expression for the fast scale as well as the slow scale.

Brownian motion is defined in continuous space, however to make progress we formulate a CTMC in discrete space that has the same macroscopic properties. We non-dimensionalise in space by setting the length of each interval to be one ($L = 1$). The intervals $[k, k+1]$ are then discretised into $N+1$ lattice sites each separated by distance $\epsilon = 1/N$ (see Figure 5.4). Consider the position of a particle on the discretised lattice that evolves according to a CTMC, where the transition rates to leave each site are symmetric and chosen to be $\lambda_{n\to n-1} = \lambda_{n\to n+1} = D/\epsilon^2$. In the limit $\epsilon \to 0$ and $N \to \infty$, the distribution of the position of a particle which evolves according to this CTMC is equivalent to the same distribution arising from a Brownian motion on the half line with diffusion coefficient D. For the remainder of this work we take $D = 1/2$. To include the periodic bias at branching points, which occur at lattice sites with indices kN for all integers $k > 0$, we choose asymmetric transition

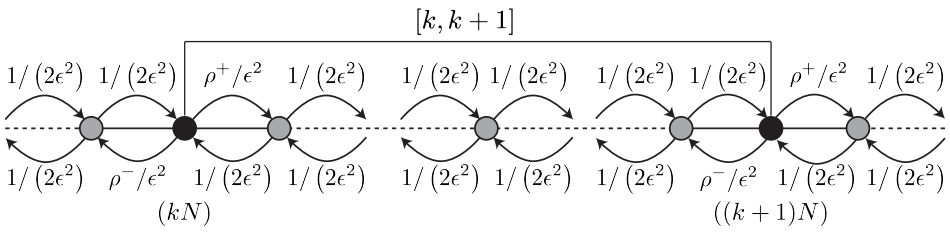

Figure 5.4: A diagrammatic representation of the CTMC on the discretised interval $[k, k+1]$. The black circles represent the lattice sites which correspond to the biased branching points, the grey circles are the lattice sites where symmetric transport occurs.

rates at these points. For a particle to exit on the right of the branching point with probability ρ^+_∞ we choose transition rates $\lambda_{kN\to kN+1} = \rho^+/\epsilon^2$ and $\lambda_{kN\to kN-1} = \rho^-/\epsilon^2$, where $\rho^- = 1 - \rho^+$ and we have dropped the ∞ subscripts from Section 5.1. For a diagrammatic representation of the CTMC see Figure 5.4.

Let $p_n(t)$ be the probability a particle occupies lattice site $n \geq 0$ at time t. The master equation for $p_n(t)$ is

$$\frac{\mathrm{d}p_n}{\mathrm{d}t} = \lambda_{(n-1)\to n} p_{n-1} + \lambda_{(n+1)\to n} p_{n+1} - \left(\lambda_{n\to(n-1)} + \lambda_{n\to(n+1)}\right) p_n. \tag{5.3}$$

Initial conditions imply $p_0(0) = 1$ and $p_i(0) = 0$ for all $i \geq 1$ as the initial winding distance is always zero. The winding distance is defined such that it is always non-negative, therefore we impose a reflective boundary condition at the origin by setting $\lambda_{-1\to 0} = \lambda_{0\to -1} = 0$ and $\lambda_{0\to 1} = 1/\epsilon^2$. We define the spatial coordinate $x = \epsilon n$, and note that, for $\epsilon \ll 1$, x evolves on a slower time scale than the lattice index n. Following Chapman and Shabala [152], let $p_n(t) = P_n(x,t)$ so the probability density for the position of a particle at time t depends on both the fast scale, n, and the slow scale x. Rewriting Equation (5.3) in terms of $P_n(x,t)$, we have

$$\begin{aligned} \frac{\partial P_n(x,t)}{\partial t} &= \lambda_{(n-1)\to n} P_{n-1}\left(x-\epsilon, t\right) + \lambda_{(n+1)\to n} P_{n+1}\left(x+\epsilon, t\right) \\ &\quad - \left(\lambda_{n\to(n-1)} + \lambda_{n\to(n+1)}\right) P_n\left(x,t\right), \end{aligned} \tag{5.4}$$

for $n \geq 0$ and $x \in [0, \infty)$. To derive a macroscopic PDE in the spatial variable x, we assume that the variables x and n are independent. This assumption reduces the infinite set of Equations (5.4) to a finite set of N distinct equations. Introducing circular notation $\overline{i \pm 1} = (i \pm 1 - 1 \bmod N) + 1$, we write the master equation for the probabilities $P_i(x,t)$ as

$$\begin{aligned} \frac{\partial P_i}{\partial t}(x,t) &= \lambda_{\overline{i-1} \to i} P_{\overline{i-1}}(x - \epsilon, t) + \lambda_{\overline{i+1} \to i} P_{\overline{i+1}}(x + \epsilon, t) \\ &\quad - \left(\lambda_{i \to \overline{i+1}} + \lambda_{i \to \overline{i-1}} \right) P_i(x,t), \end{aligned} \tag{5.5}$$

for $i \in \{1, \ldots, N\}$ and $x \in [0, \infty)$. The finite set of equations defines the dynamics on the periodic unit interval. On the periodic unit interval there are symmetric transition rates of $1/(2\epsilon^2)$ for all adjacent sites, other than the rates $\lambda_{N \to 1} = \rho^+/\epsilon^2$ and $\lambda_{N \to N-1} = \rho^-/\epsilon^2$.

Following the derivation in [152], we introduce $\vec{P}(x,t) = [P_1(x,t), \ldots, P_N(x,t)]^T$ and expand about x to obtain

$$\epsilon^2 \frac{\partial \vec{P}}{\partial t}(x,t) = \mathbf{A}\vec{P} + \epsilon \mathbf{B} \frac{\partial \vec{P}}{\partial x} + \epsilon^2 \mathbf{C} \frac{\partial^2 \vec{P}}{\partial x^2} + \mathcal{O}\left(\epsilon^3\right), \tag{5.6}$$

where

$$\mathbf{A} = \begin{pmatrix} -1 & 1/2 & 0 & \cdots & 0 & 0 & \rho^+ \\ 1/2 & -1 & 1/2 & \cdots & 0 & 0 & 0 \\ 0 & 1/2 & -1 & \cdots & 0 & 0 & 0 \\ 0 & 0 & 1/2 & \cdots & 0 & 0 & 0 \\ & \vdots & & \ddots & & \vdots & \\ 0 & 0 & 0 & \cdots & 1/2 & 0 & 0 \\ 0 & 0 & 0 & \cdots & -1 & 1/2 & 0 \\ 0 & 0 & 0 & \cdots & 1/2 & -1 & \rho^- \\ 1/2 & 0 & 0 & \cdots & 0 & 1/2 & -1 \end{pmatrix}, \tag{5.7a}$$

$$\mathbf{B} = \begin{pmatrix} 0 & 1/2 & 0 & \cdots & 0 & 0 & -\rho^+ \\ -1/2 & 0 & 1/2 & \cdots & 0 & 0 & 0 \\ 0 & -1/2 & 0 & \cdots & 0 & 0 & 0 \\ 0 & 0 & -1/2 & \cdots & 0 & 0 & 0 \\ & \vdots & & \ddots & & \vdots & \\ 0 & 0 & 0 & \cdots & 1/2 & 0 & 0 \\ 0 & 0 & 0 & \cdots & 0 & 1/2 & 0 \\ 0 & 0 & 0 & \cdots & -1/2 & 0 & \rho^- \\ 1/2 & 0 & 0 & \cdots & 0 & -1/2 & 0 \end{pmatrix}, \tag{5.7b}$$

$$\mathbf{C} = \begin{pmatrix} 0 & 1/4 & 0 & \cdots & 0 & 0 & \rho^+/2 \\ 1/4 & 0 & 1/4 & \cdots & 0 & 0 & 0 \\ 0 & 1/4 & 0 & \cdots & 0 & 0 & 0 \\ 0 & 0 & 1/4 & \cdots & 0 & 0 & 0 \\ & \vdots & & \ddots & & \vdots & \\ 0 & 0 & 0 & \cdots & 1/4 & 0 & 0 \\ 0 & 0 & 0 & \cdots & 0 & 1/4 & 0 \\ 0 & 0 & 0 & \cdots & 1/4 & 0 & \rho^-/2 \\ 1/4 & 0 & 0 & \cdots & 0 & 1/4 & 0 \end{pmatrix}. \tag{5.7c}$$

Note that when $\rho^+ = \rho^- = 1/2$ we have symmetric transition rates of $1/(2\epsilon^2)$ at all sites on the unit interval. These rates were chosen such that the time derivative on the right-hand side of Equation (5.6) appears at the same order in ϵ as the second order spatial derivatives on the left-hand side. Therefore, as $\epsilon \to 0$, the probability distribution for the displacement of a particle follows a macroscopic diffusion equation. However, when $\rho^+ \neq \rho^-$, recall that the displacement of a particle on a networked topology may transition from diffusive to ballistic behaviour. As such, we anticipate both advective and diffusive contributions to the macroscopic PDE describing the

displacement of a particle and we rescale time, $\hat{t} = \epsilon^{-1}t$, to give

$$\epsilon\frac{\partial\vec{P}}{\partial\hat{t}}(x,\hat{t}) = \mathbf{A}\vec{P} + \epsilon\mathbf{B}\frac{\partial\vec{P}}{\partial x} + \epsilon^2\mathbf{C}\frac{\partial^2\vec{P}}{\partial x^2}, \tag{5.8}$$

where the time-dependent derivative now appears at the same order of magnitude as the first order spatial derivative. We make the series expansion $\vec{P}(x,\hat{t}) = \vec{P}_0(x,\hat{t}) + \epsilon\vec{P}_1(x,\hat{t}) + \epsilon^2\vec{P}_2(x,\hat{t}) + \ldots$ and substitute into Equation (5.8). Collecting terms of $\mathcal{O}(\epsilon^0)$ yields $\mathbf{A}\vec{P}_0 = \vec{0}$, which has solution $\vec{P}_0 = f(x,\hat{t})\vec{u}_0$ where $f(x,\hat{t})$ is some function to be determined and $\vec{u}_0$ is in the kernel of $\mathbf{A}$[5] which is given by

$$[\vec{u}_0]_n = \frac{2\rho^+}{N} - \frac{2n\left(\rho^+ - \rho^-\right)}{N^2}, \tag{5.9}$$

for $1 \leq n \leq N-1$ and $[\vec{u}_0]_N = 1/N$, such that $\sum_{n=1}^{N}[\vec{u}_0]_n = 1$. Collecting terms of $\mathcal{O}\left(\epsilon^1\right)$ we find

$$\frac{\partial\vec{P}_0}{\partial\hat{t}} = \mathbf{A}\vec{P}_1 + \mathbf{B}\frac{\partial\vec{P}_0}{\partial x}. \tag{5.10}$$

Substituting in the expression for $\vec{P}_0$ and rearranging yields

$$\mathbf{A}\vec{P}_1 = \vec{u}_0\frac{\partial f}{\partial\hat{t}} - \mathbf{B}\vec{u}_0\frac{\partial f}{\partial x}. \tag{5.11}$$

Applying the Fredholm alternative theorem[6] we see that, in order for Equation (5.11) to have a solution, we need the right-hand side to be orthogonal to the null space of $\mathbf{A}^T$. The null space is spanned by the vector $\vec{v} = [1,\ldots,1]^T$, and the Fredholm alternative theorem therefore implies

$$\frac{\partial f}{\partial\hat{t}} = \frac{\vec{v}^{\,T}\mathbf{B}\vec{u}_0}{\vec{v}^{\,T}\vec{u}_0}\frac{\partial f}{\partial x}. \tag{5.12}$$

[5]The matrix $\mathbf{A}$ is the rate matrix for the CTMC on the periodic interval, therefore as $\vec{u}_0$ is in the kernel of $\mathbf{A}$ it is proportional to the equilibrium distribution of the CTMC.

[6]The Fredholm alternative theorem states that $\mathbf{M}\vec{x} = \vec{b}$ has a solution if and only if for all $\vec{y}$ such that $\mathbf{M}^T\vec{y} = \vec{0}$ we also have $\vec{y}^T\vec{b} = \vec{0}$.

Introducing $V = -\vec{v}^{\,T}\mathbf{B}\vec{u}_0/\vec{v}^{\,T}\vec{u}_0$ we can solve Equation (5.11) to give $\vec{P}_1 = f_x\vec{u}_1 + g\vec{u}_0$, where $g(x,\hat{t})$ is some function to be determined, $\vec{u}_1$ is such that $\mathbf{A}\vec{u}_1 = -\left(V\mathbf{I}+\mathbf{B}\right)\vec{u}_0$ and $\mathbf{I}$ is the identity matrix. Noting that $V = \left(\rho^+ - \rho^-\right)/N$ we can solve for $\vec{u}_1$ to obtain

$$\left[\vec{u}_1\right]_n = \beta_0 + \beta_1 n + \beta_2 n^2 + \beta_3 n^3, \tag{5.13}$$

for $1 \leq n \leq N-1$ where the coefficients are given by

$$\begin{aligned}
\beta_0 &= \frac{2\rho^+}{N} + \frac{\rho^+\left(\rho^+ - \rho^-\right)}{3}\left(1 - \frac{1}{N^2}\right), && (5.14a)\\
\beta_1 &= -\frac{\left(\rho^+ - \rho^-\right)}{N} - \frac{2\left(\rho^+ - \rho^-\right)}{N^2} + \frac{\left(\rho^+ - \rho^-\right)^2}{3N^3}, && (5.14b)\\
\beta_2 &= \frac{2\rho^-\left(\rho^+ - \rho^-\right)}{N^2}, && (5.14c)\\
\beta_3 &= \frac{2\left(\rho^+ - \rho^-\right)^2}{3N^3}, && (5.14d)
\end{aligned}$$

and the final term in $\vec{u}_1$ is given by

$$\left[\vec{u}_1\right]_N = \frac{1}{N} + \frac{\rho^+ - \rho^-}{6}\left(1 - \frac{1}{N^2}\right). \tag{5.15}$$

We now proceed to collect terms of $\mathcal{O}\left(\epsilon^2\right)$ which gives

$$\frac{\partial \vec{P}_1}{\partial \hat{t}} = \mathbf{A}\vec{P}_2 + \mathbf{B}\frac{\partial \vec{P}_1}{\partial x} + \mathbf{C}\frac{\partial^2 \vec{P}_0}{\partial x^2}. \tag{5.16}$$

As before, we rearrange Equation (5.16) to give

$$\mathbf{A}\vec{P}_2 = \vec{u}_0\frac{\partial g}{\partial \hat{t}} - V\vec{u}_1\frac{\partial^2 f}{\partial x^2} - \mathbf{B}\vec{u}_1\frac{\partial^2 f}{\partial x^2} - \mathbf{C}\vec{u}_0\frac{\partial^2 f}{\partial x^2} - \mathbf{B}\vec{u}_0\frac{\partial g}{\partial x}. \tag{5.17}$$

Applying the Fredholm alternative theorem once again implies

$$\frac{\partial g}{\partial \hat{t}} + V\frac{\partial g}{\partial x} = \frac{\vec{v}^{\,T}\mathbf{B}\vec{u}_1 + \vec{v}^{\,T}\mathbf{C}\vec{u}_0 + V\vec{v}^{\,T}\vec{u}_1}{\vec{v}^{\,T}\vec{u}_0}\,\frac{\partial^2 f}{\partial x^2}. \tag{5.18}$$

We can now rewrite the power series as

$$\vec{P} = \vec{P}_0 + \epsilon\vec{P}_1 + \ldots = (f(x,\hat{t}) + \epsilon g(x,\hat{t}))\vec{u}_0 + \epsilon f_x(x,\hat{t})\vec{u}_1 + \ldots. \tag{5.19}$$

Introducing $h_\epsilon(x,\hat{t}) = f(x,\hat{t}) + \epsilon g(x,\hat{t})$, rescaling into time coordinates $t = \epsilon\hat{t}$ and using Equations (5.12) and (5.18), we have

$$\epsilon\frac{\partial h_\epsilon}{\partial t} + V\frac{\partial h_\epsilon}{\partial x} = \epsilon D\left(\frac{\partial^2 h_\epsilon}{\partial x^2} - \epsilon\frac{\partial^2 g}{\partial x^2}\right), \tag{5.20}$$

where $D = \left(\vec{v}^{\,T}\mathbf{B}\vec{u}_1 + \vec{v}^{\,T}\mathbf{C}\vec{u}_0 + V\vec{v}^{\,T}\vec{u}_1\right)/\vec{v}^{\,T}\vec{u}_0$. Upon dividing Equation (5.20) by ϵ, taking the limit $\epsilon \to 0$ and $N \to \infty$ where $\epsilon = 1/N$, and introducing $h(x,t) = \lim_{\epsilon\to 0}\{h_\epsilon(x,t)\}$, $\hat{V} = \lim_{\epsilon\to 0}\{V/\epsilon\}$, and $\hat{D} = \lim_{\epsilon\to 0}\{D\}$ we have the following linear advection-diffusion PDE

$$\frac{\partial h}{\partial t} + \hat{V}\frac{\partial h}{\partial x} = \hat{D}\frac{\partial^2 h}{\partial x^2}, \tag{5.21}$$

for $x \in [0,\infty)$, with boundary conditions $\hat{D}h_x(0,t) + \hat{V}h(0,t) = \lim_{x\to\infty}\{\hat{D}h_x(x,t) + \hat{V}h(x,t)\} = 0$ and initial conditions $h(x,0) = \delta(x)$. Equation (5.21) is a macroscopic PDE for the evolution of the displacement (defined as the winding distance) of a particle on a network $\mathcal{G}$, valid in the long-time limit. Note that the scalar coefficient of $\vec{u}_1$ in Equation (5.19) is $\epsilon f_x(x,\hat{t})$. Upon rescaling time $t = \epsilon\hat{t}$, it is clear from Equation (5.12) that $f_x(x,t)$ is independent of ϵ, and we find that $\lim_{\epsilon\to 0}\{\epsilon f_x(x,t)\} = 0$. The entries of $\vec{u}_1$ given in Equation (5.15) are finite. Therefore, as $\epsilon \to 0$, there is no contribution to $\vec{P}(x,t)$ from the term $\epsilon f_x(x,t)\vec{u}_1(\epsilon)$. The terms $\hat{V}h_x$ and $\hat{D}h_{xx}$ in Equation (5.21) represent the effective drift and diffusion contributions, respectively, to the distribution of the displacement of a particle. The transport coefficients $\hat{V}$ and $\hat{D}$ determine the strengths of these contributions as a function of the networked topology. We use the expressions for $\mathbf{A}$, $\mathbf{B}$ and $\mathbf{C}$ in Equations (5.7), as well as $\vec{u}_0$ and $\vec{u}_1$ in Equations (5.9) and (5.15), respectively, to calculate the effective transport

coefficients as

$$\hat{V} = \rho^+ - \rho^-, \tag{5.22a}$$

$$\hat{D} = \frac{1}{2} - \frac{1}{6}\left(\rho^+ - \rho^-\right)^2. \tag{5.22b}$$

From Equation (5.21) we calculate expressions for the first two moments of the displacement as

$$\langle x(t)\rangle \sim \hat{V}t = \left(1 - \frac{2}{\bar{d}}\right)t, \tag{5.23a}$$

$$\langle x^2(t)\rangle \sim \hat{V}^2t^2 + 2\hat{D}t = \left(1 - \frac{2}{\bar{d}}\right)^2 t^2 + \left[1 - \frac{1}{3}\left(1 - \frac{2}{\bar{d}}\right)^2\right]t, \tag{5.23b}$$

where $\bar{d}$ is the average degree of the network. The ballistic term $\hat{V}^2t^2$ in Equation (5.23b) is non-zero when $\bar{d} > 2$, that is, the average degree of $\mathcal{G}_L$ must be strictly greater than two for the network to induce ballistic behaviour in the winding distance of a diffusive particle[7].

5.2.1 Full distribution of displacement

We are not in fact limited to approximating the first two moments of the displacement but can also obtain an analytical approximation to the full distribution. Recall that the distribution of the displacement of a particle whose position evolves according to the CTMC is equivalent to the same distribution as that of a Brownian particle in the limit $\epsilon \to 0$ and $N \to \infty$ such that $\epsilon = 1/N$. Note that $\vec{P}(x,t) \approx h_\epsilon(x,t)\vec{u}_0$, where $h(x,t) = \lim_{\epsilon\to 0}\{h_\epsilon(x,t)\}$ satisfies Equation (5.21) which has solution

$$h(x,t) = \frac{1}{\sqrt{\pi\hat{D}t}}\exp\left(-\frac{(x-\hat{V}\ t)^2}{4\hat{D}t}\right) + \frac{\hat{V}}{2\hat{D}}\exp\left(-\frac{\hat{V}x}{\hat{D}}\right)\operatorname{erfc}\left(\frac{x+\hat{V}t}{2\sqrt{\hat{D}t}}\right), \tag{5.24}$$

[7]We note that if $\bar{d} < 2$ the network is in fact a tree. The lack of cycles therefore implies a finite displacement tree and our theory does not apply.

where erfc$(\cdot)$ is the complimentary error function [155], and $\vec{u}_0$ is given in Equation (5.9). We introduce the function $u(x) = \lim_{N\to\infty}\{[\vec{u}_0]_n / N\}$, where $x = n/N$ and find that

$$u(x) = 2\rho^+(1-x) + 2\rho^- x, \tag{5.25}$$

for $x \in [0,1)$ and $u(1) = 1$. Extending the function $u(x)$ to be periodic on the half line with unit period, $u(x+1) = u(x)$ for all $x \in (0,\infty)$, provides us with a function that accounts for corrections on the microscopic scale to the displacement predicted from the macroscopic equation for $h(x,t)$. Then the full distribution is approximated by $P(x,t) \approx h(x,t)u(x)$. For $\mathcal{G}_{10}$, we simulate 10^6 realisations of a Brownian particle terminating at time $t = 50$. We use these realisations to empirically plot the distribution of displacement (Figure 5.5, red solid curve) and compare with the analytical approximation using the solution $h(x,t)$ in Equation (5.24) and the periodically extended function $u(x)$ in Equation (5.25) (Figure 5.5, black dashed curve). The two curves match well which suggests that the temination time $t = 50$ is sufficiently large for the transport process to have reached its equilibrium behaviour for the network $\mathcal{G}_{10}$. However, in general how does the topology of the network affect the time taken to reach equilibrium?

5.2.2 Timescale for transition to equilibrium

From Equation (5.23) we already have the dominant contributions to the first two moments of displacement for long times. Now consider short times, t, sufficiently short such that the particle has a displacement less than one, or equivalently has not reached the first branching point on the displacement tree. On this timescale, the particle undergoes unbiased Brownian motion on the half line, for which the first two

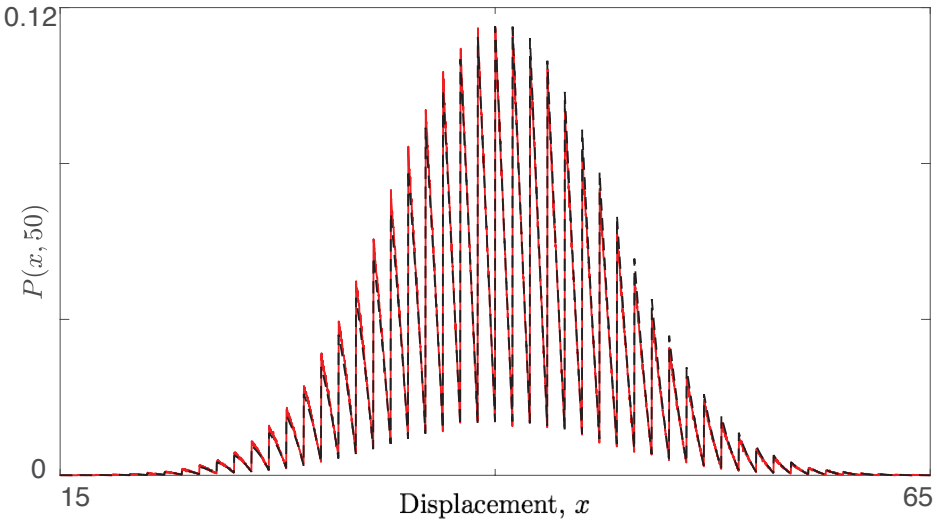

Figure 5.5: The displacement of a particle on $\mathcal{G}_{10}$ estimated using 10^6 realisation of a Brownian particle is shown by the solid red curve. The analytical expression for the displacement of a particle on the network $\mathcal{G}_{10}$ in the long-time limit is shown by the dashed black curve. All realisations of a Brownian motion were numerically integrated using the Euler-Maruyama method with timestep $\Delta t = 10^{-5}$, $D = 1/2$ and $L = 1$.

moments of displacement are

$$\langle x(t) \rangle \sim \frac{2\sqrt{t}}{\sqrt{\pi}}, \qquad \langle x^2(t) \rangle \sim t. \tag{5.26}$$

The dominant terms of the long-time and short-time analytical asymptotics in Equations (5.23) and (5.26), respectively, are plotted in Figure 5.6 (dashed and dot-dashed lines). Equating the dominant contributions to the MSD on both the long and short timescales, $\hat{V}^2 t^2$ and t, respectively, we obtain a prediction of the timescale, t_{sw}, upon which the displacement of a particle transitions from characteristically diffusive to ballistic:

$$t_{\text{sw}} \sim \left(\rho^+ - \rho^-\right)^{-2} = \left(1 - \frac{2}{\bar{d}}\right)^{-2}, \tag{5.27}$$

where $\bar{d} = 2|\mathcal{E}_L|/|\mathcal{V}_L|$ is the average degree of the network. The timescale, t_{sw}, is given by the intersection of the dashed and dot-dashed lines in Figure 5.6(b) (vertical line).

To investigate the predictive capacity of the timescale t_{sw}, we consider the MSD

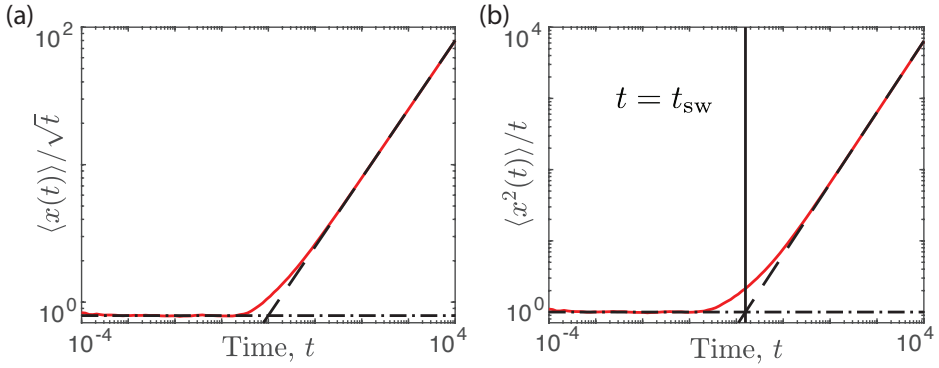

Figure 5.6: (a): The first moment of displacement of a particle on the network $\mathcal{G}_{10}$ estimated from 10^4 realisations of a Brownian particle (solid red curve). Analytical results of the first moment in the short-time (dot-dashed line) and long-time (dashed line) limits. (b): The MSD of a particle on the network $\mathcal{G}_{10}$ estimated from 10^4 realisations of a Brownian particle (solid red curve). Analytical results of the MSD in the short-time (dot-dashed line) and long-time (dashed line) limits. The predictive timescale $t_{\rm sw}$ is identified with the vertical solid line. All simulations of a Brownian motion were numerically integrated using the Euler-Maruyama method with timestep $\Delta t = 10^{-5}$, $D = 1/2$ and $L = 1$.

over an ensemble of randomly generated aperiodic networks. The MSD of a particle on a general network has dominant contribution $\langle x^2(t)\rangle \sim \hat{V}^2 t^2$ for long times. The rescaling $\bar{t} = t/t_{\rm sw}$ allows for the MSD of a particle over an ensemble of topologies to be compared on the same temporal axis, as $\langle x^2(t)\rangle/t \sim \bar{t}$. In Figure 5.7(a) the MSD of a particle over an ensemble of 100 networks is presented. The 100 networks each have 10 vertices and a range of 11 to 110 edges[8]. For each network, the particle starts at the same vertex for all realisations, but that fixed vertex is randomly selected and highlighted in Figure 5.7(c) with a star[9].

On visual inspection of the data in Figure 5.7 we see that the grey curves rarely intersect as they collapse onto the curve $\langle x^2(t)\rangle/t = \bar{t}$. As such, the curves that

[8]The sampling procedure is as follows; select a desired number of edges and vertices; draw two distinct vertices uniformly at random and join them via an edge; repeat the previous step until the required number of edges is reached; check if the network is periodic or disconnected, if so reject and start over, if not take the network as a realisation. This procedure allows for multiple edges but avoids self loops.

[9]The initial vertex is fixed among realisations of the transport process, so that the displacement tree has a fixed root and the effects of the initial conditions on transition times are not averaged out.

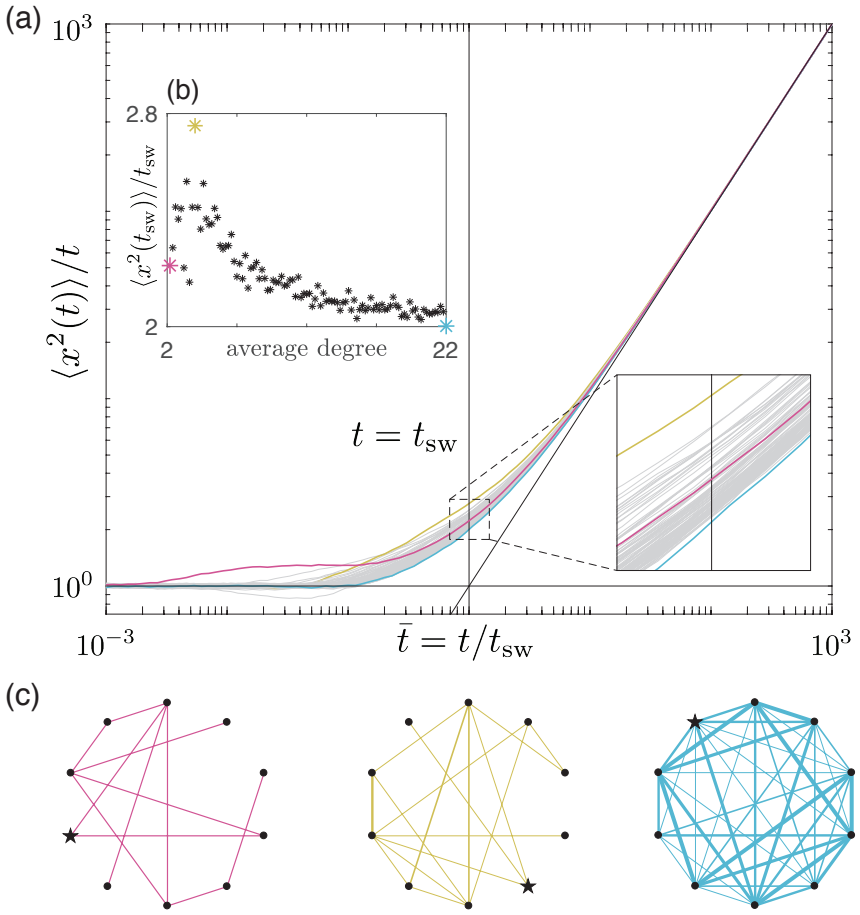

Figure 5.7: (a): The MSD of a particle on 100 randomly generated networks, estimated using 10^4 realisations of a Brownian motion on each network. The inset shows the MSD curves for all 100 networks around the predictive timescale $t = t_{\rm sw}$, which is identified by the vertical line. The short-time and long-time analytical expressions for the MSD are shown in solid black lines. (b): The y intercepts of the inset in (a) are plotted against the average degree of each network. (c): Three networks of note are shown where the width of the edges corresponds to the number of multiple edges between the two adjacent vertices. The initial vertex in each network is represented as a star. All simulations were calculated through numerical integration of a Brownian motion using the Euler-Maruyama method with timestep $\Delta t = 10^{-5}$, $D = 1/2$ and $L = 1$.

intersect the line $t = t_{\rm sw}$ (see Figure 5.7(a), inset) with a lower y intercept will transition to ballistic behaviour before those curves with a greater y intercept. Thus, we plot the y intercept, $\langle x^2(t_{\rm sw})\rangle/t_{\rm sw}$, for all 100 networks against the average degree of the network in Figure 5.7(b). We see a sharper correlation between average degree and the y intercept for networks with a higher average degree. This suggests that

t_{sw} is a good predictor of the crossover time to ballistic motion when the average degree is large (Figure 5.7, the network highlighted in blue). However, for networks with a lower average degree the predictive capacity of t_{sw} is less clear; we highlight networks in magenta[10] and yellow in Figure 5.7 that both have low average degrees yet the values of $\langle x^2(t_{\text{sw}})\rangle/t_{\text{sw}}$ are very different (Figure 5.7(b)). For topologies with a low average degree the timescale to transition from diffusive to ballistic behaviour is highly sensitive to the particular network and, as such, t_{sw} may be less reliable as a predictor of the crossover to ballistic motion.

5.3 Anomalous diffusion on networks

Thus far, the only transport process we have considered is Brownian motion. An alternative modelling framework for particle transport is a position jump process, where the position of a particle is updated instantaneously after random intervals in time. A position jump process can be formally described as a CTRW where the jump distance is sampled from $\lambda(x)$, the jump distribution, and the time between jump events is sampled from $\omega(t)$, the waiting time distribution. For a review of transport properties of these CTRWs see [156]. The freedom to prescribe any jump and waiting time distributions allows a CTRW to describe a broad range of physical processes. Consider a waiting time distribution that for long times has asymptotic power law behaviour, $\omega(t) \sim t^{-(1+\alpha)}$ for some α. If $\lambda(x)$ has zero mean and finite variance then for $\alpha \geq 1$, the position of a particle evolving according to the CTRW on the real line in the long-time limit is equivalent to the position of a Brownian particle and hence has a MSD of $\langle x^2(t)\rangle \propto t$. However, for $0 < \alpha < 1$, $\omega(t)$ is heavy tailed and the mean

[10]The magenta network has an average degree $\bar{d} = 2.2$ however the fixed initial condition is the vertex of degree two highlighted with a star in Figure 5.7(c). The environment local to the initial vertex has a significantly higher average degree than the entire network, which results in a curve that deviates from the short-time behaviour earlier (see the magenta curve in Figure 5.7(a)). The dip in the gradient of the magenta curve occurs later, when the particle has explored the global environment, which has a lower average degree than the local environment.

waiting time between jump events diverges. Such transport processes for large times have a MSD on the real line of $\langle x^2(t)\rangle \propto t^\alpha$, and are known as anomalously diffusive.

Using the displacement tree (Section 5.1), the winding distance of anomalously diffusive transport on networks can be identified with displacement of the same transport process on the half line subject to periodic bias. As before, we consider a multiple scales approach and discretise the half line into intervals, $[k, k+1]$ for integers $k \geq 0$, each of $N+1$ lattice sites separated by a distance $\epsilon = 1/N$. The position of a particle on the lattice evolves according to a CTRW rather than a CTMC because the waiting times for jumps between adjacent sites are no longer exponentially distributed. Similar to Section 5.2 we now select the fractional transition rates[11] to represent the periodic bias felt at the ends of the intervals $[k, k+1]$. Thus, for a particle to exit a lattice site with the index kN to the right with probability ρ^+ we select the transition rates $\mu_{kN\to kN+1} = \rho^+/\epsilon^2$ and $\mu_{kN\to kN-1} = \rho^-/\epsilon^2$, and all other lattice sites n have symmetric transition rates $\mu_{n\to n+1} = \mu_{n\to n-1} = 1/(2\epsilon^2)$.

Let $p_n(t)$ be the probability a particle occupies lattice site n at time t. The temporal evolution of the probability $p_n(t)$ evolves according to the fractional master equation [157], a generalisation of the master equation seen in Section 5.2. We define the operator $\partial^\alpha/\partial t^\alpha$ as the Riemann-Liouville fractional derivative

$$\frac{\partial^\alpha}{\partial t^\alpha}\{y(t)\} = \frac{1}{\Gamma(1-\alpha)}\frac{\partial}{\partial t}\int_0^t \frac{y(t')}{(t-t')^\alpha}\mathrm{d}t'. \tag{5.28}$$

The fractional master equation for the probabilities $p_n(t)$ is

$$\frac{\partial^\alpha p_n}{\partial t^\alpha} = \mu_{(n-1)\to n}p_{n-1} + \mu_{(n+1)\to n}p_{n+1} - \left(\mu_{n\to(n-1)} + \mu_{n\to(n+1)}\right)p_n, \tag{5.29}$$

where $n \geq 0$. As before, the particle is initially at the origin, therefore $p_0(0) = 1$ and

[11] The mean time for a jump to occur on the lattice diverges, as such we do not consider transition rates as we would for a CTMC. Instead we introduce a fractional transition rate [157].

$p_i(0) = 0$ for all $i \geq 1$. To account for the reflective boundary condition at the origin, we set $\mu_{-1\to 0} = \mu_{0\to -1} = 0$ and $\mu_{0\to 1} = 1/\epsilon^2$. Introducing the spatial coordinate $x = \epsilon N$ where $\epsilon \ll 1$, we write $p_n(t) = P_n(x,t)$ so that the probability density for the position of a particle at time t depends on both the fast scale n and the slow scale x. Treating the two variables x and n independently and rewriting Equation (5.29) in terms of $P_n(x,t)$ gives the finite set of equations

$$\begin{aligned}\frac{\partial^\alpha P_i}{\partial t^\alpha}(x,t) = \mu_{\overline{i-1}\to i} P_{\overline{i-1}}(x-\epsilon,t) + \mu_{\overline{i+1}\to i} P_{\overline{i+1}}(x+\epsilon,t) \\ - \left(\mu_{i\to\overline{i+1}} + \mu_{i\to\overline{i-1}}\right) P_i(x,t),\end{aligned} \tag{5.30}$$

for $i \in \{1,\ldots,N\}$ and $x \in [0,\infty)$, where $\overline{i \pm 1} = (i \pm 1 - 1 \bmod N) + 1$. For the periodic interval, as before the transition rates out of all sites are symmetric and equal to $1/(2\epsilon^2)$, other than the rates $\mu_{N\to 1} = \rho^+/(\epsilon^2)$ and $\mu_{N\to N-1} = \rho^-/(\epsilon^2)$. Introducing $\vec{P}(x,t) = [P_1(x,t),\ldots,P_N(x,t)]^T$ and expanding the right-hand side of Equation (5.30) about x, we find

$$\epsilon^2 \frac{\partial^\alpha \vec{P}}{\partial t^\alpha}(x,t) = \mathbf{A}\vec{P} + \epsilon \mathbf{B}\frac{\partial \vec{P}}{\partial x} + \epsilon^2 \mathbf{C}\frac{\partial^2 \vec{P}}{\partial x^2} + \mathcal{O}\left(\epsilon^3\right), \tag{5.31}$$

where the matrices are as given in Equations (5.7). Let $h(x,t)$ denote the macroscopic probability density function for a particle to have a winding distance of x at time t. The analysis proceeds identically to Section 5.2 and we derive the following fractional advection-diffusion PDE

$$\frac{\partial^\alpha h}{\partial t^\alpha}(x,t) + \hat{V}\frac{\partial h}{\partial x} = \hat{D}\frac{\partial^2 h}{\partial x^2}, \tag{5.32}$$

for $x \in [0,\infty)$, with boundary conditions $\hat{D}h_x(0,t) + \hat{V}h(0,t) = \lim_{x\to\infty}\{\hat{D}h_x(x,t) + \hat{V}h(x,t)\} = 0$ and initial conditions $h(x,0) = \delta(x)$. The transport coefficients $\hat{V}$ and $\hat{D}$ are given in Equations (5.22). This macroscopic fractional PDE is valid for large

times and the first two moments of displacement are

$$\langle x(t)\rangle \sim \frac{\hat{V}t^{\alpha}}{\Gamma\left(1+\alpha\right)} = \frac{1}{\Gamma(1+\alpha)}\left(1-\frac{2}{\bar{d}}\right)t^{\alpha}, \tag{5.33a}$$

$$\begin{aligned}\langle x^2(t)\rangle &\sim \frac{2\hat{V}^2t^{2\alpha}}{\Gamma\left(1+2\alpha\right)} + \frac{2\hat{D}t^{\alpha}}{\Gamma\left(1+\alpha\right)} \\ &= \frac{2}{\Gamma\left(1+2\alpha\right)}\left(1-\frac{2}{\bar{d}}\right)^2 t^{2\alpha} + \left[1-\frac{1}{3}\left(1-\frac{2}{\bar{d}}\right)^2\right]\frac{t^{\alpha}}{\Gamma\left(1+\alpha\right)}.\end{aligned} \tag{5.33b}$$

Equations (5.33) demonstrates that anomalous diffusion on a network can induce a variety of transitional behaviours. Consider the analytical expression in the long-time limit for the MSD in Equation (5.33b). At large times the dominant contribution is proportional to $t^{2\alpha}$ when $\bar{d} > 2$. If $0 < \alpha < 1/2$, the winding distance of the particle in the long-time limit remains sub-diffusive but with an increased exponent of 2α. If $\alpha = 1/2$, the winding distance becomes classically diffusive. For $1/2 < \alpha < 1$ the winding distance transitions to sub-ballistic or super-diffusive. Generalising to anomalously diffusive transport processes demonstrates that in order to capture the effect of network topology on the winding distance of a particle one must also incorporate details of the transport process itself.

As in Section 5.2 we shall compare the first two moments of displacement on both long and short timescales. On short timescales, where the particle has not left the first edge, the displacement of a particle is equivalent to the displacement of a particle whose position is described by a fractional diffusion equation on the half line. The first two moments of displacement [158] on short timescales are

$$\langle x(t)\rangle \sim \frac{t^{\alpha/2}}{\Gamma\left(1+\alpha/2\right)}, \qquad \langle x^2(t)\rangle \sim \frac{t^{\alpha}}{\Gamma\left(1+\alpha\right)}. \tag{5.34}$$

We compare the dominant short-time and long-time behaviours for the MSD to esti-

mate the transition timescale

$$t_{\text{sw}} = \left[\frac{\Gamma\left(1+2\alpha\right)}{2\Gamma\left(1+\alpha\right)}\left(1-\frac{2}{\bar{d}}\right)^{-2}\right]^{1/\alpha}, \tag{5.35}$$

where for $\alpha = 1$ we recover Equation (5.27).

Consider the limit where $\alpha \to 0$, which corresponds to a transport process where the waiting time distribution between jump events becomes increasingly heavy tailed. Expanding Equation (5.35) for small α yields

$$t_{\text{sw}} \sim \left(1+\frac{\pi^2}{4}\alpha\right)\exp\left[-\left(\gamma+\frac{\log(2)}{\alpha}+\frac{2\log\left(1-2/\bar{d}\right)}{\alpha}\right)\right], \tag{5.36}$$

where γ is the Euler-Mascheroni constant. In the limit $\alpha \to 0$ there are two cases for the limiting behaviour of the timescale t_{sw}. If the average degree of the network satisfies $\bar{d} < 2\left(2+\sqrt{2}\right)$ then $t_{\text{sw}} \to \infty$, and if $\bar{d} \geq 2\left(2+\sqrt{2}\right)$ then $t_{\text{sw}} \to 0$. To explain this, in Figure 5.8 we estimate the rescaled MSD, $m(t) = \Gamma(1+\alpha)\langle x^2(t)\rangle/t^\alpha$, from simulations of the CTRW on the networks $\mathcal{G}_3$ and $\mathcal{G}_{10}$ over an ensemble of values for α. The waiting times are Pareto distributed, $w(t) = \alpha t_m^\alpha/t^{\alpha+1}$ for $t \geq t_m$, and the jump lengths are normally distributed with zero mean and variance σ^2. We choose the minimum value of the waiting time, $t_m = \left(\sigma^2/\Gamma\left(1-\alpha\right)\right)^{1/\alpha}$, to ensure the simulations of the CTRW agree with the multiscale analysis[12]. For $\mathcal{G}_3$ the average degree is less than $2(2+\sqrt{2})$ and so $t_{\text{sw}} \to \infty$ as $\alpha \to 0$ (see intersection points with $m(t) = 1$ in Figure 5.8(a)). On inspection we see that the time to converge to equilibrium behaviour increases as expected when $\alpha \to 0$. In contrast, the average degree of $\mathcal{G}_{10}$ is greater than $2(2+\sqrt{2})$, meaning $t_{\text{sw}} \to 0$ as $\alpha \to 0$ (see intersection points with

[12]The Laplace transform of $w(t)$ for small values of s is given by $\tilde{w}(s) \approx 1 - \Gamma(1-\alpha)t_m^\alpha s^\alpha$, thus the cofficient of s^α provides a timescale, τ, upon which the Pareto distribution decays, where $\tau^\alpha = \Gamma(1-\alpha)t_m^\alpha$. Following the derivation of the fractional diffusion equation seen in [156] the fractional diffusion coefficient is equal to $\sigma^2/\left(2\tau^\alpha\right)$. The hopping rates in Equation (5.29) are selected such that as $\epsilon \to 0$, the resulting fractional diffusion coefficient is equal to $1/2$. Thus, we select $\tau^\alpha = \sigma^2$, or equivalently $t_m = \left(\sigma^2/\Gamma\left(1-\alpha\right)\right)^{1/\alpha}$.

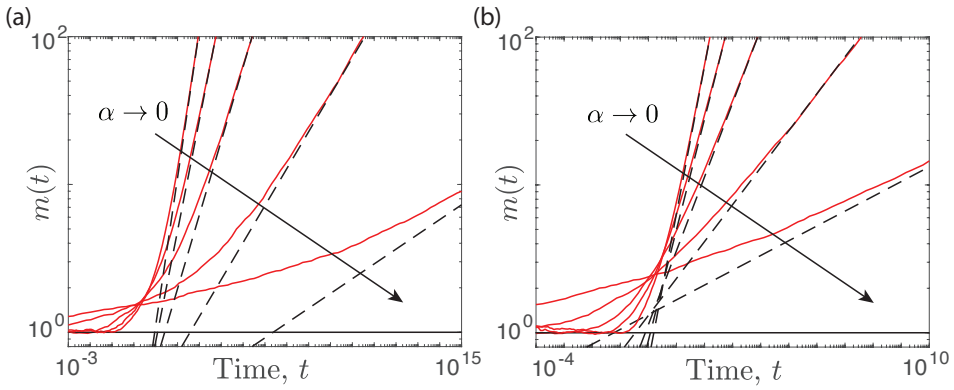

Figure 5.8: (a): The rescaled MSD of a particle on the network $\mathcal{G}_3$ estimated from 10^4 realisations of the CTRW (solid red curves) for an ensemble of α values. Analytical results of the rescaled MSD in the short-time (solid black line) and long-time (dashed black lines) limits. (b): The rescaled MSD of a particle on the network $\mathcal{G}_{10}$ estimated from 10^4 realisations of the CTRW (solid red curves) for an ensemble of α values. Analytical results of the rescaled MSD in the short-time (solid black line) and long-time (dashed black lines) limits. The selected values of α are $\{0.1, 0.25, 0.50, 0.75, 1.0\}$. For $\alpha = 1.0$ the MSD was calculated using the Brownian motion simulations from Figure 5.1 and Figure 5.6. For the other values of α, realisations of the CTRW were simulated with a normally distributed jump length distribution with zero mean and variance σ^2, and a Pareto waiting time distribution with $t_m = (\sigma^2/\Gamma(1-\alpha))^{1/\alpha}$. For the values $\alpha = \{0.1, 0.25, 0.50, 0.75\}$ the standard deviations used are $\sigma = \{10^{-2}, 10^{-2}, 10^{-2}, 10^{-2.75}\}$, respectively. The edges are all of unit length.

$m(t) = 1$ in Figure 5.8(b)). But if we inspect the curve in Figure 5.8(b) corresponding to $\alpha = 0.1$, we see it has transitioned away from the short-time behaviour significantly for times as small as $t = 10^{-4}$ and is only just converging to equilibrium behaviour at $t = 10^{10}$, a difference of 14 orders of magnitude. Thus, for small values of α, it is difficult to consider a single value (such as t_{sw}) that represents the time taken to transition to equilibrium behaviour as the change occurs gradually over a large window of time. That said, for values of α closer to one the transition occurs more rapidly, and t_{sw} provides a good predictive timescale.

5.4 Summary

In this work, we have investigated the influence of network topology on the evolution of the displacement of a particle whose position evolves according to either a diffusive or an anomalously diffusive transport process. In Section 5.1 we define our notion of displacement of a particle as the winding distance, which is a measure of how far a particle has travelled as it winds around the network. To investigate the evolution of the winding distance we introduced a topological structure we term the displacement tree and noted that the winding distance of a particle is equivalent to the displacement of a particle along the tree. Furthermore, in the long-time limit, a link between the displacement of a particle on the tree and the displacement of a particle on the half line with periodic bias was highlighted. The simpler transport process on the half line has a periodic bias with strength ρ_{∞}^{+}, a quantity that can be calculated in terms of the average degree of the network.

In Section 5.2 a multiple scales approach from [152] was used to derive an advection-diffusion PDE for the displacement of a particle whose position evolves according to a Brownian motion on the half line with periodic bias. The advective and diffusive transport coefficients are calculated in terms of the periodic bias ρ_{∞}^{+}. From these coefficients a topological condition was derived for whether the long-time behaviour of the winding distance switches to ballistic motion or remains diffusive. By comparing the MSD for the short-time and long-time limits, a prediction of the timescale upon which a network induces the qualitative switch from diffusive to ballistic behaviour was obtained. For an ensemble of 100 randomly generated networks we found that the predictive timescale performs better for networks with a higher average degree.

Finally, in Section 5.3, we discussed an extension to a class of anomalously diffusive transport processes using the CTRW framework. Through the use of the fractional master equation we derived a time fractional advection-diffusion PDE for the evolu-

tion of the displacement of a particle on the half line with periodic bias. Our results showed that the characteristic nature of the long-time behaviour depends upon the transport process itself. We found that, depending on the value of the exponent α, the displacement of a particle in the equilibrium limit can remain sub-diffusive, become diffusive, or become super-diffusive. Similarly to Section 5.2 we derived a predictive timescale upon which these transitions occur and explored its validity as a function of the parameter α, the exponent in the heavy-tailed waiting time distribution of the CTRW.

This work introduced the winding distance, a new measure of displacement for particles on networked topologies. Using the winding distance to investigate both diffusive and anomalously diffusive transport processes has highlighted that both the topology of the network and the nature of the transport process itself play critical roles in the evolution of particle displacement. Active transport through networked environments is a critical feature of many biological systems, such as the cytoplasmic streaming seen within *Drosophilia* oocytes [159, 160], the transport of bronchial mucus [161], and the transport of a broad range of biomolecules along microtubular networks [162, 163]. Explicitly incorporating network topology within these biological transport systems requires the theoretical study of models for stochastic transport in networked environments [17, 164]. Therefore, future work will extend our investigation of the winding distance to transport processes with a directional bias along each of the edges in a network.

5.5 Appendices

In this section we detail the numerical methods used in this chapter, and discuss how the results can be extended to periodic networks.

5.5.1 Simulating the transport processes

Here we present the algorithm used to compute realisations of a Brownian particle on a network $\mathcal{G} = \{\mathcal{V}, \mathcal{E}\}$, using the Euler-Maruyama method.

1: Assign orientations to each edge in the network, select an initial vertex for the particle, set $t = 0$, the termination time T and the time step Δt.

2: Sample an adjacent edge, e, to the initial vertex uniformly at random. Let $X(0) = 0$ or $X(0) = L_e$ depending on the orientation of edge e.

3: **while** $t < T$ **do**

4: **if** $t = 0$ **then** update the position as follows:

$$X\left(t + \Delta t\right) = X(t) + \sqrt{2D\Delta t}\ |\xi|, \tag{5.37}$$

where $\xi \sim \mathcal{N}(0, 1)$.

5: **else** update the position as follows:

$$X\left(t + \Delta t\right) = X(t) + \sqrt{2D\Delta t}\ \xi, \tag{5.38}$$

where $\xi \sim \mathcal{N}(0, 1)$.

6: **end if**

7: **if** $X(t + \Delta t) < 0$ **then** sample a new edge e^*, uniformly at random from the adjacent edges to edge e (not including e itself) at the end with position 0.

8: **if** the particle enters the new edge e^* at the end with position 0 **then** update the new position as

$$X(t + \Delta t) \leftarrow -X(t + \Delta t), \tag{5.39}$$

9: **else if** the particle enters the new edge e^* at the end with position L_{e^*}

then update the new position as

$$X(t+\Delta t) \leftarrow L_{e^*} + X(t+\Delta t), \tag{5.40}$$

end if

Update $e = e^*$.

else if $X(t+\Delta t) > L_e$ **then** sample a new edge e^*, uniformly at random from the adjacent edges to edge e (not including e itself) at the end with position L_e.

if the particle enters the new edge e^* at the end with position 0 **then** update the new position as

$$X(t+\Delta t) \leftarrow X(t+\Delta t) - L_e, \tag{5.41}$$

else if the particle enters the new edge e^* at the end with position L_{e^*} **then** update the new position as

$$X(t+\Delta t) \leftarrow L_{e^*} + L_e - X(t+\Delta t), \tag{5.42}$$

end if

Update $e = e^*$.

end if

Update the time $t = t + \Delta t$.

end while

For the CTRWs seen in Section 5.3 we select the jump distribution to be normal with zero mean and standard deviation σ. The above algorithm is easily adapted to simulate the CTRW on a network. Instead of fixed time steps, Δt, update the time t with random waiting times from the Pareto distribution, and replace $\sqrt{2D\Delta t}$ in Equations (5.37) and (5.38) with σ. The CTRW simulations must agree with the

multiscale analysis in Section 5.3, on both long and short timescales. In particular, on timescales sufficiently short that a particle has not left the initial edge. The multiscale analysis discretises the unit interval into $N+1$ lattice sites. As $N \to \infty$ the width of each site, $\epsilon = 1/N$, tends to zero, and a particle will undergo a large number of jumps before traversing an entire interval. Therefore, for the CTRW to agree with the multiscale analysis on short timescales, we take $\sigma^2 \ll 1$, such that many jumps must occur before a particle traverses an edge.

5.5.2 Periodic displacement trees

Recall the sequence of biased probabilities $\{\rho_1^+, \rho_2^+, \ldots\}$ in Section 5.1. The effective bias for a particle with displacement kL is given by

$$\rho_k^+ = \sum_{\nu \in \mathcal{V}_L} \frac{d_\nu - 1}{d_\nu} \times p_k(\nu), \tag{5.43}$$

where $p_k(\nu)$ is the probability of being at vertex ν given a displacement of kL. We previously assumed that the network produced an aperiodic displacement tree to guarantee the sequence converged to a unique value ρ_∞^+ given in Equation (5.2). However, if instead the displacement tree is periodic then the sequence of probabilities $p_k(\nu)$ converges to a finite periodic sequence $\{p_{\infty,1}(\nu), \ldots, p_{\infty,m}(\nu)\}$ where m is the period. Weighting these probabilities by $(d_\nu - 1)/d_\nu$ we calculate the effective probabilities to move to the right along the displacement tree as

$$\rho_{\infty,j}^+ = \sum_{\nu \in \mathcal{V}_L} \frac{d_\nu - 1}{d_\nu} \times p_{\infty,j}(\nu), \tag{5.44}$$

for $j \in \{1, \ldots, m\}$. We are now able to use the multiple scales approach of Section 5.2 for the case of periodic displacement trees. The periodic unit interval has $mN+1$ lattice sites, and there are internal lattice sites that have asymmetric rates. The analysis proceeds as before, other than the size and entries of the matrices in Equations (5.7).

Chapter 6

Discussion and Future Work

Collectively, the research in this thesis contributes to the development of mathematical frameworks designed to investigate stochastic transport processes in confined networked environments. In this chapter we summarise and discuss the main results from the thesis, and present avenues for future research.

6.1 Discussion

Each chapter in this thesis presents a study of the functional relationship between network topology and a fundamental transport statistic: equilibration times, cover times, and particle displacement. Global network heuristics, such as spectral properties of graph Laplacians or properties of degree distributions, that accurately predict the behaviour of the transport statistics are identified. A recurring theme across the thesis is topological optimisation. The uncovered relationships between transport statistics and the network topology are used to investigate the structure of optimal networks, design optimal strategies and design efficient algorithms for optimal network construction. Brief summaries of the main results from each chapter are presented below.

6.1.1 Chapter 2

This chapter concerns the equilibration of a population of diffusing particles within a heterogeneous environment. The heterogeneity arises as particles undergo volume exclusion in only certain regions of the environment. A simple CTMC is introduced, where particles diffuse between two reservoirs connected by a one-dimensional lattice, which is referred to as the narrow channel. The lattice sites in the narrow channel can support at most one particle at a time, whereas the reservoirs can support many particles whose motility is unhindered by the effects of volume exclusion. Coarse-grained models of the CTMC are derived that accurately predict the equilibration time of a population of particles. The analysis presented in this chapter quantifies analytically how the equilibration time is affected by the model parameters: population size; length of the narrow channel; and the distinct jump rates of particles in the channel and the reservoirs. The model was generalised to allow for partial exclusion in the narrow channel. This generalisation is applicable when the size of the particles is smaller, but comparable to, the width of the narrow channel.

6.1.2 Chapter 3

In Chapter 3, the framework from Chapter 2 is extended to general networked topologies. The nodes and edges of the networked environments correspond to reservoirs and narrow channels, respectively. The equilibration time for a population of particles diffusing in a network is approximated by the reciprocal of the spectral gap of a drift matrix. The remarkable low dimensionality of this drift matrix allows for a numerical study of topological optimisation for reservoirs embedded in three-dimensional Euclidean space. Important topological properties of optimal networks are uncovered, and efficient algorithms to construct optimal networks are designed. Collectively, the results in Chapters 2 and 3 represent a fundamental step towards understanding

the roles of both geometry and crowding in the transport of particles in complex environments.

6.1.3 Chapter 4

In Chapter 4, networked search processes are considered where multiple parallel searchers compete for space. The optimal density of searchers, quantified by the average per searcher parallel cover time, is explored both numerically and analytically as a function of network topology. The relationship between optimal density and the spectral gap of the single searcher transition matrix is used to develop optimal strategies for search processes with interacting searchers. The topological dependence of the optimal density is remarkably different for equilibrium and non-equilibrium search processes. Therefore, when optimising random search processes the transport process itself plays a crucial role. This work represents a key step in developing generic algorithms for topological optimisation for both equilibrium and non-equilibrium search processes. Such optimisation is important for process allocation and flow transport problems across physical and biological networked systems

6.1.4 Chapter 5

In Chapter 5, the winding distance of a particle is introduced as a new definition of displacement of a particle moving along the edges of a network. This measure of displacement incorporates more information about the actual path taken by the particle, as it includes the distance accumulated as a particle winds around edges of the network. The main result from this work is the discovery that the MSD of a diffusive particle can become ballistic for large times. The condition for whether this change occurs is a simple function of the topology of the network. Additionally a timescale on which this transition occurs is obtained also as a function of network topology. Generalising to a broader class of anomalously diffusive transport processes,

we found that the long-time behaviour of the MSD is a function of both topology and the transport process itself.

6.2 Future Work

In this section we detail some of the extensions for future work that would enhance the applicability and versatility of the framework introduced in Chapters 2 and 3.

6.2.1 Active transport in heterogeneous crowded environments

In Chapters 2 and 3 we studied the diffusion of a population of particles in a network of reservoirs and narrow channels where the jump rates of particles within the narrow channels were symmetric. However, there are many examples of active biological processes where agent-agent crowding effects are non-negligible. Examples include actin-myosin transport along microtubules within the cytoskeleton [131, 165, 166], and the hydrodynamic transport of proteins through cylindrical pores [167, 168]. The reach and impact of the work presented in Chapters 2 and 3 would be greatly improved if we could generalise our results to incorporate active transport. In this section we briefly introduce the FMM with asymmetric jump rates for the particles in the narrow channel, and derive the RMM, analogously to Chapter 2, in both the low- and high-density regimes. We conclude by discussing the scope for future work.

As in Chapter 2 we consider a domain consisting of two identical reservoirs connected by a one-dimensional lattice with K lattice sites, which we refer to as the narrow channel. A total of N particles populate this domain and their configuration at time t is described by the state vector $\vec{S}(t) = (L(t), N_1(t), \ldots, N_K(t), R(t))$. The variables $L(t)$, $R(t)$ and $N_i(t)$ denote the number of particles in the left reservoir, right reservoir, and i-th lattice site at time t, respectively. A particle in a narrow channel

lattice site attempts a jump to the adjacent lattice site to the right at rate α_R and the adjacent lattice site to the left at rate α_L. A particle attempts a jump from either reservoir into the narrow channel at rate γ. Formally, the state vector $\vec{S}(t)$ evolves according to the following CTMC. A particle in the narrow channel at lattice site i jumps to adjacent lattice site $i+1$ at rate $\alpha_R N_i(t)\,(1 - N_{i+1}(t))$ for $1 \leq i \leq K-1$. If there is no particle at lattice site i at time t, $N_i(t) = 0$, or the adjacent lattice site is occupied, $N_{i+1}(t) = 1$, the transition rate, $\alpha_R N_i(t)\,(1 - N_{i+1}(t))$, is zero. Due to the absence of volume exclusion in the reservoirs, a particle jumps from lattice site K into the right reservoir at rate $\alpha_R N_K(t)$. Similarly, a particle jumps from lattice site i to adjacent lattice site $i-1$ at rate $\alpha_L N_i(t)\,(1 - N_{i-1}(t))$ for $2 \leq i \leq K$, and a particle jumps from lattice site one into the left reservoir at rate $\alpha_L N_1(t)$. One of the particles in the left reservoir jumps into lattice site one at rate $\gamma L(t)\,(1 - N_1(t))$, which is non-zero only if lattice site one is vacant. Finally, $\gamma R(t)\,(1 - N_K(t))$ is the rate at which a particle in the right reservoir jumps into lattice site K. This CTRW is the FMM with asymmetric narrow channel jump rates. A transition matrix can be constructed from the transition rates as seen in Chapter 2. Note that the FMM no longer has an equilibrium distribution due to the asymmetric rates in the narrow channel, but it does, however, have a stationary distribution. The reciprocal of the spectral gap of the transition matrix is the canonical measurement of time taken for the FMM to reach its stationary distribution. We refer to this measurement as the convergence time. The convergence time for the FMM is shown in Figure 6.1 for a variety of different rates α_L and α_R whilst conserving their sum. For a fixed value of the reservoir jump rate, γ, increasing the asymmetry in the narrow channel rates decreases the convergence time (see Figure 6.1, arrow).

6.2.1.1 A reduced Markov model: the low-density regime

In the low-density regime we assume that the lattice sites in the narrow channel have low occupancy probability and as such the effects of volume exclusion are negligible. As in Chapter 2 the RMM is derived by considering the particle switching time, the time taken for a particle in one reservoir to enter the narrow channel and subsequently enter the reservoir at the opposite end of the narrow channel. Suppose the left reservoir is occupied by n_L particles, let $T^{L\to R}_{\text{switch}}(n_L)$ be the switching time for any of the particles in the left reservoir to successfully enter the right reservoir. The switching time is given by

$$T^{L\to R}_{\text{switch}}(n_L) = \sum_{j=1}^{G(\alpha_L,\alpha_R)} T^{j}_{\text{enter}} + T^{j}_{\text{absorb}}, \tag{6.1}$$

where $G(\alpha_L, \alpha_R)$ is a geometric random variable for which the success probability is the probability that a particle in lattice site one is absorbed into the right reservoir before the left reservoir. The variable T^{j}_{enter} denotes the time taken for a particle in the left reservoir to enter the first lattice site on the narrow channel, and T^{j}_{absorb} denotes the time taken for a particle in the first lattice site on the narrow channel to be absorbed by either reservoir. Following the derivation in Chapter 2, the transition rates for the RMM are given by $k^{L\to R}_{\text{LD}}(n_L) = \langle T^{L\to R}_{\text{switch}}(n_L)\rangle^{-1}$, where

$$\langle T^{L\to R}_{\text{switch}}(n_L)\rangle = \langle G(\alpha_L,\alpha_R)\rangle \left(\langle T_{\text{enter}}\rangle + \langle T_{\text{absorb}}\rangle\right). \tag{6.2}$$

Note that $\langle T_{\text{enter}}\rangle = (\gamma n_L)^{-1}$, as the time to enter the narrow channel is exponentially distributed. Define q_i to be the probability that a particle initially at lattice site i is eventually absorbed into the right reservoir. The success probability for the geometric random variable $G(\alpha_L, \alpha_R)$ is given by q_1. The recurrence relation for the probabilities

q_i is

$$q_i = \frac{\alpha_R}{\alpha_R + \alpha_L} q_{i+1} + \frac{\alpha_L}{\alpha_R + \alpha_L} q_{i-1}, \tag{6.3}$$

for $1 \leq i \leq K$ with boundary conditions $q_0 = 0$ and $q_{K+1} = 1$. This is a well-posed second order recurrence relation with solution

$$q_i = \frac{1 - \left(\frac{\alpha_L}{\alpha_R}\right)^i}{1 - \left(\frac{\alpha_L}{\alpha_R}\right)^{K+1}}, \tag{6.4}$$

from which we calculate $\langle G(\alpha_L, \alpha_R, K) \rangle = q_1^{-1}$. The remaining first moment in Equation (6.2) is $\langle T_{\text{absorb}} \rangle$. Let E_i be the expected time to absorption at either the left or the right reservoir given that the particle is initially at lattice site i. The variables E_i obey the following recurrence relation

$$E_i = \frac{\alpha_R}{\alpha_R + \alpha_L} E_{i+1} + \frac{\alpha_L}{\alpha_R + \alpha_L} E_{i-1} + \frac{1}{\alpha_L + \alpha_R}, \tag{6.5}$$

for $1 \leq i \leq K$, with boundary conditions $E_0 = E_{K+1} = 0$. Equation (6.5) has the solution

$$E_i = \frac{K+1}{\alpha_R - \alpha_L} \left(\frac{1 - \left(\frac{\alpha_L}{\alpha_R}\right)^i}{1 - \left(\frac{\alpha_L}{\alpha_R}\right)^{K+1}} \right) - \frac{i}{\alpha_R - \alpha_L}, \tag{6.6}$$

from which we calculate $\langle T_{\text{absorb}} \rangle = E_1$. Substituting the expression for the first moments into Equation (6.2) we calculate the transition rates for the RMM. The transition rate for a particle to switch from the left to the right reservoir in the RMM is

$$k_{\text{LD}}^{L \to R}(n_L) = \left[\frac{1 - \left(\frac{\alpha_L}{\alpha_R}\right)^{K+1}}{\gamma n_L \left(1 - \frac{\alpha_L}{\alpha_R}\right)} + \frac{1}{\alpha_R - \alpha_L} \left(K + 1 - \frac{1 - \left(\frac{\alpha_L}{\alpha_R}\right)^{K+1}}{1 - \frac{\alpha_L}{\alpha_R}} \right) \right]^{-1}. \tag{6.7}$$

Similarly, we write down an expression for $k_{\mathrm{LD}}^{R\to L}(n_R)$, the transition rate for a particle to jump from the right to the left reservoir, as

$$k_{\mathrm{LD}}^{R\to L}(n_R) = \left[\frac{1-\left(\frac{\alpha_R}{\alpha_L}\right)^{K+1}}{\gamma n_R\left(1-\frac{\alpha_R}{\alpha_L}\right)} + \frac{1}{\alpha_L-\alpha_R}\left(K+1-\frac{1-\left(\frac{\alpha_R}{\alpha_L}\right)^{K+1}}{1-\frac{\alpha_R}{\alpha_L}}\right)\right]^{-1}. \tag{6.8}$$

The state vectors of the RMM are (n_L, n_R) for non-negative integers n_L and n_R such that $n_L + n_R = N$. The state (n_L, n_R) transitions to the state $(n_L - 1, n_R + 1)$ if one of the n_L particles in the left reservoir switches to the right reservoir. This transition occurs at rate $k_{\mathrm{LD}}^{L\to R}(n_L)$ given in Equation (6.7). Similarly, a transition from state (n_L, n_R) to state $(n_L + 1, n_R - 1)$ occurs at rate $k_{\mathrm{LD}}^{R\to L}(n_R)$ given in Equation (6.8). The RMM for active transport in the low-density regime has a transition matrix Q^{LD}, from which the convergence time is calculated as the reciprocal of its spectral gap. The convergence time from the RMM accurately predicts the convergence time for the FMM for small values of the reservoir jump rate γ (see Figure 6.1, dashed curves).

6.2.1.2 A reduced Markov model: the high-density regime

We now turn our attention to the high-density regime where the occupancy probability of each narrow channel lattice site is close to one. Therefore the RMM in the high-density regime is defined on the state vectors (n_L, n_R) for non-negative integers n_L and n_R such that $n_L + n_R = N_{\mathrm{HD}}$, where $N_{\mathrm{HD}} = N - K$. The transition rates between states are calculated via the vacancy switching time as seen in Section 2.3 of Chapter 2. Recall that the time taken for a particle to switch from the left to the right reservoir is equivalent to the time taken for a vacancy to cross the narrow channel in the opposite direction. For the vacancy dynamics in the narrow channel the asymmetry in the transition rates is reversed, i.e. a vacancy jumps to the left at a rate α_R and to the right at a rate α_L. The time taken for a vacancy to switch from

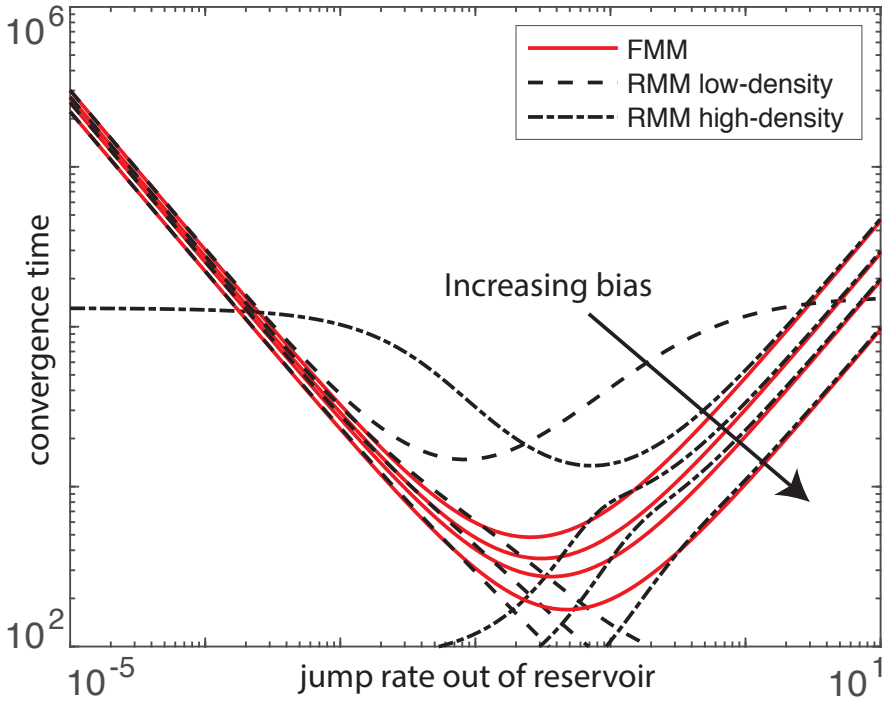

Figure 6.1: The convergence time of the FMM (solid curves), the convergence time of the RMM in the low-density regime (dashed curves), and the convergence time of the RMM in the high-density regime (dot-dashed curves). The parameters are $N = 100$, $K = 5$, $\alpha_R = \{1, 1.125, 1.175, 1.25\}$ and $\alpha_L = \{1, 0.875, 0.825, 0.75\}$.

the right to the left reservoir, $T^{R\to L}_{v,\text{switch}}(n_R)$, is given by

$$T^{R\to L}_{v,\text{switch}}(n_R) = \sum_{j=1}^{G_v(\alpha_L,\alpha_R)} T^j_{v,\text{enter}} + T^j_{v,\text{absorb}}, \tag{6.9}$$

where $G_v(\alpha_L, \alpha_R)$ is a geometric random variable, where the success probability is the probability that a vacancy initially at lattice site $K-1$ hits lattice site 1 before lattice site K. The variable $T^j_{v,\text{enter}}$ is the time taken for a vacancy to enter from the right reservoir and occupy site $K-1$, and subsequently $T^j_{v,\text{absorb}}$ is the time taken for a vacancy initially at lattice site $K-1$ to be absorbed at either lattice site 1 or lattice site K. In the RMM, the state (n_L, n_R) transitions to state $(n_L - 1, n_R + 1)$ at rate $k^{L\to R}_{\text{HD}}(n_R) = \langle T^{R\to L}_{v,\text{switch}}(n_R)\rangle^{-1}$, where the first moment of the switching time is given

by

$$\langle T^{R\to L}_{v,\text{switch}}(n_R)\rangle = \langle G_v(\alpha_L,\alpha_R)\rangle\left(\langle T_{v,\text{enter}}\rangle + \langle T_{v,\text{absorb}}\rangle\right). \tag{6.10}$$

The first moments of the random variables on the right-hand side of Equation (6.10) can be calculated analogously to Section 6.2.1.1. The transition rate $k^{L\to R}_{\text{HD}}(n_R)$ is given by

$$k^{L\to R}_{\text{HD}}(n_R) = (\alpha_R-\alpha_L)\left[\frac{\gamma(n_R+1)+\alpha_R}{\alpha_R}\left(\frac{1-\left(\frac{\alpha_L}{\alpha_R}\right)^{K-1}}{1-\frac{\alpha_L}{\alpha_R}}\right)+K-1\right]^{-1}. \tag{6.11}$$

A transition from state (n_L,n_R) to (n_L+1,n_R-1) occurs at rate $k^{R\to L}_{\text{HD}}(n_L)$ which, by symmetry, is given by

$$k^{R\to L}_{\text{HD}}(n_L) = (\alpha_L-\alpha_R)\left[\frac{\gamma(n_L+1)+\alpha_L}{\alpha_L}\left(\frac{1-\left(\frac{\alpha_R}{\alpha_L}\right)^{K-1}}{1-\frac{\alpha_R}{\alpha_L}}\right)+K-1\right]^{-1}. \tag{6.12}$$

The RMM in the high-density regime has a transition matrix Q^{HD}, from which the convergence time is calculated as the reciprocal of the spectral gap. The convergence time from the RMM accurately predicts the convergence time for the FMM for large values of the reservoir jump rate γ (see Figure 6.1, dot-dashed curves).

6.2.1.3 Future Work

To study active transport with macromolecular crowding in heterogeneous environments, the next step is to extend the results presented in this section to general networked topologies. Extending the framework will allow us to explore optimal networks for active transport processes, and investigate whether nonequilibrium transport changes the topological features of optimal networks as we saw for search processes in Chapter 4.

6.2.2 Optimal frontiers for heterogeneous reservoirs

In Chapter 3 networks that minimised the equilibration time of diffusing particles subject to a restriction in the total edge length were considered. By varying the restriction over the entire range of total edge lengths a frontier of optimal networks emerged. The topological properties of networks that lie on this frontier were explored via a weighted degree distribution. However, all numerical investigations in Chapter 3 were performed under the assumption that every reservoir in the configuration had the same reservoir jump rate. This assumption was made to ensure the topological features of optimal networks could be extracted without the influence of heterogeneity in the reservoir jump rates. However, the inclusion of heterogeneity in the reservoir jump rates has surprising consequences on the optimal frontier.

Consider a configuration, $\mathcal{X}$, of 50 reservoirs with position vectors sampled uniformly in the unit sphere. For a vector $\vec{\gamma}$ of distinct reservoir jump rates, analogously to Section 3.3.2, the equilibration factors are calculated via the spectral gap of the rescaled drift matrix, $\tilde{F}^{\mathrm{HD}}$, which has entries

$$\tilde{F}^{\mathrm{HD}}_{i,j} = \mathcal{A}_{i,j}\frac{\gamma_j}{k_{i,j}}, \tag{6.13}$$

for $i \neq j$, and $\tilde{F}^{\mathrm{HD}}_{i,i} = -\sum_{j\neq i}\tilde{F}^{\mathrm{HD}}_{j,i}$. Note that $\mathcal{A}_{i,j}$ are the entries of the adjacency matrix of the network, and $k_{i,j}$ is the Euclidean distance between two distinct reservoirs i and j. Note that the reservoir jump rates appear in the rescaled drift matrix in Equation (6.13), as they can no longer be scaled out as in Section 3.3.2. Let $\vec{\gamma}$ be a vector of independent and uniformly distributed reservoir jump rates. To make progress we introduce the vector $\vec{\Gamma}(\phi)$, to interpolate between a vector of homogeneous jump rates and the vector of heterogeneous jump rates $\vec{\gamma}$ whilst maintaining a

constant harmonic mean[1]. The vector $\vec{\Gamma}(\phi)$ is defined as

$$[\vec{\Gamma}(\phi)]_i = \left[\frac{1-\phi}{h(\vec{\gamma})} + \frac{\phi}{\gamma_i}\right]^{-1}, \tag{6.14}$$

for $1 \leq i \leq |\mathcal{V}|$. Note that $\vec{\Gamma}(0) = (h(\vec{\gamma}), \ldots, h(\vec{\gamma}))$, $\vec{\Gamma}(1) = \vec{\gamma}$ and $h(\vec{\Gamma}(\phi)) = h(\vec{\gamma})$ for all $\phi \in [0, 1]$. A representation of the configuration of reservoirs $\mathcal{X}$ and their jump rates for different values of ϕ are given in Figure 6.2. The optimal frontiers change dramatically as the heterogeneity in the reservoir jump rates is increased (see Figure 6.2). For heterogeneous reservoir jump rates $\vec{\Gamma}(0.5)$ and $\vec{\Gamma}(1)$, there is negligible additional benefit to adding more edges when the rescaled total edge length reaches 0.5 and 0.3, respectively. Heterogeneity in the reservoir jump rates has dramatically reduced the number of edges needed to achieve the global minimum equilibration times. Future work will be to study the differences in topological properties of optimal networks between configurations of reservoirs with homogeneous and heterogeneous reservoir jump rates.

Note that the configurations of reservoirs presented in this section as well as in Chapter 3, can be considered a representation of the pore space within porous environments [32, 33]. As such, the preliminary results in this section suggest that heterogeneity in the spatial structure of porous media may significantly increase the efficiency of transport processes with crowding effects.

6.2.3 Tagged particle dynamics

Over the past few decades fluorescent microscopy and high resolution imaging techniques have become widely available, resulting in a surge of particle tracking of single molecules within living cells [169, 170]. These techniques have been used to study

[1]The equilibrium density in Equation (3.7) is a function of the harmonic mean $h(\vec{\gamma})$. By insisting that the harmonic mean be kept constant, we can consider the heterogeneity of reservoir rates whilst the networks maintain a constant narrow channel density.

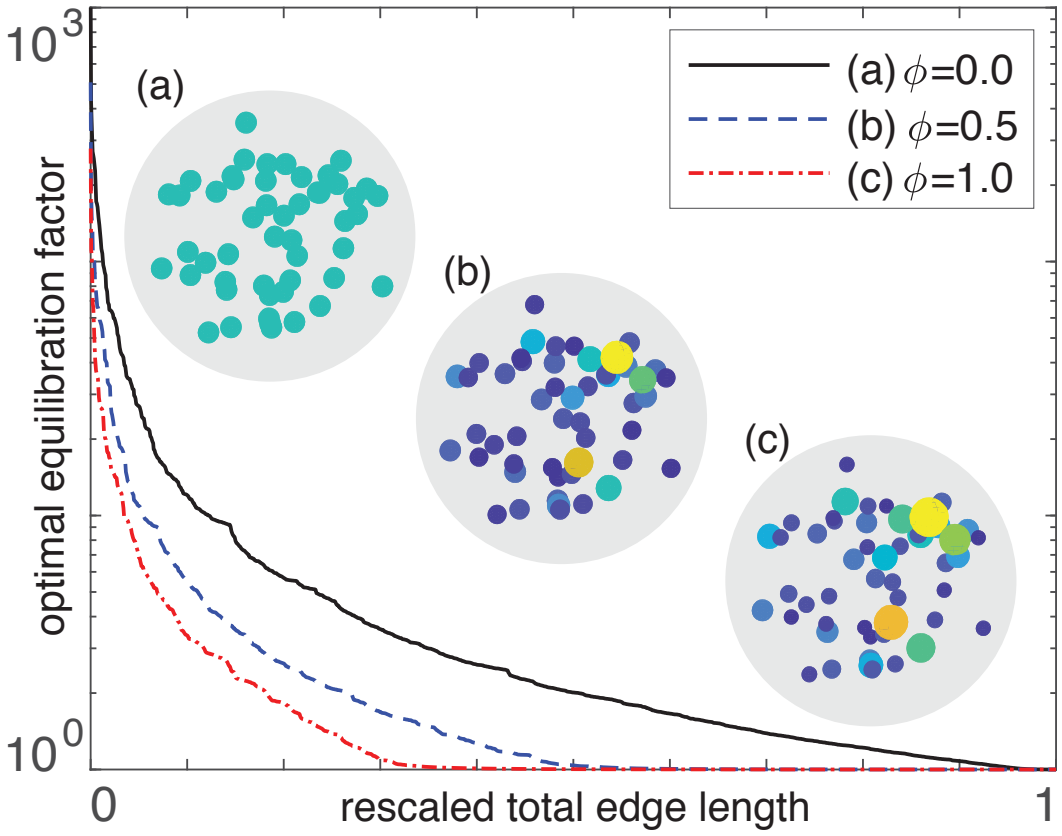

Figure 6.2: Optimal frontiers for a configuration of 50 reservoirs with the reservoir jump rates given by $\vec{\Gamma}(\phi)$, for values $\phi = 0$ (solid curve), $\phi = 0.5$ (dashed curve) and $\phi = 1$ (dot-dashed curve). The inset diagrams ((a)–(c)) represent the configuration of reservoirs and their size and colour represent the heterogeneity in the reservoir jump rates. The volumes of each sphere is inversely proportional to the reservoir jump rate, such that the total volume of spheres is conserved. The optimal frontiers are estimated using the spectral gap algorithm presented in Section 3.3.4.

the motion of organelles such as mitochondria, and even the motions of individual lipids and proteins within the cellular membrane and the cytoplasm [171, 172]. In particular the cytoplasm is reported to be a highly porous environment with up to a quarter of the free space occupied with macromolecules [35]. The work presented in Chapters 2 and 3 model the transport of interacting particles at the population level. Future work will extend the framework introduced in Chapter 2 to allow for tracking the position of a tagged particle (see Figure 6.3). We briefly outline how tagged particle dynamics will be incorporated in the two reservoir model in the high

density regime. Let $\vec{S}_m(t) = (L(t), N_1(t), \ldots, N_K(t), R(t))$ be a state vector for the configuration of m particles, i.e. $L(t) + \sum_{k=1}^{K} N_k(t) + R(t) = m$. Then a population of N particles where one particle is tagged can be described by the state vector $\vec{S}_{\text{tp}}(t) = (\vec{S}_1(t), \vec{S}_{N-1}(t))$, where the position of the tagged particle and the configuration of the $N-1$ background particles are split into two separate vectors. The corresponding FMM has higher dimensionality than the FMM in Chapter 2, thus the need for RMMs is even more prevalent. Similar to the particle switching time and the vacancy switching time seen in Chapter 2, we introduce the tagged particle switching time, $T_{\text{tp,switch}}$, as the time taken for the tagged particle initially in one reservoir (see Figure 6.3 (a)) to enter the internal narrow channel lattice sites (see Figure 6.3 (b)) and subsequently be absorbed into the opposite reservoir (see Figure 6.3 (c)). The tagged particle switching time can be written as follows

$$T_{\text{tp,switch}} = \sum_{j=1}^{G_{\text{tp}}} T^j_{\text{tp,enter}} + T^j_{\text{tp,absorb}}, \tag{6.15}$$

where G_{tp} is a geometric random variable and represents the number of times the tagged particle enters the narrow channel before finally being absorbed in the opposite reservoir. The variables $T^j_{\text{tp,enter}}$ and $T^j_{\text{tp,absorb}}$ are the times taken for a tagged particle to enter the second lattice site, and the subsequent time taken for a particle to be absorbed at either reservoir, respectively. The average time taken for a tagged particle to switch reservoirs is

$$\langle T_{\text{tp,switch}} \rangle = \langle G_{\text{tp}} \rangle \left(\langle T_{\text{tp,enter}} \rangle + \langle T_{\text{tp,absorb}} \rangle \right). \tag{6.16}$$

Future work will be to calculate the moments in Equation (6.16). In order for the tagged particle to switch reservoirs there needs to be a net exchange of K particles from one reservoir to the other. Therefore, the rates at which a tagged particle moves along the narrow channel are not constant and depend upon the occupancy of

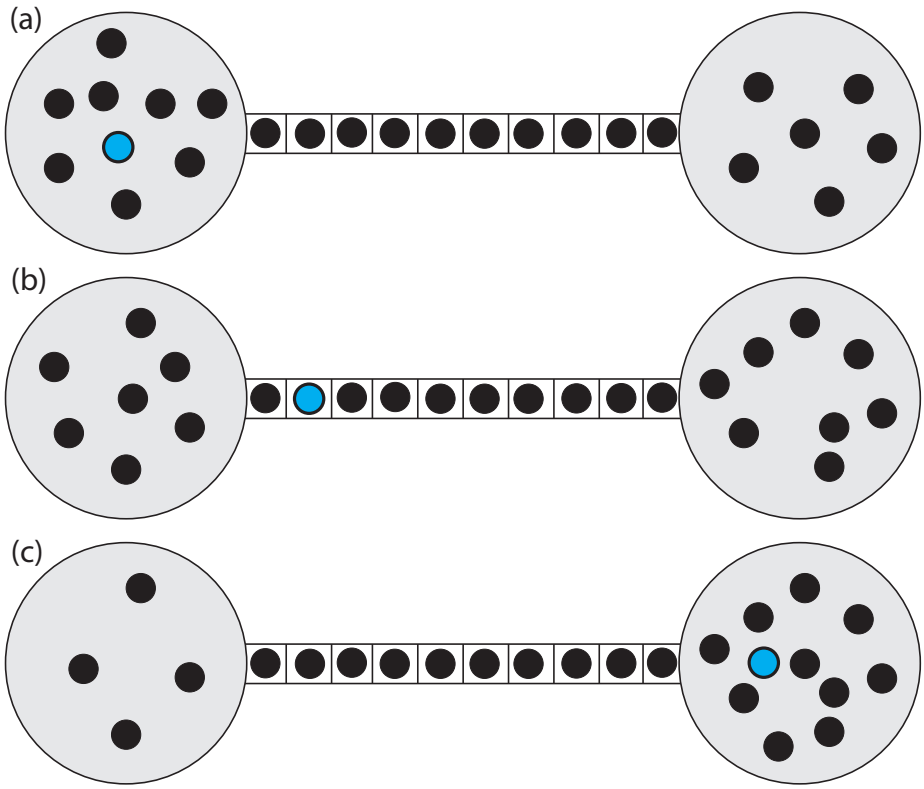

Figure 6.3: A diagrammatic representation of tagged particle dynamics in the high density regime. (a) The tagged particle is initially in the left reservoir. (b) The tagged particle has entered the internal lattice sites of the narrow channel. (b) The tagged particle has reached the right reservoir, and the occupancy of each reservoir is quite different to the initial configuration (a).

the reservoirs. However, at the very least the recurrence relations, from which first passage properties of the tagged particle are calculated, can be solved numerically. Once the framework for modelling a tagged particle in a two-reservoir model has been formalised, the extension to tagged particle dynamics on general networked topologies will be trivial. The resulting framework will allow for the study of first passage statistics for tagged particle in crowded environments over large length scales. First passage statistics in crowded environments have a range of applicability, from chromatin binding to DNA within the nucleus [170] to ligand binding to receptors within the cellular membrane [173]. The extension to tagged particle dynamics will significantly increase the impact and versatility of our work.

6.2.4 Parameters for realistic geometries

In order to associate the networked environments considered in Chapters 2 and 3 with real world heterogeneous environments we need to select the reservoir jump rates and narrow channel lengths appropriately. As an example, consider the pore-space topographies of several sandstone samples extracted from micro-CT scan data (see Figure 6.4). The maximal-ball algorithm [32] is implemented to construct a representative environment of the pore-space consisting of mutually excluding spheres of distinct radii. We therefore suppose the reservoirs in our framework are spheres with a variety of radii. We further assume that particles within the reservoirs are point particles, such that there are no volume exclusion effects in the reservoirs. Two spherical reservoirs are attached by a narrow cylindrical channel that connects to the surfaces of each reservoir. The reservoir jump rates are calculated via the narrow exit time problem introduced by Schuss et al. [174]. Consider a sphere $\mathcal{S}(R)$ of radius R with a geodesic disc on the surface of the sphere with diameter $\Delta \ll R$. The geodesic disc is a narrow opening on the surface of the sphere and is considered the entrance to a connecting narrow channel with lattice sites of width Δ. A particle performs a Brownian motion within this sphere where the boundary surface is reflecting except for the narrow opening which is absorbing. For a particle with initial position $\vec{y} \in \mathcal{S}(R)$, the mean exit time to hit the geodesic disk is

$$\tau_{\Delta}(\vec{y}) \sim \frac{\pi R^3}{3\Delta D} + \mathcal{O}(1), \tag{6.17}$$

where D is the diffusion coefficient of the particle in the sphere [174]. From Equation (6.17), the time to absorption by the narrow opening is independent of the initial position $\vec{y}$, unless the initial position is within a boundary layer of the narrow opening [174]. For our framework we select the reservoir jump rate to be the reciprocal of this mean exit time. For a reservoir with radius R, the reservoir jump rate is selected to

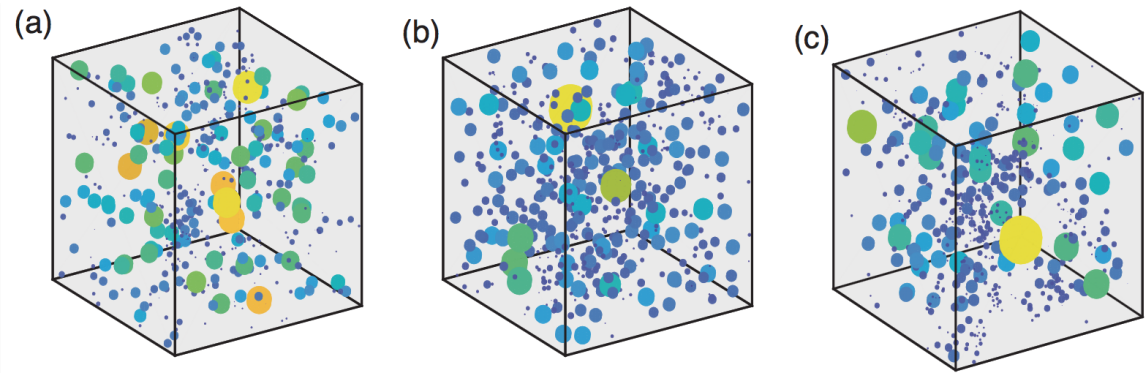

Figure 6.4: The pore space topographies of three different samples of sandstone. The spheres represent the pores and are coloured by their size. The data for the pore-space topographies can be found in Reference [175].

be

$$\gamma = \frac{3\Delta D}{\pi R^3}. \tag{6.18}$$

As the reservoirs now occupy physical space we redefine the length of the narrow channels. For two reservoirs i and j with radii R_i and R_j, respectively, the number of lattice sites in the narrow channel connecting the reservoirs is

$$K_{(i,j)} = \left\lceil \frac{||\vec{x}_i - \vec{x}_j|| - R_i - R_j}{\Delta} \right\rceil. \tag{6.19}$$

Equation (6.19) assumes the narrow channel connecting reservoirs i and j is a cylinder in three-dimensional Euclidean space with a cross sectional diameter Δ. We note that we can widen the diameter of the cylinder to be $C\Delta$, where C is the carrying capacity of the narrow channel lattice sites as seen in Section 2.4. Additionally, tortuosity in the narrow channel can be incorporated by increasing the channel length $K_{(i,j)}$ in Equation (6.19) as necessary. Identifying the FMM with a realistic environment raises two additional questions. The first of which concerns how particles enter and leave the spherical reservoirs in our current framework. The selection of the reservoir jump rate in Equation (6.18) is entirely valid when a particle is well-mixed within the sphere. However, immediately after a particle exits a narrow channel into a

spherical reservoir the position of the particle will be close to the narrow opening on the spheres surface. This is precisely the situation for which the asymptote in Equation (6.17) is no longer valid. A possible solution to overcome this problem is to introduce a two-species model. The first species is a population of well-mixed particles which enter a narrow channel at rate γ_1 in Equation (6.18). A particle that enters the reservoir from a narrow channel, enters as a second species. The particles of the second species can re-enter the narrow channel at a rate γ_2 (most likely much greater than γ) or can transition to becoming well-mixed particles at a rate β. The exact choice of the parameters γ_2 and β would be extracted from a study of Brownian particles in the sphere with initial positions within the boundary layer of the narrow opening. Spatio-temporal correlations have shown to be important for a variety of time sensitive transport processes [176]. It would be of interest to explore the consequences of including spatio-temporal correlations in our framework on equilibration times and tagged particle dynamics.

The second question that arises comes from the construction of the pore-space topographies. The maximal-ball algorithm [32], which extracts the pore representations seen in Figure 6.4, first extracts a representation of the pore-space which allows for overlapping spheres. Any collection of spheres that overlap are then replaced with a single sphere with a radius that reflects the volume of the union of the smaller spheres. Whilst this is highly convenient and allows for the reservoir jump rates to be calculated from the narrow exit time problem on the sphere, the topography of the union of spheres will have a large affect on the true narrow exit times. Future work will be to study the narrow exit time problem on the union of intersecting spheres.

6.3 Conclusion

The research presented in this thesis represents a fundamental first step in revealing the roles that both geometry and crowding have on stochastic transport processes. Each individual study explores the function of network topology on a critical transport statistic. A common theme has been the use of the uncovered functional relationships to design optimal networks, optimal search strategies, and optimal algorithms for network construction. As biological imaging techniques improve and high-level descriptions of intracellular environments become more widely available, it is our hope that the mathematical models presented in this thesis provide the groundwork from which to study the stochastic transport of biomolecules through complex crowded environments.

Bibliography

[1] D. B. Wilson, R. E. Baker, and F. G. Woodhouse. Topology dependent density optima for efficient network exploration. *Phys. Rev. E*, 97:062301, 2018.

[2] D. B. Wilson, R. E. Baker, and F. G. Woodhouse. Displacement of transport processes on networked topologies. *SIAM J. Appl. Math. (In press)*.

[3] J. R. Norris, R. J. Allen, A. T. Evan, M. D. Zelinka, C. W. O'Dell, and S. A. Klein. Evidence for climate change in the satellite cloud record. *Nature*, 536: 72–75, 2016.

[4] K. Marvel, M. D. Zelinka, S. A. Klein, C. Bonfils, P. Caldwell, C. Doutriaux, B. D. Santer, and K. E. Taylor. External influences on modeled and observed cloud trends. *J. Climate*, 28:4820–4840, 2015.

[5] M. Riegler. Insect threats to food security. *Science*, 361:846, 2018.

[6] J. K. Vasir and V. Labhasetwar. Targeted drug delivery in cancer treatment. *Technol. Cancer Res. T.*, 4:363–374, 2005.

[7] M. H. Lighthill and G. B. Whitham. On kinematic waves II: a theory of traffic flow on long, crowded roads. *Proc. R. Soc. London. Ser. A*, 229:317–345, 1955.

[8] M. Papageorgiou. Some remarks on macroscopic traffic flow modelling. *Transpn. Res. A*, 32:323–329, 1998.

[9] S. P. Hoogendoorn and P. H. L. Bovy. State-of-the-art of vehicular traffic flow modelling. *Proc. Instn. Mech. Engrs.*, 215:283–303, 2001.

[10] J. A. Adam. A simplified model of tumour growth. *Math. Biosci.*, 81:229–244, 1986.

[11] H. M. Byrne and M. A. J. Chaplain. Growth of nonnecrotic tumors in the presence and absence of inhibitors. *Math. Biosci.*, 130:151–181, 1995.

[12] E. S. Norris, J. R. King, and H. M. Byrne. Modelling the response of spatially structured tumours to chemotherapy: Drug kinetics. *Math. Comput. Model.*, 43:820–837, 2006.

[13] J. R. Branco, J. A. Ferreira, and P. d Oliveira. Mathematical modeling of efficient protocols to control glioma growth. *Math. Biosci.*, 255:83–90, 2014.

[14] N. Kumar, G. M. Cramer, S. A. Z. Dahaj, B. Sundaram, J. P. Celli, and R. V. Kulkarni. Stochastic modeling of phenotypic switching and chemoresistance in cancer cell populations. *Sci. Rep.*, 9:10845, 2019.

[15] E. Milotti and R. Chignola. Emergent properties of tumor microenvironment in a real-life model of multicell tumor spheroids. *PLOS ONE*, 5:e13942, 2010.

[16] S. Engblom, D. B. Wilson, and R. E. Baker. Scalable population-level modelling of biological cells incorporating mechanics and kinetics in continuous time. *R. Soc. open sci.*, 5:180379, 2018.

[17] P. C. Bressloff and J. M. Newby. Stochastic models of intracellular transport. *Rev. Mod. Phys.*, 85:135–196, 2013.

[18] I. D. Couzin, J. Krause, N. R. Franks, and S. A. Levin. Effective leadership and decision-making in animal groups on the move. *Nature*, 433:513–516, 2005.

[19] C. A. Yates, R. Erban, C. Escudero, I. D. Couzin, J. Buhl, I. G. Kevrekedis, P. K. Maini, and D. J. T. Sumpter. Inherent noise can facilitate coherence in collective swarm motion. *Proc. Natl. Acad. Sci. USA*, 106:5464–5469, 2009.

[20] A. Szabó and R. Mayor. Modelling collective cell migration of neural crest. *Curr. Opin. Cell Biol.*, 42:22–28, 2016.

[21] L. J. Schumacher, P. M. Kulesa, R. McLennan, R. E. Baker, and P. K. Maini. Multidisciplinary approaches to understanding collective cell migration in developmental biology. *Open Biol.*, 6:160056, 2016.

[22] A. Brugués, E. Anon, V. Conte, J. H. Veldhuis, M. Gupta, J. Colombelli, J. J. Muñoz, G. W. Brodland, B. Ladoux, and X. Trepat. Forces driving epithelial wound healing. *Nat. Phys.*, 10:683–690, 2014.

[23] R. J. Ellis and A. P. Minton. Cell biology: Join the crowd. *Nature*, 425:27–28, 2003.

[24] T. Ando and J. Skolnick. Crowding and hydrodynamic interactions likely dominate in vivo macromolecular motion. *Proc. Natl. Acad. Sci. USA*, 107:18547–18462, 2010.

[25] A. Bancaud, S. Huet, N. Daigle, J. Mozziconacci, J. Beaudouin, and J. Ellenberg. Molecular crowding affects diffusion and binding of nuclear proteins in heterochromatin and reveals the fractal organization of chromatin. *EMBO J.*, 28:3785–3798, 2009.

[26] M. Bruna and S. J. Chapman. Excluded-volume effects in the diffusion of hard spheres. *Phys. Rev. E*, 85:011103, 2012.

[27] D. B. Wilson, H. M. Byrne, and M. Bruna. Reactions, diffusion and volume

exclusion in a conserved system of interacting particles. *Phys. Rev. E*, 97: 062137, 2018.

[28] L. Dyson and R. E. Baker. Macroscopic limits of individual-based models for motile cell populations with volume exclusion. *Phys. Rev. E*, 86:031903, 2012.

[29] R. Yuste, A. Majewska, and K. Holthoff. From form to function: Calcium compartmentalization in dendritic spines. *Nat. Neurosci.*, 7:653–659, 2000.

[30] Z. Qu and J. N. Weiss. Dynamics and cardiac arrhythmias. *J. Cardiovasc. Electr.*, 17:1042–1049, 2006.

[31] P. Pathmanathan and R. Gray. Verification of computational models of cardiac electro-physiology. *Int. J. Numer. Methods Biomed. Eng.*, 30:525–544, 2014.

[32] H. Dong and M. Blunt. Pore network extraction from micro-computerized-topography images. *Phys. Rev. E*, 80:036307, 2009.

[33] M. Blunt, B. Bijeljic, H. Dong, O. Gharbi, S. Iglauer, P. Mostaghimi, A. Paluszny, and C. Pentland. Pore-scale imaging and modelling. *Adv. Water Resour.*, 51:197–216, 2013.

[34] E. Moeendarbary, L. Valon, M. Fritzche, A. R. Harris, D. A. Moulding, A. J. Thrasher, E. Stride, L. Mahadevan, and G. T. Charras. The cytoplasm of living cells behaves as a poroelastic material. *Nat. Mater.*, 12:253–261, 2013.

[35] R. J. Ellis. Macromolecular crowding: an important but neglected aspect of the intracellular environment. *Curr. Opin. Struc. Biol.*, 11:114–119, 2001.

[36] L. Dagdug, A. M. Berezhkovskii, S. Y. Shvartsman, and G. H. Weiss. Equilibration in two chambers connected by a capillary. *J. Chem. Phys.*, 119:12473–12478, 2003.

[37] M. Bruna and S. J. Chapman. Diffusion of finite-size particles in confined geometries. *Bull. Math. Biol.*, 76:947–982, 2014.

[38] L. Lizana and Z. Konkoli. Diffusive transport in networks built of containers and tubes. *Phys. Rev. E*, 72:026305, 2005.

[39] M. Karlsson, K. Scott, M. Davidson, A-S. Cans, P. Linderholm, D. Chiu, and O. Orwar. Formation of geometrically complex lipid nanotube-vesicle networks of higher-order topologies. *Proc. Natl. Acad. Sci. USA*, 99:11573–11578, 2002.

[40] J. Liu, N. P. Wickramaratne, S. Z. Qiao, and M. Jaroniec. Molecular-based design and emerging applications of nanoporous carbon spheres. *Nat. Mater.*, 14:763–774, 2015.

[41] L. Liberti and S. Kucherenko. Comparison of deterministic and stochastic approaches to global optimization. *Int. T. Oper. Res.*, 12:263–285, 2005.

[42] D. Normanno, L. Boudaréne, C. Dugast-Darzacq, J. Chen, C. Richter, F. Proux, O. Bénichou, R. Voituriez, X. Darzacq, and M. Dahin. Probing the target search of DNA-binding proteins in mammalian cells using TetR as model searcher. *Nat. Comms.*, 6:7357–7366, 2015.

[43] L. Mirny, M. Slutsky, Z. Wunderlich, A. Tafvizi, J. Leith, and A. Kosmrlj. How a protein searches for its site on DNA: the mechanism of facilitated diffusion. *J. Phys. A-Math. Theor.*, 42:434013, 2009.

[44] R. Sathyapriya, M. S. Vijayabaskar, and S. Vishveshwara. Insights into protein–DNA interactions through structure network analysis. *PLOS Comput. Biol.*, 4: e1000170, 2008.

[45] M. Chupeau, O. Bénichou, and R. Voituriez. Cover times of random searches. *Nat. Phys.*, 11:844–847, 2015.

[46] B. F. Maier and D. Brockmann. Cover time for random walks on arbitrary complex networks. *Phys. Rev. E*, 96:042307, 2017.

[47] J. Ding. On cover times for 2D lattices. *Electron. J. Probab.*, 17:1–18, 2012.

[48] J. D. Kahn, N. Linial, N. Nisan, and M. E. Saks. On the cover time of random walks on graphs. *J. Theor. Prob.*, 2:121–128, 1989.

[49] L. K. Gallos. Random walk and trapping processes on scale-free networks. *Phys. Rev. E*, 70:046116, 2004.

[50] N. Masuda, M. A. Porter, and R. Lamboitte. Random walks and diffusion on networks. *Phys. Rep.*, 716–717:1–58, 2017.

[51] R. Lipowsky and S. Liepelt. Chemomechanical coupling of molecular motors: Thermodynamics, network representations, and balance conditions. *J. Stat. Phys.*, 130:39–67, 2008.

[52] F. G. Woodhouse, A. Forrow, J. B. Fawcett, and J. Dunkel. Stochastic cycle selection in active flow networks. *Proc. Natl. Acad. Sci. USA*, 113:8200–8205, 2016.

[53] A. Kundu, A. Comtet, and S. N. Majumdar. Winding statistics of a Brownian particle on a ring. *J. Phys. A-Math. Theor.*, 47:385001, 2014.

[54] D. J. G. Pearce, A. M. Miller, G. Rowlands, and M. S. Turner. Role of projection in the control of bird flocks. *Proc. Natl. Acad. Sci. USA*, 111:10422–10426, 2014.

[55] M. Rubenstein, A. Cornejo, and R. Nagpal. Programmable self-assembly in a thousand-robot swarm. *Science*, 345:795–799, 2014.

[56] R. McLennan, L. J. Schumacher, J. A. Morrison, J. M. Teddy, D. A. Ridenour, A. C. Box, C. L. Semerad, H. Li, W. McDowell, D. Kay, P. K. Maini, R. E.

Baker, and P. M. Kulesa. Neural crest migration is driven by a few trailblazer cells with a unique molecular signature narrowly confined to the invasive front. *Development*, 142:2014–2025, 2015.

[57] D. S. Bredt and R. A. Nicoll. AMPA receptor trafficking at excitatory synapses. *Neuron*, 40:361–379, 2003.

[58] B. Alberts, A. Johnson, J. Lewis, M. Raff, K. Roberts, and P. Walter. *Molecular Biology of the Cell*. Garland, New York, 5th edition, 2008.

[59] M. J. Saxton. A biological interpretation of transient anomalous subdiffusion. I. qualitative model. *Biophys. J.*, 92:1178–1191, 2007.

[60] T. M. Newpher and M. D. Ehlers. Spine microdomains for postsynaptic signaling and plasticity. *Trends Cell Biol.*, 5:218–227, 2009.

[61] A. Biess, E. Korkotian, and D. Holcman. Diffusion in a dendritic spine: The role of geometry. *Phys. Rev. E*, 76:021922, 2007.

[62] D. Holcman and Z. Schuss. Brownian motion in dire straits. *Multiscale Model. Simul.*, 10:1204–1231, 2012.

[63] A. Biess, E. Korkotian, and D. Holcman. Barriers to diffusion in dendrites and estimation of calcium spread following synpatic inputs. *PLOS Comput. Biol.*, 7:e1002182, 2011.

[64] S. Ghosh, K. Tran, L. M. D. Delbridge, A. J. R. Hickey, E. Hanssen, E. J. Crampin, and V. Rajagopal. Insights on the impact of mitochondrial organisation on bioenergetics in high-resolution computational models of cardiac cell architecture. *PLOS Comput. Biol.*, 14:e1006640, 2018.

[65] S. M. Ross. *Introduction to Probability Models*. Academic Press, San Diego, 9th edition, 2007.

[66] M. J. Simpson, J. A. Sharp, and R. E. Baker. Distinguishing between mean-field, moment dynamics and stochastic descriptions of birth-death movement processes. *Physica A*, 395:236–246, 2014.

[67] R. E. Baker and M. J. Simpson. Correcting mean-field approximations for birth-death-movement processes. *Phys. Rev. E*, 82:041905, 2010.

[68] D. C. Markham, M. J. Simpson, P. K. Maini, E. A. Gaffney, and R. E. Baker. Incorporating spatial correlations into multispecies mean-field models. *Phys. Rev. E*, 88:052713, 2013.

[69] S. Redner. *A Guide to First-Passage Processes*. Cambridge University Press, New York, 1st edition, 2001.

[70] J. Abate and W. Whitt. A unified framework for numerically inverting Laplace transforms. *INFORMS J. Comput.*, 18:408–421, 2006.

[71] H. Risken. *The Fokker–Planck Equation: Method of Solution and Applications*. Springer, Berlin, 1st edition, 1989.

[72] H. van Beijeren, K. W. Kehr, and R. Kutner. Diffusion in concentrated lattice gases. III. Tracer diffusion on a one-dimensional lattice. *Phys. Rev. B*, 28: 5711–5723, 1983.

[73] A. R. Pries, T. W. Secomb, and P. Gaehtgens. Biophysical aspects of blood flow in the microvasculature. *Cardiovasc. Res.*, 32:654–667, 1996.

[74] B. Hille. *Ion Channels of Excitable Membranes*. Sinauer, Sunderland, 1st edition, 2001.

[75] P. R. Taylor, R. E. Baker, M. J. Simpson, and C. A. Yates. Coupling volume-excluding compartment-based models of diffusion at different scales: Voronoi and pseudo-compartment approaches. *J. R. Soc. Interface*, 13:20160336, 2016.

[76] D. M. Tartakovsky and M. Dentz. Diffusion in porous media: Phenomena and mechanisms. *Transport Porous Med.*, 129:1–23, 2019.

[77] I. Medved and R. Černý. Surface diffusion in porous media: a critical review. *Micropor. Mesopor. Mat.*, 142:405–422, 2011.

[78] V. Rajagopal, G. Bass, S. Ghosh, H. Hunt, C. Walker, E. Hanssen, E. Crampin, and C. Soeller. Creating a structurally realistic finite element geometric model of a cardiomyocyte to study the role of cellular architecture in cardiomyocyte systems biology. *J. Vis. Exp.*, 134:e56817, 2018.

[79] C. Bergemann, P. Elter, R. Lange, V. Weißmann, H. Hansmann, E.-D. Klinkenberg, and B. Nebe. Cellular nutrition in complex three-dimensional scaffolds: a comparison between experiments and computer simulations. *Int. J. Biomater.*, 2015:584362, 2015.

[80] T. Kühn, T. O. Ihalainen, J. Hyväluoma, N. Dross, S. F. Willman, J. Langowski, M. Vihinen-Ranta, and J. Timonen. Protein diffusion in mammalian cell cytoplasm. *PLOS ONE*, 6:e22962, 2011.

[81] `https://wikis.bris.ac.uk/display/ipshe/London+Tube`.

[82] V. Colizza, R. Pastor-Sattoras, and A. Vespignani. Reaction-diffusion processes and metapopulation models in heterogeneous networks. *Nat. Phys.*, 3:276–282, 2007.

[83] M. E. J. Newman. *Networks: An Introduction*. Oxford University Press, 1st edition, 2010.

[84] T. G. Baychev, A. P. Jivkov, A. Rabbani, A. Q. Raeini, Q. Xiong, T. Lowe, and P. J. Withers. Reliability of algorithms interpreting topological and geometric

properties of porous media for pore network modelling. *Transport Porous Med.*, 128:271–301, 2019.

[85] K. Chatterjee, F. W. Pratiwi, F. C. M. Wu, P. Chen, and B. C. Chen. Recent progress in light sheet microscopy for biological applications. *Appl. Spectrosc.*, 72:1137–1169, 2018.

[86] G.-W. Li, O. G. Berg, and J. Elf. Effects of macromolecular crowding and DNA looping on gene regulation kinetics. *Nat. Phys.*, 5:294–297, 2009.

[87] R. C. Prim. Shortest connection networks and some generalizations. *Bell Syst. Tech. J.*, 36:1389–1401, 1957.

[88] O. Bénichou, C. Loverdo, M. Moreau, and R. Voituriez. Intermittent search strategies. *Rev. Mod. Phys.*, 83:81–129, 2011.

[89] J.-F. Rupprecht, O. Bénichou, and R. Voituriez. Optimal search strategies of run-and-tumble walks. *Phys. Rev. E*, 94:012117, 2016.

[90] M. Coppey, O. Bénichou, R. Voituriez, and M. Moreau. Kinetics of target site localization of a protein on DNA: a stochastic approach. *Biophys. J.*, 87: 1640–1649, 2004.

[91] F. Bartmeus and J. Catalan. Optimal search behaviour and classical foraging theory. *J. Phys. A-Math. Theor.*, 42:434002, 2009.

[92] M. L. Heuzé, P. Vargas, M. Chabaud, M. Le Berre, Y. J. Liu, O. Collin, P. Solanes, R. Voituriez, M. Piel, and A. M. Lennon-Duménil. Migration of dendritic cells: Physical principles, molecular mechanisms, and function implications. *Immunol. Rev.*, 256:240–254, 2013.

[93] G. M. Viswanathan, E. P. Raposo, and M. G. E da Luz. Lévy flights and superdiffusion in the context of biological encounters and random searches. *Phys. Life Rev.*, 5:133–150, 2008.

[94] G. M. Viswanathan, S. V. Buldyrev, S. Havlin, M. G. E da Luz, E. P. Raposo, and H. E. Stanley. Optimizing the success of random searches. *Nature*, 401: 911–914, 1999.

[95] E. A. Codling, M. J. Plank, and S. Benhamou. Random walks in biology. *J. R. Soc. Interface*, 5:813–834, 2008.

[96] K. Schwarz, Y. Schröder, B. Qu, M. Hoth, and H.Rieger. Optimality of spatially inhomogeneous search strategies. *Phys. Rev. Lett.*, 117:068101, 2016.

[97] M. Herty and A. Klar. Modelling, simulation, and optimization of traffic flow networks. *SIAM J. Sci. Comput.*, 25:1066–1087, 2008.

[98] N. Bellomo and C. Dogbe. On the modelling of traffic and crowds: a survey of models, speculations, and perspectives. *SIAM Rev.*, 53:409–463, 2011.

[99] A. Fügenschuh, M. Herty, A. Klar, and A. Martin. Combinatorial and continuous models for the optimization of traffic flows on networks. *SIAM J. Optim.*, 16:1155–1176, 2006.

[100] L. A. Adamicand R. M. Lukose, A. R. Puniyani, and B. A. Huberman. Search in power-law networks. *Phys. Rev. E*, 64:046135, 2001.

[101] A. Kundu, S. N. Majumdar, and G. Schehr. Exact distributions of the number of distinct and common sites visited by n independent random walkers. *Phys. Rev. Lett.*, 110:220602, 2013.

[102] S. N. Majumdar, S. Sabhapandit, and G. Schehr. Exact distributions of cover

times for N independent random walkers in one dimension. *Phys. Rev. E*, 94: 062131, 2016.

[103] C. S. O. Yokoi, A. Hernández-Machado, and L. Ramírez-Piscina. Some exact results for the lattice covering time problem. *Phys. Lett. A*, 145:82–86, 1990.

[104] M. J. A. M. Brummelhuis and H. J. Hilhorst. Covering of a finite lattice by a random walk. *Physica A*, 176:387–408, 1991.

[105] V. Tejedor, O. Bénichou, and R. Voituriez. Global mean first-passage times of random walks on complex networks. *Phys. Rev. E*, 80:065194, 2009.

[106] B. Meyer, E. Agliari, O. Bénichou, and R. Voituriez. Exact calculations of first-passage quantities on recursive networks. *Phys. Rev. E*, 85:026113, 2012.

[107] J. Palacios. On hitting and cover times via electric networks. *Braz. J. Probab. Stat.*, 17:127–133, 2003.

[108] J. Jonasson. On the cover times for random walks on random graphs. *Comb. Probab. Comput.*, 7:265–279, 1998.

[109] T. Weng, J. Zhang, M. Small, and P. Hui. Multiple random walks on complex networks: a harmonic law predicts search time. *Phys. Rev. E*, 95:052103, 2017.

[110] T. Liggett. *Stochastic Interacting Systems: Contact, Voter and Exclusion Processes*. Springer, Berlin, 1st edition, 1999.

[111] M. J. Simpson, B. D. Hughes, and K. A. Landman. Diffusing populations: ghosts or folks? *Australas. J. Eng. Ed.*, 15:59–68, 2009.

[112] M. J. Plank and M. J. Simpson. Models of collective cell behaviour with crowding effects: comparing lattice-based and lattice-free approaches. *J. R. Soc. Interface*, 9:2983–2996, 2012.

[113] D. Chowdhury, A. Schadschneider, and K. Nishinari. Physics of transport and traffic phenomena in biology: from molecular motors and cells to organisms. *Phys. Life Rev.*, 2:318–352, 2005.

[114] I. R. Graf and E. Frey. Generic transport mechanisms for molecular traffic in cellular protrusions. *Phys. Rev. Lett.*, 118:128101, 2017.

[115] I. Neri, N. Kern, and A. Parmeggiani. Totally asymmetric simple exclusion process on networks. *Phys. Rev. Lett.*, 107:068702, 2011.

[116] M. Plischke, Z. Rácz, and D. Liu. Time-reversal invariance and universality of two-dimensional growth models. *Phys. Rev. B*, 35:3485–3495, 1987.

[117] C. Kipnis. Central limit theorems for infinite series of queues and applications to simple exclusion. *Ann. Probab.*, 14:397–408, 1986.

[118] L. Lovász. Random walks on graphs: a survey. *Combinatorics, Paul Erdös is eighty*, 2:1–46, 1993.

[119] L. Lizana and T. Ambjörnsson. Single-file diffusion in a box. *Phys. Rev. Lett.*, 100:200601, 2008.

[120] C. Lutz, M. Kollmann, and C. Bechinger. Single-file diffusion of colloids in one-dimensional channels. *Phys. Rev. Lett.*, 93:026001, 2004.

[121] Q. Wei, C. Bechinger, and P. Leiderer. Single-file diffusion of colloids in one-dimensional channels. *Science*, 287:625–627, 2000.

[122] T. Imamura, K. Mallick, and T. Sasamoto. Large deviations of a tracer in the symmetric exclusion process. *Phys. Rev. Lett.*, 118:160601, 2017.

[123] P. l. Krapivsky, K. Mallick, and T. Sadhu. Large deviations in single-file diffusion. *Phys. Rev. Lett.*, 113:078101, 2014.

[124] M. E. J. Newman and D. J. Watts. Renormalization group analysis of the small-world network model. *Phys. Lett. A*, 263:341–346, 1999.

[125] H. Chen and F. Zhang. Resistance distance and the normalized Laplacian spectrum. *Discrete Appl. Math.*, 155:654–661, 2007.

[126] B. C. Ross. Mutual information between discrete and continuous data sets. *PLOS ONE*, 9:e87357, 2014.

[127] K. S. Chong, R. Cowan, and L. Holst. The ruin problem and cover times of asymmetric random walks and Brownian motions. *Adv. Appl. Probab.*, 32: 177–192, 2000.

[128] A. Caspi, R. Granek, and M. Elbaum. Enhanced diffusion in active intracellular transport. *Phys. Rev. Lett.*, 85:5655–5658, 2000.

[129] T. Becker, K. Nelissen, B. Cleuren, B. Partoens, and C. Van den Broeck. Diffusion of interacting particles in discrete geometries. *Phys. Rev. Lett.*, 111:110601, 2013.

[130] A. Aman and T. Piotrowski. Cell migration during morphogenesis. *Dev. Biol.*, 341:20–33, 2010.

[131] M. A. Welte. Bidirectional transport along microtubules. *Curr. Biol.*, 14:R525, 2004.

[132] M. J. Kim, H. W. Coo, J. Kim, H. Kim, and B. J. Sung. Translational and rotational diffusion of a single nanorod in unentangled polymer melts. *Phys. Rev. E*, 92:042601, 2015.

[133] R. Junevicius and M. Bogdevicius. Mathematical modelling of network traffic flow. *Transport*, 24:333–338, 2009.

[134] G. Asaithambi, V. Kanagaraj, K. K. Srinivasan, and R. Sivanandan. Study of traffic flow characteristics using different vehicle-following models under mixed traffic conditions. *Transp. Lett.*, 10:92–103, 2018.

[135] R. L. Hughes. A continuum theory for the flow of pedestrians. *Transport. Res. B-Meth.*, 36:507–535, 2002.

[136] O. Bénichou, P. Illien, G. Oshanin, A. Sarracino, and R. Voituriez. Diffusion and subdiffusion of interacting particles on comblike structures. *Phys. Rev. Lett.*, 115:220601, 2015.

[137] R. Burioni, D. Cassi, G. Giusiano, and S. Regina. Anomalous diffusion and hall effect on comb lattices. *Phys. Rev. E*, 67:016116, 2003.

[138] P. Illien and O. Bénichou. Propagators of random walks on comb lattices of arbitrary dimension. *J. Phys. A-Math. Theor.*, 49:265001, 2016.

[139] E. Agliari, D. Cassi, L. Cattivelli, and F. Sartori. Two-particle problem in comblike structures. *Phys. Rev. E*, 93:052111, 2016.

[140] A. Bhattacharya. Random walk for interacting particles on a Sierpinski gasket. *Phys. Rev. E*, 49:4946–4949, 1994.

[141] R. A. Guyer. Diffusion in Sierpinski gaskets: A random walker on a fractually stuctured object. *Phys. Rev. A*, 29:2751–2755, 1984.

[142] C. Schulzky, A. Franz, and K. H. Hoffmann. Resistance scaling and random walk dimensions for finitely ramified Sierpinski carpets. *SIGSAM Bull.*, 34:1–8, 2000.

[143] R. Dasgupta, T. K. Ballabh, and S. Tarafdar. Scaling exponents for random walks on Sierpinski carpets and number of distinct sites visited: a new algorithm for infinite fractal lattices. *J. Phys. A-Math. Gen.*, 32:6503–6516, 1999.

[144] J. J. Kozak. Random walks on the Menger sponge. *Chem. Phys. Lett.*, 275: 199–202, 1997.

[145] Z. G. Huang, X. J. Xu, Z. X. Wu, and Y. H. Wang. Walks on Apollonian networks. *Eur. Phys. J.*, 51:549–553, 2006.

[146] B. B. Mandelbrot Y. Gefen and A. Aharony. Critical phenomena on fractal lattices. *Phys. Rev. Lett.*, 45:855–858, 1980.

[147] R. Haber, J. Prehl, K. H. Hoffmann, and H. Herrmann. Random walks of orientated particles on fractals. *J. Phys. A-Math. Theor.*, 47:155001, 2014.

[148] J. Rudnick and Y. Hu. The winding angle distribution of an ordinary random walk. *J. Phys. A-Math. Gen.*, 20:4421–4438, 1987.

[149] D. R. Nelson. Vortex entanglement in high TC superconductors. *Phys. Rev. Lett.*, 60:1973–1976, 1988.

[150] F. Spitzer. Some theorems concerning two-dimensional Brownian motion. *Trans. Am. Math. Soc.*, 87:187–197, 1957.

[151] A. Comtet, J. Desbois, and S. Ouvry. Winding of planar Brownian curves. *J. Phys. A-Math. Gen.*, 23:3563–3572, 1990.

[152] S. J. Chapman and A. Shabala. Effective transport properties of lattices. *SIAM J. Appl. Math.*, 77:1631–1652, 2017.

[153] M. Barlow, J. Pitman, and M. Yor. On Walsh's Brownian motions. *Lecture Notes in Math.*, 1372:275–293, 1989.

[154] P. L. Krapivsky, S. Redner, and E. Ban-Naim. *A Kinetic View of Statistical Physics*. Cambridge University Press, Cambridge, 1st edition, 2010.

[155] C. Monthus and C. Texier. Random walk on the Bethe lattice and hyperbolic Brownian motion. *J. Phys. A-Math. Gen.*, 29:2399–2409, 1996.

[156] R. Metzler and J. Klafter. The random walk's guide to anomalous diffusion: A fractional dynamics approach. *Phys. Rep.*, 339:1–77, 2000.

[157] R. Hilfer and L. Anton. Fractional master equations and fractal time random walks. *Phys. Rev. E*, 51:R848, 1995.

[158] R. Metzler and J. Klafter. Boundary value problems for fractional diffusion equations. *Physica A*, 278:107–125, 1999.

[159] S. Ganguly, L. S. Williams, I. M. Palacios, and R. E. Goldstein. Cytoplasmic streaming in Drosophilia oocytes varies with kinesin activity and correlates with the microtubule cytoskeleton architecture. *Proc. Natl. Acad. Sci. USA*, 109:15109–15114, 2012.

[160] R. Nieuwburg, D. Nashchekin, M. Jakobs, A. P. Carter, P. K. Trong, R. E. Goldstein, and D. St Johnston. Localised dynactin protects growing microtubules to deliver oskar mRNA to the posterior cortex of the Drosophilia oocyte. *eLife*, 6:e27237, 2017.

[161] P. A. Vasquez, E. Palmer Y. Jin, D. Hill, and M. G. Forest. Modeling and simulation of mucus flow in human bronchial epithelial cell cultures – Part I: Idealized axisymmetric swirling flow. *PLOS Comput. Biol.*, 12:e1004872, 2016.

[162] M. A. M. Franker and C. C. Hoogenraad. Microtubule-based transport – basic mechanisms, traffic rules and role in neurological pathogenesis. *J. Cell Sci.*, 126:2319–2329, 2013.

[163] M. A. Welte. Bidirectional transport along microtubules. *Curr. Biol.*, 14:R525, 2004.

[164] A. Kahana, G. Kenan, M. Feingold, M. Elbaum, and R. Granek. Active transport on disordered microtubule networks: The generalized random velocity model. *Phys. Rev. E*, 78:051912, 2008.

[165] A. E. Hafner, L. Santen, H. Rieger, and M. R. Shaebani. Run-and-pause dynamics of cytoskeletal motor proteins. *Sci. Rep.*, 6:37162, 2016.

[166] I. Neri, N. Kern, and A. Parmeggiani. Exclusion processes on networks as models for cytoskeletal transport. *New J. Phys.*, 15:085005, 2013.

[167] Z. Posel, M. Svobada, C. M. Colina, and M. Lisal. Flow and aggregation of rod-like proteins in slit and cylindrical pores coated with polymer brushes: an insight from dissipative particle dynamics. *Soft Matter*, 13:1634–1645, 2017.

[168] J. L. Anderson and J. A. Quinn. Restricted transport in small pores. *Biophys. J.*, 14:130–150, 1974.

[169] K. Ritchie and A. Kusumi. Single-particle tracking image microscopy. *Methods Enzymol.*, 360:618–634, 2003.

[170] S. A. Isaacson, D. M. McQueen, and C. Peskin. The influence of volume exclusion by chromatin on the time required to find specific DNA binding sites by diffusion. *Proc. Natl. Acad. Sci. USA*, 108:3815–3820, 2011.

[171] C. W. Leung, Y. Hong, and B. Z. Tang. Specific imaging and tracking of mitochondria in live cells by a photostable AIE luminogen. *Methods Mol. Biol.*, 1208:21–27, 2015.

[172] S. Jin, P. M. Haggie, and A. S. Verkman. Single-particle tracking of membrane protein diffusion in a potential: Simulation, detection, and application to confined diffusion of CFTR Cl- channels. *Biophys. J.*, 93:1079–1088, 2007.

[173] M. Klummp, A. Scheel, E. Lopaz-Calle, M. Busch, K. J. Murray, and A. J. Pope. Ligand binding to transmembrane receptors on intact cells or membrane vesicles measured in a homogeneous 1-microliter assay format. *J. Bimol. Screen.*, 6:159–170, 2001.

[174] Z. Schuss, A. Singer, and D. Holcman. The narrow escape problem for diffusion in cellular microdomains. *Proc. Natl. Acad. Sci. USA*, 104:16098–16103, 2007.

[175] `https://www.imperial.ac.uk/earth-science/research/research-groups/perm/research/pore-scale-modelling/micro-ct-images-and-networks/`.

[176] K. Takahashi, S. Tănase-Nicola, and P. Rien ten Wolde. Spatio-temporal correlations can drastically change the response of a MAPK pathway. *Proc. Natl. Acad. Sci. USA*, 107:2473–2478, 2010.